A Triple Redundant 3x3-phase Fault Tolerant Permanent Magnet Synchronous Reluctance Machine Drive

By

Bo Wang

A thesis submitted in fulfilment of the requirements for the

degree of

Doctor of Philosophy

Department of Electronic and Electrical Engineering

Faulty of Engineering

The University of Sheffield

November 2017

Abstract

Fault tolerant machine drives are key enabling technologies for safety critical applications such as electric vehicle traction, and aerospace power generation, actuation and propulsion. High performance in healthy conditions and excellent fault tolerance against various faults are required for a fault tolerant drive, however, these two aspects usually conflict with each other. Thus, this PhD study aims to develop a fault tolerant machine drive which exhibits high performance and good fault tolerance, and can be realised in a simple and cost-effective manner.

First, a novel triple redundant 3x3-phase permanent magnet assisted synchronous reluctance machine (PMA SynRM) with segregated windings is proposed. Its performance under healthy conditions and its ability to tolerate various faults with appropriate mitigation measures are investigated and assessed. Based on outcomes of the investigation, a 40kW machine is designed to tolerate all key electrical faults, including the worst single turn short circuit, and is optimised to maximise the efficiency in healthy conditions whilst satisfying the electrical, thermal and mechanical constraints.

To analyse and realise a fault tolerant machine drive, fault modelling and fault detection techniques are essential. Thus, a general model is proposed based on the magneto-motive force (MMF) decomposition. The model is capable of predicting the machine behaviour in various operation modes, including the healthy condition, open circuit, short circuit and inter-turn short circuit fault with different number of turns and different coil locations.

With the aid of the fault modelling technique, a turn fault detection technique is developed using the 2nd harmonics in the instantaneous reactive and active powers as fault indicators for motoring and generating modes, respectively. By cross-reference of the fault indicators of the three 3-phase sets, the technique can detect the turn fault during transient without false alarm.

Abstract

The optimised machine drive is constructed and the developed fault detection technique together with fault mitigation strategies is implemented in a DSP based controller. The performance of the drive under healthy conditions and its fault tolerant capability are validated by extensive tests. The accuracy of the fault modelling and the effectiveness of the detection technique are also experimentally evaluated. The test results demonstrate that the developed fault tolerant machine drive can be a competitive candidate for safety critical applications.

Acknowledgement

The four years' PhD course is coming to the end soon. I have received a lot of help and support which are indispensable for me to finish the PhD. First of all, I would like to thank my supervisor, Prof. Jiabin Wang, for his continuous guidance, support and patience during the four years' journey. I am motivated by his high level academic skill and impressed by his professional work style which will be beneficial for my career in the future. I am grateful to my 2nd supervisor, Dr. Antonio Griffo, for his continuous motivation, interesting discussions and helpful paper revision. I also want to thank Prof. Z. Q. Zhu for his encouragement and guidance.

I would like to thank Dr. Bhaskar Sen, Dr. Xiao Chen, Dr. Vipulkumar I. Patel for their help on my PhD project. I also would like to express my thanks to Mr. Andy Race, Mr. John Wilkinson, Mr. Richard Garraway and Mr. Lawrence Obodo for their efforts in preparing the experimental rig. In addition, I want to thank all the fellow students in the team and all my friends in Sheffield. I will remember those beautiful times with you guys.

Last but not the least, I would like to thank my parents and my parents in law for their unlimited love and support, without which the journey would not have come to an end. I am very grateful to my wife, Linglu Luo, for her unconditional love and endless care, I will never forget the difficult times she paid for my PhD.

List of Symbols and Acronyms

Symbols

Symbol	Description
B	Instantaneous flux density
B_m	Peak value of local flux density
d	Thickness of the lamination
f	frequency
F_k	MMF of set k
F_{ac}^k	MMF AC component of set k
F_{os}^k	MMF offset component of set k
$F_{os}^{i,j}$	MMF offset component of set i induced by set j
$i_k, k = A, B \ldots$	Current in phase k
$i_{dk}, k = 1,2,3$	d-axis current in set k
$i_{qk}, k = 1,2,3$	q-axis current in set k
I_m	Maximum phase current
i_f	Turn fault current
k_f	Stack packing factor

Symbol	Description
k_h	Hysteresis loss coefficient
k_e	Eddy current loss coefficient
L_d	d-axis inductance
L_q	q-axis inductance
MMF_k	MMF induced by currents in set/coil k
n_b	Base speed
n_m	Maximum speed
$n_k(\alpha)$	Turn function of coil k at angular α
$N_k(\alpha)$	Winding function of coil k at angular α
N	Number of turns in each coil
N_f	Number of short circuited fault turns
p	Number of pole pairs
P_p	Peak power
P_r	Rated power
P_{fe}	Total iron loss
P_h	Hysteresis loss
P_e	Eddy current loss

Symbol	Description
P_x	Excess loss
P_h^{oc}	Hysteresis loss in open circuit condition
P_e^{oc}	Eddy current loss in open circuit condition
P_x^{sc}	Excess loss in open circuit condition
P_h^{sc}	Hysteresis loss in short circuit condition
P_e^{oc}	Eddy current loss in short circuit condition
P_x^{sc}	Excess loss in short circuit condition
T_{oc}	Open circuit torque
T_{sc}	Short circuit torque
T_r	Rated torque
T_f	Temperature rise under turn fault condition
T_y	Temperature rise of stator yoke
ΔT_f	Temperature rise due to turn fault current
$u_{dk}, k = 1,2,3$	d-axis voltage in set k
$u_{qk}, k = 1,2,3$	q-axis voltage in set k
V_{dc}	DC link voltage

Symbol	Description
V_m	Phase voltage
V_{oc}	Open circuit voltage
V_{sc}	Short circuit voltage
σ	Conductivity of the lamination material
$\varphi_{dk}, k = 1,2,3$	d-axis flux linkage in set k
$\varphi_{qk}, k = 1,2,3$	q-axis flux linkage in set k
φ_m	Permanent magnet flux linkage
ρ_{oc}	Open circuit torque capability
ρ_{sc}	Short circuit torque capability
ω	Electrical angular speed
ω_c	Bandwidth of current controller

Acronyms

Acronym	Description
CPOR	constant power operating region
DC	direct current
emf	electromotive force

Acronym	Description
FSCW	fractional slot concentrated winding
GA	genetic algorithm
IAP	instantaneous active power
IGBT	insulated-gate bipolar transistor
IPM	interior permanent magnet
IRP	instantaneous reactive power
k-D, k=2,3,4	k dimensional
LPF	low pass filter
MCSA	motor current signal analysis
MMF	magneto-motive force
MOSFET	metal-oxide-semiconductor field-effect transistor
MTPA	maximum torque per Ampere
PMA SynRM	permanent magnet assisted synchronous reluctance machine
PMSM	permanent magnet synchronous machine
RMS	root-mean-square
SQP	sequential quadratic program

Acronym	Description
SRM	switched reluctance machine
SSO	sequential surrogate optimiser
TSC	terminal short circuit

Table of Contents

CHAPTER 1
Introduction to Fault Tolerant Machine Drives

1.1 Background of Fault Tolerant Machine Drives

Advanced electric drive systems are currently the focus of research activities in both academic and industrial venues [1]. A typical electric drive is composed of power converter, control unit, and electric motor as shown in Fig. 1-1. The power converter contains power electronic devices (i.e. IGBT, MOSFET, triac, diode, DC link capacitor etc.) which are responsible for driving the motor. The control unit consists mainly of microcontroller/ microprocessor and its associated electronic circuitry in addition to sensors which are used to provide the current, voltage and rotor position signals. The electric motor delivers controllable torque to its mechanical payload and in doing so converting electric power into mechanical power or vice versa.
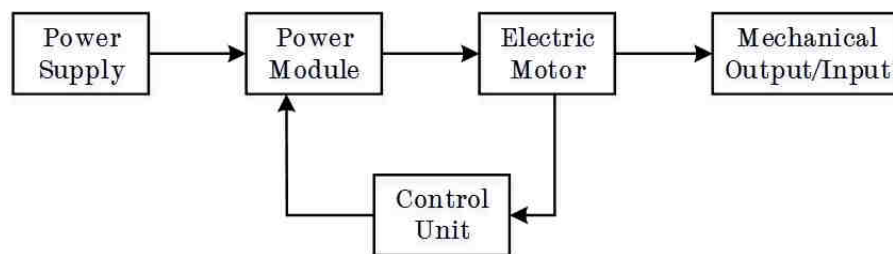
Fig. 1-1 Illustration of an integrated electric drive system

As advanced techniques emerge fast in the areas of machine design, power electronics and microprocessors, electrical drives exhibit desirable features such as high power density, high efficiency, low emission, and flexible regulation etc., compared to other counterparts, namely, mechanical, hydraulic or pneumatic systems [2]. Aircraft employing electrical actuators, electrical propulsion and power generation in terms of more electric aircraft(MEA), hybrid and all electric aircraft(AEA) would gain the merits of weight saving, economical fuel consumption, increased functionality and less maintenance [3]. Another example is the electric vehicle (EV) adopting

electrical machines rather than traditional internal combustion engine (ICE) for low CO_2 emission and environmental-friendly purposes [4, 5]. Although the electrical drives bring the merits of high efficiency and good controllability, high reliability is also an essential requirement for the safety critical applications which should be addressed in design and control [6].

In the aforementioned safety critical applications, the electrical drives are expected to continue operation if fault happens, or at least fail safely without catastrophic damage [7]. Otherwise, the unexpected fault may cause casualties and huge economic loss [8]. The high reliability requirements in safety critical applications produce high impetus to fault tolerance, and become a challenge for the application of electrical systems. Thus, fault tolerance should be considered in the electrical drives to attain the reliability requirement for the targeted applications.

Fault tolerance means the systems are capable of performing at a satisfactory level in the presence of faults. It is a key requirement that has been researched in-depth in various areas, such as fault-tolerant computing system [9], distributed power system [10], and high available internet server. In the area of electrical drives, the fault tolerance mainly means it is capable to maintain the same or an acceptable output torque or power level for the application after suffering a fault. The acceptable level defines minimum output which should be considered at the primary design stage. In many safety critical fields, the electrical drive is required to provide the rated output in the occurrence of a fault [11]. For instance, in [12] a fault tolerant permanent magnet machine for aero engine electric fuel control system was discussed. The application demands that the electrical drive can continue to output full torque with any fault in the stator windings and power converters.

1.2 Frequent Faults in Electric Drives

An electrical drive is a complex electromagnetic system, typical composed of controller, power converter, electric motor and sensors. These components are exposed to the operating environment which influences the reliability of the drive significantly. Fault may occur in each of the components. Studies in

[13, 14] carried out for investigations on the failure distribution in electric machines. The results of the survey show the bearing faults account for the majority of the failures, as much as 51%, followed by stator windings faults, up to 25%. Other faults such as rotor bars, end rings, shaft and other unidentified failures take up the remaining percentage in Fig. 1-2(a). The investigation data in [12] also illustrates the electrical winding failures amount to a failure rate of 1.4×10^{-7} failures per hour in the military machines and 1.0×10^{-6} in the industrial machines. Since these surveys are mainly focused on the induction machines, permanent magnet failure is not included. In fact, demagnetization is a frequent fault for permanent magnet (PM) machines. Demagnetization occurs when the magnetic field in the magnet is forced into the region below the knee point on the BH curve. This may take place either by running the machine at abnormally large current or high temperature [15].

(a)   (b)
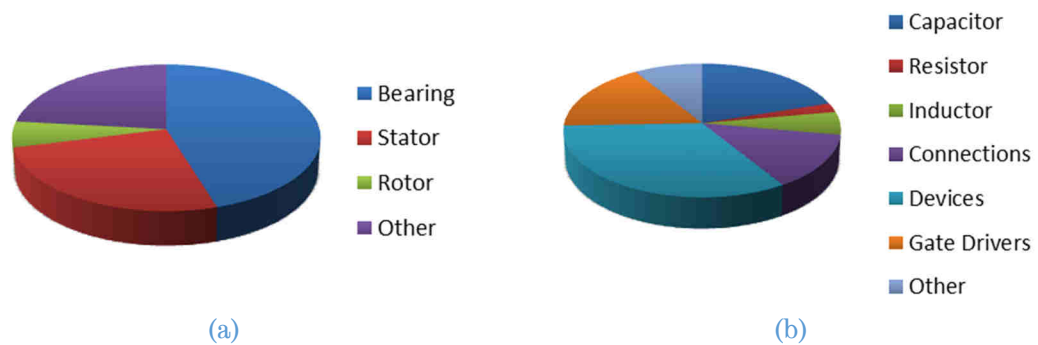
Fig. 1-2 Fault distribution in electrical drives (a) Machine side (b) Converter side

A similar industry survey was conducted on failures in converters in [16]. The survey indicates that the most vulnerable component is the switching devices, followed by capacitors and gate drive circuitry. Open phase in the connections is also a frequent fault. Failures associate with resistors and inductors are quite rare and only observed in a few applications, as shown in Fig. 1-2(b). The survey result shows most IGBT/MOSFET device failures result from thermal and power cycling, with a typical failure rate of 2.78×10^{-6} failures per hour. Additionally, the controller and sensors may also experience faults during operation. In [17] it presents a post-fault control strategy that provides fault tolerance to the major sensor faults which may occur in an electric vehicle propulsion drive system. In a prototype electrical actuator for aircraft

flaps and slats [18], three controllers are employed to control each sub-unit, and a monitoring computer is placed to inspect the operation condition of the multi-lanes. Nevertheless, it should be noted that the probability of the microcontroller and sensor faults is much lower than bearings, windings, power devices and capacitors.
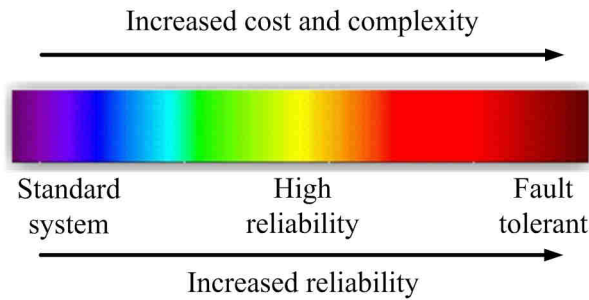
Fig. 1-3 Reliability spectrum

According to the possible faults listed above, there are many failure modes in electric drives. In fact, it is unrealistic to address all possible faults. Otherwise, the fault tolerant system would be tremendously complex with high cost and large size. No system can be thoroughly tolerant to any possible combination of faults. There are always some combinations of failures that would trigger a breakdown of the system. Therefore, not all the failures can be considered and consequently reliability is related to complexity and cost. A frequently-used illustration is the reliability spectrum shown in Fig. 1-3 [10]. A standard system without protection to the faults lies to the left while a system with improved reliability moves to the right, and the system designed to overcome all the possible failures locates in the right. Obviously, increased fault tolerance is in line with the cost and complexity. Thus, only the faults with high likelihood are addressed.

As mentioned above, many potential faults may occur in the system. In this thesis, we mainly focus on the faults in the machine and drive. The principal electromagnetic faults under consideration which may occur within the electrical drives are shown in Table 1-1.

Table 1-1 Potential faults occurring in the machine and drive

Machine side	Drive side
Winding open circuit	Switch device open circuit
Winding inter-phase short circuit	Switch device short circuit
Winding intra-phase short circuit	DC link capacitor failure
Demagnetization	Controller/sensor failure
Uncontrolled generation failure at high speed	

On the machine side, the winding insulation degrades gradually due to the electrical and thermal loading, and finally develops to open circuit and short circuit failure. The short circuit failure can be classified as inter-phase and intra-phase short circuit which occur between phases or in single phase respectively. The intra-phase turn fault is reported as the worst fault scenario since only a few turns are short circuited in the short circuited path. The resultant fault current is massive and the excessive hotspot temperature may lead to catastrophic failure. Demagnetization is another common fault to PM machines due to the excessive armature reaction field. It may cause torque reduction and increased torque ripple, etc.

On the drive side, the switch device is also subjected to open circuit and short circuit failure due to the electrical and thermal stresses. DC link capacitor which provide a transient energy buffer and filter out the voltage ripple across the DC link is exposed to combined voltage and thermal stress during inverter operation, and hence contributes considerable failure rate in electric drives [19]. Gate drive failure may be incorporated into the switch device since its consequence on the drive is the same as that of switch device failure.

Besides, another possible fault is the uncontrolled generation particular for PM machines. If the drive fails when the machine is rotating at high speed, the electromotive fore (emf) may be much higher than the DC link voltage and consequently cause uncontrolled rectification via the freewheeling diodes. This may damage the DC link components if the generated power is excessive and cannot be absorbed [20, 21].

So far, most of the fault tolerant electrical drives focus on the faults described above [8, 12], since the most frequent bearing failure can be significantly reduced by regular maintenance and replacement, whereas the controller and sensor faults can be solved by redundancy and voting mechanism.

1.3 Design Requirements of Fault Tolerant Electrical Machine Drive

The requirements for the fault tolerant systems in other areas have been proposed in [10]. The methodology for the fault tolerant electrical drives is relatively similar. The principal guideline is one fault in the system should be isolated in a sub-unit and has minor effect to the remaining healthy part which can be in place to provide the comparable output. As discussed extensively in existing literature, four design criteria for fault tolerant electrical drives are listed.

Partitioning and Redundancy: A fundamental specification for fault tolerant system is that a single fault would not disrupt the whole system. Therefore the fault must be confined in an independent subsystem. This implies the system should be partitioned into several subunits, and then a fault would only disable the subsystem which would not cause the malfunction of the whole system. When output degradation is not allowed, then redundancy should be introduced to maintain the performance. This can be realized by exploiting a spare module as a backup or overrating all the existing modules which can still meet the output requirement in a faulty condition. The trade-off between the redundancy and cost is an often debate in the final candidate [3].

Fault Isolation: Partitioning alone is not enough to protect the system breakdown from a faulty module, since certain types of fault may affect the remaining healthy subunits or even propagate to the whole system which would lead to more severe consequences. Thus many efforts are employed to

achieve fault isolation. Specifically, magnetic, electrical, thermal and physical isolation are required in fault tolerant electrical drives [11].

Fault Detection: On one hand, fault detection can help the electrical drive to isolate fault by taking appropriate fault mitigation action while on the other hand, continued operation needs fault detection to provide correct information to perform appropriate post-fault control. Fault must be detected before severe results occur. Actually, fault detections are core techniques for fault tolerant electrical drives and require in-depth research.

Continued Operation: The final aim of the drive is continued operation causing minor influence to the safety critical system. Thus, when the faults are correctly identified and well contained, appropriate post-fault control is in need to protect the system and maintain the operation for continued functionality.

The above four requirements should be taken into consideration to design a fault tolerant electric drive systems.

1.4 Current State-of-the-art Techniques of Fault Tolerant Machine Drives

To achieve an integrated fault tolerant machine drive, the techniques of fault tolerant machine drive topology, fault modelling and fault detection are essential to accommodate various failures. The fault tolerant machine drive topology enables the fault isolation and post fault operation while fault detection can identify and classify the faults, and consequently trigger the corresponding mitigation action. The fault modelling technique could help to assess machine performance in both healthy and faulty conditions, and also aid for fault detection development. As a result, they are reviewed and the main challenges are highlighted.

1.4.1 Fault Tolerant Machine Drive Topologies

First, the fault tolerant machine drive topologies are reviewed. Various fault tolerant machine topologies and techniques have been reported and

investigated in literature. The most straightforward approach is to adopt two or more redundant machine drive modules either in series or in parallel as shown in Fig. 1-4 [7, 22]. In case of a failure in one module, the fault is isolated and the other module could continue operation. However, use of multiple machine modules for redundant operation occupies large space and necessitates additional accessories to guarantee its operation in healthy and fault conditions, resulting in low power density and bulky size. Therefore, this approach becomes less attractive.
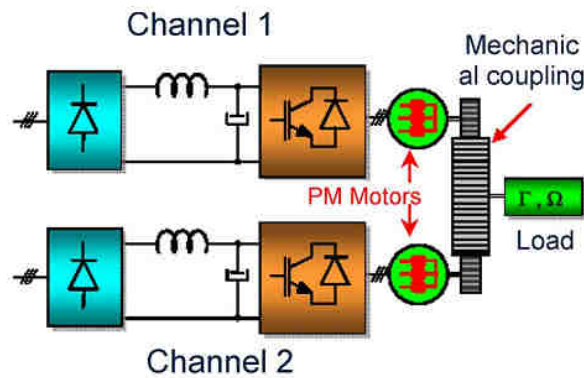
Fig. 1-4 Two machine drive modules in parallel

Alternatively, fault tolerance may be achieved on normal 3-phase machine by employing a neutral connection to the midpoint of the DC link or to a fourth inverter leg as shown in Fig. 1-5 [23]. It can cope with open circuit fault either in the inverter or in the windings. By employing the neutral connection, the two remaining phase currents can be controlled individually. Zero sequence current is utilized to generate the equivalent rotating magneto-motive force (MMF) in the machine if one phase is open-circuited.

(a)   (b)
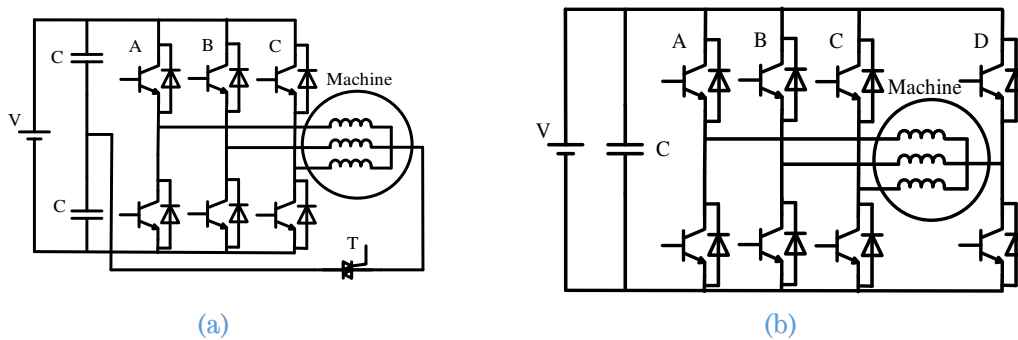
Fig. 1-5 3-phase fault tolerant machine drive (a) Full bridge with DC midpoint (b) Four leg inverter

Another common fault tolerant approach for 3-phase machine is using open end winding drives as shown in Fig. 1-6. Both terminals of a 3-phase winding are available (opened) for connections to dual standard 3-phase inverters. The dual drives can share one DC link or use independent power supplies [24]. They bring the merits of multi-level voltage output, lower dc link voltage, high efficiency and better fault tolerant capability.

(a)

(b)
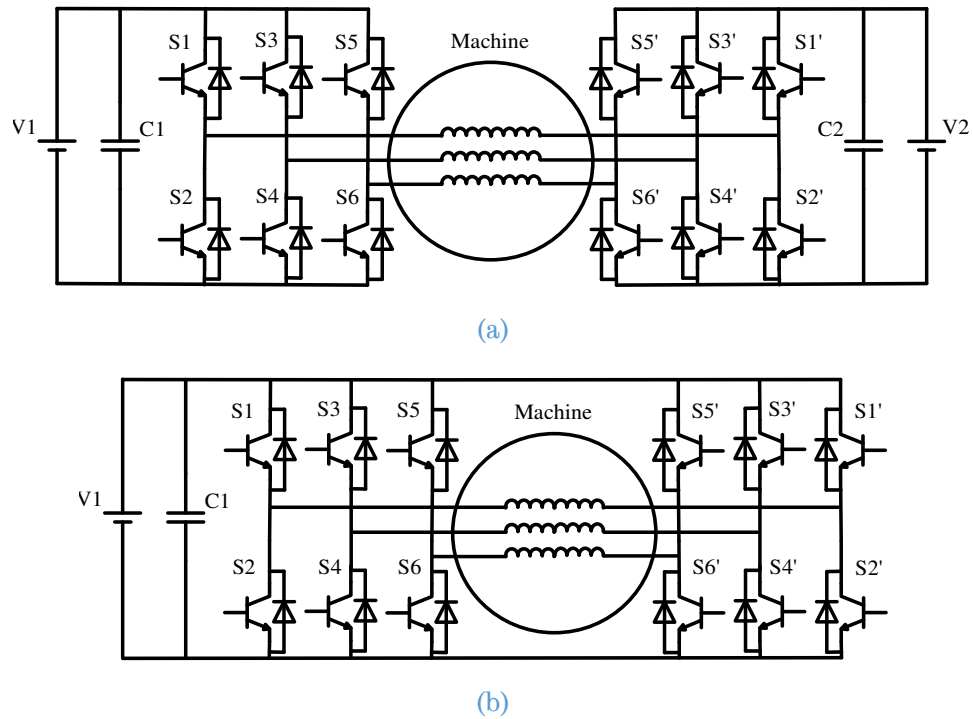
Fig. 1-6 3-phase machine using open end winding drive (a) with independent power supplies (b) with single power supply

As indicated in Fig. 1-6(a), if switch S1' in the right 3-phase inverter is open-circuited, the top three switches are turned-off and the bottom switches are closed to form a star-neutral. The drive can therefore continue to operate with the left inverter only, albeit with halved output power. Similar post-fault operation is adopted in case of switch short-circuit failure. The post fault output capability is half of the healthy state as the available voltage is reduced.

In terms of Fig. 1-6(b), where one DC supply is used for both the inverters, a star neutral cannot be created in the same way. Such a drive is fault tolerant to open-circuit faults only since any short-circuit failure in a device will results in uncontrollable current in the shorted phase. Thus, when S1' suffers from an open-circuit failure, the four switches in that phase are turned-off and

the remaining switches continue to operate with the two phases. In fact, the drive behaves like dual H-bridges and can output 0.58pu power compared to the healthy state, albeit a large torque ripple may result.

The neutral access can be eliminated by employing more than three phases in a single machine as shown in Fig. 1-7 [25, 26]. Depending on the number of phases, a multi-phase (number of phases>3) machine may be capable of continuous operation when one or more than one phase has failed. Multi-phase machine is first investigated for high power applications. By dividing the required power between multiple phases, more than the conventional three phases, higher power levels can be obtained and power electronic converter modules with limited power rating can be used to drive the multi-phase machine. It can also reduce the torque pulsation, lower the DC link harmonic current. And an important merit of multi-phase machine is of high reliability. As described above, a neutral point connecting is required for a 3-phase machine after one phase is open circuited so that the current in the remaining two phases can be controlled independently. However, in a multi-phase machine, it is possible to take advantage of the additional degrees of freedom as a result of more phases. It can still operate in case of an open circuit fault without connecting the neutral point. Five phase, six phase and seven phase machines are most extensively investigated [27-29]. Additionally, various control algorithms have been proposed to achieve the maximum attainable torque, or minimum torque ripple [30-33] under fault conditions.
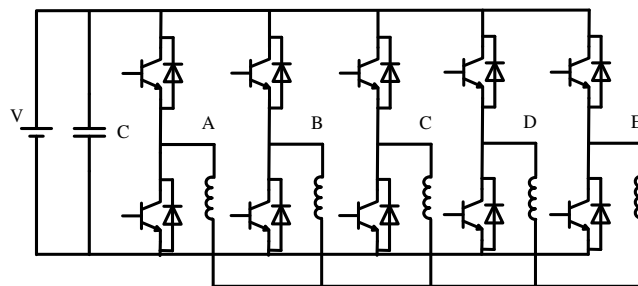

Fig. 1-7 Multi-phase (5-phase for illustration) fault tolerant machine drive

One common disadvantage of the 3-phase and multi-phase fault tolerant machine drive mentioned above is the complex post fault control since the machine no longer operates in a balanced manner. Hence, the machine

windings can be configured as multiple 3-phase windings with each driven by an independent inverter [34] as shown in Fig. 1-8. If a fault occurs in one set of 3-phase windings, the whole set of windings are taken out of service. The remaining sets of windings can continue to keep a balanced operation though with a reduced output. The post-fault strategy remains unchanged as the normal 3-phase machine which can be easily implemented. It should be noted that the strong and undesirable coupling may still exist in different sets of 3-phase windings. Consequently, the short circuit current may be excessive and the torque ripple increases due to the mutual coupling.
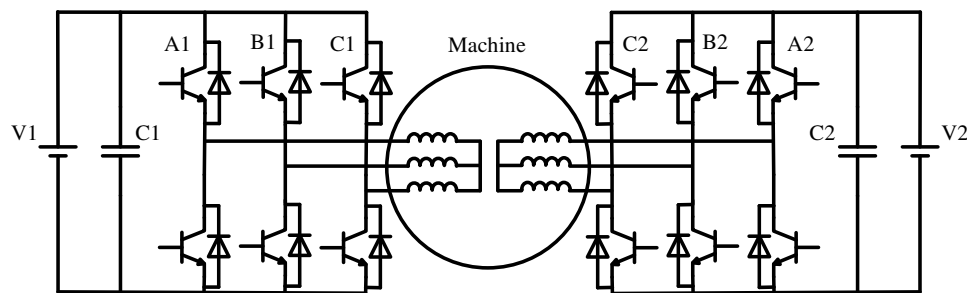
Fig. 1-8 Multiple 3-phase (Dual 3-phase for illustration) fault tolerant machine drive

The concepts mentioned above has been realized in both induction machines, synchronous machines and PM machines [27, 28, 35-37]. However, majorities of the above solutions cannot cope with the short circuit failure.

In order to accommodate short circuit failure in the power electronic switches or phase windings, advanced fault tolerant drives are developed. Owing to its rugged, magnet-free rotor structure and concentrated windings, switched reluctance machine (SRM) is inherently fault tolerant [38, 39]. Each phase winding can be magnetically, thermally and electrically isolated. Due to low mutual coupling between phases, the short circuit current can be limited in a safe region [40]. The isolation is also carried out in the inverter, each phase is excited by an independent asymmetrical half bridge. Thus a failure in one phase either in the winding or the half bridge would not influence the remaining healthy phases' operation. The faulted phase can be removed simply by disabling exciting. Additionally, the power devices in the bridge are in series with the windings, so in case of switch misfiring, there is a delay in the rise of current which prevents shoot-through fault.

However, an SRM exhibits high torque ripple, undesirable noise and vibration, and inferior torque density/efficiency. And it will be worse in fault condition. Furthermore, the machine drive may lose starting ability due to loss of one phase.
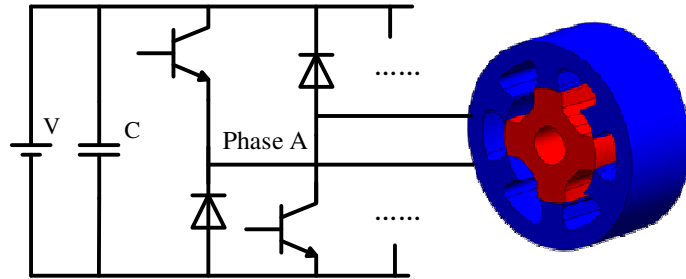
Fig. 1-9 SRM machine drive
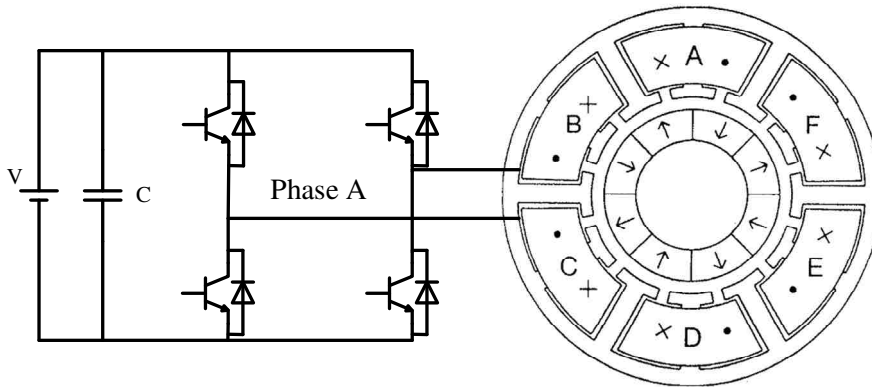
Fig. 1-10 Multi-phase FSCW fault tolerant machine drive

In [41] a single layer fractional slot concentrated winding (FSCW) PM machine is developed as shown in Fig. 1-10 that facilitates electrical, magnetic, thermal, and physical isolations between phases. In this novel topology, each winding is wound on every alternative tooth, so each slot only contains one coil, assuring thermal and physical isolation. With the help of surface mounted magnet and the unwound tooth, the magnetic isolation is also realized. The slot opening is special designed by controlling the depth and width to obtain per-unit armature self-inductance to limit the fault current in a short circuit case. And the modular design philosophy is extended to the inverter with each phase excited by a single phase H-bridge, thus each phase is electrical isolated. The machine is fault tolerant to winding/switch open circuit and short circuit, and even an inter-turn fault by applying terminal short circuit on the fault phase. This methodology has also been extended to switched flux PM machines [42].

Similarly, multiple three phase windings are employed for the FSCW fault tolerant machine as shown in Fig. 1-11 which facilitates the fast integration of standard 3-phase inverters and simple control [43]. Each 3-phase set windings is driven by independent three phase full bridge and can tolerate open circuit, short circuit and inter-turn fault.

Fig. 1-11 Multiple 3-phase FSCW fault tolerant machine drive

However, due to the concentrated windings, very little reluctance torque can be exploited in this type of machine. The output torque of FS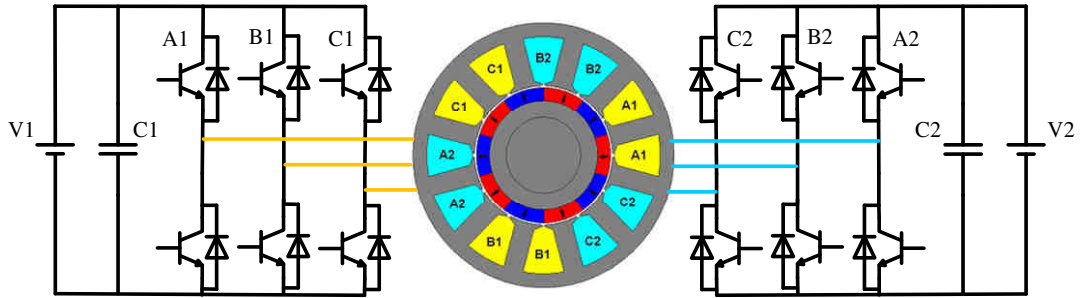CW PM machine purely relies on the PM field and, consequently, increase in torque capability leads to higher flux linkage. The presence of strong PM field poses a safety hazard to the machine as it cannot be turned off in the event of a fault [44]. The back emf may be higher than the DC link voltage at high speeds and uncontrolled rectification via the diodes may occur in case of an inverter failure. Excessive regenerative power which flows to the dc link capacitor may cause catastrophic failure to the drive system. Significant braking torque may also be imposed on the rotor causing excessive stress to the mechanical system or sudden reduction in speed which may induce accidents in traction drives. Thus, the maximum back emf should be limited [45]. However, this is in conflict with the requirements for torque production. It can be shown that if the FSCW machine with limited maximum back-emf is required to operate in a wide constant power range, the VA rating of the inverter increases linearly with the speed, which in turn increases the overall size and cost of the drive [45]. Further, the use of concentric windings also gives rise to sub- and high-order MMF space harmonics which produce extra rotor loss. Hence, the magnets need to be segmented axially or circumferentially to avoid excessive rotor temperature [46]. The magnets are also subject to the risk of

demagnetization in high temperature and in case of a drive failure [47]. The demagnetization leads to torque reduction and increase in machine currents for closed loop controlled drive under the same load condition. The vicious cycle may continue, causing further increase in temperature and demagnetization.

According to the review above, it can be concluded that the conventional 3-phase induction machine and PMSM drives are only fault tolerant to open circuit failure while SRM and FSCW PM machine could tolerate the worst inter-turn fault. Multi-phase machine drive normally has better post-fault torque capability compared to multiple 3-phase counterpart albeit requires complicated control. PM machine has the merits of high efficiency and high torque density. However, the problems of excessive short circuit current and high back emf which may induce uncontrolled generation pose challenges to the system design. In general, no existing topology could achieve high performance as well as good fault tolerance in simple and cost-effective manner.

1.4.2 Fault Modelling Techniques

For a fault tolerant machine drive system, the post-fault behaviour should be carefully assessed to ensure it can cope with the fault and operate satisfactorily during post-fault operation. For example, maximum torque capability should be identified after the fault [48]. New voltage harmonics would appear which pose an extra demand on the voltage if field weakening is required [20]. In addition, in order to optimize the output capability in fault condition, accurate fault modelling is necessary to guide machine design and control strategies leading to higher efficiency and power density [7]. Especially for inter-turn fault, which causes excessive fault current and results in local hotspot, its behaviour should be captured to facilitate the development of diagnostic techniques and corresponding mitigation action [49]. Thus, the fault modelling techniques are being actively investigated.

Inductance-based modelling is commonly employed to describe the machine in both healthy and fault conditions. The inductance value may be

extracted from numerical derivations [50], FE simulations [51] or experimental tests [52]. Based on the closed-form equations, the responses of an interior permanent magnet machine (IPM) to single phase open circuit [53], symmetrical and asymmetrical short circuit faults [54] were investigated. The induction machine was modelled and controlled in [55] considering one phase open circuited. The fault modelling has been extended to multi-phase induction machines by using the inductance matrices [56]. Circuit-oriented method is an alternative way to investigate the induction machine [57] which can model the faults in both stator and rotor sides, such as broken rotor bar. A five phase synchronous reluctance machine with open circuit faults was modelled in the synchronous frame in [58]. The current was controlled in the synchronous frame with zero steady-state error. A novel field reconstruction method was used to analyse the machine performance and vibration [59] for a FSCW PM machine. This method utilizes the fields produced by the current in a single slot and the field from the magnets to reconstruct the field distribution along the airgap with arbitrary current excitation.

It should be noted that most of the modelling methods above consider the machine as a linear system, and hence compromise the model accuracy. The post-fault behaviour can also be evaluated by FE simulations [60]. However, the FE method is quite time consuming, and not suitable for developing fault detection strategies, control methods and performing comprehensive performance assessment over a wide operation region.

Accurate inter-turn fault modelling could improve the understanding of the fault behaviour aiding the development of fault detection algorithms [61]. A survey of modelling techniques suitable for stator turn faults was presented in [62]. In [63], a transient model for an induction machine with inter-turn fault was derived using reference frame transformation theory. In [64], magnetic saturation was considered by using modulation of air gap permeance at twice of the fundamental frequency. Stator turn fault in surface mounted permanent magnet machines was discussed in [51, 65-68]. The inductance value were derived by turn ratio derivation, permeance network

and FE simulation. And the back emf harmonics was considered in [52] to improve the model accuracy. An analytical approach was proposed in [50] to capture the inductance and PM flux. Particularly, the slot leakage inductance, which has significant impact on the turn fault current, was also investigated. It is shown that the leakage inductance is dependent on the slot position of the faulted turns.

An important fact is that, the winding distributions are no longer symmetrical in turn fault conditions. Therefore, the winding distribution and resultant MMF should be modified. The winding function provides a powerful tool to calculate the inductance. The inductances for the fault turn, fault phase and other healthy phases can be obtained by integrating the product of turn function, winding function and airgap permeance as described in [69, 70], assuming linear magnetic characteristics. The theory has been applied in a salient pole synchronous machine with coils in series and in parallel connections [71, 72]. However, for an interior PM (IPM) machine, the magnetic saturation should be considered since it has a crucial influence on the field distribution. In [61], a semi-analytical model of IPM with turn fault was conducted by using the healthy dq flux maps to deduce the flux in fault condition. The magnetic non-linearity was considered in the healthy flux map. Further, a high fidelity model was developed in [73] based on the inverse of a 4 dimensional (4D) table extracted from FE simulation which exhibits high accuracy. However, it can only deal with the turn fault with fixed turns and fixed position (coil location and slot position). The investigations in [49, 74, 75] shows that both the slot location and coil location affect the turn fault current. This location dependency causes significant difference on the fault current and consequently affect fault detection and fault tolerant machine design.

It follows that although various modelling tools are available for fault behaviour prediction, the accuracy, flexibility and computationally efficiency are still limited. Particular for inter-turn fault, the impact of fault turn location on fault behaviour is worth investigation other than simply assuming that it is aligned with a phase axis.

1.4.3 Fault Detection Techniques

Fast and reliable fault detection is of key importance for fail-safe and fault tolerant machine drives in order to immediately trigger appropriate fault mitigation actions and avoid false alarms and associated unnecessary downtime. It includes the detection techniques for winding/device open circuit, short circuit and stator turn fault. The detection of open circuit, short circuit fault of switches and windings can be relatively easily implemented as discussed in [76-78]. However, turn fault is potentially more challenging to detect. This is due to the fact that turn fault typically only involves few turns, resulting in a benign fault signature as seen from machine terminals and consequently a low signal-to-noise ratio. The excessive fault current, however, requires immediate detection and mitigation action. This necessitates a fast and computationally efficient detection within a few tens of milliseconds before developing to a catastrophic failure.

The stator insulation monitoring has been extensively investigated in the literature. A few standard offline methods including the insulation resistance measurement, direct current test, alternating current test, surge comparison test and partial discharge test have been discussed in [79, 80]. Online detecting scheme would be more preferred since it provides continuous stator insulation monitoring and enables the mitigation actions. Benefiting from the features of non-invasive and no additional sensors, most of the online turn fault detection techniques are based on motor current signal analysis (MCSA) by inspecting the stator current spectrum to spot the degradation [81]. In [79, 82], the induction machine insulation failure was detected by tracking the negative sequence current and impedance which was insensitive to the machine slip. In fact, the methods in [83, 84] based on Park's Vector Approach were also employed to monitor the negative sequence current. However, it was shown in [63] that the negative sequence component was not a reliable fault indicator since it does not change in a predicable manner when exposed to the existing asymmetry or supply unbalance. Hence, a more robust fault indicator was developed by making use of the off-diagonal term of the sequence component in the impedance matrix [85, 86]. The disadvantage of this method

was that it is required to store two sets of test data under different voltage unbalance conditions. An alternative way was introduced in [87] by exploiting feedforward neural network to compensate the arbitrary supply voltage and non-idealities in the machine or instrumentation.

In [88-90], the 3rd harmonic in the line current was employed as the fault signature. However, it may be confused by the voltage supply unbalance and machine inherent asymmetry [91]. Inter-turn fault detection using model based approaches was investigated in [92-95] by monitoring the estimation errors. This method required an accurate online model which was usually achieved by adaptive state observer or online learning. In [96], the inter-turn short circuit fault was alarmed by tracking the back emf estimator for a PMSM. The temperature influence on the winding resistance was compensated by a transient thermal model, however, the influence on the PM flux was not considered which may deteriorate the accuracy.

The feasibility of fault detections by injecting high frequency signal was analysed in [97, 98] by measuring the high frequency negative sequence current and further investigated in [99] by monitoring the incremental inductances. It should be noticed that high frequency injection introduced additional noise in the current and violates the voltage limit at high speed. As a result, an advanced method was proposed in [100] by comparing the inherent high frequency PWM current ripple between different phases. The switching inverter was exploited as a natural source of high frequency signal injection into the motor. Therefore, there is no need to inject additional high frequency component, avoiding the undesirable effects.

As is well known, the turn fault current in fundamental frequency breaks the three phase symmetry and gives rise to a 2nd harmonic disturbance in the *dq* axis reference frame. Consequently, the 2nd harmonics emerge in the i_d, i_q and u_d, u_q for both the grid connected machine and closed loop controlled drive. Therefore, they were picked up as the fault indicator and monitored during operation. The amplitude of this spectral component is directly related to the degree of asymmetry of the motor winding. Essentially, the 2nd

harmonics in i_d, i_q are used as fault signal in [101]. Whilst in [102-104], the fault detection was realized by comparing the magnitude of the 2nd harmonics in the control voltage. And it was shown that the turn fault severity is proportional to the 2nd harmonic amplitude. However, the 2nd harmonics are also dependent on the machine operating point, and affected by the controller bandwidth, which complicates the implementation process.

In [105], it was demonstrated that the 2nd harmonic in instantaneous power which is the product of the current and voltage has definite advantages since it carries more information than the single current or voltage signals. Thus, the 2nd harmonics in both the instantaneous active power (IAP) and reactive power (IRP) have been investigated as a means to detect various faults in induction machine [106, 107]. It was shown that the stator turn fault leads to more pronounced 2nd harmonics in the IRP than that in the IAP [108-111]. However, limited simulation and experimental results were provided, and the underlining cause of this trend was not explained.

It should be noted that for the turn fault detection techniques reviewed above, the respective fault indicators vary with speed and load and this variation should be compensated in order to improve sensitivity and robustness of the detection. On the other hand, the speed and load transients usually cause false alarm in harmonic based fault detection techniques which should be eliminated. Last but not least, the classification of different faults is of paramount importance in order to apply appropriate mitigation action.

In summary, the fault-tolerant machine drive topology, fault modelling and fault detection techniques should be further investigated, integrated into a complete drive system and demonstrated.

1.5 Motivation for Doctoral Research Work

Due to their numerous benefits, electric drives are seen as a key enabling technology for many emerging markets, such as transportation where heat engines are currently a dominant prime mover. Recently, electrification of

transport has been under active development in both automotive and aerospace industries to hybridise or replace the conventional powertrain by electric drives. However, high reliability/availability is an essential requirement for these safety critical applications. The failure rate of the electrical drives is higher than that of required applications [12]. A fault in the electrical drives may result in a complete loss of power and lead to an accident. Thus, the various failure modes discussed above should be addressed comprehensively to achieve a reliable product, avoiding the undesirable power loss and unsafe modes of operation.

Fault tolerant machines drives are capable of uninterrupted operation in case of a fault, therefore being favoured by many safety critical applications. An integrated fault tolerant machine drive system contains many key components and subsystems, including advanced machine drive topology, fault tolerant machine design, fault modelling, fault detection and suitable mitigation actions. Each of them requires further research in order to develop the technology to sufficient level of maturity. The advanced machine drive topology needs to achieve the desired fault tolerance without having significant negative impact on the machine performance in healthy condition. The fault tolerant machine design has to ensure that the machine can meet the required torque target in both healthy and fault conditions with optimum performance. Generic and comprehensive fault modelling technique should be developed to predict the machine fault behaviour and to facilitate fault detection and post fault operation. The fault detection and mitigation action will finally realize the fault tolerant operation when a fault occurs. Thus, all these aspects should be investigated to obtain an optimum fault tolerant machine drive.

Besides, various failures may occur in the electrical drives, including the open/short circuit, turn fault, demagnetization and uncontrolled rectification, etc. In the current state of art, most of the fault tolerant machine drives only consider one or two fault scenarios, such as the open circuit and short circuit. Other failures, inter-turn short circuit in particular, are not considered or

fully addressed. However they are likely to occur and cause serious adverse effect. Thus, all these failure modes should be addressed in the machine drives to avoid the unexpected power loss. As illustrated in Fig. 1-3, more faults the system could tolerate, more complicated the system will be. Therefore, it is important to achieve high reliability/availability machine drive at reasonable cost.

Hence, the aim of this doctoral research is to achieve a high reliability/availability fault tolerant machine drive system for the safety critical applications. The main objectives of the research are summarized as follows.

1. To develop a machine drive configuration which could achieve high performance as well as excellent fault tolerance at reasonable cost.

2. To investigate the fault behaviour and fault tolerant capability against various fault scenarios and provide the insights for the design.

3. To design and optimise the machine geometry based on the proposed machine topology against a given set of specifications under electrical, thermal and volumetric constraints in both healthy and fault conditions.

4. To develop a fault modelling technique to understand the proposed machine fault behaviour, including the healthy condition, open circuit, short circuit, inter-turn fault, with and without application of terminal short circuit.

5. To develop a fast and reliable turn fault detection technique for the proposed machine drive to activate the mitigation action.

6. To validate the machine performance and fault tolerance by systematic experimental tests on a prototype machine drive based on the design optimisation.

7. To further improve the machine drive configuration based on the understanding of the proposed machine.

1.6 Main Contributions of the Thesis

With a focus on the development of a high reliability/availability fault tolerant machine drive for safety critical applications, the main contributions of the doctorial work that will be presented in this thesis are outlined as follows:

1. A novel triple redundant 3x3-phase PMA SynRM with full pitched segregated windings has been developed. The machine has high performance in healthy condition while exhibiting excellent fault tolerance against various faults, including the open circuit, short circuit, intra-phase turn fault, inter-phase turn fault, DC link capacitor failure, uncontrolled rectification and demagnetization. The machine drive could be implemented in a simple and cost effective manner.

2. An integrated design procedure for the proposed machine has been established. A 40kW machine has been designed, constructed and tested, which can tolerate the worst case turn fault while satisfying the electrical, thermal and mechanical constraints.

3. A general modelling technique has been developed for the proposed machine which can be used to predict the performance in the healthy operation, open circuit and short circuit. The model is also adapted for turn fault considering the fault location and the impact of terminal short circuit.

4. A fast and reliable turn fault detection algorithm has been developed based on the 2nd harmonics in the instantaneous active and reactive power with high signal to noise ratio. False alarm during speed and load transients can be avoided by cross referencing the fault indicators of different 3-phase sets.

5. A novel PMA SynRM with hybrid pitched segregated windings has been proposed after the investigation of the full pitched winding machine. It has the same healthy performance compared with the full pitched winding machine while exhibiting improved fault tolerance due to the reduced mutual coupling between different 3-phase sets.

1.7 Outline of the Thesis

The thesis is organized in 8 chapters. Each of the chapters can be summarised as follows:

This Chapter introduces the background knowledge of fault tolerant machine drives. The frequent failure modes in electrical drives are explained. To accommodate the fault, common design requirements for the drive system are discussed. This Chapter also reviews the current state of art of fault tolerant machine drives which provides the rationales and insight for the doctoral research work.

A novel triple redundant 3x3-phase PMA SynRM with segregated windings is proposed in **Chapter 2**. Its performance is compared with the conventional 3-phase configuration and the fault tolerance against various faults are investigated. The investigation shows that the proposed machine have high performance in healthy condition while exhibiting excellent fault tolerance. And the machine drive can be implemented in a simple and cost effective manner.

Based on the proposed machine topology in Chapter 2, the design optimisation of a 40kW machine is described in **Chapter 3**. An integrated design procedure is developed. The machine has been optimised to meet the torque target in both healthy and fault conditions while satisfying the electrical, thermal and mechanical constraints. Finally, the performance of the optimised machine is evaluated and presented.

A general modelling technique has been developed in **Chapter 4** considering the healthy operation, open circuit, short circuit and unequal current operation condition. The model has also been adapted for turn fault considering the fault location. The influence of terminal short circuit is also investigated. The accuracy of the model is verified by FE prediction.

To obtain an integrated fault tolerant machine drive, a fast and reliable turn fault detection technique is developed in **Chapter 5** for the proposed machine drive. The 2nd harmonics in the IAP and IRP are developed as fault

indicators. By cross referring the fault indicatorS of different 3-phase sets, false alarm during speed and load transients can be avoided. The effectiveness of the developed detection algorithm is validated by model prediction in various operation conditions.

Based on the design optimisation in Chapter 3, a prototype has been built as presented in **Chapter 6**. A 9 phase inverter, consisting of three 3-phase inverters, is developed to drive machine prototype. The turn fault detection has also implemented in the control system. Systematic experimental tests have been performed on the prototype to examine the machine performance in both healthy and fault conditions. The modelling and turn fault detection techniques developed in Chapter 4 and Chapter 5 are validated by extensive test results. Integrated fault tolerant operation has been demonstrated when a single turn fault occurs.

The previous investigation indicates that mutual coupling exists between the different 3-phase sets. It would cause undesirable effects, such as deteriorated current control, increased torque ripple and fault current. Thus, a novel PMA SynRM with hybrid pitched segregated windings is proposed in **Chapter 7**. The mutual coupling effect is reduced and the fundamental reason is explained. Its performance in both healthy and fault conditions has been compared with the previous machine based on the same machine geometry.

Chapter 8 summarise the doctoral research work on triple redundant 3x3-phase PMA SynRM drive, followed by the future scope of research that can be continued for further improvement of the fault tolerant machine drive.

CHAPTER 2
A Fault Tolerant Machine Drive Based on PMA SynRM with Segregated Windings

2.1 Introduction

Fault tolerant machine and drives are capable of providing uninterrupted operation during fault conditions, therefore being attractive in safety critical applications, such as aerospace and electric traction [8, 17]. While electrical drives possess enhanced functionality, adaptability and controllability compared with conventional mechanical, hydraulic, and pneumatic driven systems [3], relative low reliability of electric drive systems restricts their wide applications since an unexpected fault would cause serious consequences or economic losses. Thus, fault tolerance is an essential requirement for electrical drives to attain high availability in safety critical applications.

The fault tolerant capability of a machine drive is mainly determined by the machine topology and drive configuration. While various solutions reported in literature have been reviewed in section 1.4.1, it is still a technical challenge to achieve high performance as well as good fault tolerance with reasonable cost when employing the existing technology.

Recently, permanent magnet assisted synchronous reluctance machine (PMA SynRM) has gained increasing interests as a viable candidate for various applications due to reduced magnets usage, extended field weakening range and comparable performance with conventional PM machines [112, 113]. This machine usually utilizes a transversally or axially laminated rotor which typically has a high saliency ratio. Small amount of magnets or cheap ferrite magnets are embedded in the rotor which reduces the cost. These unique characteristics are mainly attributed to the combined torque production mechanism, both the PM torque and reluctance torque. The reluctance torque enables use of less magnet material and results in low back emf which

improves the machine's fault tolerant capability. This machine typically exhibits 1 per-unit characteristic current or lower. However the distributed overlapping windings used in this type of machine yield strong inter-phase coupling and physical contacts between the coils in different phases. Consequently, a fault in one phase may propagate to or affect other phases. For a conventional 3-phase machine drive, a single failure in any part of the drive will lead to a complete failure [53, 54, 114].

In order to develop a machine drive with high performance and good fault tolerance, a novel fault tolerant machine drive based on PMA SynRM topology is proposed in this chapter. By employing appropriate winding configuration, the machine can be optimized to have high torque density while exhibiting excellent fault tolerant characteristics. Detailed FE analysis has been conducted to assess its performance under healthy and various fault conditions.

2.2 Proposed PMA SynRM with Segregated Windings

Conventional 3-phase windings of a PMA SynRM are usually distributed as shown in Fig. 2-1 in order to produce a nearly sinusoidal MMF in the air gap albeit they are not conducive to fault tolerance. For the purpose of triple redundancy, it is possible to configure the windings as three isolated 3-phase sets, with each driven by an independent standard inverter. However, the windings of different sets are overlapped and bundled together which is prone to inter-phase short circuits. Strong magnetic coupling also exists between different 3-phase sets. In addition, the heat produced by a faulty 3-phase set may spread to the other healthy sets via the overlapped windings. Hence, fault in one phase cannot be isolated and is quite possible to affect other healthy parts.
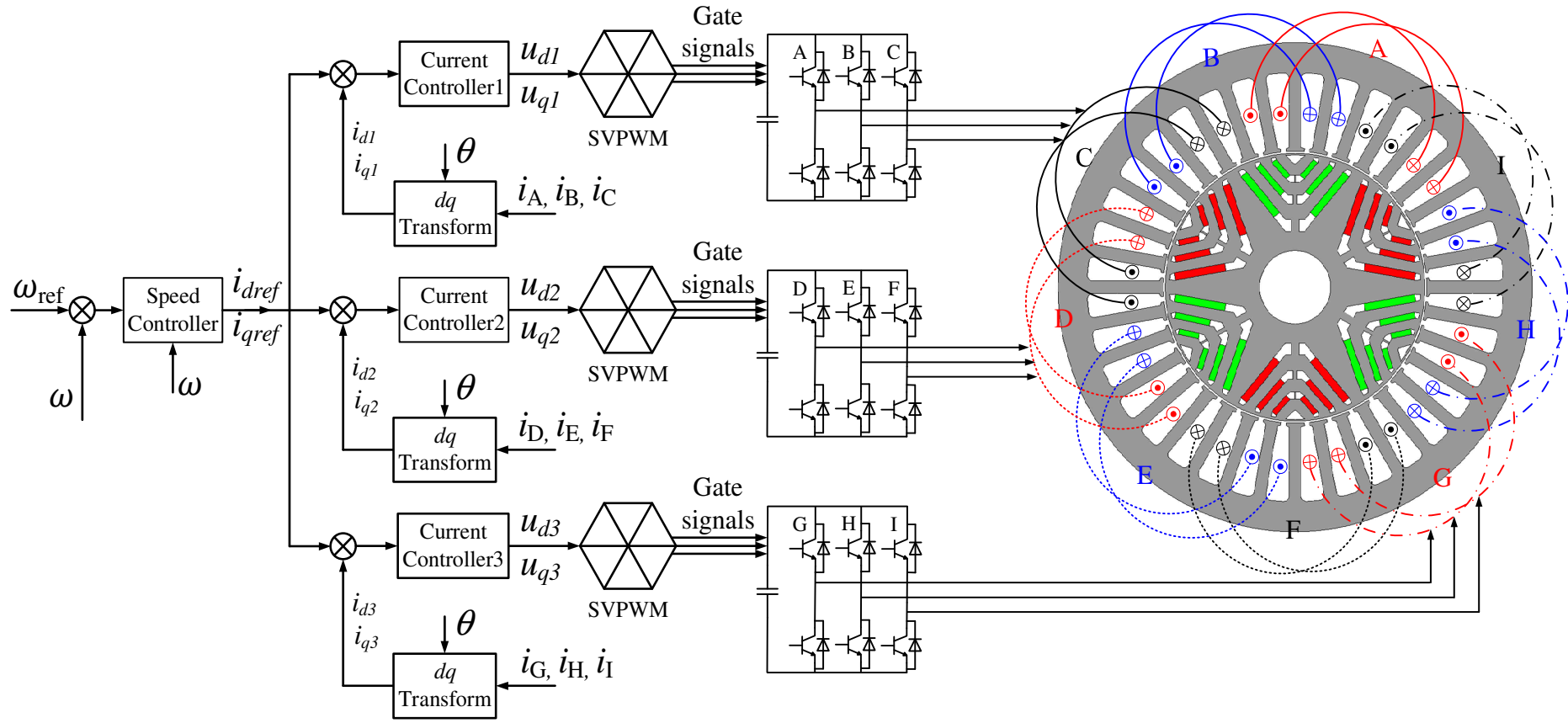
Fig. 2-1 PMA SynRM with conventional overlapped windings
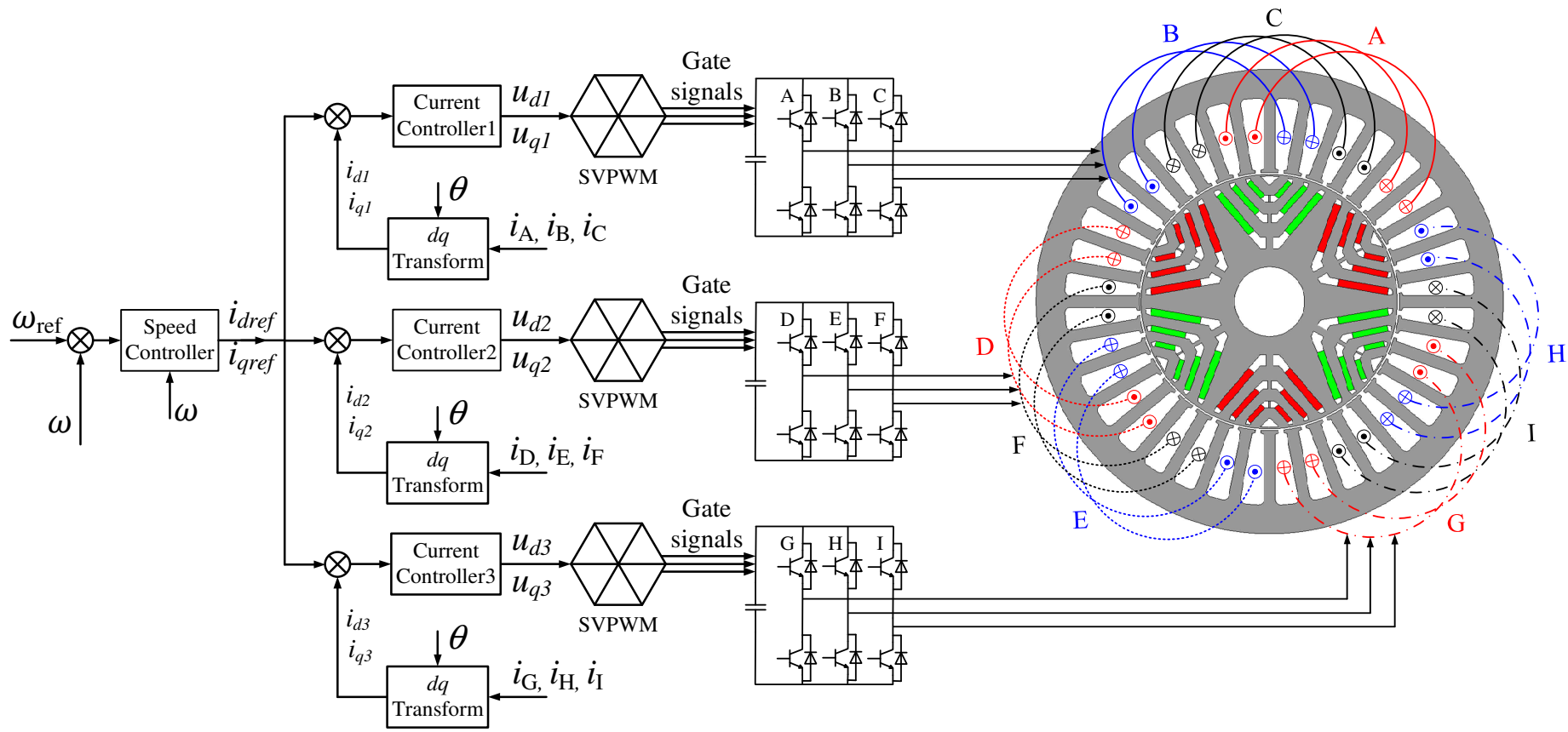
Fig. 2-2 PMA SynRM with segregated windings

In order to achieve the physical, electrical and thermal isolations to provide enhanced fault tolerance for the PMA SynRM, a segregated triple-redundant 3-phase winding configuration is proposed as shown in Fig. 2-2 [115]. The conventional overlapped windings are divided into three separate 3-phase winding sets so that there is no contact between different sets, resulting in physical and thermal isolation. The electrical isolation is achieved by using three standard inverters to drive each 3-phase set.

According to Fig. 2-2, the "go" and "return" positions of the coils in phases C, F and I are reversed whilst the induced voltages in phases C, F and I are unchanged owing to the periodic airgap flux density distribution. As a result, each winding set ABC, DEF and GHI forms a balanced 3-phase winding. Since the currents in the slots are not affected by the new winding configuration, the MMF distribution and the performance of the machine in healthy conditions are exactly the same as the original one shown in Fig. 2-1. Thus, all the merits of the PMA SynRM, such as reduced magnet usage, low back emf, inherent large reluctance torque, high efficiency and high torque density are maintained. Most importantly, the segregated windings and independent inverters lead to excellent fault tolerance since the risk of fault propagation between different 3-phase winding sets is minimized and the three independent modules provide redundancy for various faults [14].

In case of an open-circuit fault in an inverter switch or the windings, the faulty 3-phase winding set can be simply deactivated by opening all the switches in that set, and the remaining two healthy 3-phase sets are capable to continuous operation in a balanced manner, with about one third reduction in output torque or power. If a short circuit failure occurs in an inverter switch or in one 3-phase winding, a terminal short circuit (TSC) can be applied on the faulty set by closing the entire bottom or the top switches of the 3-phase inverter. Since the PM flux in the machine is quite low, the short circuit current is restricted below or close to the rated value. And if an inter-turn short circuit takes place, the current of the faulted turn can be alleviated by applying TSC to nullify the flux linkage of the faulted turns. Thus, owing to the

winding separation, a fault in one 3-phase system can be isolated and the other two 3-phases can continue operation to generate torque or power. The magnets are better protected by the rotor core, but even if in an unlikely event that magnets are partially demagnetized, the reduction in torque capability will be insignificant since the magnet torque only accounts for ~30% torque in this type of machines. The low back-emf of the machine also means that in the event of inverter or control failure, the effect on the drive is benign with no uncontrollable rectification even at high speed. This inverter fail-safe feature is very attractive in many applications.

It follows that the PMA SynRM with the segregated winding configuration exhibits good performance as well as excellent fault tolerance. The segregated windings are realized with no penalties and no additional cost. Only a winding reconfiguration is required to form multiple 3-phase winding sets and each 3-phase set is driven by a standard 3-phase inverter. Separating a 3-phase winding into multiple 3-phase sets reduces the currents in each 3-phase set, spreading heat more evenly in the inverter switches and hence facilitating machine-inverter integrations, particularly for high power drives. Although the proposed winding segregation is primarily aimed for PMA SynRM, it is also applicable to the other machines with distributed windings to enhance the fault tolerance, such as synchronous reluctance machines, surface mounted PM machines, synchronous wound field machines and induction machines [116]. The number of 3-phase modules can be selected according to application requirements. It should be noted that while the proposed winding segregation is not new [34], its exploitation in PMA SynRM to achieve desirable fault tolerance has not been reported and demonstrated in literature to date.

2.3 Fault Tolerant Capability Investigation of the Proposed Machine Drive

During operation, various faults may occur on both the machine and drive sides as discussed in Table 1-1. Understanding of the failure modes and relevant fault tolerant capabilities is particularly important for developing the modelling, control and detection techniques. In this section, the fault

tolerant capabilities of the PMA SynRM with segregated windings are investigated against various faults.

Without loss of generality, a PMA SynRM machine whose specifications are given in Table 2-1 is taken as an example to examine different failure modes and post fault operations using FE analysis. The gamma angle is defined as the angle between the current vector and the q-axis. All simulations are performed at the base speed 4000rpm with rated current excitation unless otherwise stated.

Table 2-1 Specifications of the machine

Specification	Symbol	Value
Base speed	n_b	4000rpm
Maximum speed	n_m	19200rpm
Rated power	P_r	35kW
Rated current and gamma angle	I_{rated}	120A(51°)
Nominal DC link voltage	V_{dc}	270V
Number of turns per coil	N	8

2.3.1 Healthy Operation

First, the machine is evaluated in healthy condition. The machine is excited with the rated current 120A, the optimal gamma angle for maximum torque per Ampere (MTPA) is evaluated as 51°. The resultant torque waveform is shown in Fig. 2-3. The machine outputs an average torque of 89.2Nm at the rated operating point. The torque ripple is evaluated as 14.1% which is mainly due to the 6th and 12th harmonic produced by the interaction of the rotor saliency and stator slotting. The PM torque and reluctance torque account 30% and 70%, respectively [117]. Although the PM usage of the machine is relatively low, the machine still achieves high torque density since 70% of the torque is produced by the reluctance torque component.

Fig. 2-4 and Fig. 2-5 show the 2D flux distribution and flux density under rated conditions, respectively. It is evident the distribution repeats 3 times periodically over 360 degrees. Thus, the flux linkages of the three 3-phase sets are identical under healthy conditions. By way of example, Fig. 2-6 shows the

flux linkage waveforms of set ABC. While distortions due to space harmonics and magnetic saturation are visible, the waveforms exhibit the 3-phase symmetry.
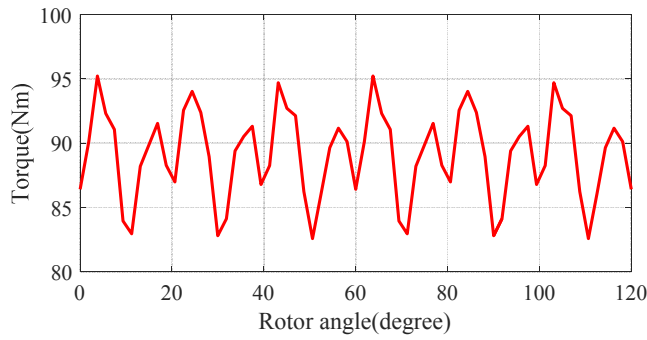
Fig. 2-3 Torque in healthy condition
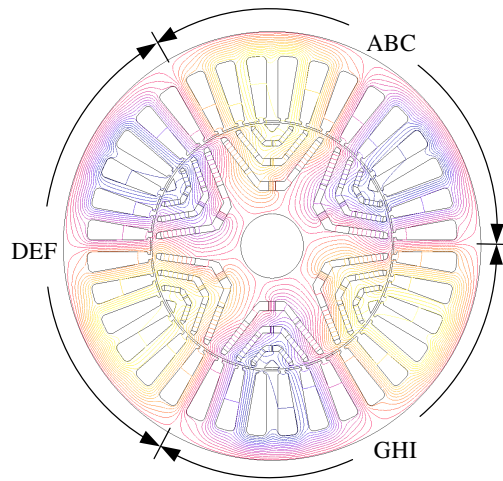
Fig. 2-4 Flux distribution in healthy condition
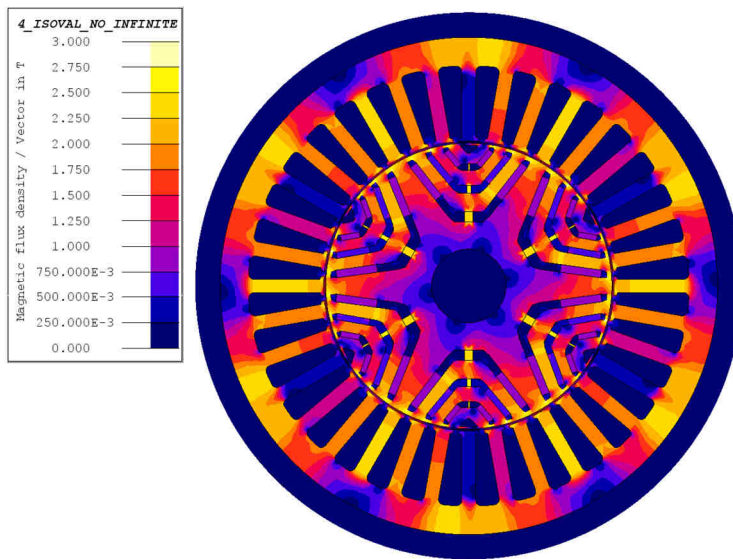
Fig. 2-5 Flux density distribution in healthy condition
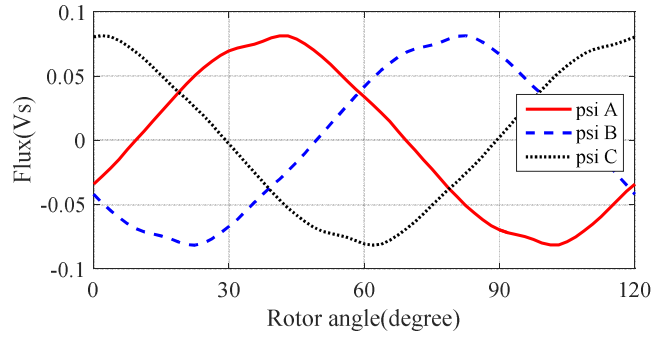
Fig. 2-6 Phase flux linkages in healthy condition

2.3.2 One Set Open Circuit

In case of a winding open circuit, switch open-circuit failure or control failures, the faulty set of 3-phase winding should be deactivated by opening all the inverter switches. The currents in the faulty set become zero, leading to one set open-circuit failure mode. The remaining two 3-phase sets are excited by the same currents and the resulting torque waveform is shown in Fig. 2-7. The average torque of the machine in this condition is 50Nm. Thus, the open circuit torque capability ρ_{oc}, defined as the percentage ratio of open circuit torque, T_{oc} to the rated torque T_r, can be calculated as:

$$\rho_{oc} = T_{oc}/T_r \times 100\% = 56\%$$

(2-1)

The torque reduction is slightly higher than 1/3 pu. Given that the thermal load under this condition is much reduced due to one set being open circuited, the currents in the remaining two healthy 3-phase sets can be increased to offset the torque reduction. The torque ripple under the open circuit condition is 15.8% with respect to the rated torque. In addition to the 6th and 12th harmonic torque ripples, a 2nd harmonic torque ripple is clearly visible in the torque waveform. This is caused by the electromagnetic unbalance resulting from the open-circuit fault, which is evident from the flux distribution shown in Fig. 2-8 under the open circuit condition of the ABC set.
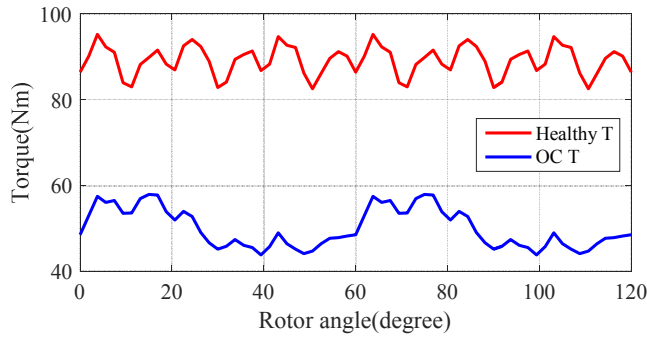
Fig. 2-7 Torque with set ABC open circuited
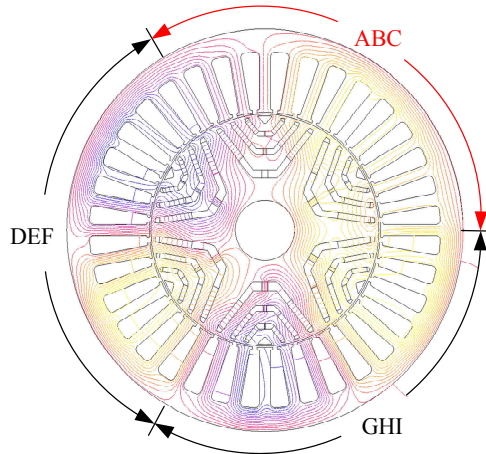
Fig. 2-8 Flux distribution with set ABC open circuited

As shown in Fig. 2-9, the phase flux linkages in the open-circuited ABC set are heavily distorted. This indicates that mutual coupling still exists in the three 3-phase winding sets of the machine. In fact, although the currents of the fault set are zero, the currents in the other two healthy sets will produce a nonzero MMF over the fault set region. Hence, the distorted flux linkages are the combined effect of the rotor magnets and currents in the other two healthy sets.
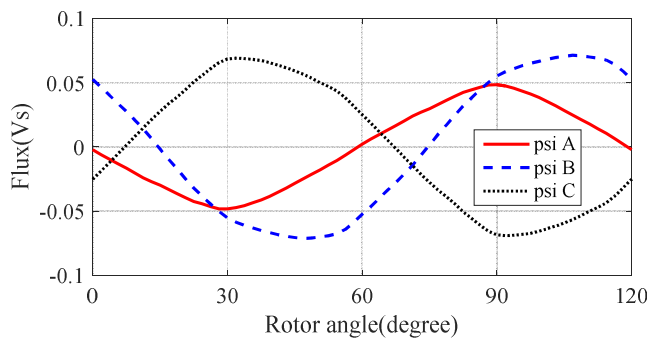
Fig. 2-9 Faulty phase flux linkages with set ABC open circuited

Similarly, the flux linkage waveforms of the healthy DEF and GHI sets shown in Fig. 2-10 are no longer balanced. The amount of distortion in the flux linkage waveforms due to the unbalance is different in each phase. The distortions in phases D, F, G and I are relatively small while more distortions are noticed in phases E and H. This may be attributed to local saturation caused by asymmetrical MMF distribution.
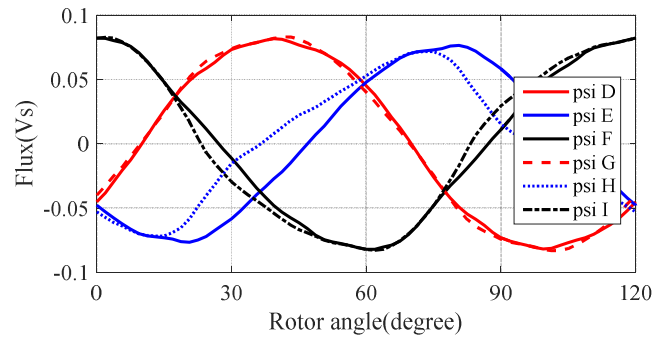
Fig. 2-10 Healthy phase flux linkages with set ABC open circuited

2.3.3 One Set Short Circuit

If a switch in the inverter or the phase winding is short-circuited, that particular inverter should turn-on all its top or bottom switches to create a terminal short circuit for the faulty 3-phase set. The healthy sets are still excited by the inverter for continuous operation similarly to the case of the one set open-circuit fault. The resultant short-circuit phase currents are shown in Fig. 2-11 and their root-mean-square (RMS) values are much lower than the rated current since the PM flux in the machine is relatively low. Hence, no excessive heat will be produced in the faulty set and the machine will be safe to continue its operation. Such low short-circuit current is an inherent property of this type of machine and no penalty like the small slot opening is required in the machine design to achieve this advantage. It is observed that the short circuit phase currents are asymmetrical. Again, this is attributed to the mutual coupling between the healthy sets and the faulty set since they are not completely magnetically isolated.

The flux distribution under the short circuit condition is shown in Fig. 2-12. As can be seen, the flux in the region occupied by the short-circuited ABC set is almost nullified by the short-circuit currents. The flux density in this region

is quite low. The resultant flux linkage waveforms of the fault set are plotted in Fig. 2-13. It is evident that the flux linkages are much lower than those in the healthy condition. The remaining flux linkages consist of mainly zero sequence components since there is no zero sequence currents in the star connected 3-phase winding to nullify them. It is also seen that phase B exhibits the highest flux linkage which is consistent with the highest phase current shown in Fig. 2-11. In contrast, the flux-density distribution in set DEF and GHI regions is almost normal as is evident from the flux-linkage waveforms shown in Fig. 2-14.
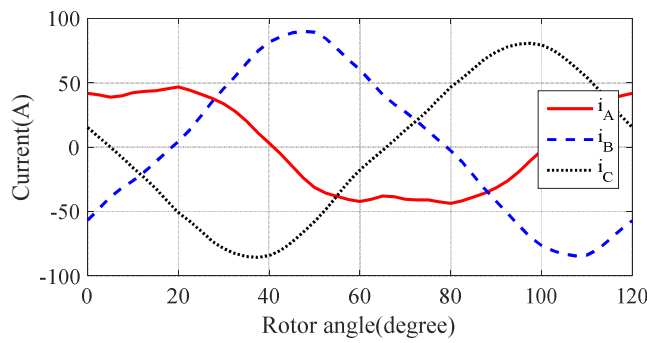
Fig. 2-11 Short circuit phase currents
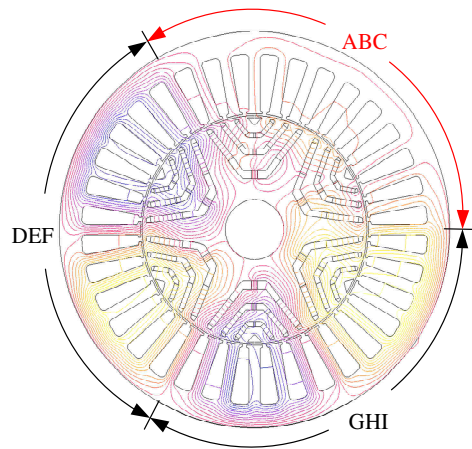
Fig. 2-12 Flux distribution with set ABC short circuited
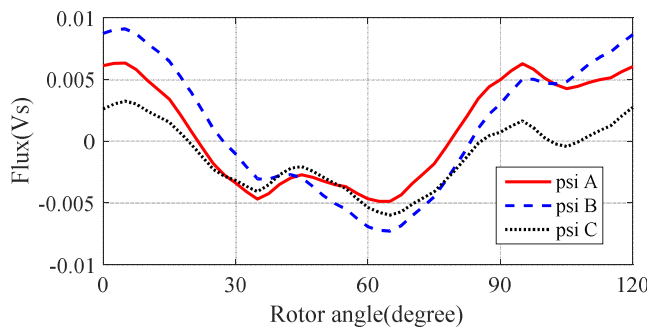
Fig. 2-13 Faulty phase flux linkages with set ABC short circuited
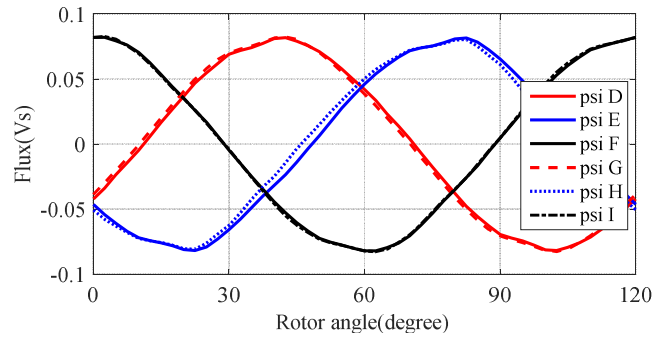
Fig. 2-14 Healthy phase flux linkages with set ABC short circuited

The torque waveform under the short circuit condition is plotted in Fig. 2-15 where the average torque and torque ripple are 58Nm and 14%, respectively. The short circuit torque capability ρ_{sc} is evaluated to be 65%, very close to two thirds of the rated and slightly higher than that in the open circuit case. The torque ripple is lower than the open circuit case and contains mainly the 2nd and 12th harmonics. These results confirm that the short-circuit fault can be accommodated by the proposed machine.
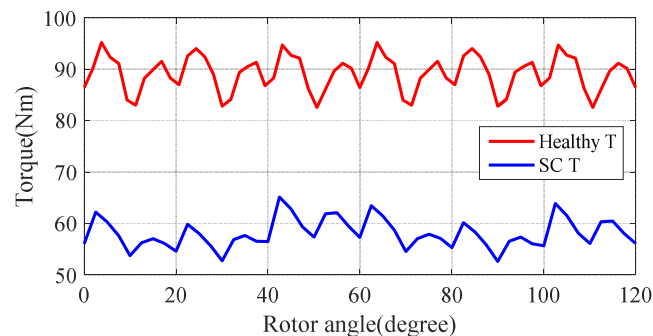
Fig. 2-15 Torque with set ABC short circuited

2.3.4 Intra-phase Turn Fault

Due to winding insulation break down, short circuit fault may occur in a single phase or between different phases as shown in Fig. 2-16. The intra-phase turn fault is reported as the worst fault scenario since only a few turns are short circuited as shown on the left of Fig. 2-16. The resultant fault current is massive and it decreases with increase in the number of short circuit turns. The worst case is one turn short circuit located close to slot opening.
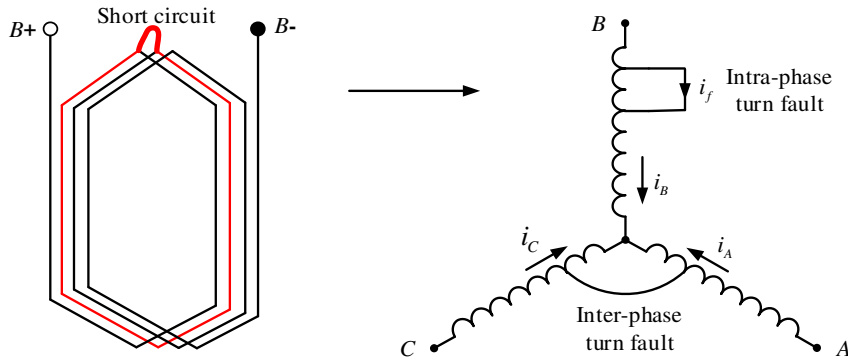
Fig. 2-16 Intra-phase and inter-phase turn fault illustration
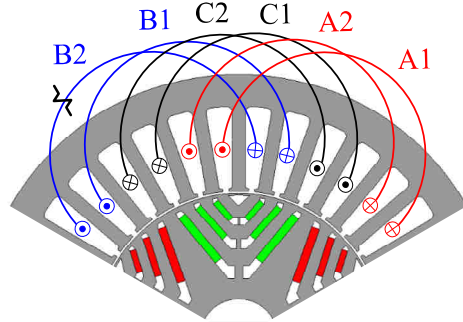
Fig. 2-17 Coil location of the fault turn

Without loss of generality, a single turn fault located in the top of the slot is assumed in coil B2 of set ABC as shown in Fig. 2-17, when all phase windings are loaded with rated current (120A, 51°) at 4000rpm. The fault is simulated in FE and the resultant fault current i_f reaches 1100A as shown in Fig. 2-18. This severe fault should be detected and mitigated immediately before developing to a catastrophic failure. Fig. 2-19 shows the flux distribution of the fault condition. Close examination reveals that the flux in coil B2 region is reduced by the fault current in the single short-circuited turn when compared with those in the healthy coils E2 and H2.
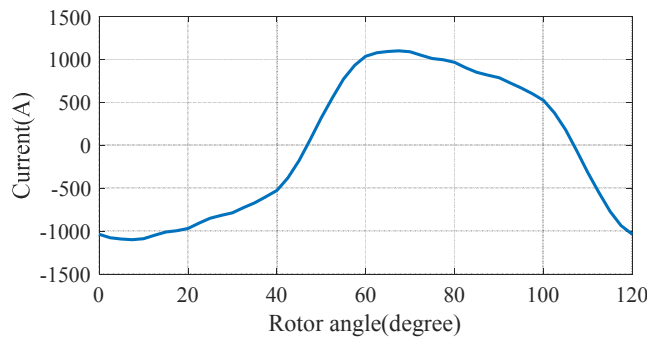
Fig. 2-18 Turn fault current in coil B2 with 120 load current at 4000rpm
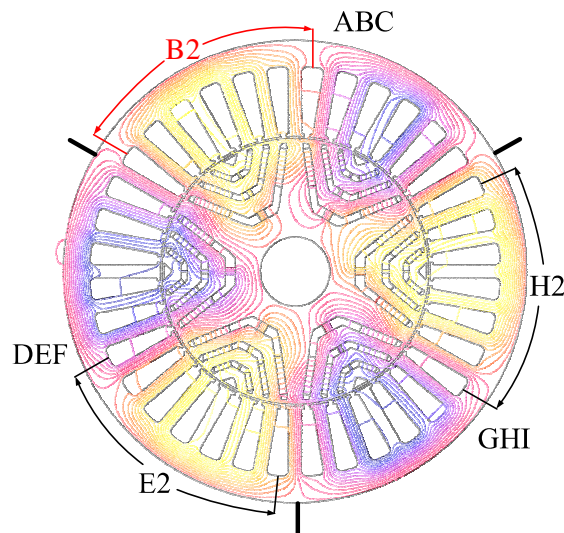
Fig. 2-19 Flux distribution with turn fault in coil B2

In order to limit the fault current to an acceptable level, TSC is applied via the inverter of the faulty 3-phase set. Short circuit currents are induced in the healthy turns and coils, and tend to nullify the external flux in the fault region which is produced by the magnets and currents in the healthy sets. Consequently, the residual flux linked by the fault turn is much lower and the turn fault current is reduced accordingly. According to the analysis in [49, 115], the fault current is dependent on the coil location where the turn fault occurs, and the currents in the healthy 3-phase sets. As will be shown later, the induced short circuit phase currents are unbalanced after application of the TSC on the fault set. Again the unbalanced currents are caused by the mutual coupling between the three 3-phase sets which are not magnetically isolated. After TSC, the flux linked by the fault turn is the combined effect of the magnets, currents in both the fault and healthy sets. Now the currents in the fault set are unbalanced and they are unequal with those in healthy sets, the flux linkage of the fault turn is therefore different and leads to unequal fault current in different coil locations. Since one 3-phase set consists of 6 coils as shown in Fig. 2-17, the fault has been examined in 6 different coil locations by varying the currents in the healthy sets under MTPA condition. The variations of RMS fault current after TSC with load currents in the healthy sets at 4000rpm are shown in Fig. 2-20. It is seen that the fault current is almost always higher if the fault takes place in coil B2, and increases with load current. The worst case is therefore identified as single turn fault in B2 with 120A

current in healthy sets. This implies that in design optimisation, this most severe fault case should be examined to ensure that the machine could tolerate it.
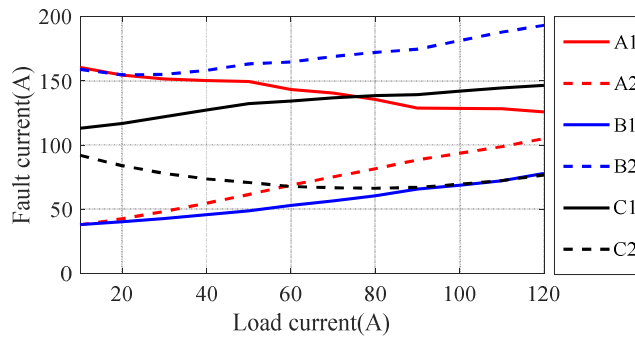
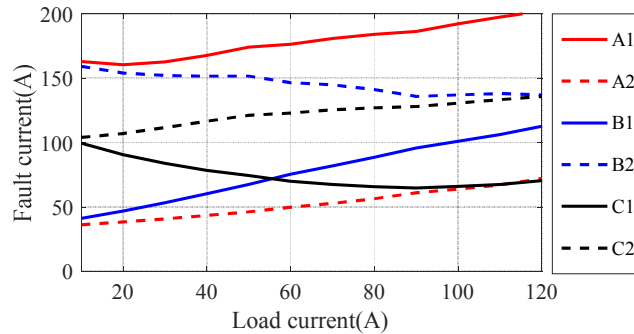Fig. 2-20 Variations of RMS turn fault currents in 6 coils with load current in healthy 3-phase sets in motoring mode

Fig. 2-21 shows the current waveforms in the faulted turn and healthy turns of the ABC 3-phase set after application of TSC. The resultant phase currents are unbalanced but they are much lower than the rated value. This unbalanced phase currents together with the currents in the healthy sets lead to unequal fault current in different coil locations. Although the turn fault current is 2.6pu in the worst case, the induced heat can be accommodated by the machine since the total heating effect is reduced as will be examined by thermal modelling and experimental tests. The flux distribution is shown in Fig. 2-22 where it is evident that the external flux in ABC region is virtually nullified by the short circuit phase currents compared with Fig. 2-19. Hence, the turn fault current is reduced due to lower residual flux. Fig. 2-23 compares the torque waveforms under the healthy and the fault conditions. It is evident that the machine can still output about 2/3 of healthy torque after the TSC.
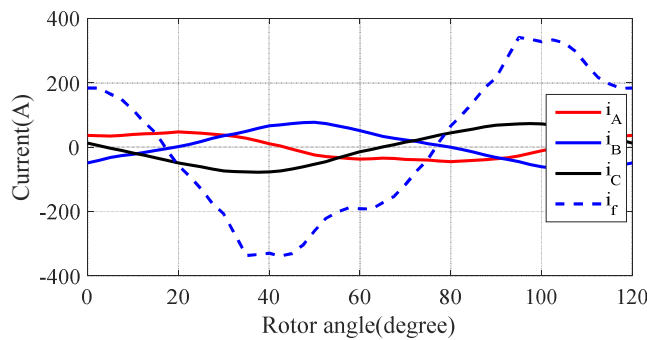
Fig. 2-21 Turn fault current and phase currents in ABC with turn fault in coil B2 set after TSC
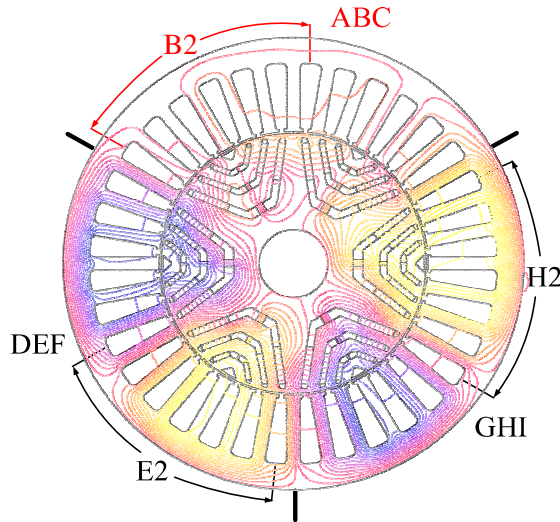
Fig. 2-22 Flux distribution in turn fault condition after TSC
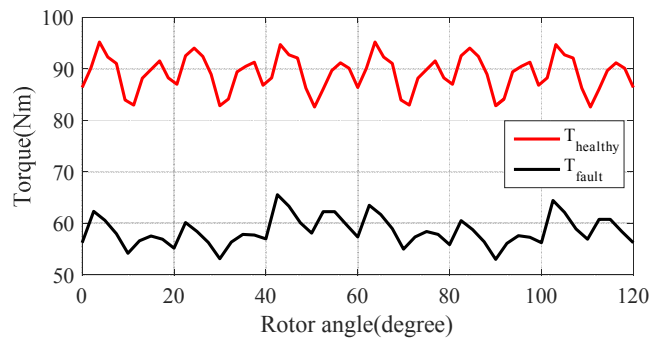
Fig. 2-23 Comparison of torque waveform under healthy and turn fault condition after TSC

Fig. 2-24 Variations of RMS turn fault currents in 6 coils with load current in healthy 3-phase sets in generating mode

It should be noted that the maximum turn fault current occurs in coil B2 when the machine is rotating in anticlockwise direction under motoring mode. However, if the machine is operating in generating mode, the worst turn fault case will occur in coil A1 as shown in Fig. 2-24. And it is found that the fault current dependency on the coil location exhibits an opposite sequence compared with that of motoring mode. This is because in generating mode, the sequence of the currents in the fault and healthy sets are reversed. Consequently, the flux linked by the fault turn in coil A1 is the

highest and leads to the highest fault current. Likewise, if the machine rotates in the clockwise direction in motoring or generating modes, the worst fault current after TSC occurs in A1 or B2, respectively.

2.3.5 Inter-phase Turn Fault

If the short circuit fault occurs between different phases, it becomes an inter-phase turn fault as shown in Fig. 2-16. Although the windings of different 3-phase sets are segregated for this machine, the end windings of different phases in the same set are still bundled together. The phase insulation may fail and cause turn fault between phases.

For more clear illustration, the winding of set ABC is shown in Fig. 2-25. As can be seen, each slot only contains one coil and, therefore, the inter-phase fault may only occur in the end winding region. Considering the winding layout, the inter-phase fault is more likely to occur between phases A and C, and between phases B and C because phases A and B do not have any direct contact.
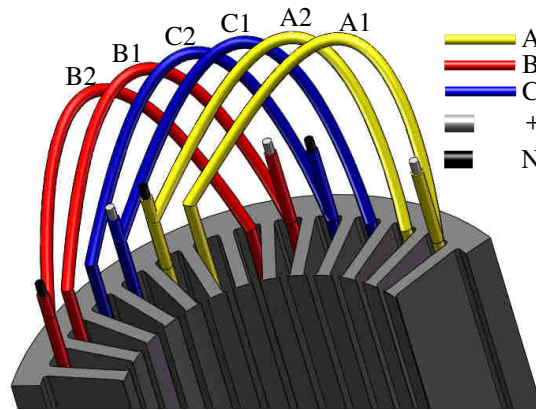
Fig. 2-25 Winding illustration of set ABC

Since coils A2 and C1 are physically overlapped an inter phase fault between these two coils is possible. As can be seen in Fig. 2-26, if there is a short circuit between A2 and C1, coil C2 will be in the short circuit loop. Thus, the number of short circuited turns is always higher than 8, leading to much lower fault current than the intra-phase turn fault. Similar condition is true for short circuit between coils B1 and C2 as shown by the dotted line in Fig.

2-26. In this case, Coil B2 is included in the short circuit path, resulting in less severe level of fault current.
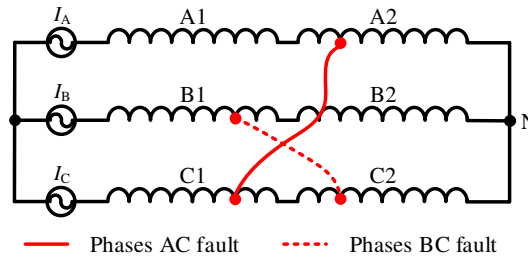
Fig. 2-26 Inter-phase fault illustration

Although the fault current in inter-phase short circuit is lower than the intra-phase short circuit, TSC still should be applied to the faulted 3-phase set in order to reduce torque pulsation and to avoid excessive local hotspot. It is therefore necessary to assess the worst fault case after TSC. The number of short circuited turns may vary depending on the position of short circuit point as shown in Fig. 2-26. However after application of TSC, inter-phase short circuits with the least number of short-circuited turns are shown in Fig. 2-27. In case (a) to case (d), coils A1, C2, C1 and B2 are effectively short circuited via the neutral or drive switches. Hence the least number of short-circuited turns is 8 for the machine under study.
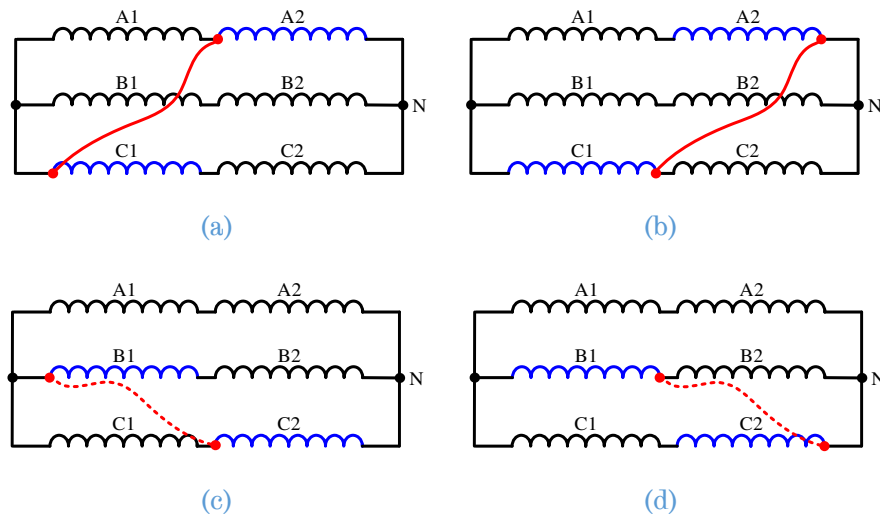
Fig. 2-27 Extreme inter-phase faults (a) Case 1 for phases AC fault (b) Case 2 for phases AC fault (c) Case 3 for phases BC fault (d) Case 4 for phases BC fault

These four extreme inter-phase faults are evaluated when the two healthy 3-phase sets are loaded with rated currents at 4000rpm in motoring mode. Again, the highest fault current is observed in case 4 where coil B2 is short

circuited. The short circuit currents after TSC are shown in Fig. 2-28. i_{B1} and i_{B2} represent the current in coil B1 and B2, respectively. It is seen that the peak current of i_{B2} is 135A, slightly higher than the rated value. Since the currents of other phases are much lower, the heat produced by the single coil can be sustained. In addition, the machine can still output 2/3 of healthy torque as shown in Fig. 2-29.
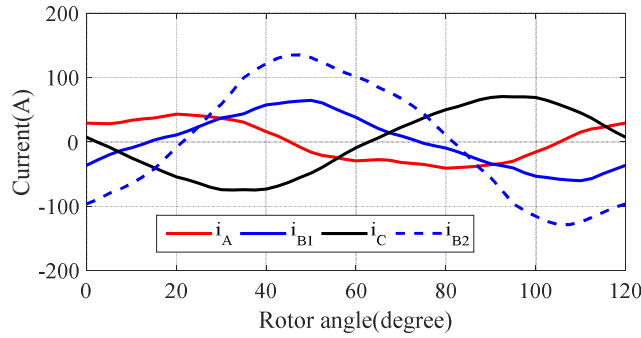
Fig. 2-28 Short circuit currents for case 4 inter-phase fault
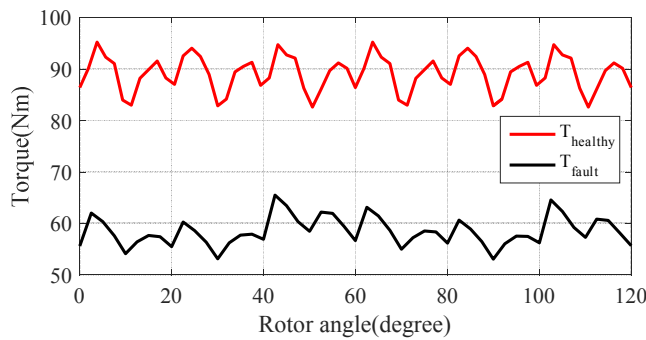
Fig. 2-29 Torque for case 4 inter-phase fault

However, if the sequence of coil connections is different from those shown in Fig. 2-25 and Fig. 2-26, for example, coils C1 and C2 are swapped, it is quite possible that the last few turns of coils A2 and C1 are short circuited without including another coil in the loop. The resultant fault current will be much higher. Hence, the winding layout and coil connection should follow Fig. 2-25 and Fig. 2-26 to avoid this undesirable condition. Further, insulation paper should be inserted between the phases to enhance the phase-to-phase insulation and reduce the risk of insulation failure.

It should be noted that theoretically two coils may be short-circuited through the stator core even if they do not have direct contact in the end winding region. However, this requires the ground wall insulation breakdown in both coils and hence much less likely.

2.3.6 Uncontrolled Rectification Fault

At high speeds, the machine line-to-line back emf may be higher than the DC link voltage, especially for a machine drive requiring a wide constant power operating region (CPOR). This will not be a problem as long as the inverter operates properly in field weakening mode [118]. However, if the inverter fails or applies self-protection due to device overheating or sensing errors, etc., the gate drive signals may be inhibited. The back emf could be much higher than the DC link voltage and uncontrolled rectifier operation via diodes would take place. Mechanical power is converted to electrical power and flows to the DC link which may damage the whole drives if the regenerated power cannot be absorbed [119]. Imposing a maximum back emf limit on the machine design would cause a penalty on the machine size and inverter VA rating [45]. Design tradeoff also has been made between CPOR and uncontrolled generation operation. It is shown that high rotor saliency is beneficial to have a wide CPOR with a low back emf [120]. Due to its high rotor saliency, PMA SynRM mainly relies on the reluctance torque, and therefore is an excellent candidate for wide CPOR with low back emf, reducing the possibility of uncontrolled power generation in the event of inverter failure.
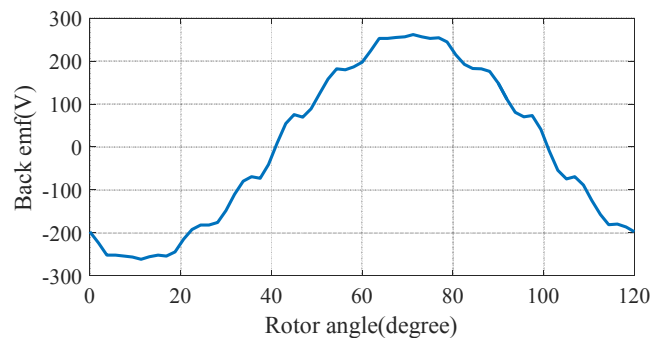
Fig. 2-30 Line back emf at max speed 19200rpm

The line-to-line back emf of the machine is evaluated at maximum operation speed 19200rpm as shown in Fig. 2-30. The peak value of the back emf is 262V which is lower than the DC link voltage 270V. The voltage applied on the diodes is always reverse biased. Therefore, the uncontrolled rectification will not occur even if the inverter fails. This unique feature is attributed to the low PM field of PMA SynRM which minimizes the risk in the fault conditions.

It should be noted that though the PMA SynRM is featured with low magnets usage, not all PMA SynRMs have back emf lower than the DC link voltage, especially for the wide CPOR applications. Therefore, for a specific design, the back emf also should be examined to eliminate the possibility of uncontrolled rectification.

2.3.7 Demagnetization Fault

For PMA SynRM, the permanent magnets are also subject to the risk of demagnetization due to high temperature and excessive armature reaction field under heavy load or fault conditions [47, 121]. The demagnetization leads to torque reduction and increase in machine currents for closed loop controlled drive under the same load condition. The vicious cycle may continue, causing further increase in temperature and demagnetization.
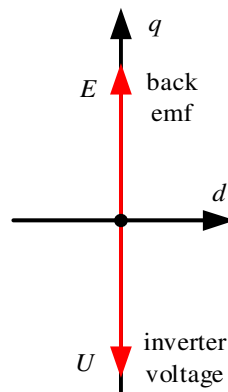
Fig. 2-31 Illustration of inverter loss of synchronization
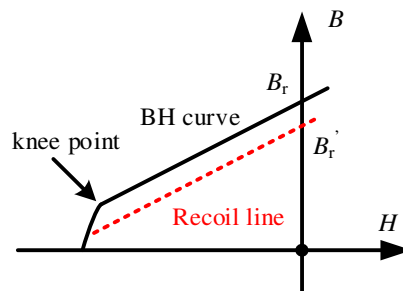
Fig. 2-32 PM demagnetization BH curve

It has been identified that inverter loss of synchronization is the worst case since the applied voltage U may be out of phase with the back emf E as shown in Fig. 2-31. These two voltage components combine and produce peak transient current an order of magnitude higher than the rated value,

primarily in the negative d-axis direction. Consequently, the magnets will be partially demagnetized. According to the PM demagnetization BH curve in Fig. 2-32, if the flux density of any magnet element is lower than the knee point during the fault process, it will operate on the recoil line with reduced remanence in subsequent steps. This fault condition is evaluated in FE by repeating the procedures described in [47, 121]. Partial demagnetization is observed in the magnets, and the back emf is reduced by 31% compared with the original value. The resultant torque is only 9% lower than the rated as shown in Fig. 2-33.
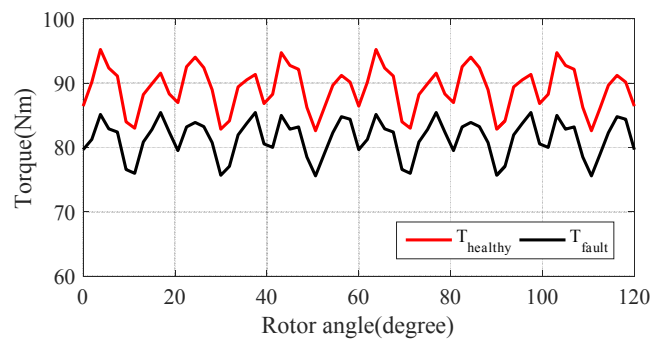
Fig. 2-33 Output torque after demagnetization fault

As can be seen, although the machine experiences partial demagnetization during the worst case, the torque reduction is quite modest. This is because the PM torque only contributes about 30% of the total torque. Thus, the demagnetization fault has a mild impact on the output torque capability for the PMA SynRM. Indeed, it was confirmed in [122] that the PM machine with this type of rotor configuration has the best resistance against demagnetization compared with the surface mounted PM machine, V shape interior PM machine and spoke PM machine. Therefore, the PMA SynRM is insensitive to the demagnetization fault.

2.3.8 DC Link Capacitor Fault

In the drives, the DC link capacitor is utilized to provide a transient energy buffer and filter out the voltage ripple across the DC link. It is exposed to combined voltage and thermal stress during inverter operation, and hence contributes considerable failure rate in electric drives [19].

Capacitor aging due to electrolyte evaporation and open circuit are the two main failure modes [123]. In case of an open circuit fault, the corresponding inverter should be shut down because of insufficient filtering in the DC link and possible instability of the drive system [124]. The capacitor aging increases the equivalent series resistance and decreases the capacitance. Both effects result in higher current ripple and higher temperature which deteriorates the machine drive performance. The inverter also should be turned off to avoid developing to total breakdown if the capacitor parameters change considerably. Like the open circuit/short circuit fault in the switches, the DC link capacitor failure in one of the 3-phase inverters can also be tolerated by the proposed machine drive with about 2/3 of the healthy torque owing to the triple redundancy.

To tolerate any failure in the DC supply, each 3-phase inverter should be fed by an independent DC source. In this case, loss of DC power in one 3-phase inverter only leads to 1/3 reduction in torque capability.

The faults discussed above are summarised as shown in Table 2-2 in terms of post fault torque and resultant fault current. Therefore, it can be concluded that the intra-phase single turn fault in coil B2 is the worst fault case which should be addressed in the machine design process.

Table 2-2 Summary of the faults in the machine drives

Fault type	Output torque	Fault current
One set open circuit	56%	NA
One set short circuit	65%	96A
Intra-phase short circuit	~65%	340A
Inter-phase short circuit	~65%	135A
Uncontrolled rectification fault	0	NA
Demagnetization fault	91%	NA
DC link capacitor failure	~56%	NA

2.4 Summary

In this chapter, a triple redundant 3x3-phase machine drive based on PMA SynRM with segregated windings is proposed. The performance evaluation and fault tolerant capability investigation show that the machine exhibits high performance as well as good fault tolerance against various faults, including one set open circuit fault, one set short circuit fault, intra-phase turn fault, inter-phase turn fault, uncontrolled rectification, demagnetization and DC capacitor fault. The high performance are mainly attributed to the combined torque mechanism while the excellent fault tolerance are owing to the segregated windings, independent drives and the rotor configuration which leads high saliency and low PM field. The fault investigation provides insights for the machine design optimization. Therefore, this machine is chosen as the candidate topology under study.

CHAPTER 3
Design Optimisation of the Triple Redundant 3x3-phase PMA SynRM

3.1 Introduction

This Chapter aims to perform a design optimisation based on the chosen topology of PMA SynRM with segregated windings for aerospace application. The design process of fault tolerant machine is more complex than the conventional machine since it is necessary to achieve high performance and enhanced fault tolerance while satisfying the electrical, thermal, mechanical and volumetric constraints for both healthy and fault conditions. Especially for aerospace applications, the machine drives operate in extreme harsh environment with limited space, strong vibration, high temperature and heavy load cycles which make the design more challenging.

Numerous efforts have been made to achieve the required fault tolerance or reduce the fault impact on the machine drive. In order to avoid the undesirable uncontrolled generation at high speed, maximum back electromotive force (emf) limit has been imposed on the machine design, which increases the machine size and VA rating [45, 120]. Various machine winding and redundancy configurations were analysed for electrification in more electric aircraft to attain the required failure rate [125]. By limiting the PM flux and choosing proper saliency ratio, the braking torque and short circuit current can be restricted at an acceptable level for an electric power steering [7]. Regarding the worst fault scenario, viz. inter-turn fault, it was addressed by altering the slot geometry to achieve per unit inductance for fractional slot concentrated winding machine and flux switching machine [126, 127], albeit excessive turn-to-turn short-circuit current may still result depending on fault location. Further attempts have been made on the advanced copper wire material, optimised conductor placement and different slot pole combinations [44, 75, 128] to limit the turn fault current. Therefore, it can be concluded that the design process is quite complex. And in general,

the machine performance has to be compromised to achieve the required fault tolerance.

This Chapter is devoted to develop an integrated design procedure for the fault tolerant machine. The design optimisation is performed by using various design tools to assess its electrical, thermal, mechanical behaviours. Both the machine performance and fault tolerance have been addressed during optimisation. The machine efficiency is maximised at the rated operation point while ensuring the safety and fault tolerance for the worst fault case. The machine performances in healthy condition as well as in various fault conditions have been examined based on the final design candidate.

3.2 Design Specifications

A fault tolerant machine is required by the aerospace application whose specifications are listed in Table 3-1. The required torque-speed envelop is shown in Fig. 3-1. The application requires a high torque output at low speed range, and a wide constant power output speed range. The constant power speed ratio is 4.8 times of the base speed.

Table 3-1 Machine specifications

Specifications	Symbol	Value
Base speed	n_b	4000rpm
Maximum speed	n_m	19200rpm
Peak power	P_p	50kW
Rated power	P_r	40kW
DC link voltage	V_{dc}	270V
Max phase current	I_m	200A
Cooling medium		Aeroshell oil
Coolant inlet temperature		110°C
Max axial length		<400mm
Max diameter		<220mm
Yield Strength		450MPa (Vacodur 50)
Redundancy		Triple or quadruple
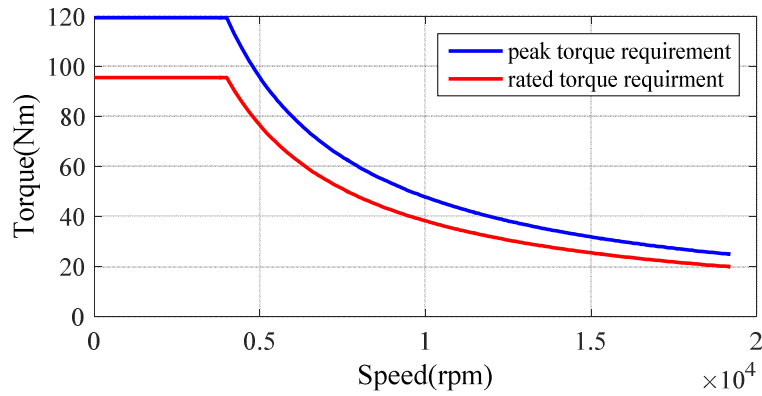
Fig. 3-1 Required torque speed envelop

Due to the high output torque required at low speed, the current density in the slot is estimated to be around 10~12A/mm². To sustain such a high current density, oil cooling of the windings is essential. Considering the high ambient temperature is 100°C, copper material with class-R insulation is adopted for the windings. For aerospace applications, the average lifetime is expected to be 300,000 hours. Thus, the maximum temperature limit for the winding is estimated to be ~180°C for the chosen insulation class. As indicated in Table 3-1, the ambient temperature is 100°C and the coolant inlet temperature is assumed as 110°C. The resulting margin for the temperature rise is thus limited to 70°C. Thus, the oil cooling facility requires careful design to avoid excessive temperature rise.

The maximum speed is relatively high at 19200rpm. It leads to large centrifugal forces, which may exceed the yield strength of the employed lamination material. Thin iron bridges are employed to retain the magnets in the rotor. The minimum width of iron bridge in the rotor lamination should be determined by designing the maximum von Mises stress within the lamination yield strength limit so as to avoid excessive deformation under high speed rotation. In addition, the rotor dynamics may experience significant vibration or even resonance at high speed. The first order critical speed should be designed to be sufficiently larger (typically 1.2~1.5 times) than the maximum speed.

Since this machine is aimed for an aerospace application, high reliability is essential. A triple or quadruple redundancy is required, implying the machine should have three or four independent modules, which could

continue operating if one module fails. And, the faults listed in Table 1-1 should be examined to ensure they do not cause complete system failure. Therefore, the machine design should not only maximise the machine efficiency, but also consider the fault tolerance against various faults and the electrical, mechanical and thermal constraints for both healthy and fault conditions, which makes the design more challenging.

3.3 Design Optimisation Process

This section describes a rigorous design optimisation process and evaluates the characteristics of the fault tolerant PMA SynRM machine. The devised design process aims to maximize the efficiency against the required torque-speed operating range, subject to a number of specified electrical, thermal and mechanical and other volumetric design constraints. The resultant machine design should deliver high torque at low speed and high power over a wide operating speed range.

The machine should sustain all the fault scenarios listed in Table 1-1. According to the investigation in Chapter 2, inter-turn fault in coil B2 with rated current in motoring mode is the worst fault which should be examined in the design. Furthermore, the machine back emf should be designed to be close or lower than the DC link voltage to avoid the undesirable uncontrolled generation. Hence, the requirement of high reliability imposes significant challenges for the machine design optimisation making it more complex and time consuming. As a result, an integrated design tool and methodology is developed to facilitate the machine design optimisation process.

3.3.1 Optimisation Tools

Initially, the machine is optimised with 3-phase configuration in healthy condition to accelerate the FE computation. Based on comparative studies among the PMA SynRM machines with various rotor geometries, the rotor with three magnetic barriers is selected, as it ensures a good balance between enhanced reluctance torque capability, rotor structural integrity and manufacturability. The multi-layer rotor configuration, characterised by high

nonlinearity and local saturation, in combination with the demanding mechanical constraints due to the high operating speeds, increases the difficulty for the machine design. Besides, the fault behaviour can only be evaluated in a full machine model with 9 phase configuration due to the asymmetry between the three 3-phase sets. Thus, in order to achieve the design optimisation objective while satisfying all design constraints in both healthy and fault conditions, effective optimisation techniques and computationally efficient tools are essential[129].

The coupling of Cedrat's FE electromagnetic analysis tool Flux 2D/3D with a dedicated optimisation tool GOT-It, provides a powerful design optimisation platform for electrical machine design. The optimisation algorithm is realized in an independent optimisation software "GOT-It". GOT-It is a powerful and reliable optimisation tool that allows solving any constrained or unconstrained optimisation problem with one or several objectives. A full range of optimisation algorithms such as Genetic Algorithm, Sequential Quadratic Programming, Niching, etc, enables the user to select the best method for their considered application. In GOT-It, the parameters to be optimised and their ranges, the objective functions and the constraints to be met are defined. The GOT-It features an advanced coupling technology with FE software Flux 2D/3D, known as the Flux communicator. Each time when the optimiser requests a run of the finite element model which represents the physical device to be optimised, the GOT-It feeds the geometry design parameters to FE models (new mesh is necessary when the geometry is changed). The solving process is automatically launched. The results in terms of objectives and constraints which are evaluated in FE calculation are sent back as functions of the geometry design parameters. Then the results are evaluated using an optimisation algorithm (Sequential Surrogate Optimiser-SSO), which can find the global optimum point for the FE based optimisation problem with multiple parameters [130].

The objectives and constraints of each design from the FE model are analysed by the SSO to build two response surfaces for the constraints and

objectives, respectively. The behaviours of the objectives and constraints are estimated and then combined to form a surrogate. Since this surrogate is an analytical function, SSO can apply genetic algorithm (GA) or sequential quadratic program (SQP) to it, and estimate a refined parameter search region which is closer to the global optimum design. Subsequently, the process repeats in iterations. Typically after three iterations, the optimisation problem converges and the optimum design is found. The flow chart of the whole optimisation process is illustrated in Fig. 3-2.
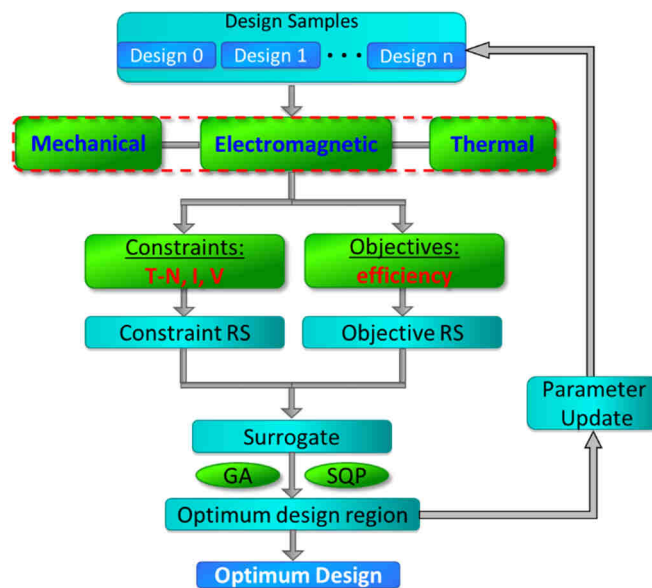
Fig. 3-2 SSO optimisation process

3.3.2 Inverse Machine Model Based on FE Computation

Usually an FE machine model has current as input, and torque-speed as output. However, for the design process, the most important task is to find the optimum current vector for a given torque and speed command. In order to evaluate the performance for a particular design sample at a specific torque and speed, an inverse machine model [129, 130] is established to determine the optimal current vector for a given torque-speed input.

First, static electromagnetic FE computations are carried out to obtain the d-axis and q-axis flux linkage maps with d and q-axis currents (i_d, i_q) as shown in Fig. 3-3. For the machine design under study, 6 samples of i_d and 7 samples

of i_q are selected. Hence, the flux linkages can be represented as a function of (i_d, i_q). Then, the flux linkage at any operating point with a particular (i_d, i_q) can be derived either by curve fitting or interpolating with marginal difference compared to the FE results. Using equation (3-1), the torque and voltage as functions of the particular current vector can be derived.
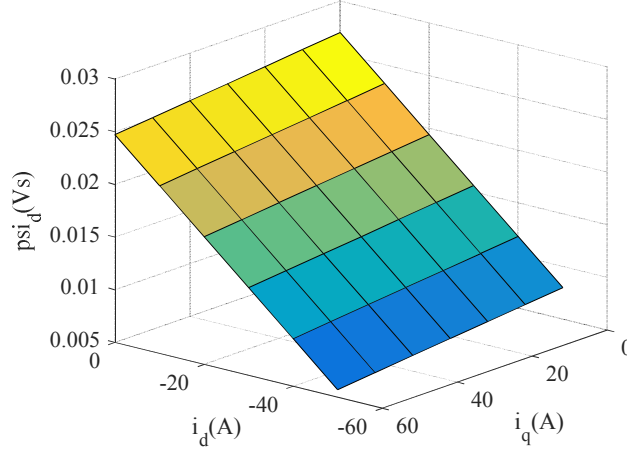
Fig. 3-3 Flux map of φ_d versus (i_d, i_q)

$$T(i_d, i_q) = 1.5p\left[\varphi_d(i_d, i_q) \times i_q - \varphi_q(i_d, i_q) \times i_d\right]$$

$$V(i_d, i_q) = \omega\sqrt{\varphi_d(i_d, i_q)^2 + \varphi_q(i_d, i_q)^2}$$

(3-1)

In the above equations, p is the number of pole pairs and ω is the electrical angular speed. In order to find an optimum (i_d, i_q) for a given torque-speed command, a searching algorithm based on the torque function and the voltage constraint is developed. The power loss is minimized, and the voltage is kept below or equal to the DC link voltage limit when the speed becomes higher than the base speed. This searching algorithm is a purely analytical method without FE simulation. It provides results within a few seconds. As a result, the machine design process is greatly accelerated by this inverse flux machine model.

3.3.3 Iron Loss Model

The machine loss mainly includes copper loss and iron loss. While the copper loss can be evaluated by the winding resistance and phase current, the

iron loss is dependent on the geometry dimension and flux distribution. The FE model is required to run for an electrical cycle to calculate the iron loss which is extremely time-consuming for each operating point. A fast iron loss model is therefore essential for the optimisation process.

The iron loss in the laminations of a machine includes three components [131], i.e. the hysteresis loss P_h, eddy current loss P_e, and excess loss P_x. Equation (3-2) shows the calculation based on Bertotti iron loss model via FE analysis.

$$P_{fe} = P_h + P_e + P_x$$

$$P_{fe} = k_f \int \left(k_h f B_m^2 + \frac{\sigma d^2}{12} \left(\frac{dB}{dt}\right)^2 + k_e \left(\frac{dB}{dt}\right)^{1.5} \right)$$

<div align="right">(3-2)</div>

In the equation above, k_f is the stack packing factor. k_h is the hysteresis loss coefficient. k_e is the eddy current loss coefficient. f is the frequency. B_m is the peak value of the local flux density and B is the instantaneous flux density. σ is lamination material conductivity. d is the thickness of the lamination. According to [132], each iron loss component under a given machine operation can be estimated by using its open-circuit and short-circuit iron loss behaviours, together with phase voltage and d-axis voltage for the specific operating point, as shown in (3-3). The parameters in (3-3) are evaluated in the short circuit and open circuit FE simulations. As a result, only two typical conditions (short circuit and open circuit) need to be calculated to evaluate the iron loss for each design sample. Thus the FE computation time is reduced significantly, while maintaining the accuracy within 2%. This iron loss model is integrated in the searching algorithm in section 3.3.2 to support the minimum loss operating point searching algorithm.

$$P_h = P_h^{oc} \times \frac{V_m}{V_{oc}} + P_h^{sc} \times \frac{V_d}{V_{sc}}$$

<div align="right">(3-3)</div>

$$P_e = P_e^{oc} \left(\frac{V_m}{V_{oc}}\right)^2 + P_e^{sc} \left(\frac{V_d}{V_{sc}}\right)^2$$

$$P_x = P_x^{oc} \left(\frac{V_m}{V_{oc}}\right)^{1.5} + P_x^{sc} \left(\frac{V_d}{V_{sc}}\right)^{1.5}$$

In the equation above, V_m is the phase voltage for a specific operating point. V_d is d-axis voltage for a specific operating point. V_{oc} is the open-circuit phase voltage, viz. back emf.

3.3.4 Full Model Integration for Inter-turn Fault Current Prediction

Since this machine is aimed for the aerospace application, fault tolerant capabilities should be examined during optimisation process. According to the previous investigation, this machine can cope with the open circuit, and short circuit fault easily. The most severe fault scenario is the single turn short circuit fault. And the results indicate that the turn fault current would be the highest if it occurs in coil B2 close to the slot opening under motoring mode. For a successful design, the turn fault current should be sustained without exceeding the defined thermal limit. Therefore, the turn fault current in B2 coil should be evaluated during the optimisation process. In order to shorten the computation time, the performance of the machine under healthy condition is evaluated based on the 1/6 model due to symmetry. However, the turn fault current can only be predicted using the full machine model since it operates in asymmetric mode. Therefore, the optimisation process facilitates a systematic transition between the 1/6 model and the full model for each design sample to evaluate the performance under both (healthy and faulty) operation modes.
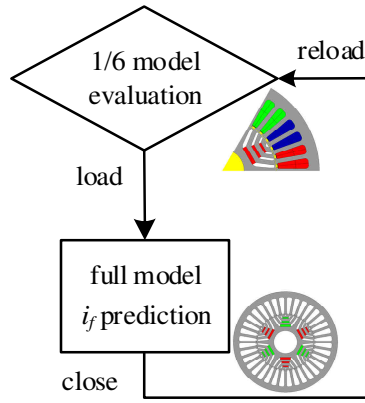
Fig. 3-4 Full model integration

A large number of transient cycles in FE is required for the turn fault current to reach steady state where its RMS value of the fault current can be accurately calculated. Therefore, a fast fault current prediction method is desired to reduce the computation time. Here we assume that the steady state fault current can be represented by: $i_f = \sum_{k=1}^{n} i_k \sin \vartheta_k$, with only AC components. However, there is a DC offset in the fault current during the transient process, which decays very slowly. It is also observed that the AC components set down relatively quickly. Hence, the transient fault current after a few cycles may be appropriately described by: $i_f = d + \sum_{k=1}^{n} i_k \sin \vartheta_k$. At steady state, the RMS value is calculated as:

$$rms_s = \sqrt{\sum_{k=1}^{n} (i_k)^2/2} \tag{3-4}$$

While in the transient state, the RMS value can be obtained similarly as:

$$rms_t = \sqrt{\sum_{k=1}^{n} (i_k)^2/2 + d^2} \tag{3-5}$$

If the transient RMS value and offset value are known, the steady RMS value can be predicted as:

$$rms_s = \sqrt{(rms_t)^2 - d^2} \tag{3-6}$$

As a result, the RMS value of the steady state fault current can be predicted through FE computation over a small number of electrical cycles from the start of the transient solving process. This in turn leads to reduced computation time in determining the steady state RMS value of fault current. The value predicted by (3-6) has been confirmed to be around 10% lower that of (1-4). Hence, the steady state fault current RMS value and the resultant heat can be estimated.

3.3.5 Cooling Design

As previously mentioned, the current density in the slot is around $10{\sim}12 A/mm^2$, whilst the ambient and the coolant inlet temperature is 100^oC and 110^oC, respectively. However, the maximum winding temperature is required to be restricted under 180^oC for the chosen insulation class copper wire to achieve a 300,000 hours lifetime. Thus, both the operation condition and high ambient temperature requires effective heat dissipation. Effective cooling facilities are essential to minimize the temperature rise. As a result, three different cooling solutions are investigated, namely, spiral cooling jacket, housing ducts and slot ducts. Their cooling effects are also evaluated in Motor-CAD [133].

A. Spiral cooling jacket
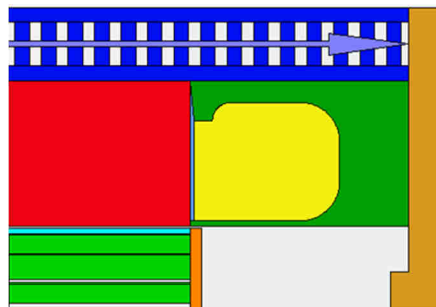
Fig. 3-5 Illustration of spiral cooling jacket

The spiral cooling jacket is one of the most frequent-used liquid cooling solutions. The cooling jacket is integrated on the housing frame as shown in Fig. 3-5. The grooves are cut out on the cooling chamber to carry the coolant oil all around the stator surface. The cooling sleeve fits outside of the cooling chamber, making it a sealed environment for the coolant fluid. Coolant oil is

flowing in the path determined by the grooves to cool the machine. An outside pump and cooling system helps cool the coolant oil and provide the circulating pressure. Since the diameter for the machine is 220mm, the maximum available diameter for the stator lamination is set as 180mm, leaving 40mm for the spiral cooling jacket space. The machine can be designed with a small air gap (0.75mm). Then the stator lamination together with copper windings are in inserted into the housing frame. In order to have a better cooling effect, the windings are potted with a high thermal conductivity material (Stycast 2676FT, 1.3W.m/K, service temperature, 185°C~260°C) to enhance the heat dissipation capability.

B. Housing ducts
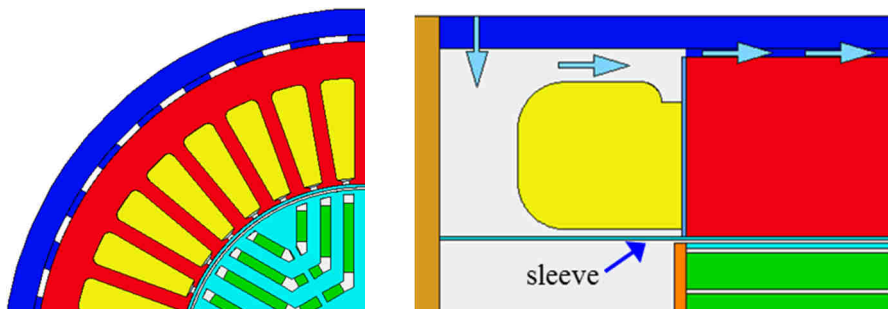
Fig. 3-6 Illustration of housing ducts

The second cooling solution is the housing ducts. Axial parallel ducts are cut out in the housing frame as shown in Fig. 3-6. 36 ducts distribute on the stator outer surface evenly as the path for the coolant. The coolant coil flows into the stator chamber from the inlet, then goes through the housing ducts, and finally flows out from the outlet. As indicated in Fig. 3-6, the stator lamination and windings are immerged in the coolant which can take the heat away directly. In order to seal the oil, a 1mm thick PEEK sleeve is attached on the stator inner surface. As a result, the air gap has to be 1mm larger, taken as 1.75mm. And the available diameter for stator lamination is 200mm due to the thinner enclosure.

C. Slot ducts

The third cooling solution is the slot ducts. The ducts are now located in the slot area as shown in Fig. 3-7. Coolant oil now flows through the slot ducts

other than the housing ducts. The stator lamination and windings are also immerged in the coolant. PEEK sleeve is required on the stator inner surface to seal the oil. As a result, the air gap is also taken as 1.75mm. The maximum available diameter for stator diameter is 200mm, too.

In order to compare the cooling abilities of these three cooling solutions, two machines are initially optimised as shown in Fig. 3-8. Due to the different cooling solutions, diverse stator diameter and air gap are adopted as discussed above. The leading parameters and losses of the two initial samples are listed in Table 3-2. The losses are evaluated with the rated torque at base speed which is the worst case for the cooling systems.
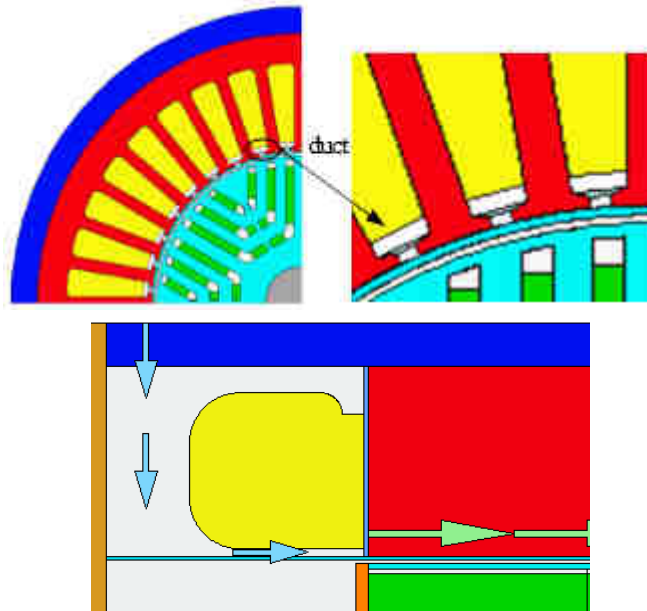
Fig. 3-7 Illustration of slots ducts
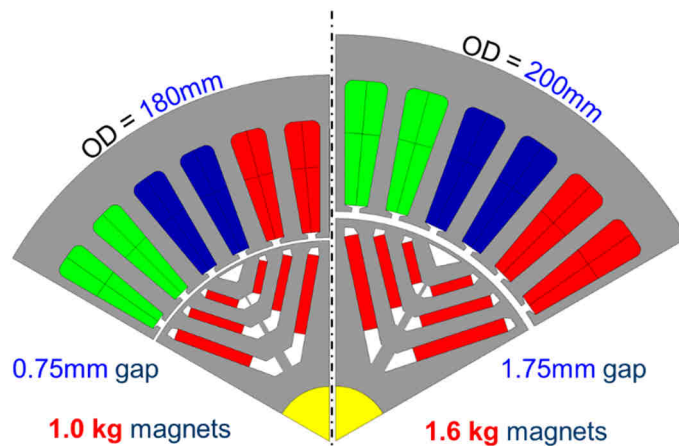
Fig. 3-8 Initially optimised samples

Table 3-2 Leading parameters and losses of the initial samples

Parameter	Spiral housing jacket	Housing ducts	Slot ducts
Stator outer diameter	180mm	200mm	200mm
Housing diameter	220mm	220mm	220mm
Air-gap	0.75mm	1.75mm	1.75mm
Copper loss(160 ^{o}C)	1234W	1301W	1301W
Iron loss	324W	261W	261W

Table 3-3 Average and maximum winding temperature for different cooling solutions

Temperature	Spiral housing jacket	Housing ducts	Slot ducts
Average	148.2^{o}C	171°C	159.3^{o}C
Maximum	167°C	200°C	180°C

(a) Spiral housing jacket

(b) Housing ducts

(c) Slot ducts
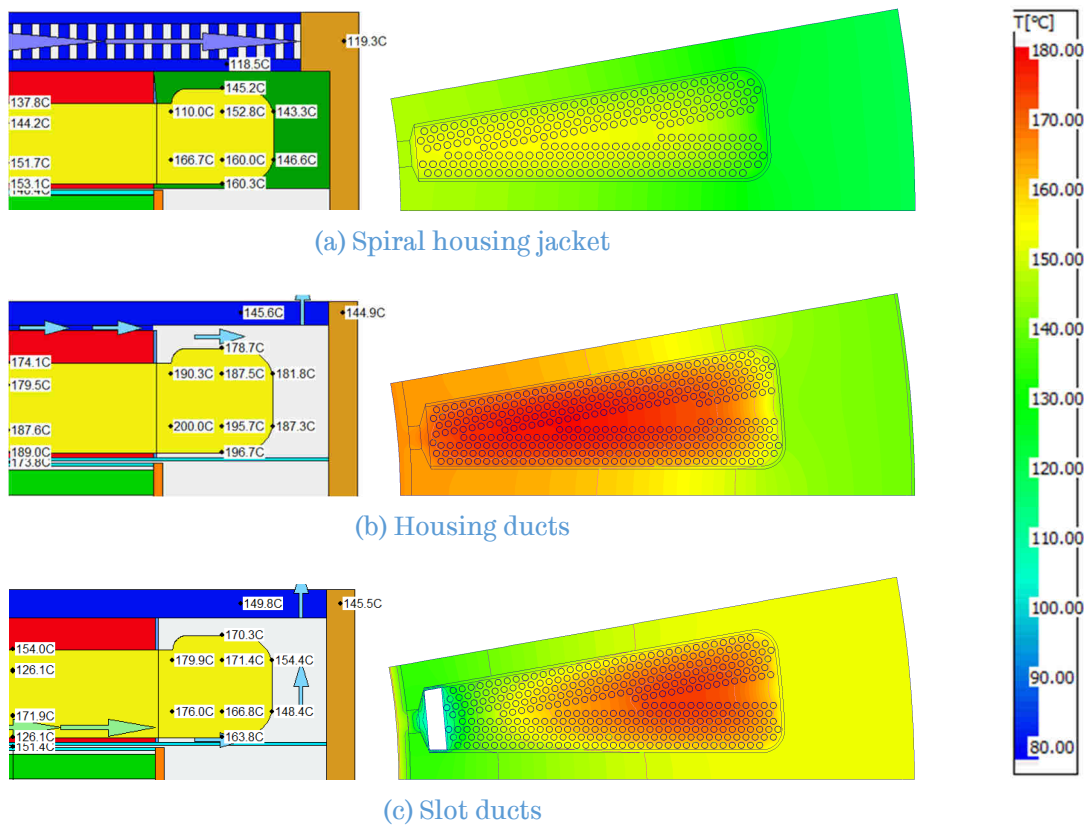
Fig. 3-9 Evaluated results for initially optimised samples

Due to larger airgap, the design with 1.75mm airgap requires 60% more magnets to achieve the same torque capability. And the rotor bridge thickness is increased to restrict the maximum Von Mises stress. The copper loss for the small airgap design is slightly lower than the design with the larger airgap. The copper loss and iron loss are loaded to the three cooling models in Motor-

CAD. The coolant oil flow rate is set as 6 litre/min for the three cooling models. The resultant temperatures distributions in the stator are shown Fig. 3-9. The average and maximum winding temperatures are listed in Table 3-3.

It is found the spiral housing jacket exhibits the best cooling effect, the second is the slot ducts, with the housing ducts least effective. Under same volumetric constraint, only for the spiral housing jacket, the maximum temperature is restricted under the defined thermal limit (180°C). This is because the spiral grooves on the housing jacket gives the largest heat convection area, and the pressure of the fluid in the spiral housing jacket is also the highest. In contrast, the windings are impregnated and the oil cannot flow into the winding inside for the housing ducts, therefore leading to poorer cooling performance. However, the oil can flow in the small slot ducts for the third cooling option. The oil contact with the copper winding directly, as a result, performing better than the housing ducts. It is worth noting that the maximum winding temperature always arises in the end winding part close to the lamination side. This gives rise a local hot spot because it is far away from the cooling ducts. Of course, it is possible to optimise the cooling with cooling options B and C. However, the large airgap reduces the attainable reluctance torque, and hence more magnets and large contribution of PM torque are required. Consequently, the capability to tolerate various faults is compromised.

According to the analysis above, the spiral housing jacket is therefore selected as the cooling solution for this machine. The grooves in the jacket are appropriately designed to maximise the cooling effect while ensuring structural integrity in Motor-CAD. And in fact, it is also with the lowest cost because of less magnets and active materials being used, and simple implementation.

3.3.6 Lumped Parameter Thermal Model

The spiral housing jacket has been designed and selected as the cooling solution for this machine. However, one disadvantage of the Motor-CAD model is that it cannot be incorporated into the optimisation process in GOT-

IT for thermal performance evaluation of each design sample. Therefore, a lumped parameter thermal model is developed as shown in Fig. 3-10 [134].
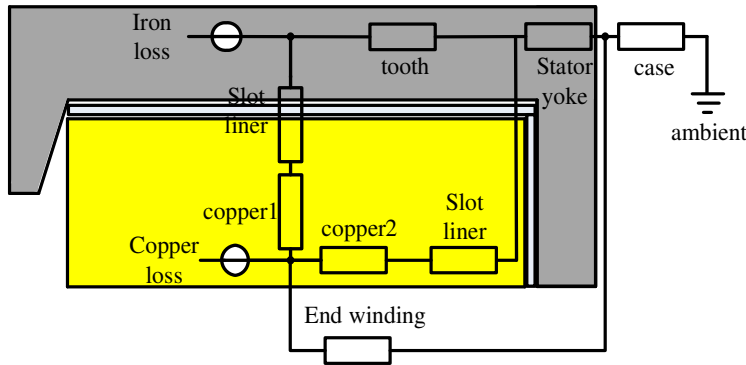
Fig. 3-10 Lumped parameter thermal model

The thermal dissipation in the machine is assumed to be predominant in the radial direction, so the thermal dissipation in the axial direction is neglected. The thermal network models only half of the tooth pitch due to the symmetry. In the thermal network, the thermal resistances of each part can be derived using the governing principle of the heat conduction [135]. The resistance of the case (housing) shown in Fig. 3-10 is evaluated in Motor_CAD which captures the cooling capability of the spiral housing cooling jacket. Whilst the copper loss and stator iron loss are loaded from the FE evaluation during optimisation. The temperatures predicted by the lumped parameter thermal model are compared with the Motor_CAD as shown in Table 3-4. The results estimated by the two methods are quite close. The copper loss dependency on the temperature has been considered by updating the copper loss with the calculated temperature for a few times. Therefore, the thermal performance of the machine can be predicted by this lumped parameter thermal model during design optimisation.

Table 3-4 Comparison of the predicted temperatures

Average temperature	Rated torque, base speed		Rated torque, max speed	
	Winding	Stator yoke	Winding	Stator yoke
Motor_CAD	162.1°C	127.6°C	134.4°C	119.5°C
Lumped parameter thermal model	165.8°C	130.2°C	138.1°C	120.8°C

Single turn fault in B2 coil has been identified as the worst fault scenario whose fault current is evaluated during optimisation for each design sample. The resultant hotspot temperature under this extreme fault condition also should be estimated which provides the reference to select the final design sample. Thus, an adapted lumped parameter thermal model is developed for the turn fault as shown in Fig. 3-11. As described in Chapter 2, upon detection of a turn fault, TSC will be applied via the 3-phase inverter. The thermal analysis is therefore performed against this condition. As for the turn fault, only the current of the faulted turn is noticeably higher but it has minor influence on the other regions. Thus, the temperature of the stator yoke T_y is mainly determined by the phase currents under the short circuit condition which are close to the characteristic currents (terminal short circuit current under healthy condition). Then, the temperature rise of the faulted turn against the stator yoke can be calculated by the adapted model. The copper winding is divided into two parts, i.e., healthy copper and faulty copper parts. The faulty copper loss of the faulted turn is dependent on the turn fault current while the normal copper loss of the healthy part are determined by the characteristic currents.
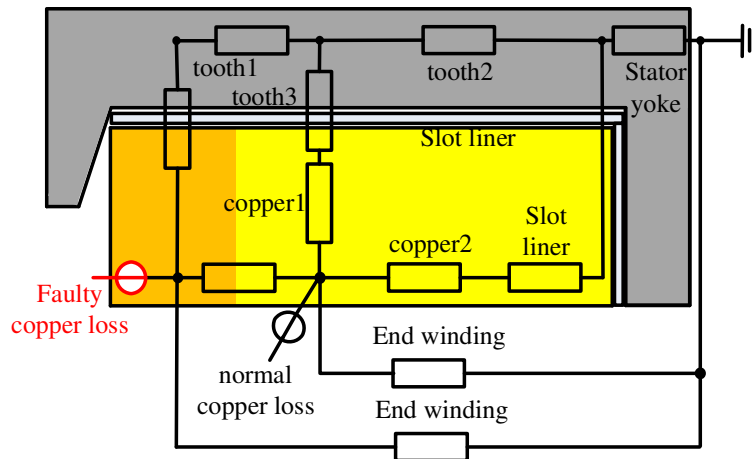
Fig. 3-11 Lumped parameter thermal model for turn fault

Finally, the temperature rise of the faulty copper part, ΔT_f, with respect to the stator yoke is estimated by the thermal model for turn fault. Thus, the actual temperature of the faulty copper winding is obtained by (3-7).

$$T_f = \Delta T_f + T_y$$

Hence, the temperature rise in both healthy and the worst fault condition will be fed to the GOT-IT for evaluation of the objective function and constraints. If the temperature has exceeded the maximum temperature limit, the design sample will be discarded.

3.3.7 Optimisation Objective, Constraints and Parameters

The optimisation objective is set to maximize the efficiency at the rated operating point (i.e., rated torque at the base speed). The efficiency is evaluated for each design sample after calculating the copper loss and iron loss based on the developed design tools. From the torque-speed envelope, the peak torque at base speed point is 119.4Nm/4000rpm, the peak torque at max speed is 24.9Nm/19200rpm. These two points determine the basic shape of the envelope. As long as all the defined design constraints (see Table 3-5) are satisfied against these two operating points, the design sample is judged as feasible in the optimisation process. The maximum current density is used just as initial gauge and indeed the maximum winding temperature is imposed as a strict constraint.

Table 3-5 Design constraints of the machine

Name	Value
Stack length	100mm
Max current	200A
DC Link Voltage	270V
Maximum current density	12.5A/mm^2
Max temperature in the windings	180°C
Von Mises stress	450MPa

The PMA SynRM machine with 36 slots and 6 poles is selected for the design study as shown in Fig. 3-12. This slot/pole configuration is selected considering the trade-off between high torque production capability at low speed and low iron loss at high speed. The absence of low order space harmonics combined with the multilayer rotor and 0.2mm Cobalt iron

lamination lead to low iron loss production under high speed operation. The selection of three embedded layers and cutout in the rotor leads to enhanced insulation ratio (ratio of air to iron parts), and hence reluctance torque capability, whilst ensuring good structural integrity and manufacturability of the rotor.
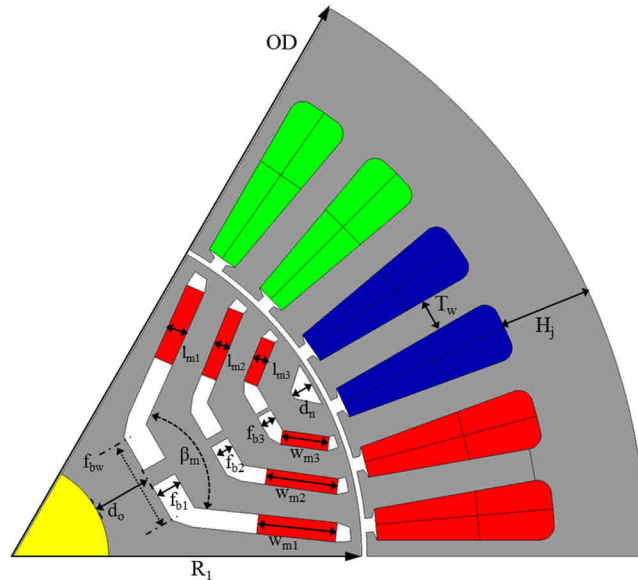
Fig. 3-12 PMA SynRM machine and geometry parameters

The maximum permissible outer diameter of 180mm (considering the space required for the spiral housing jacket shell, i.e., 40mm) is selected for the purpose of fully exploiting the reluctance torque capability, whilst maintaining a minimum current density in the slots. The axial length should be parametrically scanned on a reference design in order to find the minimum length that brings the design close to its thermal limit whilst satisfying the required operating envelope and the remaining design constraints. The resulting length of 100mm forms a good starting point for the optimisation process.

The magnet arrangement in the rotor is selected based on the findings of previously conducted rigorous topologic and parametric design optimisation process. The placement of the magnets on the sides of the rotor flux barriers leads to a drastic reduction of the magnet amount for the same flux linkage compared with other magnet configurations (e.g. single magnet in the middle of the flux barrier or combination of middle and side magnets in the flux

barrier). This can be attributed to the fact that this magnet configuration fully exploits the flux-focusing effect which concentrates the flux in the airgap, and also arranges all the magnets to be closer to the airgap leading to less flux loss due to leakage flux [136].

The optimising parameters of the PMA SynRM are illustrated in Fig. 3-12, and they are also listed in Table 3-6. The techniques discussed above, namely, the inverse machine model, iron loss calculation, turn fault current prediction and thermal estimation are all integrated in the global optimisation platform. The objective is set to maximize the efficiency at rated operating point, while satisfying the required torque-speed operating range and the defined design constraints listed in Table 3-5. Finally, the optimisation process is initiated, and the results will be discussed in the following sections.

Table 3-6 Parameters to be optimised

Name	Symbol
Back iron thickness	H_j
Tooth width	T_w
Rotor radius	R_1
Magnet thickness	l_{m1}, l_{m2}, l_{m3}
Magnet width	w_{m1}, w_{m2}, w_{m3}
Middle flux barrier thickness	f_{b1}, f_{b2}, f_{b3}
Middle flux barrier width	f_{bw}
Magnet layer's angular span	β_m
Magnet layer's depth	d_0
Turn number	TN
Split ratio	R_1/OD

3.4 Selected Design Alternatives and Performance Comparison

Three iterations with 405 samples are conducted by GOT-IT to build the response surfaces and find the optimum design sample. The efficiency of the design samples are shown below. After each iteration, the design samples move towards a higher efficiency range. The efficiency of the design sample increases from the initial 95.10% to 96.23% finally.
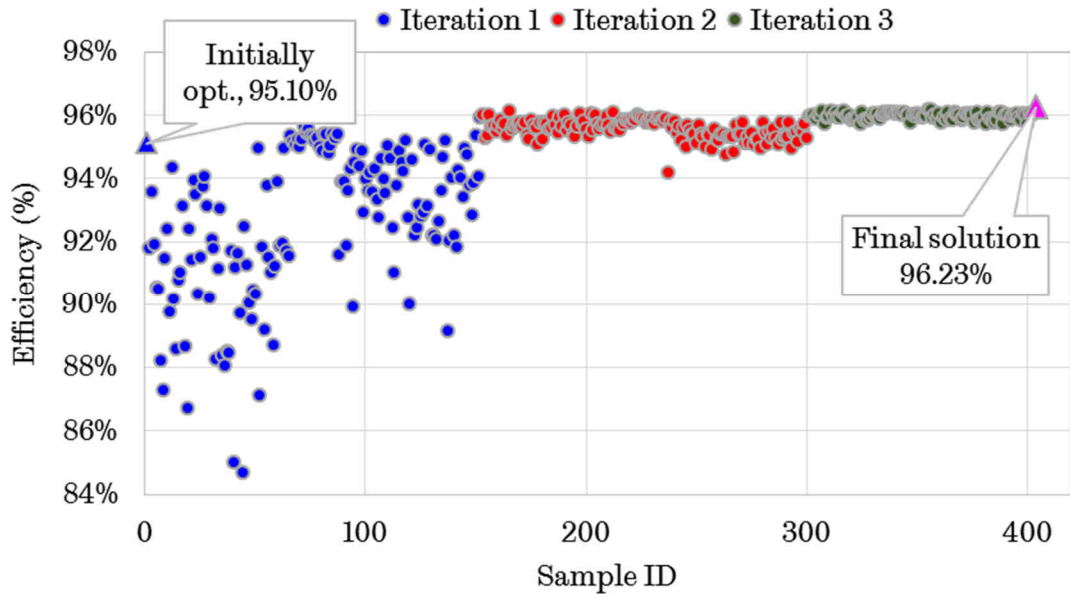
Fig. 3-13 Efficiencies of the design samples

3.4.1 Performance Comparison of Selected Alternatives

As can be seen from Fig. 1-13, the differences in efficiencies of the designs in the third GA iteration are very small. This implies that there are many designs that yield very similar efficiency, and it is of interest to examine typical designs in this group. After examination of the design samples, two designs, namely sample A and sample B, become promising in the optimisation as shown in Fig. 3-14. Sample A exhibits the highest efficiency while it is slightly lower for sample B. The key features of two samples are compared in Table 3-7. Sample A utilises 18% more magnets than sample B whilst sample B has a larger inner bore. The different geometries lead to that more PM torque is produced in sample A for higher back emf while more reluctance torque is exploited in sample B due to the higher inductance difference of q axis and d axis. Due to higher magnets usage, the back emf of sample A at maximum speed is higher than the DC link voltage 270V, therefore uncontrolled rectification may occur if the inverter fails. Further, the high back emf will incur higher fault current in case of a turn short circuit fault. In terms of sample B, the back emf is 30% lower which eliminates the possibility of uncontrolled generation even if the inverter fails. It also reduces the fault current in case of a short circuit fault.
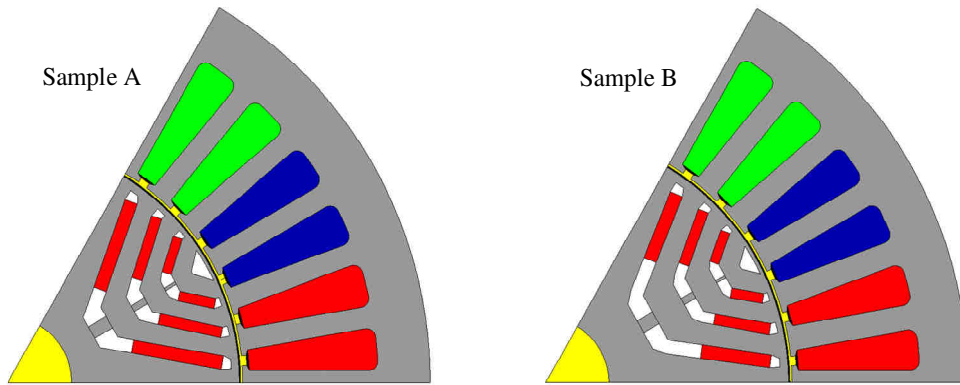
Fig. 3-14 Cross sections of sample A and B

Table 3-7: Key features of sample A and sample B

	Sample A	Sample B
No. of turns/coil	8	8
Magnets usage	1.02kg	0.86kg
Rotor radius	49.3mm	51.8mm
Peak line back emf at 19200rpm	356V	257V
Inductance difference (L_q-L_d)	0.85mH	0.93mH
Characteristic current	108.6A	75.5A

The electrical performances of the two candidates are further compared in Table 3-8 at rated operation point where an iron loss built factor of 1.3 is considered. Sample A requires less current with the help of greater PM field while sample B exhibits a larger gamma angle which is beneficial for reluctance torque. The current density and the copper loss of sample A is 15% and 25.8% less than the sample B, respectively. As a result, the efficiency of sample A is slightly higher than sample B. The predicted copper temperature is 166°C and 179°C for samples A and B, respectively.

Table 3-8: Performance comparison of sample A and sample B

	Sample A	Sample B
Efficiency	96.23%	95.43%
Current and gamma angle	122.4A/48.9°	130A/54.5°
Current density	9.3A/mm²	10.9A/mm²
Phase resistance	19.3mΩ	21.6mΩ
Copper loss	1302W	1638W
Iron loss (1.3x)	266W	275W
Copper temperature	166°C	179°C

Turn fault current (rms)	320A	266A
Fault turn temperature	295°C	233°C

Since the machine is aimed for fault tolerant application, the performances under fault condition are also examined. Considering the worst fault scenario, viz. single turn short circuit fault in B2 coil, after TSC the RMS turn fault currents are 320A and 266A for samples A and B respectively. They are significantly higher than the rated value. According to the adapted turn fault thermal model in Fig. 3-11, the induced hotspot temperatures of the faulted turn are predicted as 295°C and 233°C. The maximum continuous operation temperature of class-R insulation copper wire is 220°C. However the hotspot in sample A is 75°C higher than it. This high temperature would degrade the winding insulation quickly and lead to further damage. As for sample B, it is only 13°C higher in ideal short circuit condition. In real operation, due to the extra impedance of the short circuited path, the fault current and the resultant temperature will be lower, which can be sustained by the machine.

It can be seen that the uncontrolled generation fault and inter-turn fault still poses risk for sample A though it has higher efficiency. Whilst sample B could tolerate these two faults with slightly lower efficiency. Therefore, sample A is discarded and sample B is selected as the potential candidate.

3.4.2 Axial Length Tuning to Meet Thermal Constraints

The copper temperature in Table 3-8 represents the average temperature of the copper windings which is predicted by the lumped parameter thermal model as in Fig. 3-10. The average temperature of sample B is 179°C which is close to the maximum allowable temperature 180°C. Thus, the copper temperature in other position is quite likely to be higher than 180°C. As a result, the thermal performance of sample B is examined in Motor_CAD with improved accuracy as shown in Fig. 3-15. The maximum temperature of sample B arises to 190.4°C in the end winding region. The over-heated winding will

lead to a significant lifetime reduction which is undesirable for aerospace application.
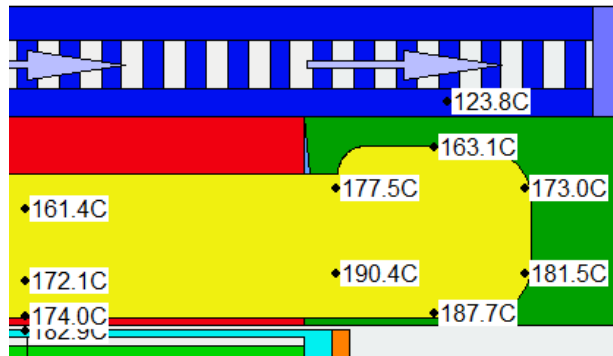
Fig. 3-15 Temperature rise prediction of sample B by Motor_CAD

The analysis implies that in healthy condition sample B cannot accommodate the heat in such a limited space. The maximum permissible outer diameter of 180mm has been selected. However, the axial length 100mm is initially chosen as a starting point. Hence, the axial length should be increased since no design samples meet the design requirements as well as the fault tolerance.

Table 3-9: Axial length tuning of sample B

	B	B-1	B-2	B-3
Stack length	100	105	110	115
Efficiency (%)	95.43	95.65	95.83	95.95
Current (A)	130	124.3	119.2	114.6
Current density (A/mm²)	10.9	10.4	10	9.6
Phase resistance (mΩ)	21.6	22.1	22.7	23.2
Copper loss (W)	1638	1537	1449	1373
Iron loss 1.3x (W)	275	283.4	289	297
Max copper temperature (°C)	190.4	183.5	177.1	171
RMS turn fault current (A)	266	266	266	266
Fault turn temperature (°C)	233	232.7	232	231.7

As a result, the axial length of sample B is tuned to find the optimum value as shown in Table 3-9. The evaluation results show that as the axial length increases, lower current is required for the rated torque, resulting in less copper loss, and hence leading to improved efficiency. Meanwhile, the heat conduction area of the stator lamination with the oil cooling housing jacket is

increased which improves the thermal dissipation. As a result, the copper winding temperature decreases. The thermal performance of the 4 samples are examined in Motor_CAD, the maximum copper temperatures are given. It is found the maximum copper temperature of samples with 110mm length or larger is lower than 180 °C, satisfying the thermal constraints. Regarding the turn fault, the fault currents and resultant hotspots almost remain unchanged due to the same flux level. So the machine can still continue operation in case of the worst fault case by application of TSC.

Considering the machine performance in both healthy and faulty conditions, B-2 sample satisfies all the requirements and constraints with a minimum axial length. Thus B-2 sample is selected as the candidate for the application. It should be noted that the exact hot spot temperature that the machine can sustain is dependent on how long the fault tolerant operation needs to last. With rule-of-thumb estimation, the insulation life time will be halved for every 10 degree increase in winding temperature. Thus, 13 degrees higher temperature than the Class R rated would still give at least thousands of hours of lifetime under the worst case fault condition because loss of lifetime under normal operation when the winding temperature is around 180 degrees is very little and hence negligible. In reality, it is unlikely that fault-tolerant operation needs to last more than a few hundreds of hours. However, at this point of study, representative lifetime requirement for the fault tolerant operation is not available and hence the design can be considered conservative.

3.5 Mechanical Design

During design optimisation, the mechanical behaviour should also be evaluated. Rotor stress analysis and rotor dynamics study are performed to ensure rotor system operates without any significant vibrations that could lead to any potential problems in the rotor and the shaft.

3.5.1 Rotor Stress Analysis

For the multi-layer rotor configuration under study, the magnets and inner iron parts are purely retained by the thin middle and circumferential iron bridges which will experience large centrifugal force at high speed. The widths of the bridges should be proportional to the weight of material it needs to support. During optimisation, the iron bridges of each design sample are adjusted based on a reference design to guarantee that the mechanical stress is within the limit [137, 138]. For accurate evaluation, the mechanical stress of these iron bridges should be examined in Ansys to ensure it does not exceed the yield strength which is the criteria to prevent mechanical failure.
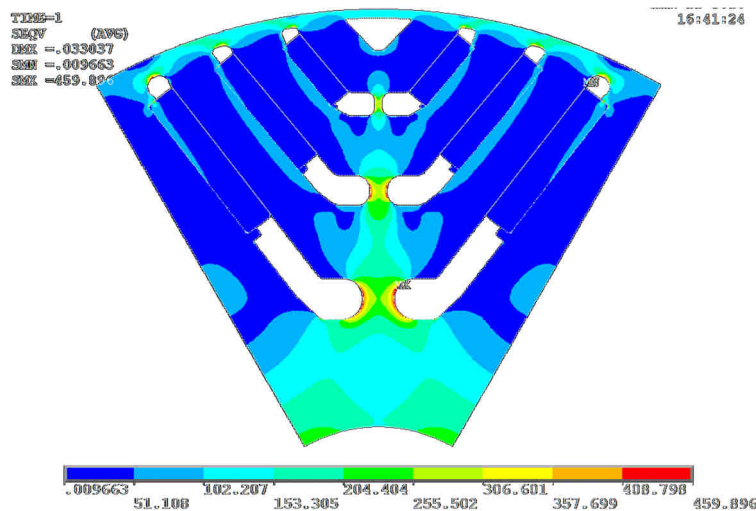
Fig. 3-16 Rotor stress analysis of sample B-2

The mechanical stress analysis of the selected B-2 sample is assessed at 20% over speed, i.e., 23040 rpm as shown in Fig. 3-16. The examination shows the maximum von Mises stress of the rotor is 460MPa which is marginally higher than the yield strength of the lamination material, viz. Vacodur 50 steel. Hence, mechanical design has been performed to bring the stress under the design limit by modifying the respective bridges. Various iterations are performed to select the best possible combination of bridge widths. Two final iterations are compared as shown in Table 3-10. As will be seen, the von Mises stress reduces with the increase of iron bridge thickness. The maximum von Mises stress is lower than 450MPa in Iteration-II as shown in Fig. 3-17, and therefore it is selected as final design. It should be noted that the slightly increased iron bridges lead to higher flux leakage and have negative impact on

the electromagnetic performance. However, the influence is insignificant and will be fully accounted in subsequently modelling and predictions.

Table 3-10: Iron bridge tuning of sample B

	B-2	Iteration-I	Iteration-II
Middle bridge 1	2.9mm	3.0mm	3.05mm
Middle bridge 2	1.5mm	1.6mm	1.55mm
Middle bridge 3	0.6mm	0.6mm	0.6mm
Max. von Mises stress	460MPa	450MPa	448MPa
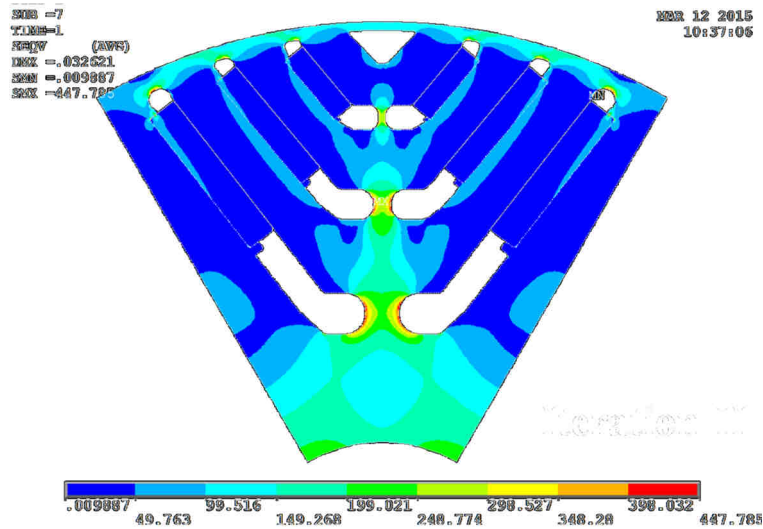
Fig. 3-17 Rotor stress analysis of iteration-II

3.5.2 Rotor Dynamics Study

In a rotor-bearing system, the bearing stiffness is much lower than that of the rotor, resulting in a relatively low natural frequency. When the rotation frequency of the rotor, which is usually unbalanced, approaches to its natural frequency, resonance will occur and may cause a mechanical failure because the damping in the rotor-bearing is usually small. Therefore, the rotor dynamics should be analysed to ensure the maximum cruise speed is much lower than the first order critical speed which corresponds to the first order natural frequency.

Fig. 3-18 illustrates the schematic of the rotor-bearing system modelled in Ansys. According to the balance grade of the rotor, the maximum eccentricity on the rotor can be predicted. Then, the maximum radial load on the bearing

is calculated, 188N for each bearing in this application. Furthermore, based on the relationship between the bearing stiffness and its radial load, measured by the bearing supplier, the radial stiffness is interpolated to be $6.67 \times 10^7 N/m$. The resultant Campbell diagram is depicted in Fig. 3-19.

In Fig. 3-19, "BW" and "FW" represents "backward" and "forward" respectively. The critical speed at a given order is obtained at the intersection of the forward natural frequency curve at the corresponding order and the dashed line whose slope is 1 when the x- and y-axes shown in Fig. 3-19 are converted into the same unit. In this way, the first order critical speed is predicted to be 30,797 rpm, which is higher than 1.4 times the maximum operating speed of 19,200 rpm. Hence, the rotor will not have any significant vibration issues.
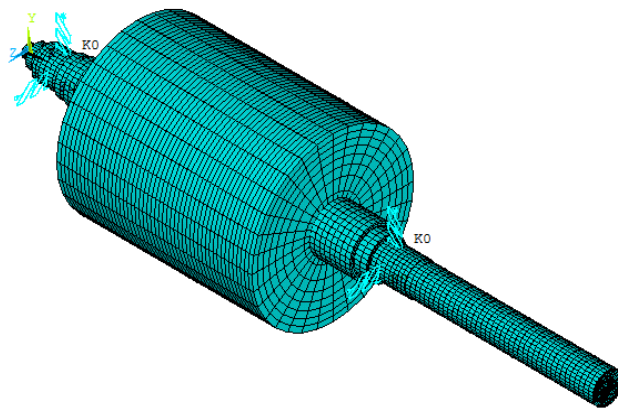
Fig. 3-18 Schematic of the rotor-bearing system for rotor dynamics analysis
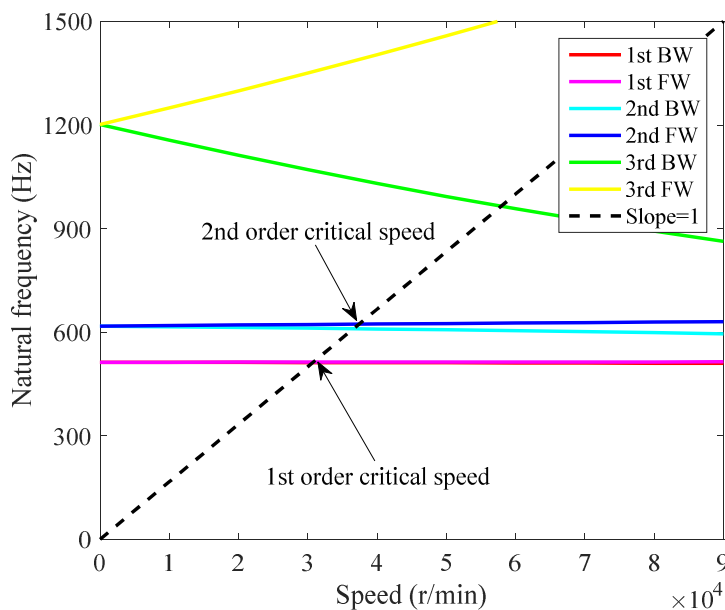
Fig. 3-19 Campbell diagram of the rotor-bearing system

Finally, the final design is obtained which satisfies all the constraints in both healthy and fault conditions. The performance of the design will be evaluated thoroughly both in healthy condition and various faulty scenarios in the next section.

3.6 Performance Evaluation of the Final Design
3.6.1 Healthy Condition

A. Back emf

First, the phase back emfs of the ABC set is evaluated, as shown in Fig. 3-20, and exhibits symmetry between the three phases. The back emfs of the other two sets are not shown because they are identical to those of ABC set. The line back emf is also calculated at maximum operating speed 19200rpm as shown in Fig. 3-21. The peak value is 273.3V which is slightly higher than the DC link voltage. Considering the bias voltage on the diodes, there is no risk of uncontrolled generation via the diodes in case of inverter failure at the maximum speed. It is achieved by chosing a design sample with low back emf which is also beneficial for better fault tolerance. The tooth ripple harmonics are clearly visible in the back-emfs. They will also give rise to torque ripple and increase the peak voltage at high speed. Stator skew by one slot is therefore employed to minimise the tooth ripple effect. For the simplicity of FE analysis, the skew is not considered in this Chapter because its effect on performance and fault behaviour is not significant.
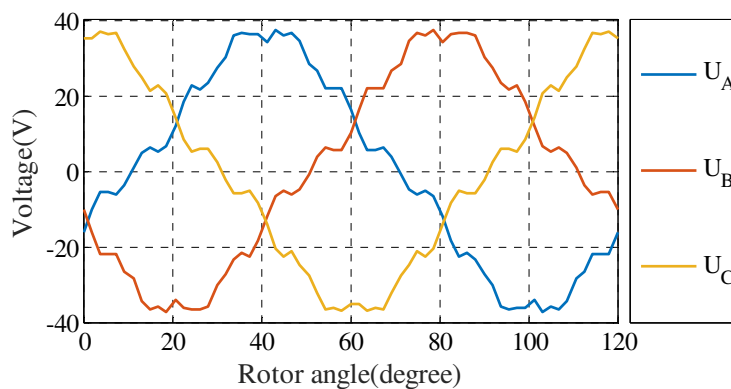
Fig. 3-20 Phase back emf at 4000rpm
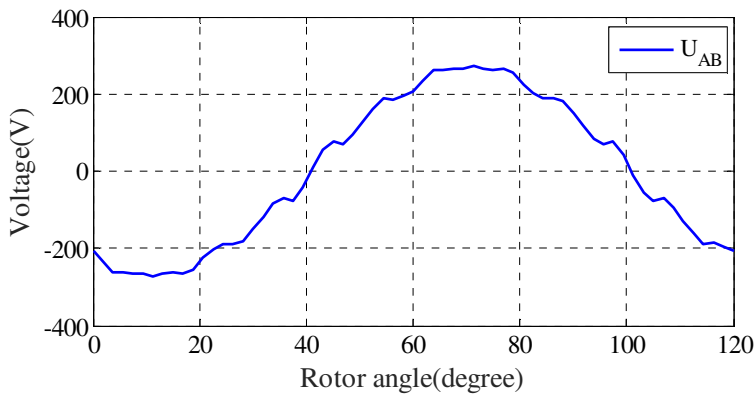
Fig. 3-21 Line back emf at 19200rpm

B. Load performance

Secondly, the performance of the final design in healthy condition is evaluated in terms of torque capability and efficiency. The maximum achievable torque under the voltage and current limit in Table 3-1 is evaluated as shown in Fig. 3-22. It can be found that the maximum achievable torque is higher than the required peak torque. So the torque requirement is satisfied and this machine has very good overload capability. Its output power is also illustrated in Fig. 3-23. The power curves confirm it has wide constant power speed range.
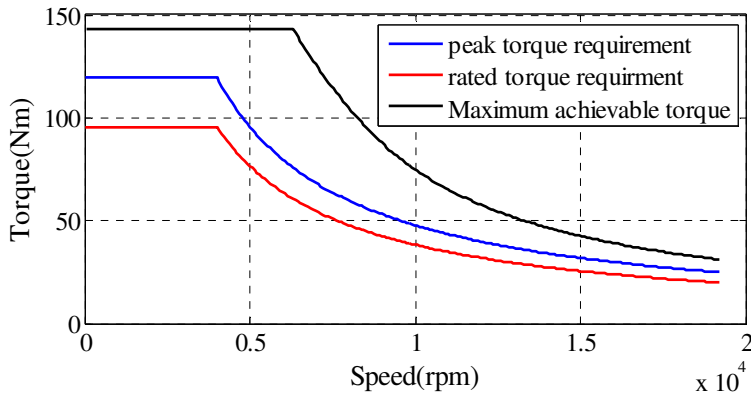
Fig. 3-22 Maximum achievable torque
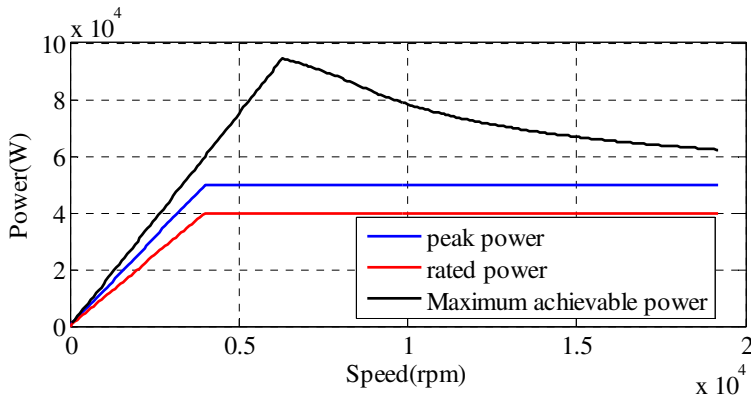
Fig. 3-23 Maximum achievable power
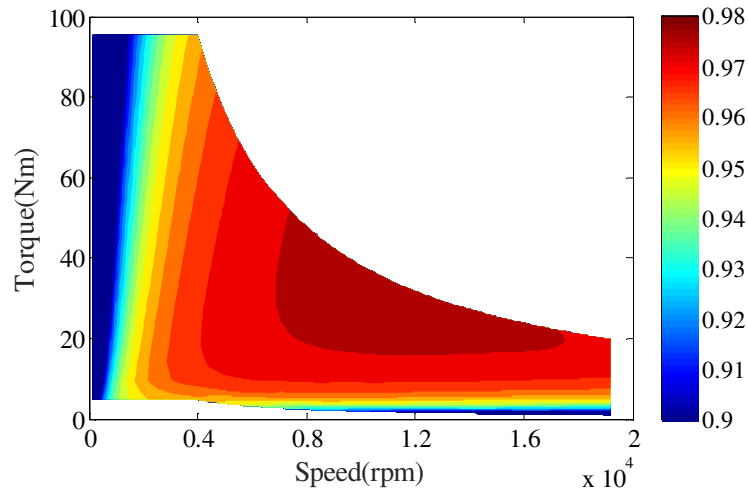
Fig. 3-24 Efficiency under rated power region

The efficiency map under the rated torque and power over the whole speed range are assessed in Fig. 3-24. Owing to the PM torque and reluctance torque, this machine exhibits very high efficiency in most regions, especially in the high speed range. The efficiency at the rated torque at the base speed is 95.83%.

The torque waveform at the rated current and base speed is shown in Fig. 3-25. This machine outputs an average torque of 95.5Nm at the rated operating point with 16.8% torque ripple. The torque ripple is mainly due to the 6th and 12th harmonic which is produced by the poles and stator slots. This ripple can be reduced, if necessary, by skewing and other techniques which are widely discussed in the literature [139, 140].
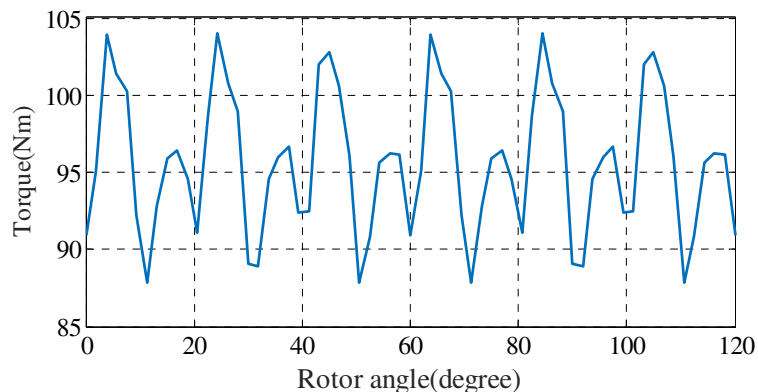
Fig. 3-25: Healthy torque waveform

The results show that the optimised design satisfies the torque requirements and generates the required power with high efficiency. And it

can provide a wide constant power operation range, therefore meeting the requirements in healthy conditions.

3.6.2 Fault Tolerant Capability Analysis

The performance under fault conditions is also analysed. The failure modes include one set open-circuit, one set short-circuit, inter-turn SC faults occurred in intra-phase and inter-phase. All the fault scenarios are evaluated at the base speed of 4000rpm with optimal current vector angle for MTPA operation.

A. One set open-circuit

In case of an open-circuit failure in the switches of the inverter or the phase windings, the particular set can be deactivated by opening all the switches. The current in the faulty set is zero, and the remaining two sets are still excited by the rated current. The torque waveform and its spectrum is shown in Fig. 3-26. The machine drive is capable of delivering around 2/3 rated torque with one set open-circuit. Besides the 12th harmonic, noticeable 2nd harmonic arises in the torque waveform. Therefore, the open-circuit fault can be coped with ~1/3 reduction in output torque or power. Since the thermal loading with one 3-phase open circuit is lower than the rated, it is possible to increase the current in the two healthy 3-phase sets to offset the output torque or power reduction.
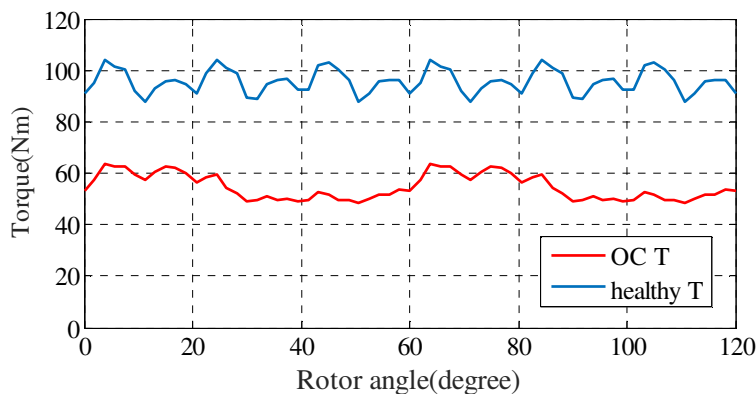
Fig. 3-26: Torque waveform with one set open-circuit

B. One set short-circuit

Similarly, if there is a short circuit failure in the switches of the inverter, it can be mitigated by closing all the top or the bottom switches of the inverter according to the position of the failed switch. In this way, a terminal short circuit is applied on the phase windings. The resultant currents and torque are analysed by exciting the healthy part with rated currents. The short circuited currents in the faulty set are shown in Fig. 3-27. It is found that the short circuited currents are lower than the rated. The heat produced by the short circuited currents can be easily dissipated by the machine. The torque under one set short-circuit is shown in Fig. 3-28. The machine drive can still generate about 2/3 of the rated torque. The main torque harmonics are also the 2nd and 12th harmonics. As a result, the short-circuit fault can be accommodated with about 1/3 reduction in torque or power.
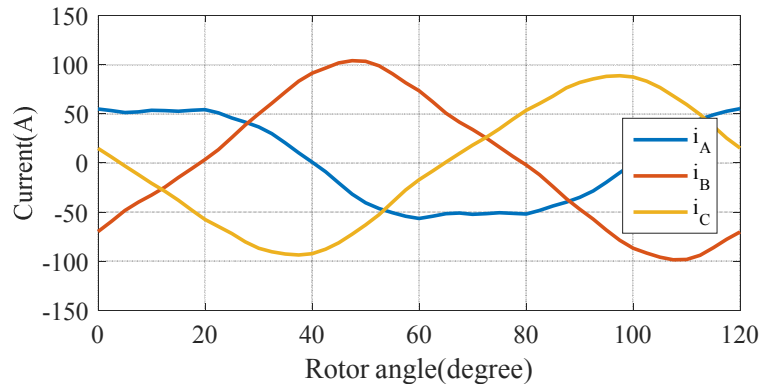
Fig. 3-27: Short circuit currents with one set short-circuit
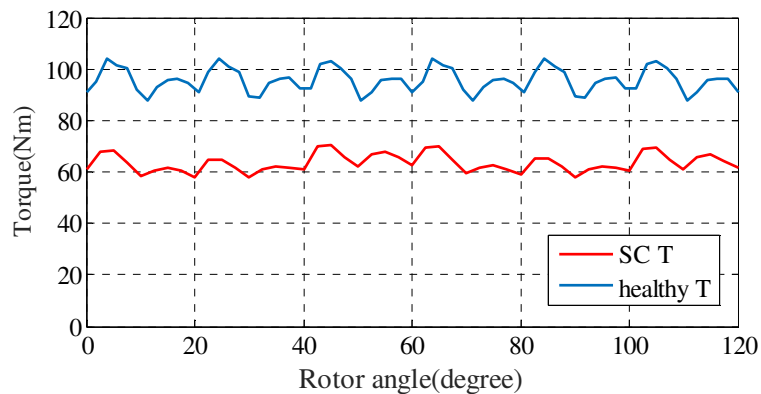
Fig. 3-28: Torque waveform with one set short-circuit

C. Intra-phase turn fault

As discussed in the previous section, the turn fault in B2 coil would be the worst fault case for the machine drive in motoring mode. Thus, it is examined with the healthy sets excited by the rated currents. TSC is immediately applied

on the faulty set, and the resultant phase currents as well as the turn fault current are illustrated in Fig. 3-29. The phase currents are similar to the one set short circuit case in Fig. 3-27 while the RMS value of the turn fault current is 266A. The resultant hotspot temperature is 232°C as mentioned in Table 3-9. Considering the extra impedance in the short circuit path, the turn fault current may be lower and the hotspot temperature will be close to 220°C. The torque output is also similar as that of the one set short-circuit since the single turn fault current produces neligible influence on the machine performance. As a result, the turn short-circuit fault can be accommodated.
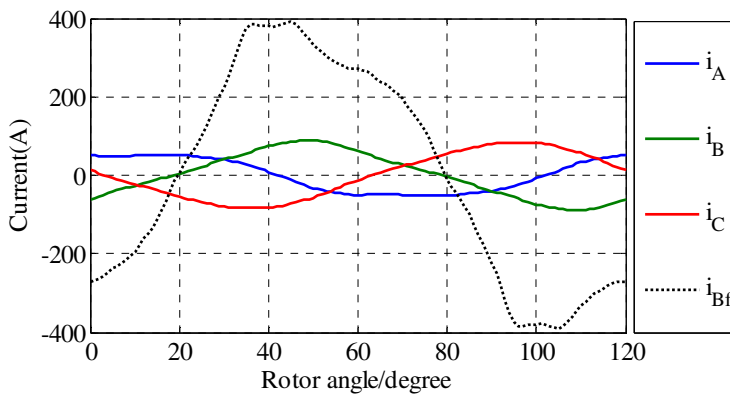
Fig. 3-29: Short circuit currents and turn fault current with intra-phase turn fault
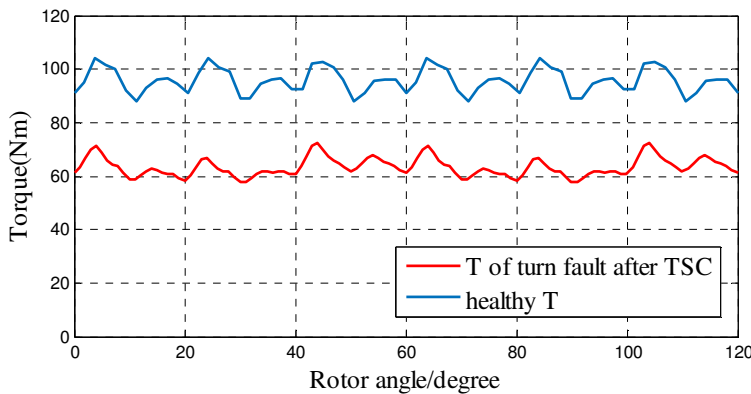
Fig. 3-30: Torque waveform with intra-phase turn fault

D. Inter-phase turn fault

The inter-phase turn fault is also analysed. The worst inter-phase fault case has been identified as shown in Fig. 3-31 where coil B2 is short circuited. It is evaluated by exciting the healthy sets with rated currents. TSC is applied on the fault set as a mitigation action. The fault currents and output torque is shown in Fig. 3-32 and Fig. 3-33. The peak fault current is 137A which is slightly higher than the rated value. It will not cause any significant overheating for

the machine since the short-circuited currents in other slots are much lower than the rated value. After TSC, the machine also could output about 2/3 of the rated torque. The main harmonics of the torque ripple are still 2nd and 12th harmonics. As a result, the machine is safe in case of an inter-phase turn fault.
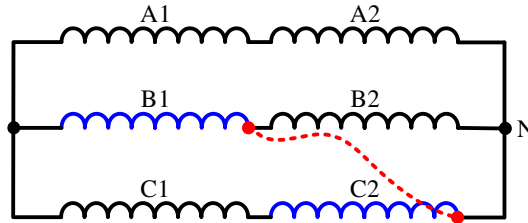
Fig. 3-31: Extreme inter-phase turn fault
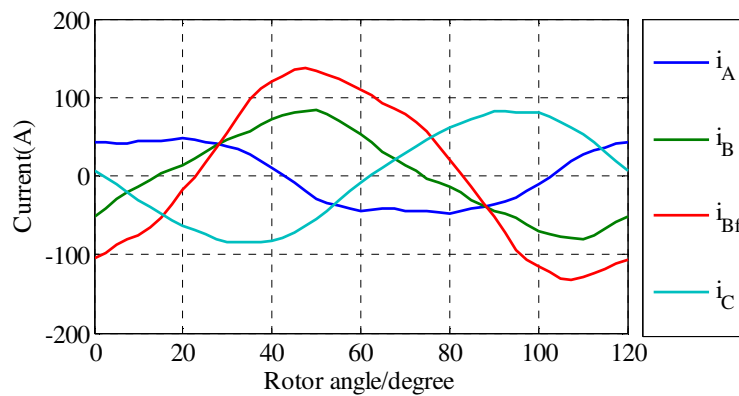
Fig. 3-32: Short circuit phase currents and fault current of inter-phase turn fault after TSC
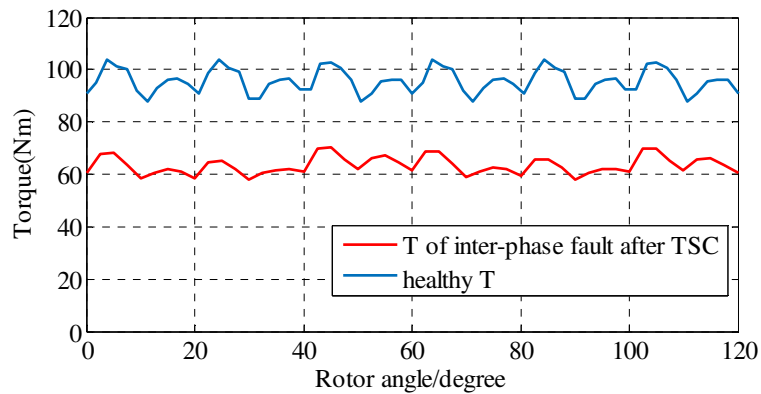
Fig. 3-33: Output torque of inter-phase turn fault after TSC

E. Other faults

Other faults, like the partial demagnetization and DC link capacitor failure are not analysed as the machine has the similar behaviour due to the same configuration as discussed in Chapter 2. They can be accommodated by the machine drive in the same way.

3.7 Summary

In this Chapter, a 40kW triple redundant 9 phase fault tolerant PMA SynRM has been designed for aerospace application. Various optimisation techniques are integrated for the machine design to maximize the efficiency while satisfying all the electrical, thermal and mechanical constraints. The machine is optimised to exhibit high efficiency and good fault tolerance against different faults. Some fine tunings have been conducted to meet the mechanical and thermal constraints. The performance of the final designed PMA SynRM machine is evaluated in both healthy and faulty conditions. The machine satisfies the torque envelope and exhibits high efficiency over a wide speed range. The failure modes which have to be addressed for aerospace applications including one set open circuit, one set short circuit, intra-phase turn fault, inter-phase turn fault and uncontrolled rectification have been examined. The results show that these faults can be tolerated by the optimised machine. As a result, this optimised machine exhibits both high performance and good fault tolerant capability.

CHAPTER 4
A General Modelling Technique for the Triple Redundant 3x3-phase PMA SynRM

4.1 Introduction

The fault tolerant machine drive requires modelling techniques to assess its fault behaviour in a computationally efficient way and facilitate the development of suitable control and fault detection algorithms in various fault scenarios.

For the proposed triple redundant 3x3-phase PMA SynRM drive, although the different 3-phase modules are physically, thermally and electrically isolated, they are not magnetically isolated. Hence, the three 3-phase sets are mutually coupled and cannot be regarded as independent when the machine operates in fault mode. In addition, the winding inductance cannot be considered as constant due to the complex rotor geometry. For the machine drive under study, it could operate in healthy, open circuit and short circuit conditions. In general, the currents in three 3-phase sets may be all different and this condition is referred to as unequal current operation mode. For the drive system with three 3-phase sets, it has 6 independent current variables. Together with the rotor position, the machine flux linkages are non-linear functions of 7 variables. The current state-of-the-art modelling techniques are not sufficient to describe this complex machine drive in a computationally efficient manner. Hence, it is valuable to develop a model technique that can present the machine behaviour and capture its main characteristics.

During operation, stator insulation failure may occur within the same phase or between phases. As has been shown, the stator turn fault (STF) within single phase is typically more severe. Since the faults only involve a few turns, a large current is induced in the short circuit path, producing excessive heat and causing local hotspot. This further deteriorates the insulation and may result in permanently damage and lead to complete failure [49]. Hence, the

STF behaviour should be carefully investigated [128, 141]. For the machine under study, the fault current is not only affected by the currents in the fault set, but also influenced by the currents in the healthy sets. It is also dependent on the number of fault turns, their position in slot and coil location. In addition, the STF current after the remedial TSC action becomes even more critical since the currents in each 3-phase set are very different and accurate estimation of the fault current is essential for thermal assessment of the post-fault operation. However, it is impossible to evaluate all the possible fault scenarios to find the worst case by repeating computationally expensive FE simulations. Hence, a fast model which accounts all factors affecting the fault behaviour, including the currents in each 3-phase set, the number of fault turns, coil location and slot position, will be of great value.

To this end, a general modelling technique is proposed for the triple redundant PMA SynRM accounting for various fault scenarios, including the healthy, open circuit, short circuit, and unequal current operation. The model can also be adapted for inter-turn fault accounting the factors described above. In this way, the machine performance and behaviour under healthy and fault conditions can be predicted by this model with great flexibility.

4.2 MMF Analysis at Set Level

The triple redundant 3x3-phase PMA SynRM under study are re-plotted as in Fig. 4-1. The three independent 3-phase windings, denoted as ABC, DEF and GHI, are distributed over 360 mechanical degrees. Each 3-phase winding occupies 120 degrees with each phase consisting of two coils in series. By way of example, the 6 coils of set ABC windings are denoted as A1, A2, B1, B2, C1 and C2. The turn functions of the 6 coils, which describes the coil distribution in space, are plotted in Fig. 4-2 according to the coil displacement [61], where N is the number of turns per coil. It should be noted that the turn functions of phase C are negative due to the reversed go-return polarity relative to those in phases A and B. The turn functions of set DEF and GHI can be obtained by 120° and 240° phase shift, respectively, which are not plotted.
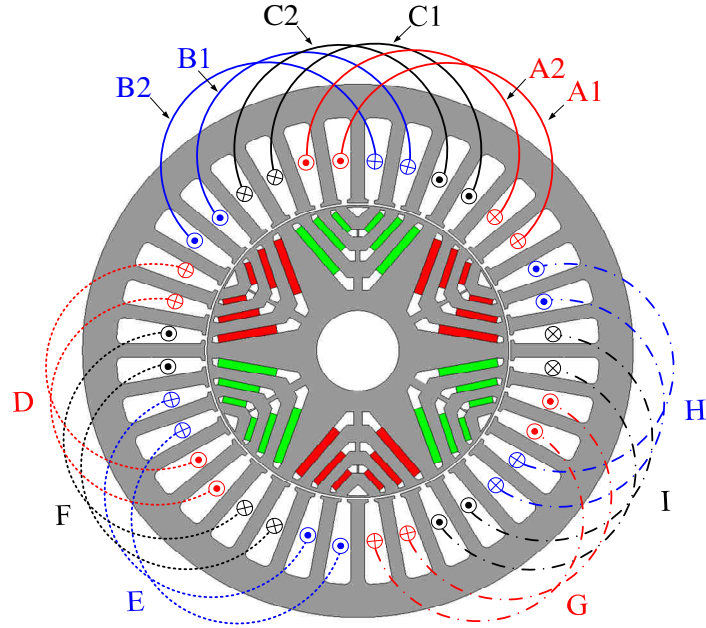
Fig. 4-1 PMA SynRM with segregated windings
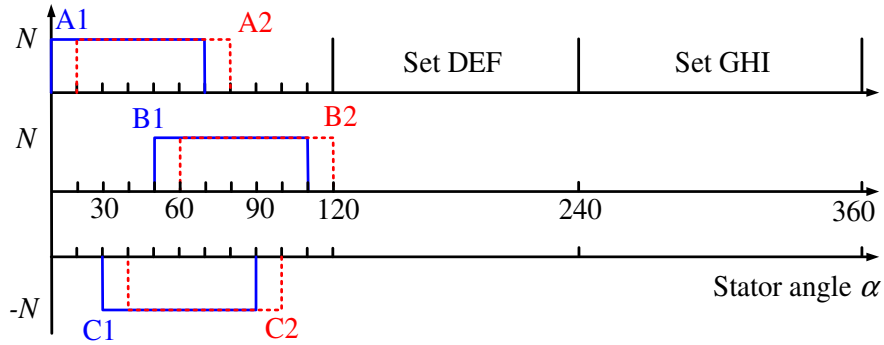
Fig. 4-2 Turn functions of the 6 coils in set ABC

Since the airgap is uniform, the winding function of each coil is derived as in (4-1) where $n_k(\alpha)$ denotes the variation of the turn function of coil k (k = A1, A2, …,)with the angular displacement α in the airgap while $\langle n_k(\alpha) \rangle$ represents the average value of $n_k(\alpha)$ over the whole airgap [142]:

$$N_k(\alpha) = n_k(\alpha) - \langle n_k(\alpha) \rangle$$

(4-1)

In healthy conditions, the currents of each 3-phase set are the same; however the currents will differ in case of a fault. Hence, the MMF induced by each set should be analysed separately and their influence to other sets is fully accounted. Neglecting the slotting effect and core saturation, the MMF produced by set ABC can be calculated by multiplying the winding function with relevant currents as in (4-2) [143].

$$MMF_{ABC}(\alpha) = \sum_{k=A1,A2....C2} N_k(\alpha)i_k$$

(4-2)

For the sake of discussion, the ampere-turns of each coil with rated current are denoted as 1 pu. Assuming at time instant $t = 0$, the phase currents are $i_A = 1pu$, $i_B = i_C = -0.5pu$, according to equation (4-2), the MMF produced by set ABC is plotted in Fig. 4-3.
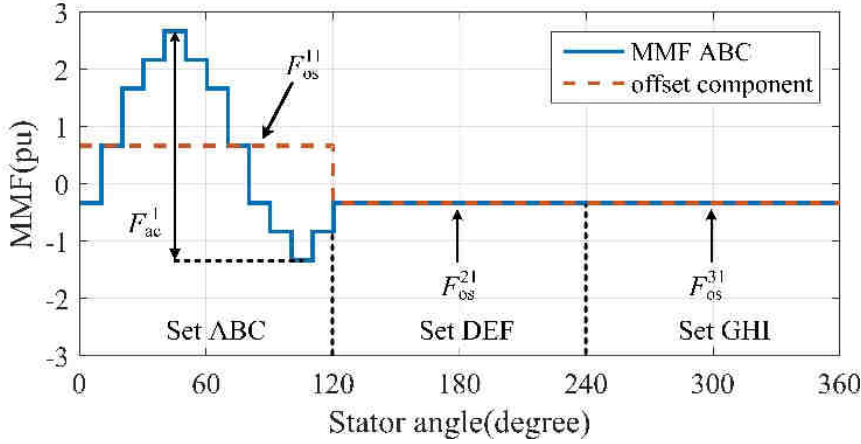
Fig. 4-3 MMF produced by set ABC

As can be seen, the currents in set ABC produce MMF not only over the set itself, but also over the other two sets. More specifically, the MMF over set ABC region consists of an AC component and an offset component while only an offset component exists over the other regions. They can be expressed as:

$$MMF_{ABC} = \begin{cases} F_{ac}^1 + F_{os}^{11} & 0° \leq \alpha < 120° \\ F_{os}^{21} & 120° \leq \alpha < 240° \\ F_{os}^{31} & 240° \leq \alpha < 360° \end{cases}$$

$$F_{ac}^1 = \sum_{n=1,3,5...} A_n \cos(3n\alpha + \delta_n)$$

(4-3)

$$F_{os}^{11} = \frac{2}{3}(i_A + i_B - i_C)$$

$$F_{os}^{21} = -\frac{1}{3}(i_A + i_B - i_C)$$

$$F_{os}^{31} = -\frac{1}{3}(i_A + i_B - i_C)$$

where F_{ac}^1 is the MMF AC component of the set ABC, A_n and δ_n denote the amplitude and phase angle of the nth MMF harmonic which are functions of the phase currents [144]. F_{os}^{ij} represents the MMF offset component over set i caused by set j. Set ABC, DEF and GHI are denoted as sets 1, 2, and 3, respectively, for notational convenience.

The analysis above is made on set ABC only. In fact, the MMFs produced by other two sets can be obtained with appropriate phase shifts as shown in Fig. 4-4. The resultant MMF AC components and offset components can be calculated similarly as in (4-3).
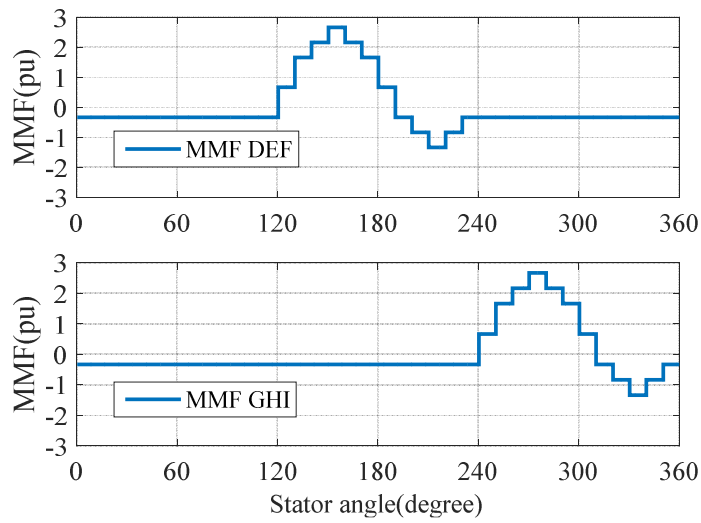
Fig. 4-4 MMF produced by set DEF and GHI

It is seen that the currents in each set produce the AC component only in the region occupied by the set itself while they contribute to the offset component over the regions occupied by the other sets. The total MMF over one set region can be obtained by adding the MMF contributions of all three sets. For the simplicity, the total MMF over set ABC, denoted as F^1, is expressed as:

$$F^1 = F_{ac}^1 + F_{os}^1$$

$$F_{os}^1 = F_{os}^{11} + F_{os}^{12} + F_{os}^{13}$$

(4-4)

$$= \frac{2}{3}(i_A + i_B - i_C) - \frac{1}{3}(i_D + i_E - i_F) - \frac{1}{3}(i_G + i_H - i_I)$$

The total MMF over set ABC is also composed of an AC component and offset component. The AC component is only dependent on the currents in the set itself and angular position in the airgap while the offset component is the combined effect of the currents in all three sets but it is independent of angular position. Due to nonexistence of zero sequence current, the phase currents i_A, i_B, i_C can be represented as i_{d1}, i_{q1} in a dq reference frame. Together with the offset component F_{os}^1, the MMF over set ABC can be determined by a function of (θ, i_{d1}, i_{q1}, F_{os}^1) as:

$$F^1 = F_{ac}^1 + F_{os}^1 = f(\theta, i_{d1}, i_{q1}, F_{os}^1)$$

<div align="right">(4-5)</div>

where θ is the rotor electrical angular displacement of the d-axis with respect to phase A winding axis. The total MMFs over sets DEF and GHI can be similarly expressed as:

$$F^2 = F_{ac}^2 + F_{os}^2 = f\left(\theta, i_{d2}, i_{q2}, F_{os}^2\right)$$

$$F^3 = F_{ac}^2 + F_{os}^2 = f\left(\theta, i_{d3}, i_{q3}, F_{os}^3\right)$$

<div align="right">(4-6)</div>

The variables are defined similarly as above. It can be shown that under healthy conditions the dq currents of each set are the same, the offset components are cancelled according to (4-4) and all three sets will produce the same AC component as in a 3-phase machine. In case of one set open circuit condition, the AC component is zero for the fault set due to zero phase currents and the offset component still exists due to the other sets, whilst the other sets exhibit both an AC and offset component. If one set is short circuited, short circuit currents will flow in the fault set. The resultant MMF can be deduced accordingly as a combination of the AC component and offset component for each set. In the extreme condition where the currents in each set are all different, the MMF of each set can still be expressed by (4-5) and (4-6).

Therefore, it follows that in any conditions the MMF over the whole airgap can be divided into three parts. Each of them is associated with a 3-phase set and can be expressed by $f(\theta, i_d, i_q, F_{os})$ where i_d, i_q are the currents in that

set while F_{os} is the combined offset component due to the currents in all three sets.

The MMF analysis confirms that different 3-phase sets are not magnetically isolated and they could affect each other via the MMF offset component. And only in healthy condition, the offset component is cancelled by each other due to the same current excitation and hence the machine behaves as a normal 3-phase machine. In contrary, in any fault conditions the residual MMF offset component exists and it will cause the machine to operate in non-symmetrical condition.

4.3 General Modelling Technique for Set Level

4.3.1 Proposed General Modelling Approach

As discussed, the MMF over one 3-phase set can be described by the 4 variables $(\theta,\ i_d,\ i_q, F_{os})$. And the flux density in the airgap depends on the MMF and PM field whose combined effect determines the flux linkages and torque. Therefore, the flux linkages and torque of each 3-phase set can be expressed as 4D functions $f(\theta,\ i_d,\ i_q, F_{os})$ which can be established by FE analysis, as will described in section 4.3.2. As a result, the performance of each 3-phase set can be predicted by interpolating the 4D tables via the four variables $(\theta,\ i_d,\ i_q, F_{os})$.
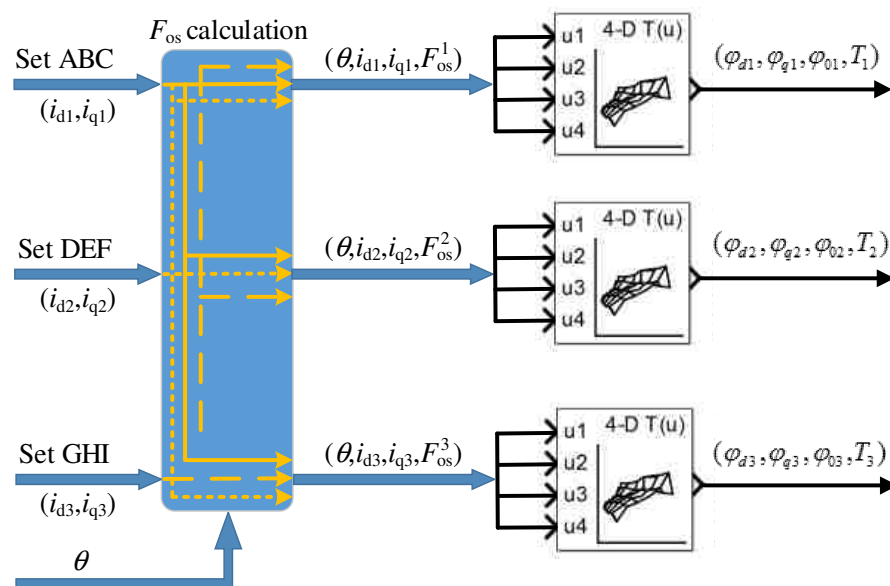
Fig. 4-5 General modelling diagram

Thus, a general modelling method is proposed as shown in Fig. 4-5. The currents of each 3-phase set (i_d, i_q) together with θ are fed into the MMF offset block to calculate F_{os} for each set according to (4-4). Then, the obtained 4 variables (θ, i_d, i_q, F_{os}) form the inputs to the 4D tables which determine the resultant flux linkages and torque of the 3-phase set. It should be noted that the flux linkages and torque of each set are interpolated separately. The total torque is obtained by adding the torque contribution of all three sets. The voltage equations of each 3-phase set are expressed as:

$$u_{di} = Ri_{di} + \frac{d\psi_{di}}{dt} - \omega\psi_{qi}$$

$$u_{qi} = Ri_{qi} + \frac{d\psi_{qi}}{dt} + \omega\psi_{di}$$

$$(4\text{-}7)$$

The u_{di}, u_{qi} denote the applied voltages in dq axes while R represents the phase resistance. The key merit of the proposed modelling method is that it can predict the machine behavior under healthy, open circuit, short circuit and unequal currents operating conditions without any modification, hence, saves significant efforts for predicting the machine performance under different conditions. It should be noted that the proposed modelling technique can only deal with faults in set level at this stage. However, it will be adapted for modelling with stator turn fault in section 4.5.

4.3.2 4D Table Construction

Since the machine under consideration is subject to magnetic saturation, FE analysis is performed to extract the data for the 4D tables. The aim of table production is to determine the flux linkages and torque of one 3-phase set as functions of (θ, i_d, i_q, F_{os}) which indicate the MMF over that 3-phase set. It is worth noting that the three 3-phase sets are identical because the electrical phase shift between each set is 360°. Therefore, the 4D tables only need to be constructed for one 3-phase set and the other two sets can use the same table. Hence, 2D FE simulations of the full machine model are performed to extract the flux linkages and torque data of set ABC.

The key of table construction is to generate the same MMF over set ABC defined by (θ, i_d, i_q, F_{os}). As discussed previously, the MMF AC component is determined by the currents of its own set. Thus, for given (i_d, i_q) and the rotor electrical angle θ, the phase currents of set ABC can be derived by dq transform as:

$$i_A = i_d \cos \theta - i_q \sin \theta$$

$$i_B = i_d \cos(\theta - 120°) - i_q \sin(\theta - 120°) \tag{4-8}$$

$$i_C = i_d \cos(\theta + 120°) - i_q \sin(\theta + 120°)$$

However, the MMF offset component F_{os} is the combined effect of currents in all three 3-phase sets. To represent this offset component, specific currents should be injected to sets DEF and GHI to generate the required F_{os}. Hence, the currents in sets DEF and GHI can be specified as (4-9) where x, y, z are appropriate values to be determined to produce the required F_{os}:

$$i_D = i_G = i_A + x$$

$$i_E = i_H = i_B + y \tag{4-9}$$

$$i_F = i_I = i_C + z$$

The F_{os} over set ABC is obtained by substituting (4-8) and (4-9) into (4-4) as:

$$F_{os} = -\frac{2}{3}(x + y - z) \tag{4-10}$$

Zero sequence current cannot circulate, therefore:

$$x + y + z = 0 \tag{4-11}$$

Based on (4-10) and (3-2), it can be deduced that:

$$x + y = -\frac{3}{4}F_{os} \tag{4-12}$$

$$z = \frac{3}{4}F_{os}$$

In order to obtain a unique solution for x, y, their values should be chosen as to minimize the saturation effect because the MMF offset is derived by ignoring the magnetic saturation. Thus, x, y are defined as:

$$x = y = -\frac{3}{8}F_{os} \tag{4-13}$$

which results in the lowest peak value over one electrical period for phases D, E, F and G, H, I. Therefore, for a given set of $(\theta,\ i_d,\ i_q,\ F_{os})$, their physical effect is replicated over set ABC by injecting the currents in (4-8) and (4-9) in the machine 2D FE model, and the resultant flux linkages and torque are calculated for the region of the ABC set. The flux linkages are directly obtained from FE analysis whilst the torque is calculated by Maxwell stress tensor in the airgap under set ABC. As a result, the 4D lookup table data are extracted.

It is worth noting that the MMF offset value calculated by (4-4) neglects the magnetic saturation. Thus, the reconstructed MMF offset component may not represent the actual value exactly. However, the saturation effect of the MMF AC component, slot effect and space harmonics are considered by the FE model directly. Therefore, it would only cause relatively small error to the prediction. The accuracy of the proposed model will be examined by FE simulation and experimental tests.

4.4 Simulation Validation at Set Level

In this section, the accuracy of the proposed modelling method is examined by comparing the prediction with FE results under healthy, open circuit, and short circuit and unequal current conditions.

4.4.1 Healthy Operation

For healthy condition, the currents in each set are the same. Thus, the F_{os} is zero for all the three 3-phase sets. The machine behavior is purely determined by $(\theta,\ i_d,\ i_q)$. Test is conducted at the based speed with the rated

current 120A. The predicted results together with the FE results are compared in Fig. 4-6 and Fig. 4-7. It shows that the model and FE predicted flux linkages and torque are essentially the same [145].
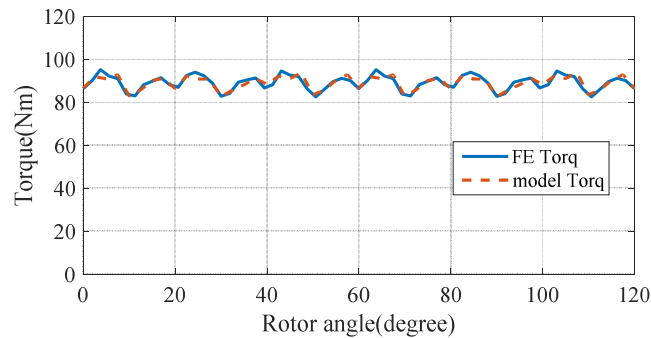
Fig. 4-6 Torque comparison in healthy condition
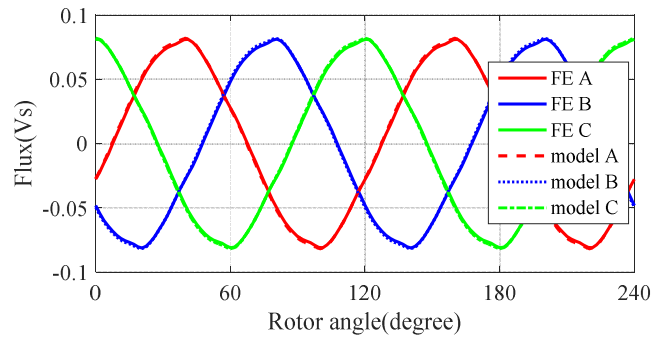
Fig. 4-7 Comparison of flux linkages in set ABC in healthy condition

4.4.2 Open Circuit

An open circuit fault is assumed in set ABC, the phase currents are zero while the currents in DEF and GHI sets are the same rated as in the healthy condition. Thus, the currents of set ABC are zero while other variables remain unchanged as in Fig. 4-5. Similarly, the 4 variables which describes the MMF over each 3-phase set are obtained and fed into the 4D tables.

Fig. 4-8 and Fig. 4-9 compare the torque and flux linkages predicted by the model and FE. As can be seen, the model-predicted torque follows the main trend of the FE result, albeit being slightly higher. The 2nd harmonic is observed in the torque waveform which is captured by the prediction. Since the behaviours of sets DEF and GHI are similar, only the flux linkage results of set DEF are compared. The predicted flux linkages also match well with the FE results with small error. It is noticed that the flux linkages are no longer

balanced under the fault condition which confirms mutual coupling between three 3-phase sets due to the nonzero MMF offset component.
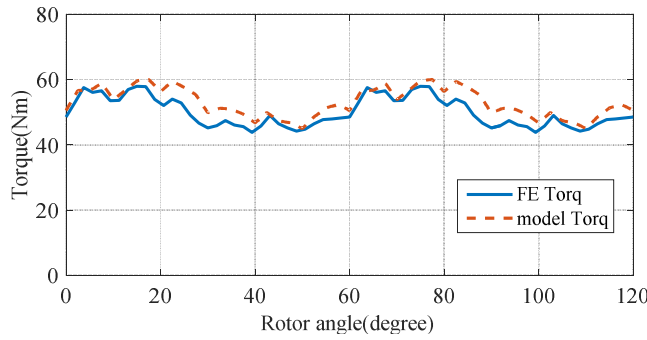
Fig. 4-8 Torque comparison in open circuit condition
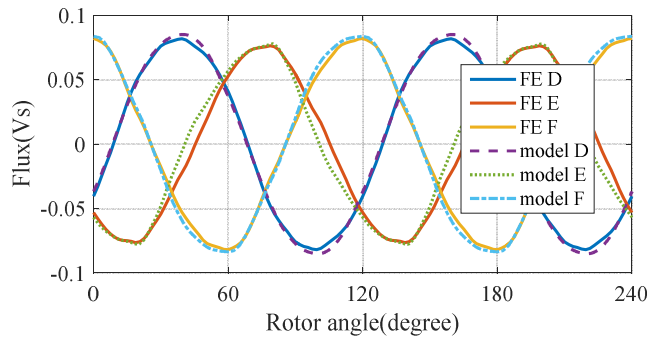
Fig. 4-9 Comparison of flux linkages in healthy set

4.4.3 Short Circuit

In case of a switch or winding short circuit, terminal short circuit is applied to the fault set to mitigate the fault. The induced short circuit currents are determined by the flux linkages of the faulty set. Since the 3-phase winding is star connected, zero sequence current is 0. Thus, the short circuit currents are governed by:

$$i_d = (\omega\psi_q - \frac{d\psi_d}{dt})/R_s$$

$$i_q = -(\omega\psi_d + \frac{d\psi_q}{dt})/R_s$$

(4-14)

The behaviour of the machine is evaluated with set ABC terminal short circuited while the other sets are excited with the rated currents. The currents in set ABC is obtained from (4-14) with the dq flux linkages predicted by the model. The model predicted torque matches well with the FE result as shown

in Fig. 4-10. Good agreements are also observed in the short-circuit currents and the flux linkages comparisons in Fig. 4-11-Fig. 4-13. It is seen that the short-circuit currents in each phase of the ABC set are asymmetrical. The flux linkages in the faulty set are effectively nullified except for the zero sequence components due to the MMF offset.
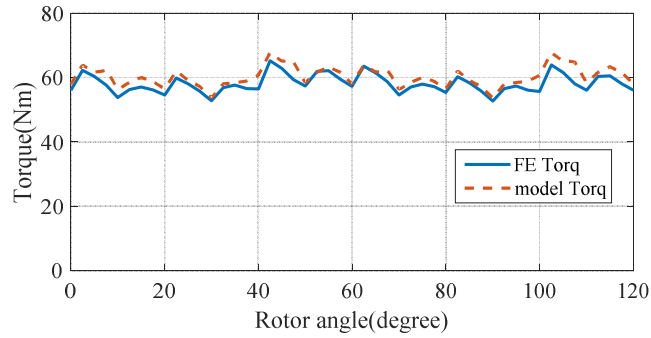
Fig. 4-10 Torque comparison in short circuit condition
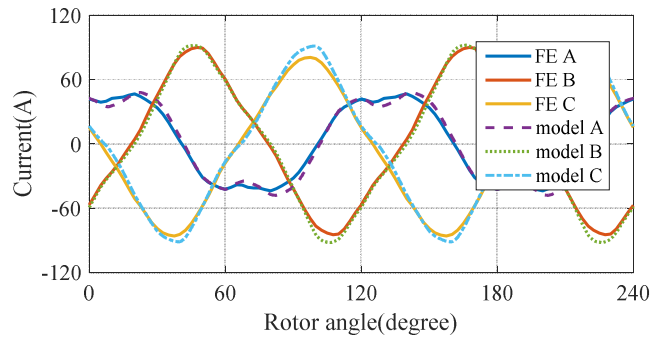
Fig. 4-11 Short circuit currents comparison
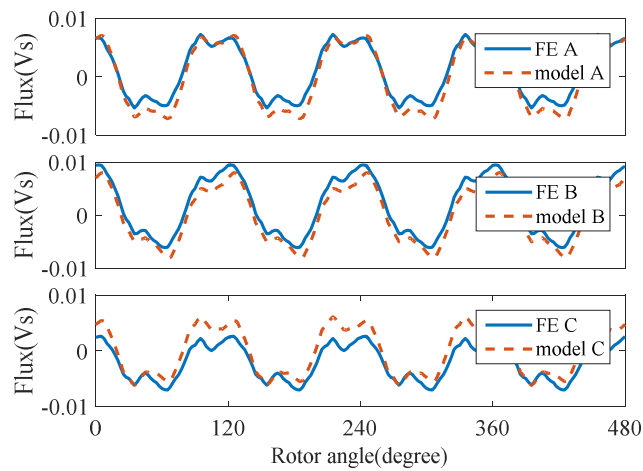
Fig. 4-12 Comparison of flux linkages in the short circuit set
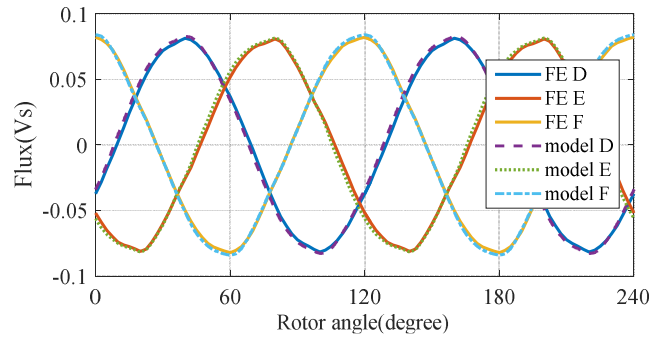
Fig. 4-13 Comparison of flux linkages in healthy set

4.4.4 Unequal Current Operation

In practical applications, the currents in each set may be unequal due to limited current control bandwidth and current sensor accuracy, leading to unequal current operation mode in the three 3-phase sets. Without loss of generality, the unequal current operation is exaggerated by assuming that set ABC has 1pu current excitation, while set DEF and GHI have 0.9pu and 0.8pu current, respectively. The predicted flux linkages and torque are compared with the FE results in Fig. 4-14 and Fig. 4-15. Since the flux linkages of three sets are similar, only the flux linkages of set ABC are compared. The two predicted results coincide with each other. In addition, with the proposed model, the torque contribution of each set can be identified as in Fig. 4-15 providing more insight into the machine behaviour. The torque contribution of each set increases with the current. Set ABC is excited with the highest current, therefore inducing the maximum MMF AC component which is the working harmonic. It reacts with the PM field and rotor saliency and hence produces the highest torque among the three 3-phase sets.
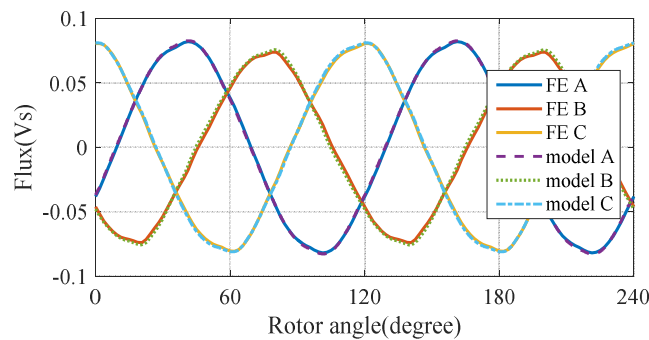
Fig. 4-14 Flux linkages comparison of set ABC
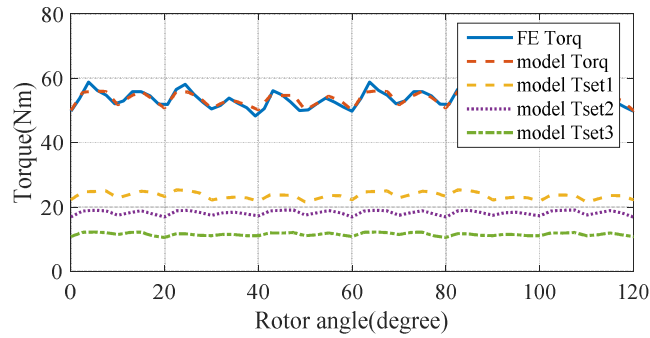
Fig. 4-15 Torque comparison in unequal current operation

4.5 General Modelling Considering STF

4.5.1 Turn Fault Description

As discussed above, the general modelling technique is capable of predicting the flux and torque of each 3-phase set with great flexibility and satisfactory accuracy in set level. It would be desirable if the model can predict the STF behaviour. Thus, a STF model is developed by adapting the general model for turn fault condition.

Without loss of generality, the STF is assumed to occur in phase B of set ABC, particularly in coil B2 as shown in Fig. 4-1. The schematic circuit connection is illustrated in Fig. 4-16, phase B has been divided into two parts, denoted as B_h for the healthy part, and B_f for the faulty part. The number of short circuited turns N_f over the turn number of a healthy coil N is defined as the STF ratio μ. R_f and L_f represent the external resistance and inductance associated with the fault current path while i_f is the current in the faulty path.
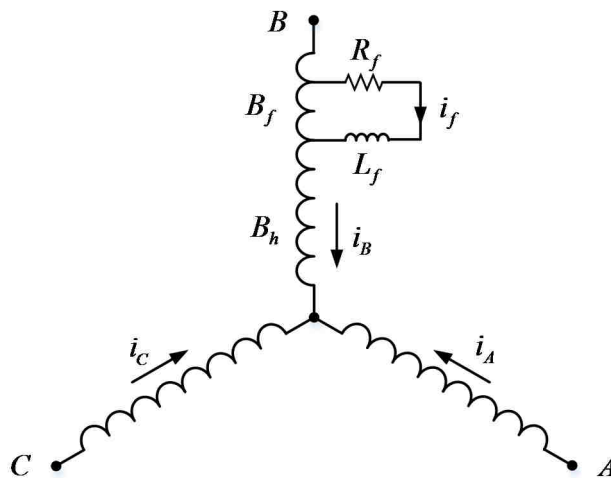
Fig. 4-16 Schematic circuit for set ABC with STF in phase B

4.5.2 Equivalent Input for the General Model

According to the general modelling theory, the MMF of each 3-phase set can be described by $f(\theta, i_d, i_q, F_{os})$. In order to incorporate the STF into the model, the first step is to derive the equivalent input for the 4D tables considering the influence of fault current i_f.

In STF condition, the fault current i_f flows in the short circuit path which affects the MMF distribution. In addition, since i_f only exists in the fault part in coil B2, its induced MMF differs from that of phase B. This difference can be accounted by using rotating field theory to calculate the MMF caused by i_f as described in [61]. In healthy condition, the MMF of phase B is contributed by the two coils as shown in Fig. 4-17. It can be expressed in phasor form of (4-15) considering the fundamental component only.

Coil B1 MMF Ni_B

$15°$ $2Ni_B \cos 15°$

Phase B MMF

Coil B2 MMF Ni_B
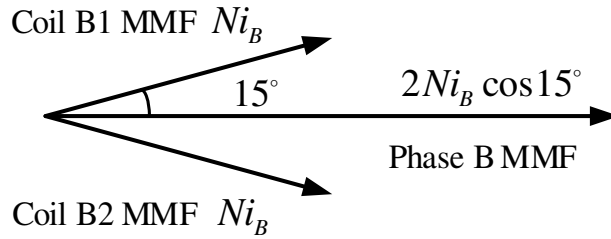
Fig. 4-17 MMF phasor of phase B

$$MMF_B = Ni_B(e^{-j(\theta - 120° + 15°)} + e^{-j(\theta - 120° - 15°)})$$

$$= 2Ni_B \cos 15° \, e^{-j(\theta - 120°)}$$

(4-15)

Under STF conditions, the fault current i_f will alter the MMF of phase B. Consider the worst case when the STF occurs in coil B2, the resultant MMF phasor due to i_f is given in (4-16) which is proportional to the number of fault turns N_f.

$$MMF_{Bf} = -N_f i_f e^{-i(\theta - 120° - 15°)}$$

(4-16)

Due to MMF_{Bf}, the MMF AC component of set ABC is changed and hence, the dq axes currents, i_{d1}, i_{q1}, should be modified accordingly. The additional $\Delta i_{df}, \Delta i_{qf}$ due to i_f can be calculated by dq transformation according to (4-15),

(4-16) and are given in (4-17). These two components are added to the original i_{d1}, i_{q1} to obtain i_{df}, i_{qf} under the STF condition.

$$\Delta i_{df} = -\frac{2}{3} * \frac{N_f}{2N \cos 15°} i_f \cos(\theta - 120° - 15°)$$

$$\Delta i_{qf} = \frac{2}{3} * \frac{N_f}{2N \cos 15°} i_f \sin(\theta - 120° - 15°)$$

(4-17)

On the other hand, the MMF offset component is also altered. The extra offset component ΔF_{osf}^1 over set ABC caused by i_f can be written as in (4-18) according to the fault turn function.

$$\Delta F_{osf}^1 = -\frac{2}{3} * \frac{N_f}{2N} i_f$$

(4-18)

Similarly, the new F_{osf}^1 is calculated by adding ΔF_{osf}^1 to the original F_{os}^1. It is worth noting that the i_f also affects the offset components of other two 3-phase sets. They can be deduced similarly and are given in (4-19).

$$\Delta F_{osf}^2 = \Delta F_{osf}^3 = \frac{1}{3} * \frac{N_f}{2N} i_f$$

(4-19)

F_{osf}^2 and F_{osf}^3 can be calculated by adding ΔF_{osf}^2, ΔF_{osf}^3 to the F_{os}^2, F_{os}^3 respectively. Finally, the modified four variables $(\theta, i_{df}, i_{qf}, F_{osf}^1)$ form the inputs for the lookup tables in Fig. 4-5 to determine the flux and torque for the faulty set, while $(\theta, i_{d2}, i_{q2}, F_{osf}^2)$ and $(\theta, i_{d3}, i_{q3}, F_{osf}^3)$ are the inputs for DEF and GHI sets, respectively.

4.5.3 Flux linkage of Fault Turn

The general model only provides the flux linkages in $d, q, 0$ axes for each 3-phase set. In order to predict the fault current, it is necessary to derive the flux linkage of the fault turn based on the $dq0$ axes flux linkages, $\varphi_{d1}, \varphi_{q1}, \varphi_{01}$ of set ABC shown in Fig. 4-5.

The flowchart of deriving flux linkage of the fault turn from the fault set flux linkages is illustrated in Fig. 4-18. The flux linkage of the faulted ABC set

consists of leakage and airgap flux linkages while only the airgap component will be linked by the fault turn [74]. The airgap flux linkages can be separated by (4-20) where φ_{mk}, (k= d, q, and 0) denotes the airgap flux linkage in the kth axis while L_l is the phase leakage inductance. φ_{m0} equals φ_0 since the lookup table is produced without zero sequence currents.

Flux linkage of set ABC
$\varphi_{d1}, \varphi_{q1}, \varphi_{01}$

Leakage
$d: L_l i_{df}$
$q: L_l i_{qf}$
$0:0$

Airgap flux linkage
$d: \varphi_{md}$
$q: \varphi_{mq}$
$0: \varphi_{m0}$

PM flux linkage
$d: \varphi_{acd}$
$q: \varphi_{acq}$
$0: \varphi_{ac0}$

MMF AC component

MMF offset component
$d: \varphi_{osd}$
$q: \varphi_{osq}$
$0: \varphi_{os0}$

Transform 1

Transform 2

φ_{acBf}

φ_{osBf}

Fault turn leakage
φ_{lBf}

Flux linkage of fault turn
φ_{Bf}
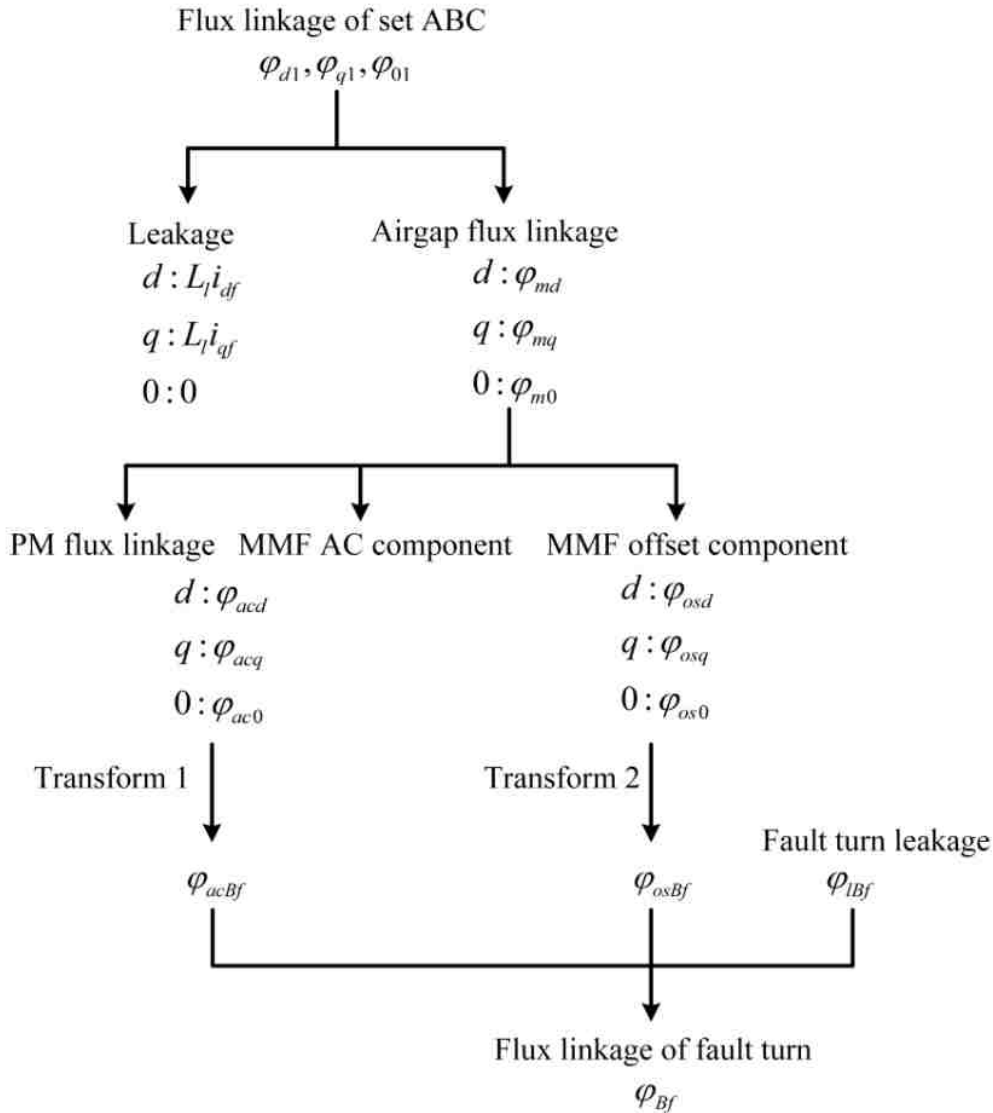
Fig. 4-18 Derivation of flux linkage of fault turn

$$\varphi_{md} = \varphi_{d1} - L_l i_{df}$$

$$\varphi_{mq} = \varphi_{q1} - L_l i_{qf} \tag{4-20}$$

$$\varphi_{m0} = \varphi_{01}$$

The airgap flux linkages are contributed by the PM flux linkage and the flux linkage due to the MMF. The PM flux linkage has a sinusoidal distribution in

the airgap when the high order harmonics are ignored. Whilst as discussed in section 4.5.2, the MMF in the airgap consists of an MMF AC component and an offset component. The resultant flux linkage is proportional to the MMF. Thus, the flux linkage produced by the MMF AC component also has a sinusoidal distribution in the airgap if the high order harmonics are ignored. However, this is not the case for the flux linkage produced by the MMF offset component. All the airgap flux linkage components will be linked by the fault turn, however, they should be accounted separately due to different distribution.

First, the flux linkage produced by the MMF offset component is considered. By way of example, the flux linkage of phase A due to the offset component F_{osf}^1 can be evaluated by (4-21) [146] where φ_{osA1} and φ_{osA2} indicate the resultant flux linkages for coils A1 and A2, respectively. n_{A1}, n_{A2} are the turn functions for coils A1 and A2 as shown in Fig. 4-2. r denotes the radius of the stator inner bore and l is the axial length of the stator stack. $g^{-1}(\alpha)$ is the inverse airgap function given in (4-22). The resultant flux linkages in phases B and C, φ_{osB} and φ_{osC}, can be derived similarly.

$$\varphi_{osA} = \varphi_{osA1} + \varphi_{osA2}$$

$$= \mu_0 r l \int g^{-1}(\alpha)\,(n_{A1} + n_{A2}) F_{osf}^1 d\alpha$$

(4-21)

$$g^{-1}(\alpha) = a + b\cos(2\alpha + \alpha_0)$$

(4-22)

Since the coils are full-pitched and F_{osf}^1 is a constant value over the region occupied by the ABC 3-phase winding, it can be derived that φ_{osA1} equals φ_{osA2}, and they are independent of the rotor position. Similarly, it can be deduced that φ_{osA} equals φ_{osB}. Due to the opposite polarity of the turn function for phase C compared to that of phases A and B, the offset flux linkage of phase C winding has an opposite polarity as shown in (4-23) and Fig. 4-19.

$$\varphi_{osA} = \varphi_{osB} = -\varphi_{osC}$$

(4-23)

$$\varphi_{osA1} = \varphi_{osA2} = \varphi_{osB1} = \varphi_{osB2} = -\varphi_{osC1} = -\varphi_{osC2}$$

$$\varphi_{osA1}$$

$$\varphi_{osA2}$$

$$\varphi_{osC1} \qquad \varphi_{osB1} \qquad \varphi_{osA}$$

$$\varphi_{osC} \qquad \varphi_{osC2} \qquad \varphi_{osB2} \qquad \varphi_{osB}$$
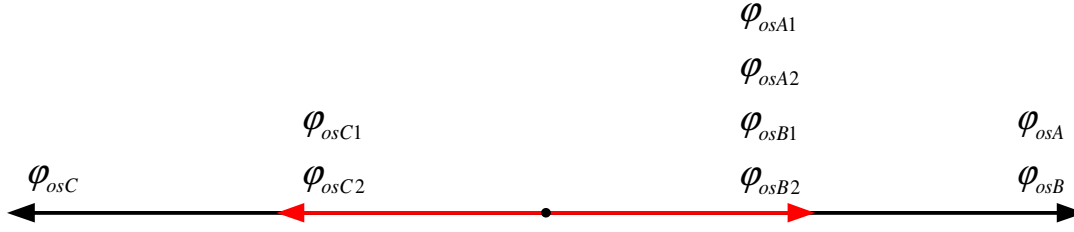
Fig. 4-19 Flux linkage distribution induced by the offset component

Considering that the turn fault is located in coil B2, the flux linked by the fault turns is proportional to φ_{osB2}. While the above analysis gives a qualitative understanding of the relationships of the offset flux linkage components, it is not convenient to calculate them using (1-21) and (1-22).

Instead, the flux linkages produced by the offset component, φ_{osA}, φ_{osB}, φ_{osC}, can be estimated from the 4D flux linkage table established previously by (4-24) where dq^{-1} represents inverse dq transform. In the bracket, the first component denotes the flux linkage produced by the MMF AC and offset components together with the PMs while the second component denotes the flux linkage without the MMF offset component. By subtracting the two components, the flux linkages of set ABC produced by the offset component are obtained when the effect of magnetic saturation is neglected. Nonetheless, the saturation is insignificant in a turn fault case since the short circuit current will reduce the flux density in the fault region. Thus, the error caused by (4-24) would be relatively small as will be validated by FE simulation and experimental tests.

$$\begin{pmatrix} \varphi_{osA} \\ \varphi_{osB} \\ \varphi_{osC} \end{pmatrix} = dq^{-1} \begin{pmatrix} \varphi_{osd} \\ \varphi_{osq} \\ \varphi_{os0} \end{pmatrix} = dq^{-1} \begin{pmatrix} \varphi_d(\theta, i_{df}, i_{qf}, F^1_{osf}) - \varphi_d(\theta, i_{df}, i_{qf}, 0) \\ \varphi_q(\theta, i_{df}, i_{qf}, F^1_{osf}) - \varphi_q(\theta, i_{df}, i_{qf}, 0) \\ \varphi_0(\theta, i_{df}, i_{qf}, F^1_{osf}) - \varphi_0(\theta, i_{df}, i_{qf}, 0) \end{pmatrix} \qquad (4\text{-}24)$$

The flux linkage of the fault turns due to the MMF offset component is proportional to the number of fault turns and can be expressed as in (4-25).

$$\varphi_{osBf} = \frac{N_f}{2N} \varphi_{osB} \qquad (4\text{-}25)$$

On the other hand, the flux linkages due to the PMs and MMF AC component have a sinusoidal distribution in the airgap and are denoted as AC flux linkages (φ_{acA}, φ_{acB}, φ_{acC} for each phase). The phasors of the AC flux linkages are illustrated in Fig. 4-20. The AC component of flux linkage of the fault turns is therefore proportional to the AC flux linkage of coil B2, φ_{acB2}, where the fault happens. It is worth noting that now φ_{acB2} has different amplitude and phase angle of φ_{acB}. This is the main reason why the flux linkage components of the faulted turns have to be dealt with differently.
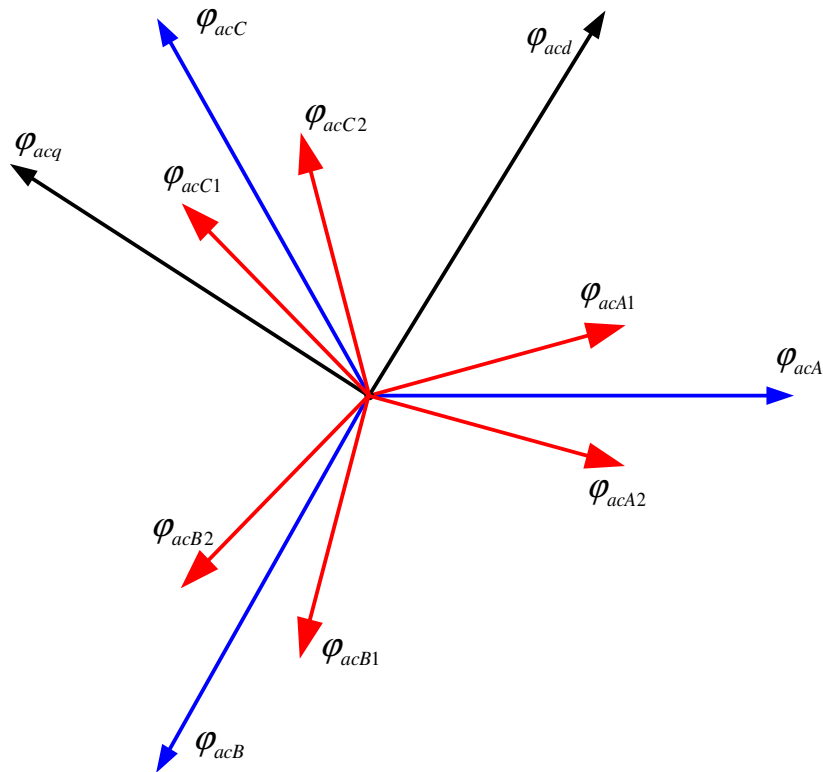
Fig. 4-20 Phasor diagram AC components of flux linkages

Subtracting the total airgap flux linkage in (4-20) by the offset flux linkage component in (4-24) in dq frame, the AC flux linkages of set ABC, φ_{acd}, φ_{acq}, φ_{ac0}, can be obtained as in (4-26).φ

$$\begin{pmatrix} \varphi_{acd} \\ \varphi_{acq} \\ \varphi_{ac0} \end{pmatrix} = \begin{pmatrix} \varphi_{md} \\ \varphi_{mq} \\ \varphi_{m0} \end{pmatrix} - \begin{pmatrix} \varphi_{osd} \\ \varphi_{osq} \\ \varphi_{os0} \end{pmatrix} \tag{4-26}$$

The result can be projected to the fault turn in coil B2 by inverse dq transform given in (4-27). The coil location of the fault turn is considered by the angle of B2 coil with respect to the d axis.

$$\varphi_{acBf} = \frac{N_f}{2N \cos 15°} (\varphi_{acd} \cos(\theta - 120° - 15°)$$

$$-\varphi_{acq} \sin(\theta - 120° - 15°) + \varphi_{ac0})$$

(4-27)

Hence, the airgap flux linkage of the fault turns has been obtained.

In addition, as shown in Fig. 4-18, the slot leakage flux induced by the phase current and the turn fault current should be considered since it has noticeable impact on the fault current [74, 128]. It is accounted by (4-28), where L_{lf} is the self-leakage inductance of the fault turns whereas M_{lf} is the mutual leakage inductance between the healthy turns and the fault turns in the same slot. It is worth noting that L_{lf} and M_{lf} are dependent on the slot position of the fault turns. They are calculated according to the formulas in [50, 74]. Consequently, the influence of the slot position of the fault turns is included. Finally, the total flux linkage of the fault turns can be obtained as shown in (4-29).

$$\varphi_{lBf} = M_{lf} i_B + L_{lf} (i_B - i_f)$$

(4-28)

$$\varphi_{Bf} = \varphi_{acBf} + \varphi_{osBf} + \varphi_{lBf}$$

(4-29)

4.5.4 Voltage Equations

Based on the derived flux linkages of the fault turns and fault set ABC, the voltage equations of the fault turns and whole set are written as follows.

$$R_f i_f + L_f \frac{di_f}{dt} = \frac{\mu}{2} R(i_B - i_f) + \frac{d\varphi_{Bf}}{dt}$$

$$u_{d1} = R i_d + \frac{d\varphi_{d1}}{dt} - \omega \varphi_{q1} - \frac{\mu}{3} R i_f \cos(\theta - 120°)$$

(4-30)

$$u_{q1} = R i_q + \frac{d\varphi_{q1}}{dt} + \omega \varphi_{d1} + \frac{\mu}{3} R i_f \sin(\theta - 120°)$$

The voltage equations for the other sets are the same as healthy condition since the influence of the fault current has been considered in equation (4-19). Thus, the general model has been adapted for the STF, taking into the account for the fault in different coil location, slot position and number of fault turns.

4.6 Simulation Validation for STF Modelling

The developed STF model is examined by comparing the prediction with FE results under different fault scenarios, including different coil location, with and without TSC.

4.6.1 STF without Terminal Short Circuit

First, a single STF without TSC is evaluated. The STF is assumed to occur in coil B2 as discussed above. All 3-phase sets are excited by 120A at 4000rpm. The predicted turn fault current matches well with the FE results as shown in Fig. 4-21. The fault current is 9 times of the rated value. It causes significant distortion to the phase flux linkage as can be seen in Fig. 4-22. The phase flux linkages predicted by the equivalent lookup table with the inputs $(\theta, i_{df}, i_{qf}, F_{osf}^1)$ are close to the FE results. The flux linkage of phase B where the faulty turn is located is noticeably lower than those of phases A and C due to flux nullifying effect of the turn fault current.

The resultant torque is also accurately predicted by the proposed model as illustrated in Fig. 4-23. The results indicate that the torque contribution of the healthy sets is more or less unchanged, however, a large 2nd harmonic is observed in the fault set. This is mainly due to the distortion in the flux linkages caused by the STF. This phenomenon provides an important insight for the STF detection which will be analysed in the next Chapter.
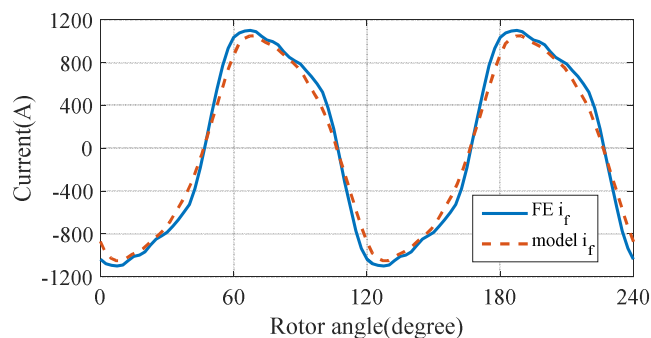
Fig. 4-21 Turn fault current with STF in coil B2 without TSC
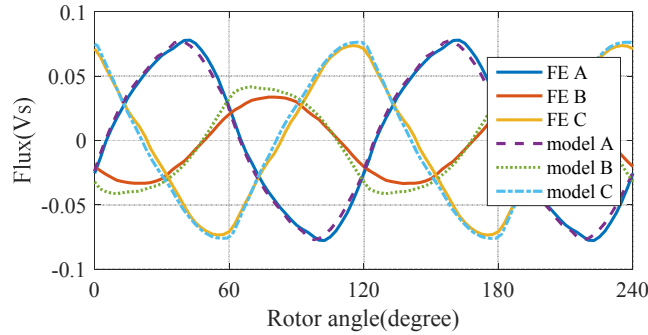
Fig. 4-22 Phase flux linkages with STF in coil B2 without TSC
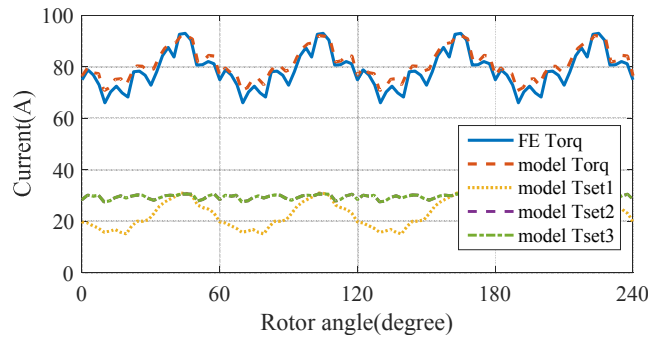
Fig. 4-23 Torque with STF in coil B2 without TSC

Since a STF may occur in other coils, one turn short circuit in coil A1 is also examined. The resultant turn fault current is shown in Fig. 4-24 which matches well with the FE result. The phase flux linkage and torque are also accurately predicted and they are not given due to similar behaviour. Thus, the model is capable of analysing the STF behaviour in different coils.
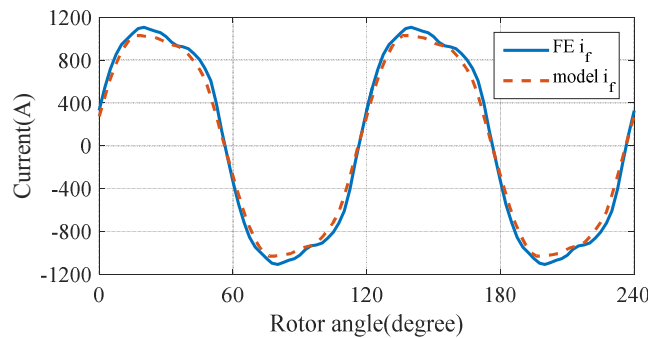
Fig. 4-24 Turn fault current with STF in coil A1 without TSC

4.6.2 STF with Terminal Short Circuit

The excessive turn fault current would cause catastrophic damage to the machine which may lead to complete failure. Fault detection should be in place and trigger correct fault mitigation action immediately upon detection of a turn fault. For this fault tolerant machine, the STF can be alleviated by

applying TSC to the fault set. After the TSC, the voltages applied on the fault set are set as zero in (4-30).

Initially, the single STF behaviour in coil B2 with TSC is analysed. The other two sets are excited by the rated currents. The resultant turn fault current and the phase currents predicted by the proposed model and FE are plotted in Fig. 4-25 and Fig. 4-26. Both the predicted turn fault current and phase currents by the model are reasonably close to the FE predictions. Small error is noticed in the peak of the fault current which may be caused by ignoring the high order harmonics in the PM flux linkage and MMF AC component as in the previous derivations. After TSC the fault current is much lower, about 2.4pu which is thermally sustainable for the machine since it only circulates in the single fault turn. Besides, the machine is still capable of providing ~2/3pu torque as shown in Fig. 4-27.
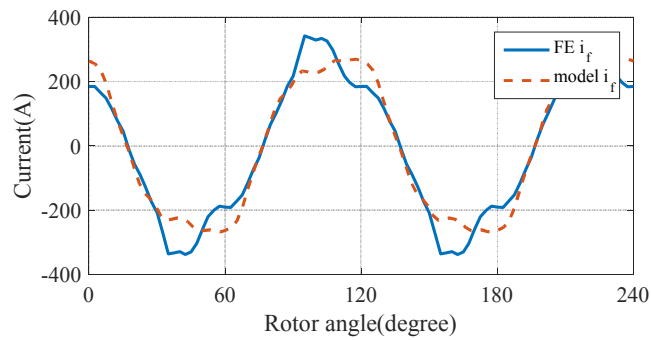
Fig. 4-25 Turn fault current with STF in coil B2 with TSC
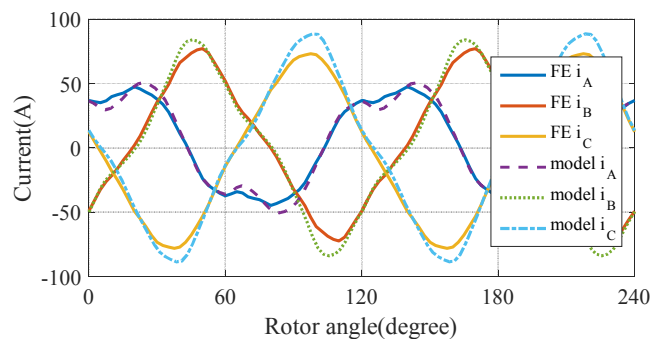
Fig. 4-26 Phase currents with STF in coil B2 with TSC
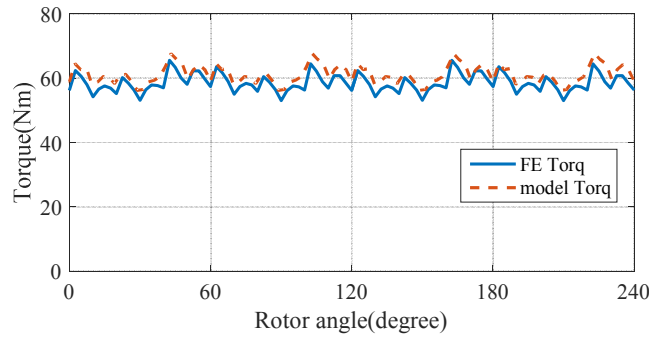
Fig. 4-27 Torque with STF in coil B2 with TSC

Similarly, one turn STF in coil A1 is evaluated with TSC. The predicted turn fault current and phase currents by the model are compared in Fig. 4-28 and Fig. 4-29 with those of FE. They match well with the FE results. It is seen that the turn fault current in coil A1 is much smaller than that when the turn fault occurs in coil B2. This further confirms the findings in Chapter 2.
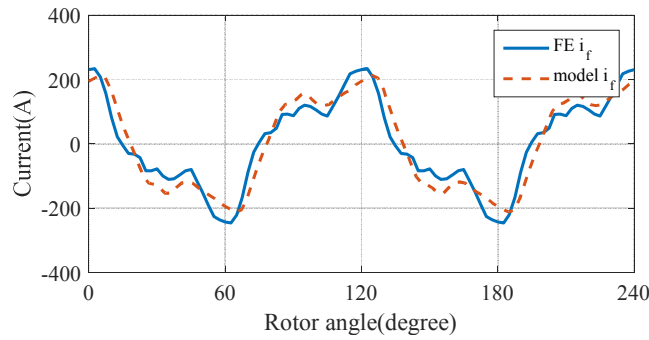
Fig. 4-28 Turn fault current with fault in coil A1 with TSC
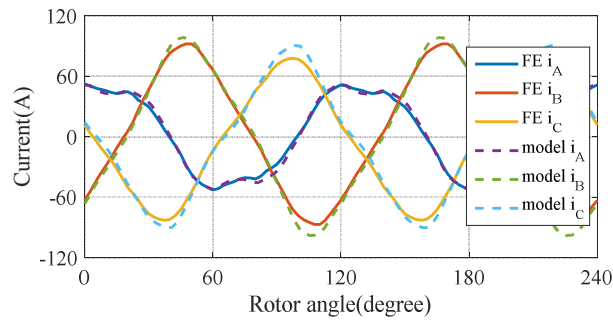
Fig. 4-29 Phase currents of faulty set with fault in coil A1 with TSC

4.7 Summary

In this Chapter, a general modelling technique has been proposed for a triple redundant, fault tolerant 3x3-phase PMA SynRM. It is capable of accurately predicting the behaviour in all operating modes, including the healthy operation, open circuit, short circuit and unequal current operation.

The proposed model is not limited to a particular operation mode, and, therefore, offers great flexibility and computational efficiency compared to FE.

The general model has also been adapted to incorporate the prediction of machine behaviour under STF. The coil location, slot position, number of fault turns all can be considered in the proposed model. The model is also capable of analysing STF behaviour with and without TSC. Therefore, it offers flexibility for predicting machine behaviour with STF in numerous different scenarios, including the behaviour of other healthy sets. The effectiveness of the model has been confirmed by extensive FE simulations and will be validated by experimental tests in Chapter 6.

The proposed modelling technique can be extended to other multiple 3-phase machines with similar winding configuration, providing a useful tool for the performance evaluations under normal and abnormal conditions as well as for the design and development of fault detection and fault-tolerant control strategies.

CHAPTER 5

A Turn Fault Detection Technique by 2nd Harmonic in Instantaneous Power

5.1 Introduction

Stator insulation is subject to progressive degradation due to electrical loading, thermal cycling, winding vibration and environmental contamination [147]. Stator winding degradation may lead to inter-turn, phase to phase or phase to ground failure [62]. Among these failure modes, inter-turn fault is known as a worst fault case since the resultant fault current is the highest. For the triple redundant 3x3-phase PMA SynRM drive, the turn fault could be mitigated by applying TSC on the fault set. However, fast and reliable detection is essential for application of appropriate fault mitigation actions.

Accurate and fast turn fault detection is a prerequisite technique for any fault-tolerant system as it enables the application of fault mitigation actions. Reliable fault detection is also of paramount importance in order to avoid false alarms and associated unnecessary downtime. This Chapter presents an inter-turn fault detection technique for the machine under study. Detailed analysis of the behaviour of a closed loop controlled permanent magnet machine drive under inter-turn fault conditions will be investigated analytically. It is shown that significant 2nd harmonic components in the dq voltages, currents, instantaneous active power (IAP) and instantaneous reactive power (IRP) are generated during turn fault conditions. The analyses further show that the increase of the 2nd harmonic in IAP and IRP during fault conditions is comparatively higher than that of voltage and current, making them ideal candidates as turn fault indicators. A turn fault detection technique based on 2nd harmonic in IAP and IRP is implemented and demonstrated for the machine drive. For the machine drive under study, the fault indicator of each 3-phase set could serve as a cross reference to avoid the false alarm during transients. The effectiveness of the proposed detection

technique is verified under both motoring and generating modes based on the model developed in section 4.5.

5.2 Turn Fault Signal Analysis

For the triple redundant 3x3-phase PMA SynRM drive under study, each 3-phase is driven by three standard 3-phase inverters. The three inverter drive modules share the same speed controller which provides the same current references which are tracked by three independent current controllers.

Without loss of generality, a single turn fault, which has the least fault signature but leads to the highest fault current, is assumed in coil A1 of set ABC as shown in Fig. 2-2. And the schematic circuit of set ABC windings is shown in Fig. 5-1. The analysis in section 4.5 has shown that a large turn fault current i_f of approximately 9 times of the rated value is induced in the short circuited path. Therefore, this severe fault should be detected immediately to trigger the mitigation action TSC for the fault set.
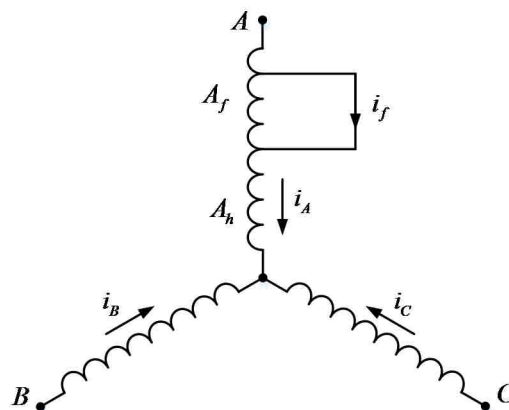
Fig. 5-1 Schematic circuit for set ABC with turn fault in phase A

In order to develop a reliable turn fault detection method, it is necessary to analyse the fault behaviour of the drive under closed loop control and select the fault indicator with the highest signal-to-noise ratio. The 2nd harmonics in the voltage, current and power are of particular interests. These quantities are fundamentally influenced by flux linkages of the windings. In healthy condition and neglecting high order harmonics, the flux linkage of the turn which may be short circuited under turn fault condition is expressed as:

$$\psi_{th} = \varphi \cos(\omega t + \theta_0)$$

<div align="right">(5-1)</div>

where φ, ω and θ_0 represent the magnitude, electrical angular speed and phase angle, respectively.

In case of a turn fault, the turn fault current is predominantly reactive and produces flux linkage which opposes the flux linkage in healthy condition. Thus, the flux linkage induced by the fault current can be approximated as:

$$\psi_{tf} = -\varphi_f \cos(\omega t + \theta_0)$$

<div align="right">(5-2)</div>

where φ_f denotes the magnitude of the flux linkage. Transforming this flux linkage to the dq axes yields:

$$\Delta\psi_d = -\frac{1}{3}\varphi_f(\cos\theta_0 + \cos(2\omega t + \theta_0))$$

$$\Delta\psi_q = -\frac{1}{3}\varphi_f(\sin\theta_0 - \sin(2\omega t + \theta_0))$$

<div align="right">(5-3)</div>

They appear as 2nd harmonics in in the dq flux linkages. The 2nd harmonics are seen as disturbances to the current controllers, and consequently cause 2nd harmonics in the dq voltages and currents. In order to analyse the resultant 2nd harmonic currents and voltages, the current control block diagram illustrated in Fig. 5-2 will be considered. The PI current controller is simplified as a proportional control since the integral control has limited bandwidth and therefore negligible influence on the components of 2nd harmonic frequency.
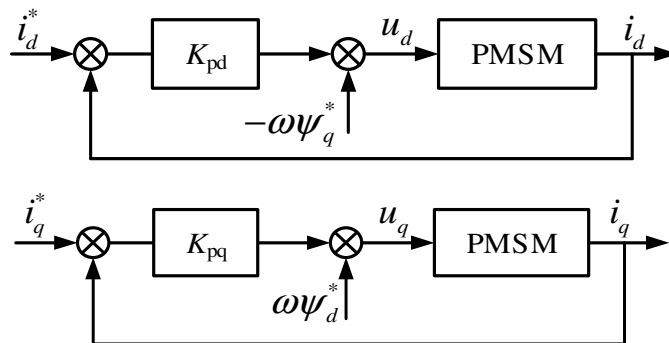
Fig. 5-2 dq axes current control diagram

The machine voltage equations can be written as:

$$u_d = \frac{d\psi_d}{dt} - \omega\psi_q$$

$$u_q = \frac{d\psi_q}{dt} + \omega\psi_d$$

(5-4)

where the small stator resistive drop has been omitted to facilitate the derivation. ψ_d, ψ_q, L_d, L_q denote the d- and q-axes components of flux linkages and inductances, respectively. ψ_d, ψ_q can be expressed as in (5-5) by accounting for the flux linkage induced by the turn fault current, where the DC components in $\Delta\psi_d$, $\Delta\psi_q$ are neglected since they do not affect the resultant 2nd harmonics in dq voltages and currents. ψ_m represents the PM flux linkage.

$$\psi_d = \psi_m + L_d i_d - \frac{1}{3}\varphi_f \cos(2\omega t + \theta_0)$$

$$\psi_q = L_q i_q + \frac{1}{3}\varphi_f \sin(2\omega t + \theta_0)$$

(5-5)

The cross coupling compensations, $-\omega\psi_q^*$ and $\omega\psi_d^*$, in the current controller of Fig. 5-2 are implemented with the estimated values of the dq axes flux linkages as in (5-6).

$$\psi_d^* = \psi_m + L_d i_d$$

$$\psi_q^* = L_q i_q$$

(5-6)

As a result, the voltage equations in (5-4) by the current feedback control in Fig. 5-2 can be simplified to:

$$-K_{pd} i_d - \frac{\omega}{3}\varphi_f \sin(2\omega t + \theta_0) = L_d \frac{di_d}{dt}$$

$$-K_{pq} i_q - \frac{\omega}{3}\varphi_f \cos(2\omega t + \theta_0) = L_q \frac{di_q}{dt}$$

(5-7)

The gains K_{pd} and K_{pq} are selected as $\omega_c L_d$ and $\omega_c L_q$, respectively, based on pole-zero cancellation, where ω_c is the current controller bandwidth which is set to 200Hz. By analytically solving (5-7), the 2nd harmonic currents and voltages in steady state, denoted as i_{d2}, i_{q2} u_{d2}, u_{q2}, can be derived as:

$$i_{d2} = -\frac{k}{L_d}\sin(2\omega t + \theta_1)$$

$$i_{q2} = -\frac{k}{L_q}\cos(2\omega t + \theta_1)$$

$$u_{d2} = k(\omega_c \sin(2\omega t + \theta_1) + \omega \cos(2\omega t + \theta_1))$$

$$u_{q2} = k(\omega_c \cos(2\omega t + \theta_1) - \omega \sin(2\omega t + \theta_1))$$

$$k = \frac{\omega \varphi_f}{3\sqrt{\omega_c^2 + 4\omega^2}}, \theta_1 = \theta_0 - \tan^{-1}\frac{2\omega}{\omega_c}$$

(5-8)

Defining i_{d0}, i_{q0} as the DC components of i_{dq}, the synchronous currents and voltages can be derived as:

$$i_d = i_{d0} - \frac{k}{L_d}\sin\delta$$

$$i_q = i_{q0} - \frac{k}{L_q}\cos\delta$$

$$u_{d2} = -\omega L_q i_{q0} + k(\omega_c \sin\delta + \omega \cos\delta)$$

$$u_{q2} = \omega\psi_{d0} + k(\omega_c \cos\delta - \omega \sin\delta)$$

$$\psi_{d0} = \psi_m + L_d i_{d0}, \ \delta = 2\omega t + \theta_1$$

(5-9)

It can be seen that the turn fault induces 2nd harmonics in both currents and voltages. The magnitudes of the 2nd harmonics are influenced by the current control bandwidth. The IAP and IRP can be calculated as [148]:

$$p = 1.5(u_d i_d + u_q i_q)$$

(5-10)

$$q = 1.5(u_q i_d - u_d i_q)$$

The 2nd harmonics of the active power and reactive power are extracted from (5-10) and given in (5-11).

$$p_2 = 1.5k\left(\left(\frac{L_q}{L_d} - 1\right)\omega i_{q0} + \omega_c i_{d0}\right)\sin\delta +$$

$$1.5k\left(\omega i_{d0} - \frac{\omega\psi_{d0}}{L_q} + \omega_c i_{q0}\right)\cos\delta$$

(5-11)

$$q_2 = 1.5k\left(-\frac{\omega\psi_{d0}}{L_d} - \omega i_{d0} - \omega_c i_{q0}\right)\sin\delta +$$

$$1.5k(\omega_c i_{d0} - 2\omega i_{q0})\cos\delta$$

Since the PM flux linkage ψ_m is relatively small and negative i_d is often required for maximum torque per Ampere (MTPA) operation in IPM, ψ_{d0} is quite small compared to the other terms in (5-11). Hence, the magnitude associated with the *cosine* component of p_2 approximately equals that with the *sine* component of q_2. Consequently, the magnitude of p_2 depends mainly on its *sine* component while the magnitude of q_2 mostly on its *cosine* component. Comparing the *sine* component of p_2 and the *cosine* component of q_2, it can be deduced that the magnitude of q_2 will be higher than p_2 when i_{q0} is positive. On the contrary, the magnitude of q_2 will be lower than p_2 with a negative i_{q0}. This means that in motoring mode ($i_{q0} > 0$), the 2nd harmonic in IRP is higher than that of IAP while it is lower than that of IAP in generating mode ($i_{q0} < 0$). It should be noted that the above analysis is based on simplifying assumptions and additional causes of the 2nd harmonics in IAP and IRP due to natural machine unbalance and magnetic saturation are not considered. Nonetheless, since the major contributor to the 2nd harmonics is the turn fault, the analysis above demonstrates the relative effects on the proposed fault indicators based on 2nd harmonic characteristics of the IAP and IRP.

In order to understand the 2nd harmonic behaviour in the IAP and IRP in turn fault condition over the whole operating region, the turn fault model established in section 4.5 for the machine under study has been used to estimate the resultant 2nd harmonics in the IAP and IRP. Fig. 5-3 shows the simulated 2nd harmonics of the IAP and IRP of the faulted 3-phase set in motoring mode and generating mode, respectively. It can be observed that in motoring mode, the induced 2nd harmonic of the IRP in the fault set is higher than that of IAP over the whole torque-speed range while it is lower than that of IAP in generating mode. These results are consistent with the analysis above. Further, the turn fault influence on the 2nd harmonic of IRP in motoring mode and on the 2nd harmonic of IAP in generating mode is more linear across the whole operating region. Therefore, for the purpose of turn fault detection, in motoring mode, the 2nd harmonic in IRP proves to be a stronger signal whereas in generating mode, the 2nd harmonic of the IAP is more preferable. It is also evident that turn fault detection at low speed becomes challenging since the magnitude of the 2nd harmonics diminishes as speed approaches zero.
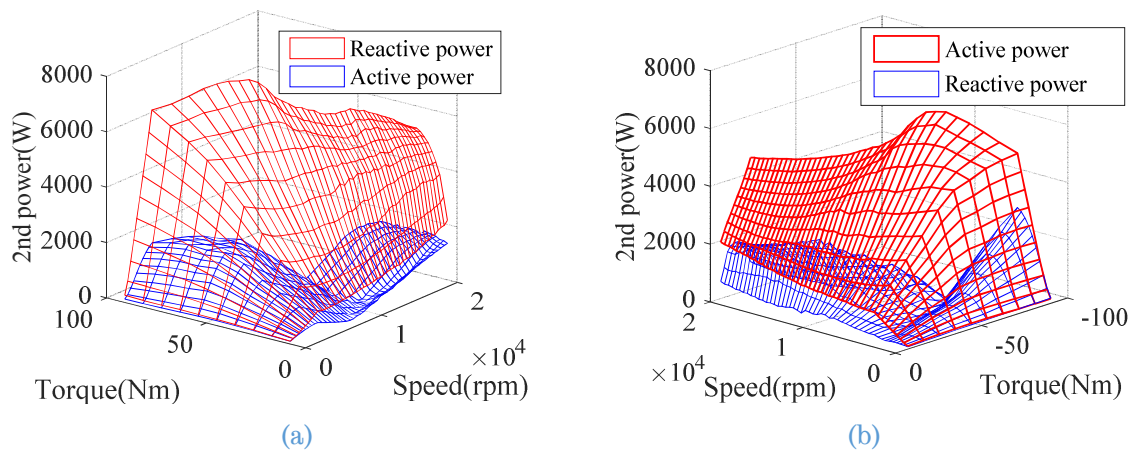
Fig. 5-3 Comparison of 2nd harmonics in IAP and IRP (a) Motoring mode (b) Generating mode

5.3 Fault Detection Design

The implementation of the proposed fault detection based on 2nd harmonics in instantaneous power for the closed loop controlled 9-phase fault tolerant machine is presented in this section.

It is worth noting that the machine inherent asymmetry and unbalance is inevitable due to manufacturing tolerance, limited accuracies of current sensors [149], and disparity in inverter characteristics. All these factors will contribute to 2nd harmonics in healthy condition. In order to compensate the background 2nd harmonics, lookup tables are produced for each 3-phase set to record the 2nd harmonics in healthy conditions. This process can be performed automatically during drive operations before any fault occurs.

The 3-phase set with a turn fault due to insulation failure exhibits large 2nd harmonic in the fault indicator. However, the indicator would be significantly lower for the remaining healthy sets. The 2nd harmonics of the healthy set are also simulated and compared with the fault set as shown in Fig. 5-4 for both operation modes. It can be seen that the induced 2nd harmonics of the fault set are much higher than that of the healthy set. Thus, the 2nd harmonic of each 3-phase set can provide an inherent cross reference to enhance the fault detection. Any harmonics based fault detection might be sensitive to spurious harmonics generated during speed and load changes resulting in false alarms. The application of cross reference between three 3-phase sets can significantly reduce the influence of the speed and load transients on the fault indicators, as such transients will be common to all three sets, while 2nd harmonic is only significantly higher in the fault set, eliminating the risk of false alarm.

(a)

(b)
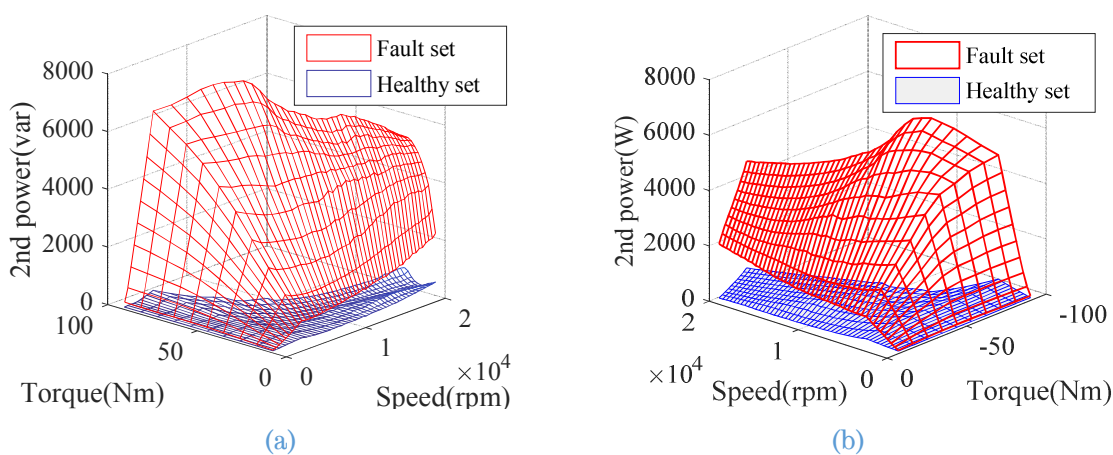
Fig. 5-4 Comparison 2nd harmonics of faulty and healthy sets (a) IRP in motoring mode (b) IAP in generating mode
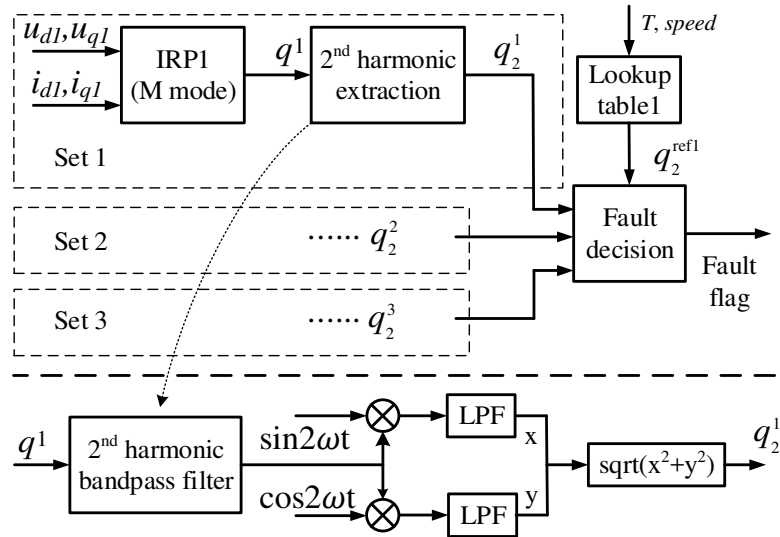
Fig. 5-5 Fault detection diagram in motoring mode

A block diagram illustrating the turn fault detection method for motoring mode is shown in Fig. 5-5, where for notational convenience sets 1, 2 and 3 represent 3-phase winding sets ABC, DEF and GHI, respectively. The resultant 2nd harmonics in IRP are denoted as q_2^k, k=1,2,3. First, the IRP is calculated based on the control voltages and measured currents using (5-10). Then the amplitude of the 2nd harmonic is extracted by the filter as shown in the bottom of Fig. 5-5. Look-up tables provide the reference 2nd harmonic in healthy conditions which will be produced in experimental tests. It captures the 2nd harmonics caused by inherent asymmetry, like phase misalignment, different resistance/inductance, rotor eccentricity and unequal magnets magnetisation, which could reduce the possibility of false alarm. Finally, the fault indicators are processed by a fault decision block. The fault flag is triggered if:

$$q_2^1 > 2q_2^{ref1} \text{ AND } q_2^1 > 1.5\max(q_2^2, q_2^3) \tag{5-12}$$

where q_2^1, q_2^2 and q_2^3 denote the 2nd harmonic in IRP of the ABC, DEF and GHI sets, respectively, and q_2^{ref1} denotes the reference 2nd harmonic of set ABC in healthy condition. The first inequality is verified if the 2nd harmonic is two times higher than its reference in healthy condition while the second inequality indicates that it is also 1.5 times higher than that of the other two sets. The coefficients in the two inequalities can be tuned to maximize

detection sensitivity whereas eliminating any false alarm. By means of lookup table and cross reference, the influences of machine unbalance and transients are compensated, ensuring the reliable and accurate detection. The same detection mechanism is also implemented in sets DEF and GHI. The detection in generating mode has been implemented similarly with the only difference being that detection is based on the 2nd harmonic in IAP.

5.4 Simulation Validation

In this section, the turn fault model established in section 4.5 is used to investigate the turn fault behaviour and verify the effectiveness of the proposed detection technique. The 2nd harmonics in the dq currents, voltages, the IAP and IRP are compared. The proposed detection technique is examined at both steady state and transient conditions.

First, the turn fault detection algorithm is tested with 60A load currents in motoring mode. The machine speed is set as at 1000rpm which is more representative since it is more difficult to detect the fault at low speed. The machine behaviour is shown in Fig. 5-6. Initially the machine is operating in healthy condition, the dq voltages, currents, the resultant IAP and IRP are the same for the three sets. For the simplicity, only the variables of set 1 and set 2 are plotted. Then, a turn fault is injected at 0.05s in set 1. The turn fault current quickly reaches 370A. Disturbance is noticed in the dq voltages and currents which is mainly the 2nd harmonics. The set 2 is less affected by the fault which is the healthy set. Due to the closed loop control, higher harmonics appear in the dq voltages while less harmonics are in the dq currents.

According to the proposed detection, the resultant IAP and IRP are calculated as in Fig. 5-6(d). And it can be found the induced 2nd harmonics are much higher than the dq voltage and current signals. Besides, the 2nd harmonic in IRP is significantly higher than that of IAP which is consistent with the analysis above. Therefore, the 2nd harmonic in IRP is more suitable for fault signal. The detected 2nd harmonics are shown in Fig. 5-6(e). The induced 2nd harmonic is much higher in the fault set. Hence, the fault can be alarmed.

(a)

(b)

(c)

(d)

(e)
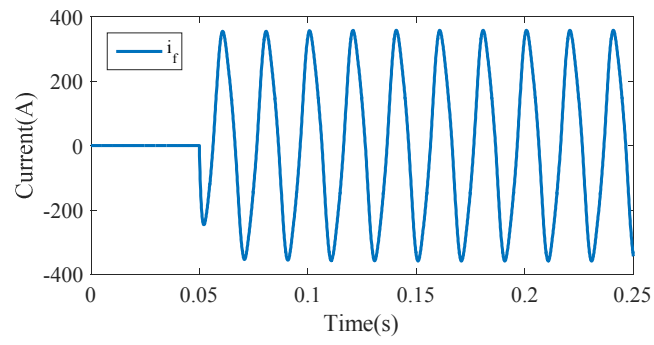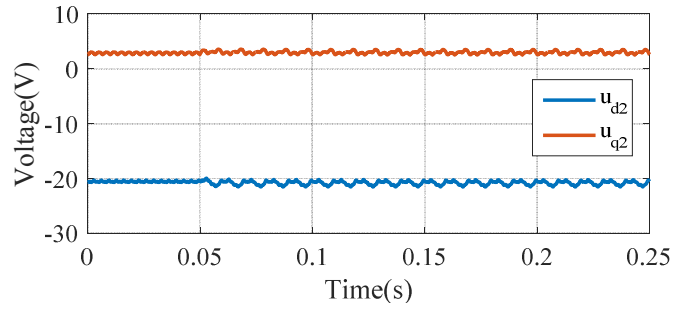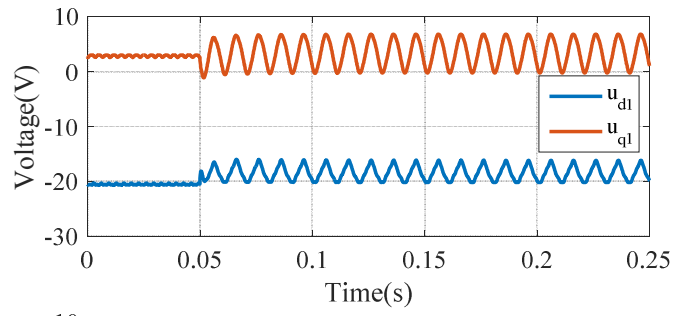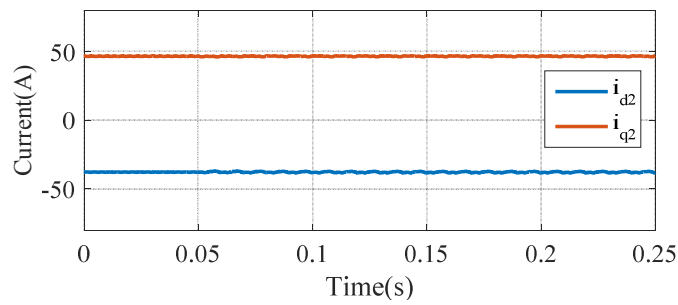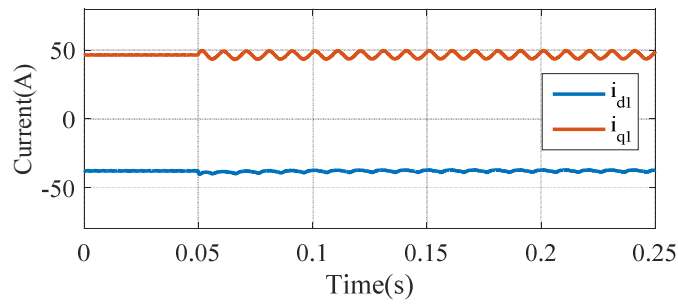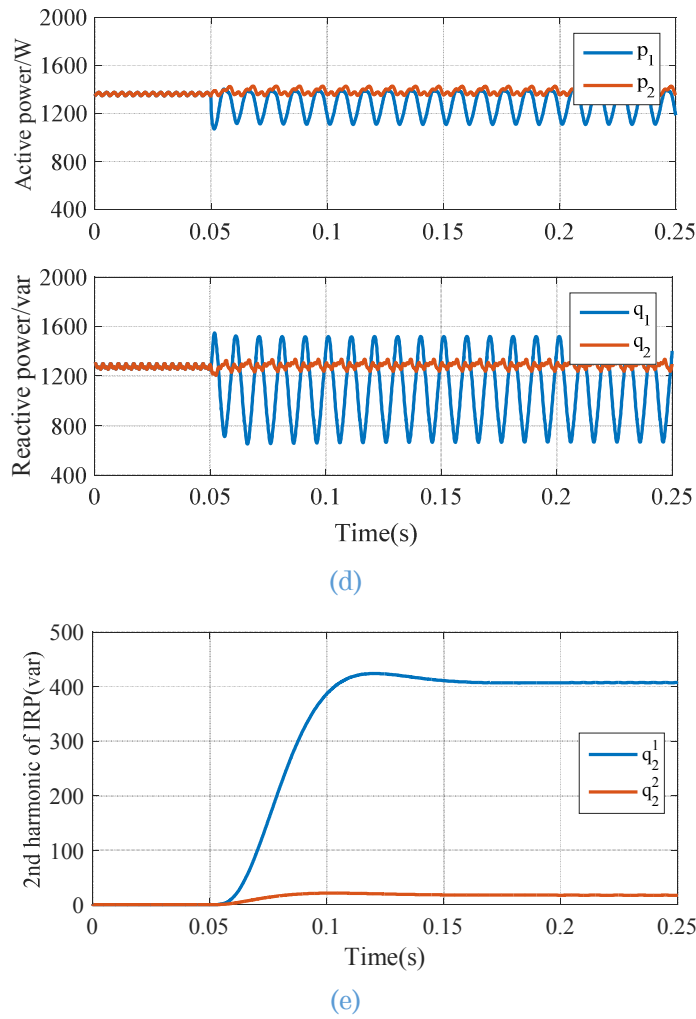
Fig. 5-6 Turn fault detection behaviour at 1000rpm with 60A load currents in motoring mode (a) turn fault current (b) dq voltages (c) dq currents (d) IAPs and IRPs (e) detected 2nd harmonics in IRPs

Similarly, the detection algorithm has been tested under generating mode with the same load currents at 1000rpm. The turn fault is also injected at 0.05s in set 1. Here, only the IAP and IRP are plotted as in Fig. 5-7(a) since the dq voltages and currents are similar as that in motoring mode. Unlike the motoring mode, now the 2nd harmonic in IAP is higher than that of IRP which is also confirms the previous conclusion. Thus, in generating mode, the 2nd harmonic in IAP other than IRP is more suitable for fault indicator. The detected 2nd harmonics in the fault and healthy sets are shown in Fig. 5-7(b) where the turn fault can be detected in set 1.

(a)

(b)
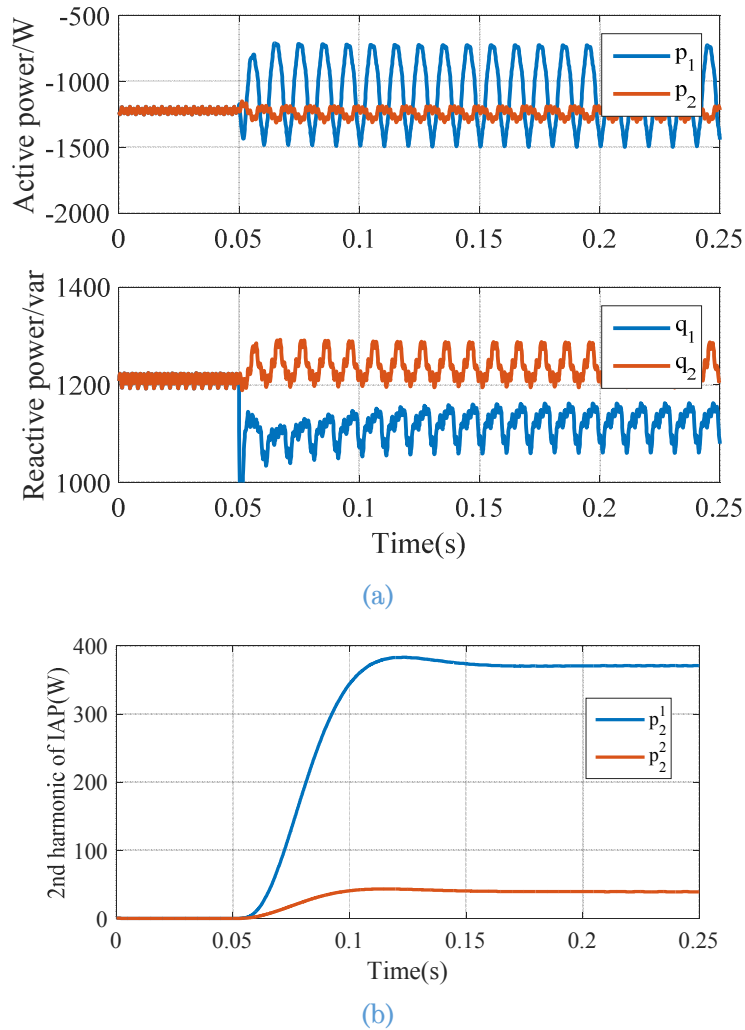
Fig. 5-7 Turn fault detection behaviour at 1000rpm with 60A load currents in generating mode (a) IAPs and IRPs (b) detected 2nd harmonics in IAPs

It is well known that the detection based on harmonics would cause false alarm during transients. For the machine under study with three 3-phase modules this problem can be avoided by cross-reference of the fault indicators in three 3-phase sets as described previously.

First, the influence of the current transient is assessed as shown in Fig. 5-8. Initially, the machine is operating with 20A load currents at 1000rpm in motoring mode. The currents and IRP of the three sets are the same in healthy condition. Then the load currents increase in step from 20A to 60A at 0.05s. The IRPs increase accordingly. As can be seen in Fig. 5-8(d), due to the step change in the current and IRP, a momentary increase is seen in the 2nd harmonic IPRs in all 3-phase sets. However, no false alarm will be triggered

owing to the cross-reference. This feature of rejecting false alarm is very desirable for the detection.

At 0.25s, the load currents increase in step from 60A to 120A and a turn fault is injected in set ABC simultaneously. As can be seen, though the momentary increases in the 2nd harmonic IRPs still appear in all 3-phase sets during the transient, the induced 2nd harmonic in set 1 is much higher than that of sets 2 and 3. Thus, the turn fault can be detected.
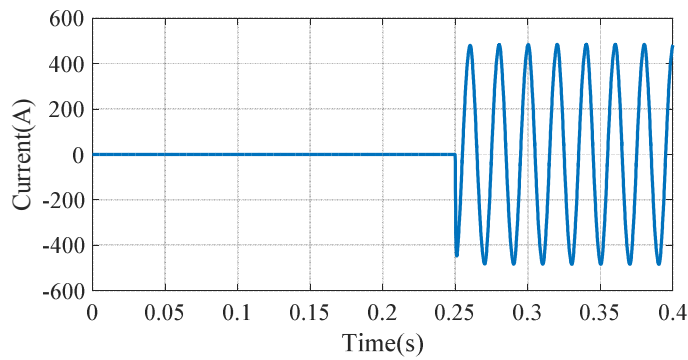
(a)
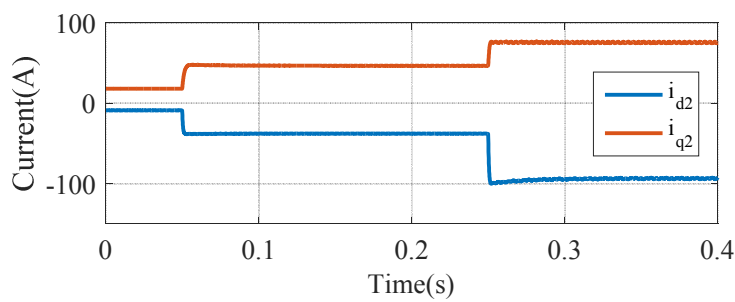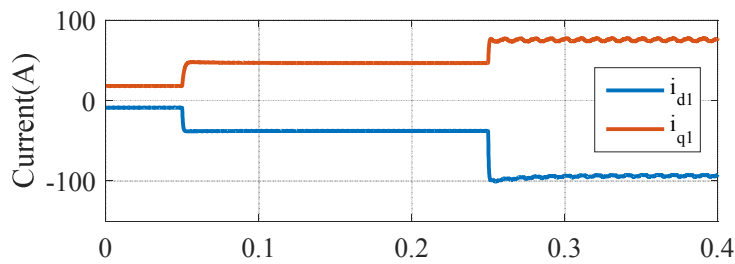
(b)
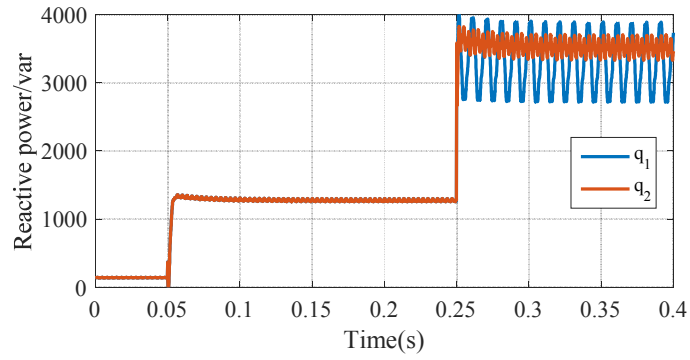
(c)
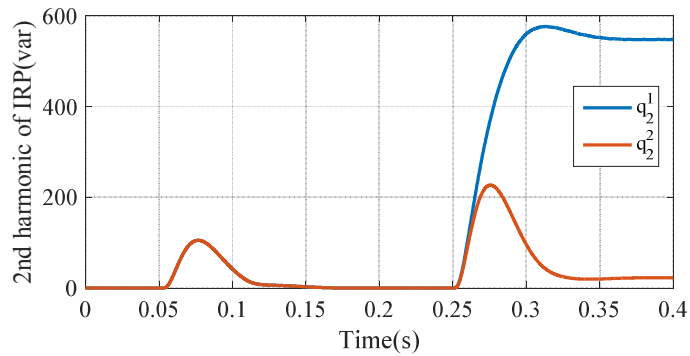
(d)

Fig. 5-8 Turn fault detection behaviour at 1000rpm during current transients in motoring mode (a) turn fault current (b) dq currents (c) IRPs (d) detected 2nd harmonics in IRPs

Similarly, the influence of speed transient on the proposed fault detection is analysed as shown in Fig. 5-9. The speed of the machine increases from 2000rpm to 2200rpm in 0.2s with 60A load current. The IRP increases proportionally to the speed as the output torque is constant. At 0.1s, a turn fault is injected in set 1. Obviously, the fault can be detected according to the 2nd harmonic of IRPs in Fig. 5-9(d). Therefore, the turn fault could be detected without false alarm during transients.
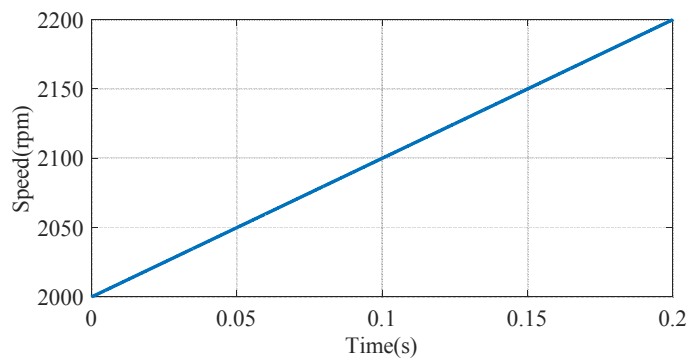
(a)
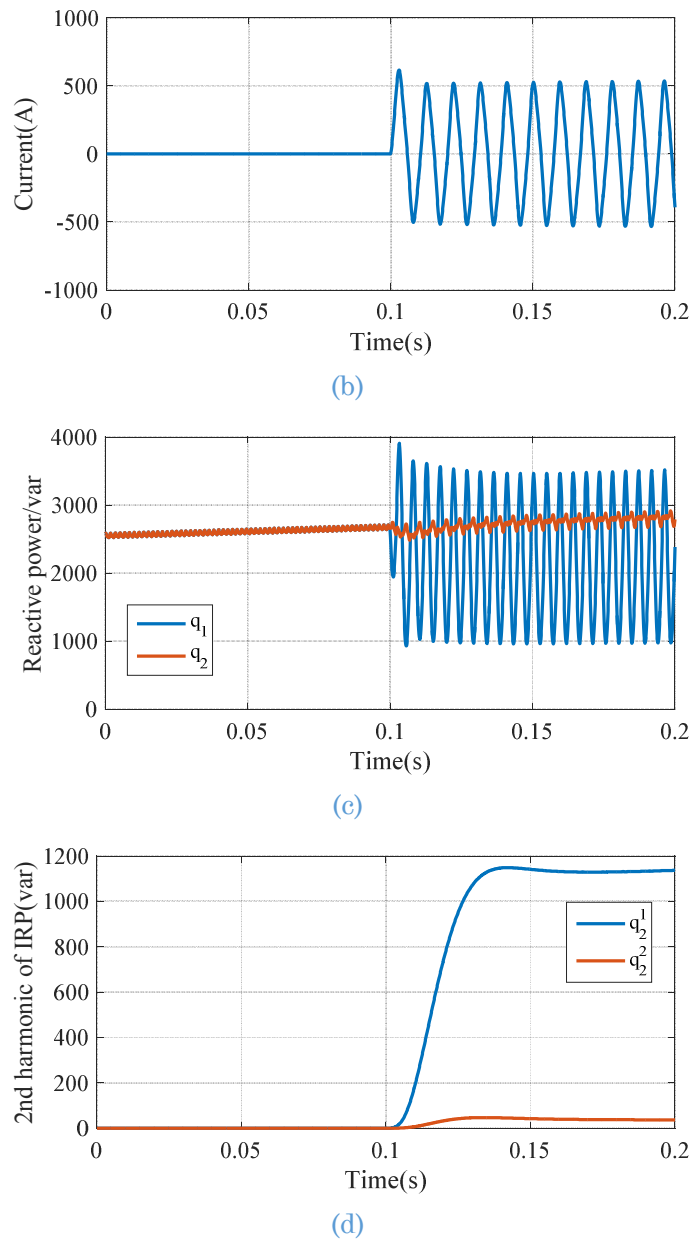
Fig. 5-9 Turn fault detection behaviour at 1000rpm during speed transient in motoring mode (a) speed (b) turn fault current (c) IRPs (d) detected 2nd harmonics in IRPs

The detection is based on assumption that a large 2nd harmonic in IRP or IAP is caused by a turn fault. However, other faults, such as high resistance or rotor eccentricity, demagnetization, etc. may also give rise to such increase.

First, the behaviour of the proposed detection method in case of a high resistance fault is simulated as shown in Fig. 5-10. Initially, the machine operates in healthy condition with 100A excitation at 1000rpm. Then, phase A resistance is increased by 100% at 0.05s. A small disturbance is noticed in the IRPs and their 2nd harmonics. The resultant 2nd IRP harmonic in set ABC is very small though it is slightly higher than those in the other two sets. It

should be noted that the increase in its amplitude is even lower than the reference 2nd IRP harmonic of set ABC q_2^{ref1} due to natural unbalance of the 3-phase windings. This will be seen in the experimental tests presented in Chapter 6. Thus, the first criterion in equation (5-12) is not true in this case, implying that the detection technique is not sensitive to the high resistance fault when the increase in one phase resistance is less than 100%. To illustrate the difference, a turn fault is injected in set GHI at 0.25s. It can be seen the resultant 2nd harmonic in IRP is much higher than that of high resistance fault. Obviously, the turn fault can reliably be detected. Thus, the high resistance fault has insignificant influence to the detection technique.

(a)

(b)
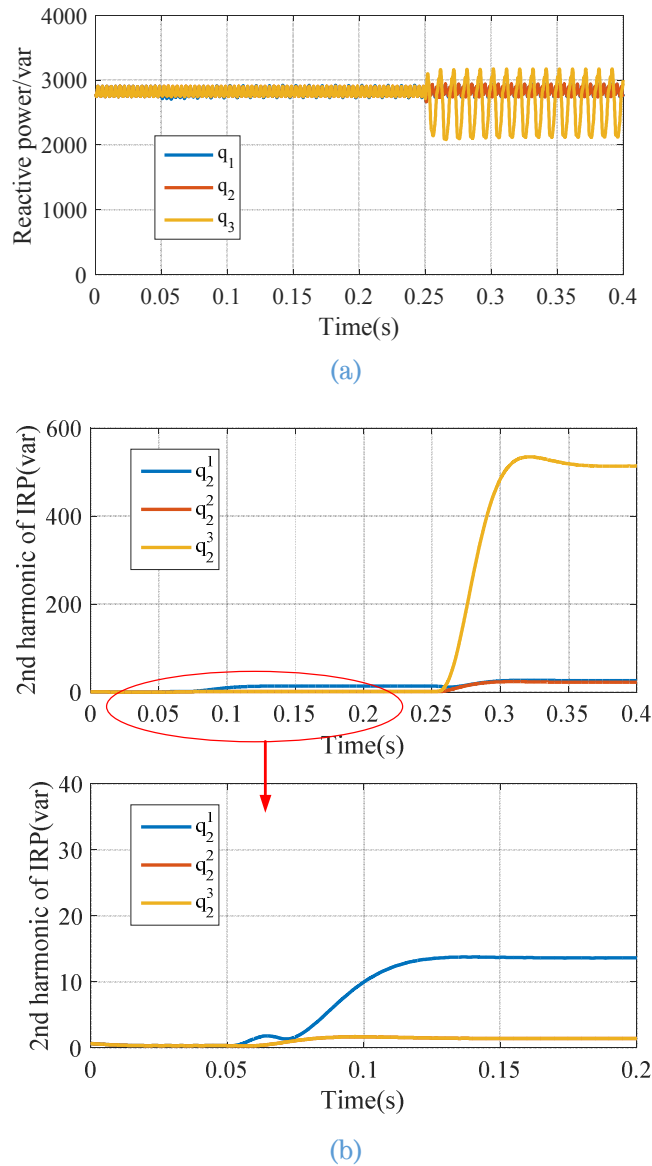
Fig. 5-10 Turn fault detection behaviour at 1000rpm with high resistance fault at 0.05s in motoring mode (a) IRPs (b) detected 2nd harmonics in IRPs

Both rotor eccentricity and asymmetric demagnetisation will lead to increase in 2nd IRP or IAP harmonics. However, the effects will be similar on all the three 3-phase sets which will be accounted in the stored lookup tables. Thus, the proposed detection employing the cross-reference of the 2nd IRP harmonics in all three 3-phase sets would be insensitive to these two faults too.

5.5 Summary

In this Chapter, a turn fault detection technique has been developed based on the 2nd harmonic in IAP and IRP for the triple redundant, fault tolerant PM machine drive under closed loop control. Analytical derivations confirm that the 2nd harmonic in IRP is higher than that of IAP in motoring mode, whilst the opposite is true in generating mode. The analysis demonstrates that the 2nd harmonics in IRP and IAP are suitable indicators for turn fault detection in motoring mode and generating mode, respectively. The implementation of the proposed detection has been explained and validated by simulations based on the model established in section 4.5. It will be further verified by experimental tests in Chapter 6. The impact of some other faults are investigated. The analysis shows that the proposed detection technique is insensitive to high resistance, rotor eccentricity and demagnetization faults.

CHAPTER 6

Prototyping and Experimental Validation of the Triple Redundant 3x3-phase PMA SynRM Drive

6.1 Introduction

In this Chapter, a triple redundant 3x3-phase PMA SynRM drive is built according to the outcomes of the design optimization described in Chapter 3. The machine drive prototype is introduced and the manufacturing errors are analysed. A systematic test setup is prepared for the machine drive. It is capable of operating in healthy conditions and emulating various fault scenarios in a controlled manner.

Comprehensive experimental tests are performed on the triple redundant PMA SynRM drive under both healthy and various fault conditions. The accuracy of the general model in Chapter 4 is examined in different operation modes. And the turn fault detection technique in Chapter 5 is verified in a wide operation range in both steady state and transient conditions.

6.2 Machine Construction and Characterisation

6.2.1 Machine Construction

A machine prototype has been built according to previous optimization. The stator stack is skewed by one slot, i.e. 10 degrees to reduce the torque ripple and voltage harmonics due to slotting as shown in Fig. 6-1(a). The rotor stack is shown in Fig. 6-1(b), in which the magnets have been inserted in the cavity. Epoxy has been injected to the void area to protect the magnets and improve thermal dissipation. 0.2mm Cobalt-iron lamination with high saturation flux density has been used for the stator and rotor cores. The magnets are Vacomax 225HR whose remanence is 1.1T, and it is insensitive to temperature variation. All of the materials are from VACUUMSCHMELZE GmbH & Co. KG. The lamination is processed by laser cutting and glued in high

quality. Then the sheets are annealed according to VAC specification. Rotor laminations are annealed for optimum mechanical properties whilst stator laminations are annealed for optimum magnetic properties. Two keyways have been cut on both the stator and rotor stack for fixing purpose. It should be noted that the rotor stack is made of 2mm longer than the stator to compensate for axial flux leakage.

(a)   (b)
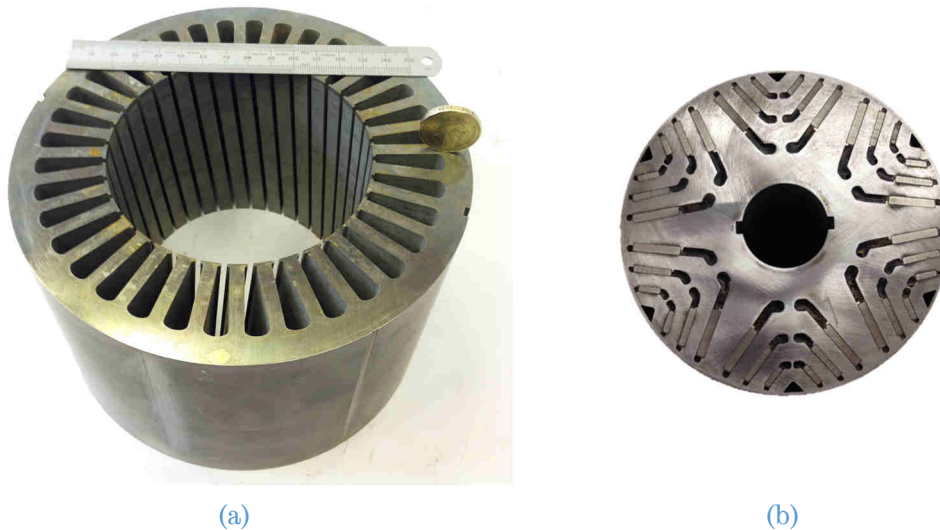
Fig. 6-1 Stator and rotor stack (a) stator stack (b) rotor stack

The rotor assembly is shown in Fig. 6-2. The rotor stack is clamped by two endplates with fins. The rotating components are fixed to the shaft by a M25 nut. The nut is specially designed so that in case the nut loosens, it would only touch the rotating part of the bearing, avoiding any destructive contact with the stationary and rotary components. Since the machine is required to operate at relatively high speed 19200rpm, the rotor system has been balanced in AMB Engineering LTD, and the report is shown in Fig. 6-3. As can be seen, the rotor has been balanced to Grade 6.3 which is superior to the required Grade 16.

Fig. 6-2 Rotor assembly

Permissible Maximum Residual Unbalance For Rotor
In accordance with ISO 1940/1

Rotor Type:	PM Rotor		
Service Speed	20000 RPM	Weight	8.6 Kg
Balance Quality Required	G 6.3		
Left Plane	12.9 gmm	Right Plane	12.9 gmm

Residual Unbalance Results (after Balancing)

Left Plane		Right Plane	
Amount	Angle	Amount	Angle
9.6 μm	237 deg	10.5 μm	92 deg
11.54 gmm	264 deg	6.97 gmm	179 deg

Fig. 6-3 Rotor balancing report

The windings are completed by Portland Electrical Ltd, using Polyester C200 copper wire from PAR Ltd. The maximum continuous operation temperature is 200°C. The coils are made up of 17 strands of 0.8mm varnished wire. The key feature of the fault tolerant machine is the segregated windings as shown in Fig. 6-4(a). It can be seen that the windings of different 3-phase sets have been separated by the proposed winding configuration. Insulation paper is inserted between different phases to enhance the phase-to-phase insulation. K type Thermocouples have been buried in the slots and end windings to monitor the winding temperatures during operation. The cable leads are shown in Fig. 6-4(b). The thinner cables are the leads of the 9 phases which carry the phase currents. In order to emulate the worst inter-turn fault case, a single turn tap is brought out in coil B2 of set ABC. Thick cables have been connected to the fault emulation tap to minimize the additional impedance in the short circuited loop. The thick cable leads are connected to a high current relay as shown in Fig. 6-5 to emulate the inter-turn fault in a

controlled manner. It is worth noting that the fault turn is located in coil B2 when the rotor rotates anti-clockwise. However, the fault location is equivalent to that in coil A1 if the rotor rotates clockwise as illustrated in Fig. 2-2. Hence, the turn fault could be tested in both coil locations with the simple scheme.

(a)　　　　　　　　　　　(b)
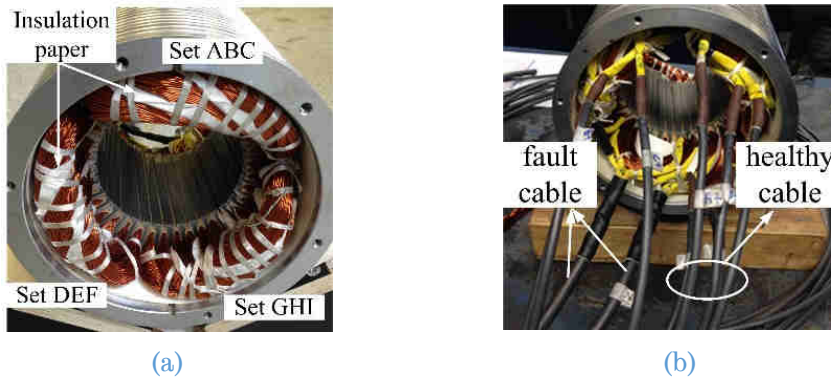
Fig. 6-4 Machine windings and leads (a) segregated windings (b) leads

Fig. 6-5 Turn fault emulating relay

In order to improve the windings thermal dissipation capability, the windings are potted by Stycast 2762 with Catalyst 17. The machine is potted in a vacuum chamber as shown in Fig. 6-6(a). An air pump is used to create a vacuum space in the chamber and then the Stycast mixed with Catalyst is sucked into the machine assembly due to the pressure difference. The potted machine assembly is shown in Fig. 6-6(b). After potting, the whole machine is placed in the oven at 160°C over two days for curing purpose. And finally the machine windings is successfully potted as shown in Fig. 6-7 where the windings are buried inside the Stycast and the machine heat dissipation capability is improved.

(a)   (b)
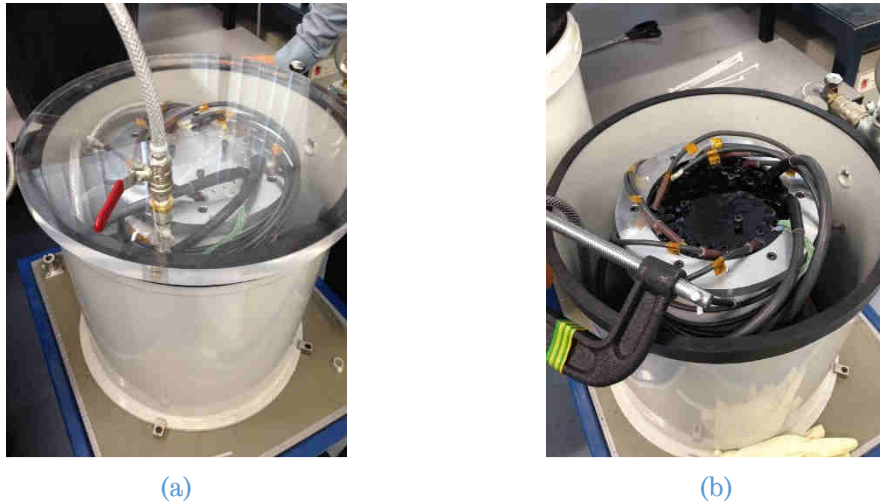
Fig. 6-6 Potting setup (a) vacuum chamber (b) potted machine
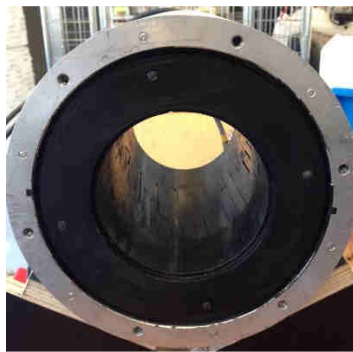
Fig. 6-7 Potted winding

According to the previous design, oil cooling system is employed to take the heat out of the machine more effectively. Fig. 6-8 shows the oil cooling jacket and sleeve which forms the closed flow path for the oil inside the machine. The oil will be injected and extracted via the inlet and outlet connections. The flowing oil carries the heat out from the machine. The whole cooling system is shown in Fig. 6-9. The temperatures of the oil at the inlet and outlet connections can be measured by two K type thermocouples.

(a)   (b)
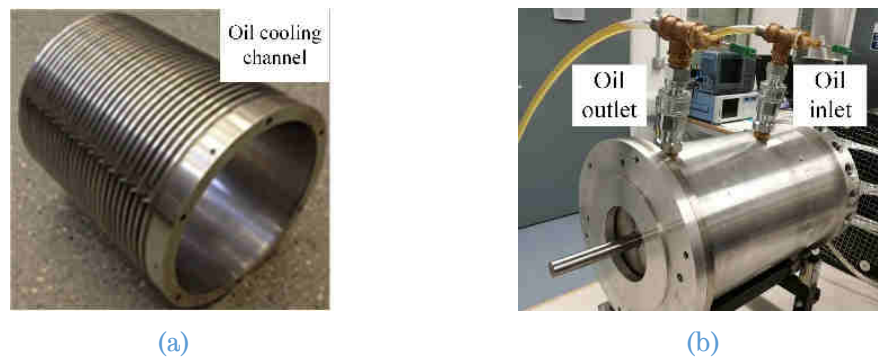
Fig. 6-8 Oil cooling jacket and sleeve (a) water jacket (b) cooling sleeve

<center>(a)   (b)</center>

Fig. 6-9 Oil cooling system (a) oil cooling pump (b) cooling pipes and connections

6.2.2 Test Setup

In order to perform systematic tests on the machine prototype, an integrated test bench is developed. The test bench should be capable to control the environment, test the machine performance, emulate various fault scenarios and record the relevant experimental data. The required instruments are listed in Table 3-1 with their functions.

Table 6-1 List of instruments used in the test bench

No.	Instruments	Function
1	Prototype	Target machine
2	9 phase inverter	Provide current excitation and control
3	AVL dyno	Emulate various operation modes
4	Torque transducer Magtrol 308	Torque range: 0~20Nm
		For noload test
5	Torque transducer Magtrol 312	Torque range: 0~200Nm
		For load test
6	Coupling 1 (Ø14- Ø10)	Couple dyno and torque transducer
7	Coupling 2 (Ø19- Ø10)	Couple machine and torque transducer
8	Coupling 3 (Ø30- Ø30)	Couple dyno and torque transducer
9	Coupling 4 (Ø19- Ø30)	Couple machine and torque transducer
10	Bidirectional DC power supply	Provide DC voltage source for inverter

No.	Instruments	Function
11	Current sensors	Measure three phase currents and DC link current
12	Voltage sensors	Measure three phase voltages and DC link voltage
13	Yokogawa power analyser	Measure and calculate various quantities: Input power of machine Output power of machine
14	Pico temperature logger	Record machine temperature via the pre-installed thermocouples
15	Water cooling machine	Drive the water cooling to circulate in the drive modules
16	Water flow rate meter	To monitor the water flow rate
17	Accelerometer	To monitor the machine vibration
18	Connection box	Create various terminal connection scenario for different fault tests
19	Relay switch	Trigger and clear the turn fault
20	Yokogawa scope	Record/observe the interested signals
21	Oil pump	Drive the aeroshell oil to circulate in the cooling loops

Based on the equipment listed above, the schematic test bench is set up as shown in Fig. 6-10 to operate the prototype machine under various operation conditions. The data acquisition system is also developed to monitor the machine operation.
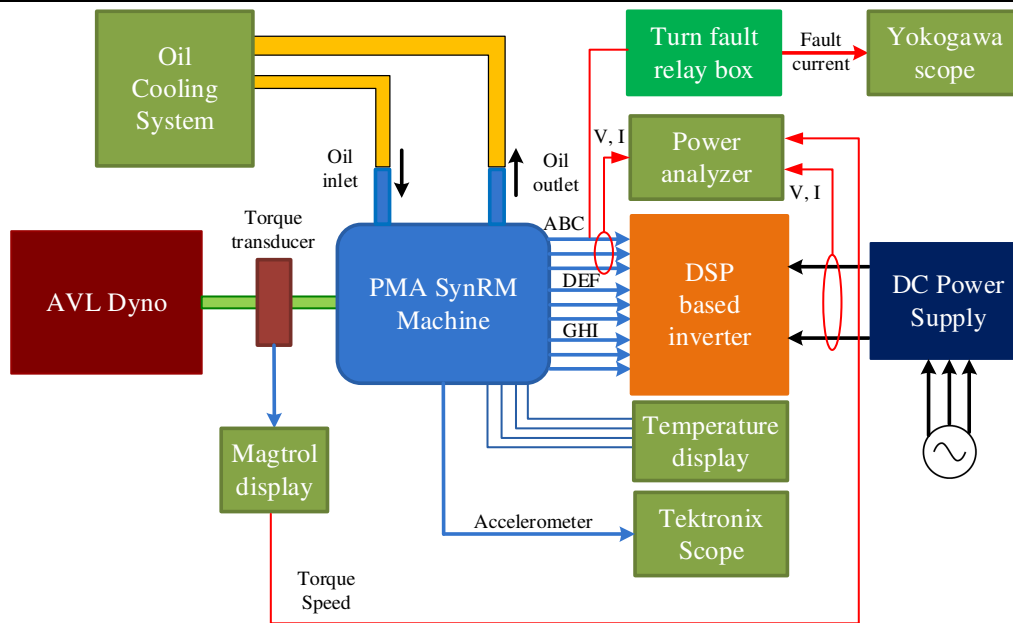
Fig. 6-10 Schematic test bench with data acquisition

As illustrated in Fig. 6-10, the prototype is connected to the AVL dyno via couplings with in line torque transducer. The AVL dyno is operated in speed control mode at a given speed command. The machine is excited by a DSP based 9 phase inverter which is configured as three 3-phase inverters in torque control mode. The DC link voltage of the inverter is fed by a bidirectional DC power supply. The connection box and turn fault relay box are in place to emulate different fault scenarios. Machine temperatures are recorded by the pre-installed thermocouples embedded in the slots and end windings. The machine vibration is monitored by an accelerometer during all operation conditions.

In addition, oil cooling and water cooling systems are employed for the machine and inverter to control the temperature rise, respectively. The aeroshell turbine oil 3 is selected as coolant which is pumped by the oil cooling machine through the grooves on the machine cooling jacket. While independent water cooling is provided for the 9 phase inverters. The oil flow rate and water flow rate are controlled at 7 liter/min and 3 liter/min respectively. Ambient temperature is maintained around 20°C by the air conditioner of the test cell.

Besides, various instruments are in place to monitor and record the machine operation quantities. The torque and speed are captured by the

torque transducer and sent to the Yokogawa WT 3000 power analyser. While the phase voltages and currents signals together with DC link voltage and current are measured separately and sent to the power analyser. Finally, these signals are synthesized. Then the input power, output power and efficiency can be calculated. The real test bench is shown in Fig. 6-11. A LeCroy HDO6054 oscilloscope has been used to measure the phase currents with high precision, high bandwidth current probes. During tests, the 9 phase currents are mainly measured by current sensors in the inverters due to limited current probes. The currents data are stored in the DSP RAM.
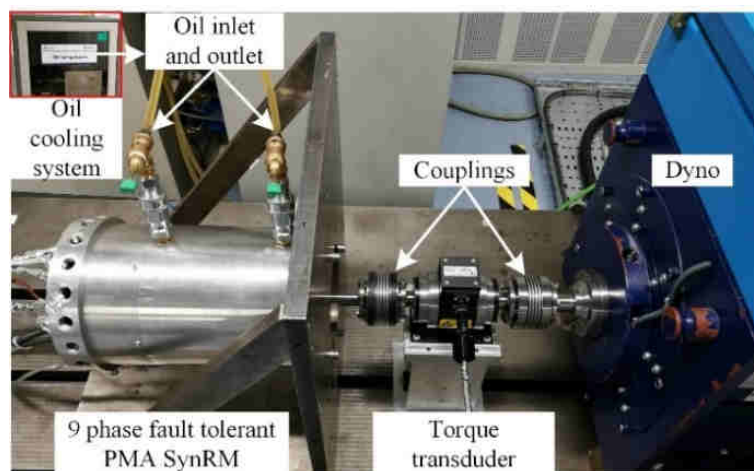
(a)
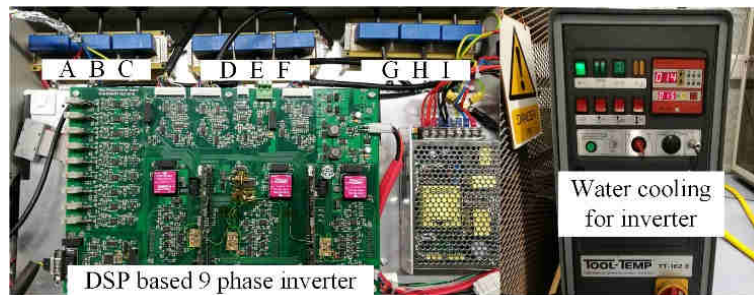
(b)

Fig. 6-11 Real test bench (a) 9 phase PMA SynRM with dyno (b) 9 phase inverter

6.2.3 Manufacture Tolerance Calibration

During manufacturing, some geometry tolerances and material deterioration were reported. They affect the machine performance and therefore should be considered in the machine model for comparison purpose.

First the BH curves of the laminations deterioration during process is observed when compared with datasheet. The measured BH curves of the

stator and rotor laminations are shown in Fig. 6-12. The BH curve of M270-35A lamination is also plotted for comparison. It is found in low magnetic field strength region, the BH curve is lower than the ideal one in the datasheet, though they can achieve comparable flux density in saturated region which is much higher than M270-35A. It is also seen that the Vacoflux 50 has better magnetic performance than Vacodur 50 because of different annealing processes. The measured BH curves for Vacoflux 50 and Vacodur 50 are updated in the machine FE model for test comparison purpose.

(a)   (b)
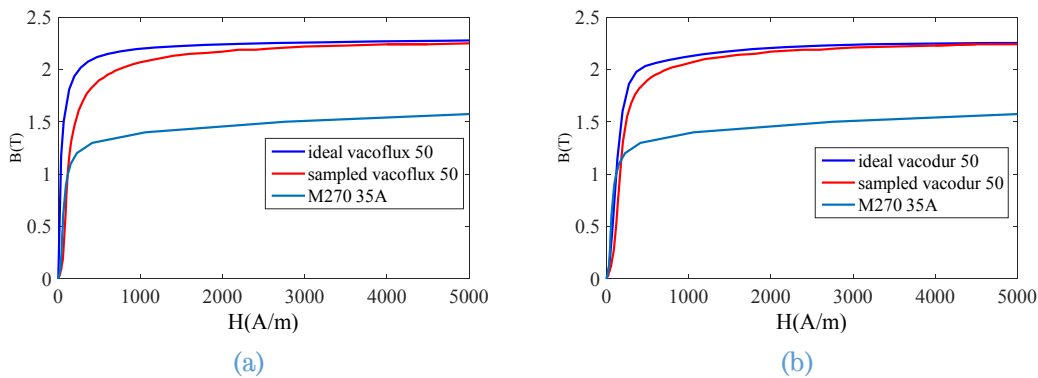
Fig. 6-12 Lamination BH curve comparison (a) Vacoflux 50 BH curve (b) Vacodur50 BH curve

Secondly, appropriate tolerances were placed on magnets and rotor core to make sure that the magnets can be inserted into the rotor cavities without much difficulty. Meanwhile the rib was also made slightly wider than the magnets. The tolerances of magnets are listed in Table 6-2 and the tolerance of the rib width is reported as positive 0.02mm for each layer. Since this machine has three layers, these accumulative tolerances have considerable influence on the machine performance, and their values are represented in the machine FE model.

Table 6-2 Magnets tolerances

Magnet dimension	Layer1	Layer2	Layer3
Designed /mm^3	28x6.94x2.05	28x12.02x2.28	28x14.88x2.80
Measured/mm^3	27.96x6.87x2.00	27.96x11.95x2.25	27.96x14.82x2.76
Percentage	96.4%	98%	98%

Hence, the resultant line back emfs with different BH curves and tolerances are calculated and compared in Fig. 6-13. The waveforms show that all the three factors have noticeable influence on the back emf. In total, the back emf is reduced by 14%.
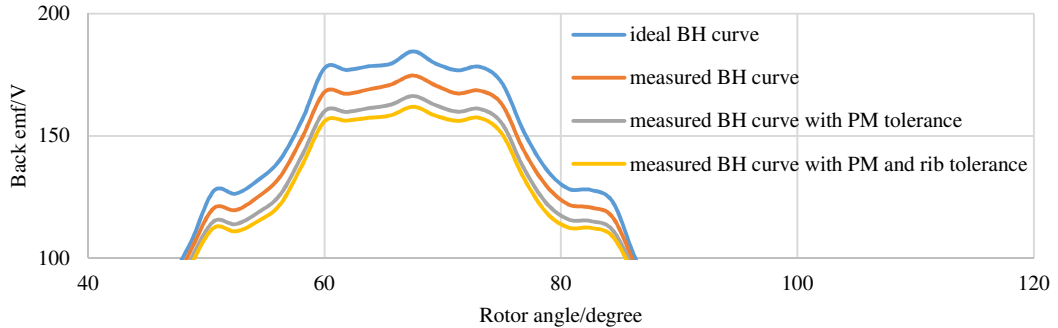
Fig. 6-13 Influence of manufacturing tolerances

Thirdly, the stator stack is skewed by 10 degrees to reduce the voltage harmonics and torque ripple due to slotting effect. The skew effect is considered according to the technique described in [150]. Here, the skewed an unskewed back emfs are compared in Fig. 6-14. Owing to the skew, the tooth harmonics of back emf has been effectively reduced. It can be expected that the harmonics in the control voltage and torque would be much smaller.
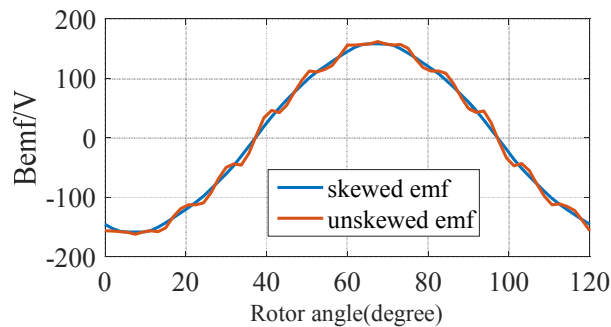
Fig. 6-14 Comparison of skewed and unskewed back emfs

6.3 No load Test

6.3.1 Insulation Test

Insulation test is performed across different sets of windings, and between the windings and the stator frame to ensure that there is no damage to insulation during potting process using Megger meter. The test shows that the insulation is qualified for the prototype machine.

6.3.2 Resistance Measurement

The terminal connections of the 9 phase PMA SynRM machine windings, configured in 3x3-phases, are illustrated in Fig. 6-15. As can be seen, two additional terminals are brought out in 3-phase set ABC for emulation of turn fault. Thus, the phase resistance of set ABC together with the resistance of fault emulation turn, shown in red in Fig. 6-15(a) can be measured via the neutral cable 'Bf-'. While for the other two sets, only the line resistance can be measured which is about two times of the phase resistance.
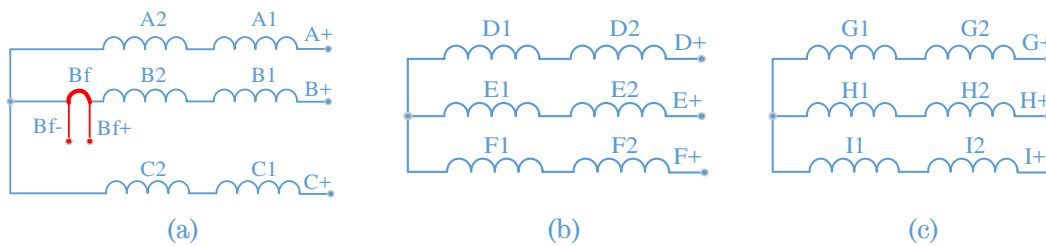
Fig. 6-15 Terminal connection of the three 3-phase sets (a) set ABC (b) set DEF (c) set GHI

The resistances of each set are measured and compared with the predicted values in Table 6-3. It is seen that in all cases, the measured resistance was 9%~12% higher than the predicted value. This may be due to inaccurate estimation of the coil length of the distributed windings and the soldering connection which contribute additional resistance. In addition, the error of sets DEF and GHI are slightly higher than those of set ABC. This could be caused by the soldering since the measurement path of the line resistance contains more soldering connections than the measurement path of the phase resistance.

Table 6-3 Resistance measurement and comparison

	Measured resistance/mΩ (including terminal cable)	Predicted resistance/mΩ (including terminal cable)
1	Set ABC	
R_A	20.8	19
R_B	21	19
R_C	20.8	19

	Measured resistance/mΩ (including terminal cable)	Predicted resistance/mΩ (including terminal cable)
R_{Bf}	2.4	2
2	**Set DEF**	
R_{DE}	40.6	36
R_{DF}	40.6	36
R_{EF}	40.7	36
3	**Set GHI**	
R_{GH}	40.7	36
R_{GI}	40.5	36
R_{HI}	40.6	36

6.3.3 Back Emf Measurement

Back emf is an important indicator of the prototype machine. According to the terminal connections in Fig. 6-15, the phase back emfs of set ABC and line back emfs of sets DEF and GHI are measured.

First, the phase back emfs of set ABC are measured at the room temperature of 20℃ from 500rpm to 12000rpm in steps of 500rpm. The peak value of the measured back emf is compared with the predicted value in Fig. 6-16. The predicted value is obtained from the refined FE model with the measured BH curves and considering all the manufacture tolerances as discussed previously. It shows that the back emf is proportional to speed and the measurements are in good agreement with predictions. According to the peak value curve, the back emf constant K_e can be identified to be 8.13mV/rpm. In addition, the measured and predicted phase back emf waveforms are plotted in Fig. 6-17. It is observed that the two waveforms match very well.

The line back emfs of sets DEF and GHI are also measured and assessed. In the 9 phase prototype machine under study, the three 3-phase sets are in phase and only the line back emf are measurable in sets DEF and GHI. Hence, the

measured line back emfs of the three 3-phase sets are compared with the prediction in Fig. 6-18. It is evident that the line back emfs of the three sets are essentially overlapped, confirming good symmetry between the three 3-phase sets. Again the measured line back emfs match well with the prediction.
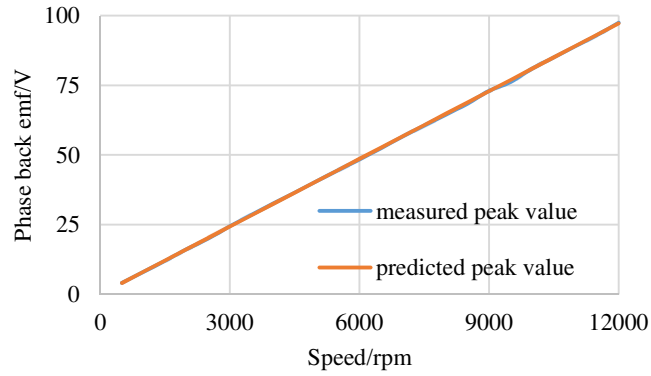
Fig. 6-16 Comparison of peak value variations of phase back emf with speed
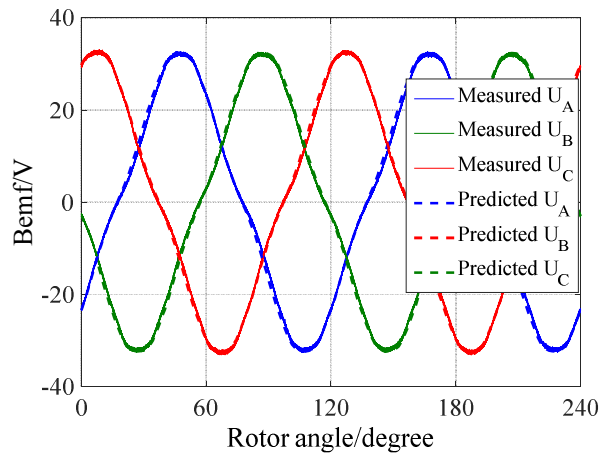
Fig. 6-17 Comparison of phase back emf waveforms at 4000rpm
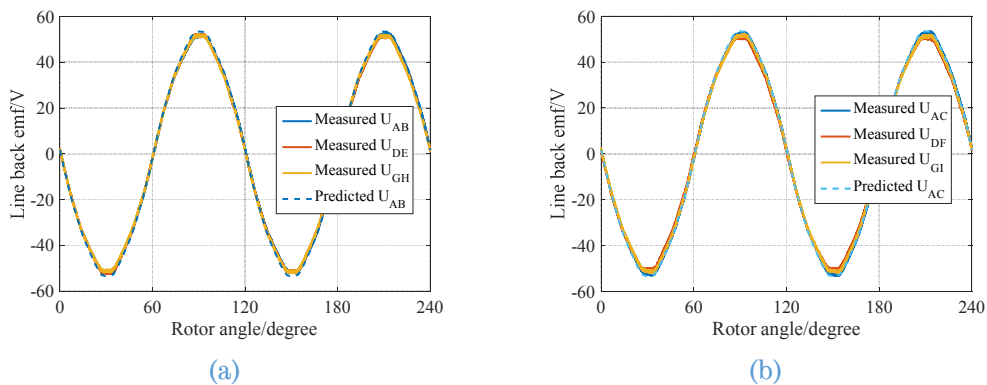
Fig. 6-18 Comparison of line back emf waveforms at 4000rpm (a) line back emf U_{AB} (b) line back emf U_{AC}

Based on Fig. 6-18, the line back emf at the maximum speed 19200rpm can be derived as 246.5V which is lower than the DC link voltage. Therefore,

uncontrolled rectifier generation will not occur even if the inverter fails. This fail-safe feature is desirable for the PM machine drives which require to operate in high speed region.

6.3.4 No load loss

No load loss is measured by rotating the prototype machine without current excitation by the AVL dyno. The no load loss mainly consists of iron loss and mechanical loss. The iron loss includes hysteresis loss, classical eddy current loss and excess eddy current loss, and can be predicted by Steinmetz's equation or Bertottie loss model. Additionally, eddy current is also induced in rotor magnets and causes eddy current loss. The mechanical loss mainly includes the bearing loss and windage loss. In practice, the mechanical loss can be measured by building a dummy rotor with the same dimension and weight by removing the magnets. Instead, the mechanical loss of this prototype machine is estimated from the machine with similar dimensions in [151] by using the technique in [152] as shown in Fig. 6-19.
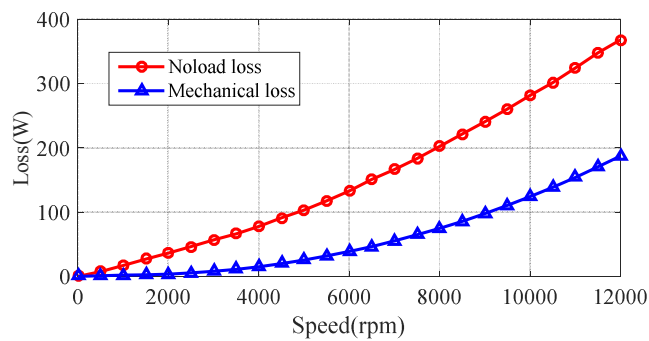
Fig. 6-19 No load loss and Mechanical loss
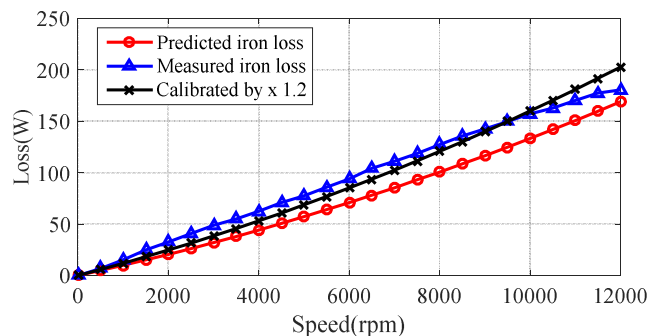
Fig. 6-20 No load iron loss variations with speed

Since the no load torque is very small, torque transducer Magtrol 308 with 20Nm measuring range is employed for high precision purpose. The no load

loss of the prototype machine is measured as shown in Fig. 6-19 up to 12000rpm. Subtracting the estimated mechanical loss from the no load loss, the no load iron loss can be obtained as shown in Fig. 6-20. Meanwhile, the iron loss is calculated in FE analysis and the results are also shown in Fig. 6-20. There is small difference between the predicted and measured iron losses which may be attributed to the manufacture process, machine assembly and limited accuracy of torque transducer. This difference can be reduced by a multiplying "built factor". It can be seen that by introducing a built factor of 1.2, the calibrated iron loss is reasonably close with the measured values.

6.3.5 Characteristic Current Measurement

The characteristic current I_{ch} is expressed by (3-6) where φ_m is the phase PM flux linkage and L_d is the d-axis inductance for each 3-phase set. It can be measured by short circuiting all three 3-phase sets.

$$I_{ch} = \varphi_m / L_d \tag{6-1}$$

The measured characteristic currents at 4000 rpm are shown in Fig. 6-21. As will be seen, the peak current is only 53.6A which is slightly lower than the prediction. The error could be attributed to the additional impedance of the terminal cables. The low characteristic current is mainly due to the low PM field. The short circuit currents do not cause any thermal risk to the machine and, therefore, terminal short circuit in one 3-phase set can be employed as a mitigation action in case of an inter turn short circuit fault in that set.
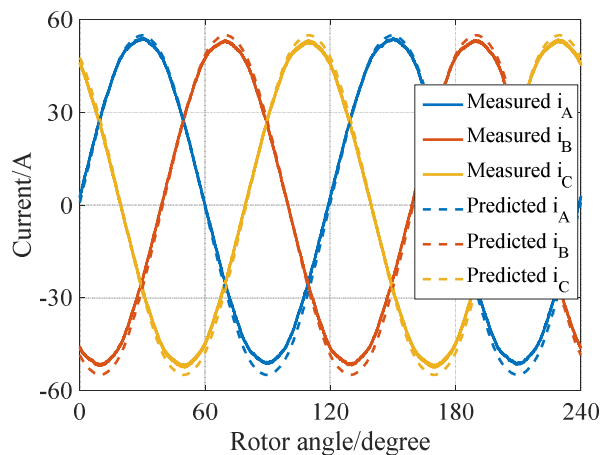
Fig. 6-21 Phase currents of set ABC at 4000rpm with three 3-phase sets short circuited

6.4 Load Test under Healthy Conditions

6.4.1 Current Control Test

Load tests are performed by driving the prototype machine using the 9 phase inverter. Now torque transducer Magtrol 312 with 200Nm measuring range is used to measure the output torque. The measured machine drive performance is compared with prediction and the results are analysed.

According to previous analysis, the triple redundant 3x3-phase machine behaviour in healthy conditions is the same as the conventional 3-phase configuration and the behaviours of the three sets are the same. So the conventional vector control is employed to control the three 3-phase inverter drives. The three inverter drive modules share the same current references from the speed controller but track them by independent current controllers as shown in Fig. 2-2. Hence, failure in one 3-phase set does not significantly affect the operation of the other sets, and each drive can response independently to accommodate the fault.

First, the current control performance of the 9 phase inverter are examined from 500rpm to 12000rpm. The typical rated phase currents of set ABC at 4000rpm are measured by a LeCroy oscilloscope as shown in Fig. 6-22. The currents are well controlled with small distortion near the peak. Switching harmonics can be seen in the waveforms. Good symmetry is also observed between the three 3-phase sets as shown in Fig. 6-23, where the data are obtained from the DSP RAM. Due to the limited current probes of the oscilloscope, the 9 phase currents are mainly measured by the inverter current sensors and stored in the DSP RAM, and consequently the switching harmonics are not visible due to limited sampling frequency and anti-alias filtering. The tests show that the phase currents are well controlled. In addition, the set ABC phase currents at 12000rpm when the machine operates in field weakening are measured as shown in Fig. 6-24, which demonstrates that the current commands are also well tracked.
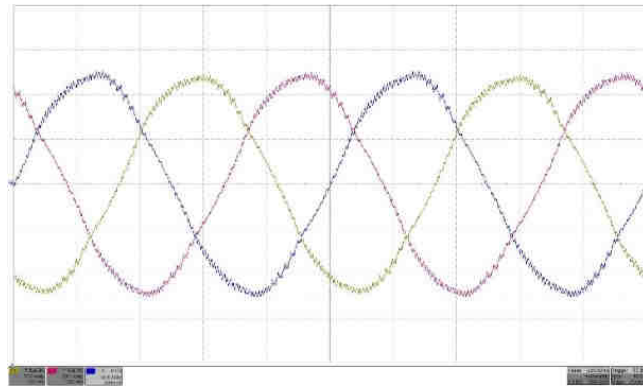
Fig. 6-22 Phase currents of set ABC at 4000rpm in healthy condition, x-axis, 1ms/div, y-axis, 50A/div, yellow, i_A, red, i_B, blue, i_C
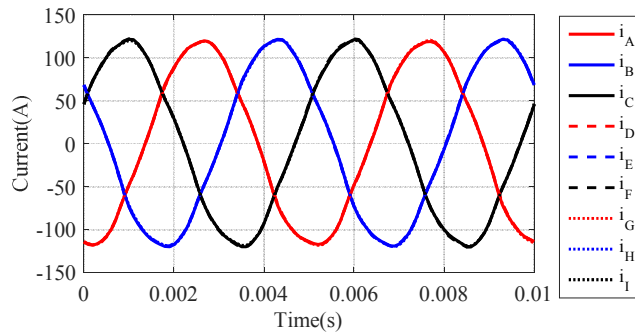
Fig. 6-23 9 phase currents at 4000rpm in healthy condition
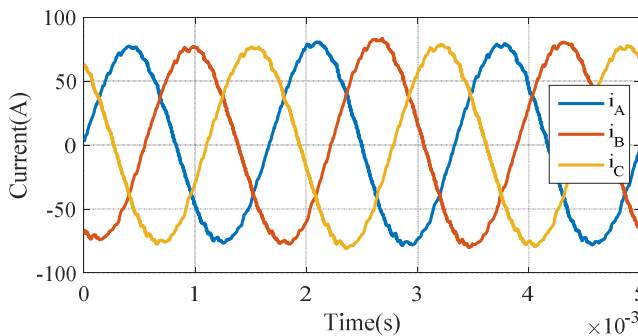
Fig. 6-24 Phase currents of set ABC at 12000rpm in healthy condition

6.4.2 Optimal Gamma Test

Optimal gamma test, or known as maximum torque per ampere (MTPA) test is performed to determine the current vector angle with respect to the q axis. As discussed previously, torque in the PMA SynRM is contributed by both PM torque and reluctance torque. Therefore, MTPA points should be identified for required torque with minimum current. For a given current magnitude, the MTPA point is determined by scanning the current vector angle with respect to the q-axis as shown in Fig. 6-25, denoted as gamma angle γ in a wide range at 500rpm. The measured torque gamma angle loci when the current

magnitude is varied from 20A to 120A is shown in Fig. 6-26. As can be seen, the optimum gamma angle increases with current magnitude (or load torque).
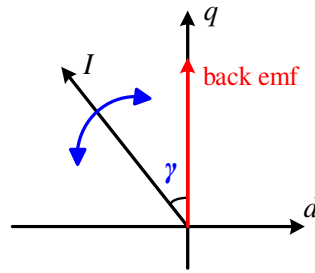
Fig. 6-25 Illustration of current vector and gamma angle γ
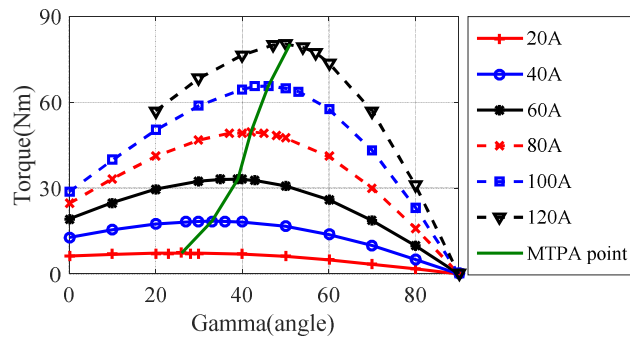
Fig. 6-26 Torque variations with current magnitude and gamma angle

Fig. 6-27 compares the measured and predicted torque variations with current under the MTPA condition. The measured torque is ~5% lower than the predicted values. This is attributed to measurement error, prediction error and frictional torque not accounted for in the prediction.

The reluctance torque ratio has been obtained using frozen permeability method as shown in Fig. 6-28 [117]. When the current magnitude is greater than 50% of the rated, the reluctance torque becomes dominant. Thus, even in an unlikely case of partial demagnetization, the machine can still output considerable torque by exploiting the reluctance torque.
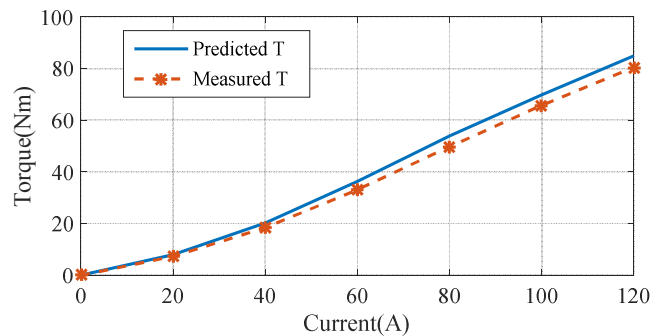
Fig. 6-27 Torque comparison in healthy condition
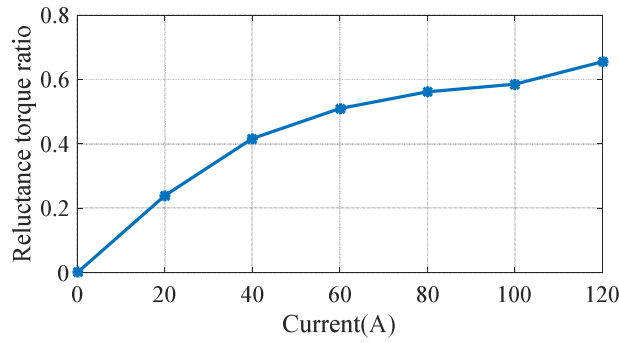
Fig. 6-28 Reluctance torque ratio against the current magnitude

6.4.3 Efficiency Measurement

The machine efficiency is measured by Yokogawa WT 3000 power analyser with high bandwidth and precision current and voltage transducers, and in-line torque transducer. Since the power analyser can only measure the electrical input power for one 3-phase set, the input powers of the three 3-phase sets are measured separately and then added together to obtain the total input power.
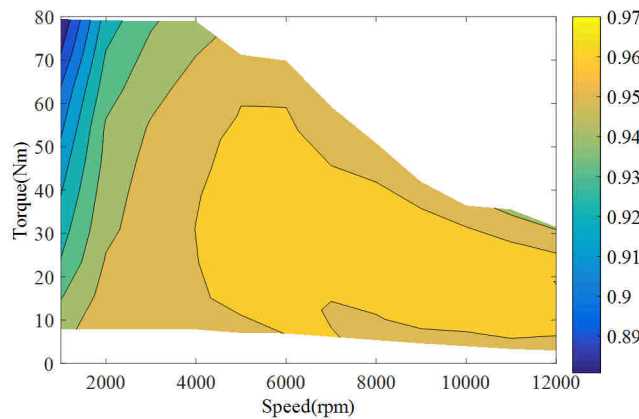
Fig. 6-29 Measured machine efficiency up to 12000rpm
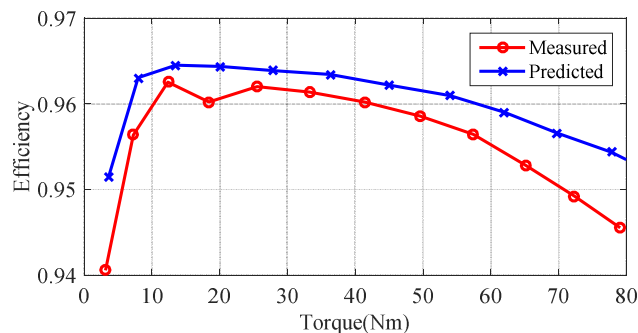
Fig. 6-30 Comparison of Test and Predicted machine efficiency at 4000rpm

The machine is tested up to the rated current 120A accounting for the thermal constraints. The machine efficiency map up to 12000rpm has been

measured as shown in Fig. 6-29. Under the base speed, the machine is operated in MTPA as determined previously while in high speed region the machine is controlled with field weakening considering the voltage limit. As can be seen that the machine efficiency is higher than 95% in most torque range. And the measured efficiency at 4000rpm is compared with the prediction in Fig. 6-30. As can be seen, the measured efficiency shows similar trends, however it is slightly lower. It can be attributed to the additional resistance due to terminal cables and soldering as shown in Table 6-3. The high efficiency is mainly due to the hybrid torque production mechanism which exploits considerable reluctance torque.

6.4.4 Thermal Test in Healthy Condition

The machine thermal behaviour affects the winding insulation degradation rate and remaining life time. The temperature rise also changes the conductivity of the copper wire considerably and influences the copper loss. Though the machine is designed for high temperature application, it is tested at 20°C ambient temperature.

Thus, the thermal test is performed by operating the machine drive in healthy condition for 2 hours. The machine is loaded with the rated current 120A at base speed with oil cooling at a flowrate of 7 litre/min. The variations of the temperatures in the oil inlet, oil outlet and windings are recorded by the thermocouples as shown in Fig. 6-31. Due to the limited capacity of the heat exchanger, the temperatures of the oil inlet and outlet increase from 24°C to 44°C and from 25°C to 57°C, respectively. Since the machine is operating in healthy condition, the temperature rise of the three 3-phase sets should be similar due to the same load current. It is noticed that the temperatures in the slots, i.e. in B1 slot, E2 slot and B2 slot where a tap for emulation of a single turn short circuit is placed, are quite close. The differences are less than 4 degrees. However, the temperature in set DEF end winding is 11 degrees higher than that of ABC set. This can be attributed to the loss caused by the neutral connection. For set ABC, the neutral is connected outside of the machine for easy access while the neutral of DEF is terminated in the end winding region.

The neutral connection is made by soldering the three phase terminals which leads to additional resistance and loss. Since the corresponding thermocouple is placed close to the neutral point of set DEF, a higher temperature rise would be expected in set DEF end winding region. If the measured copper loss is updated in the Motor_CAD thermal model, the predicted maximum temperature is 138°C which is quite close to the measurement of set ABC.
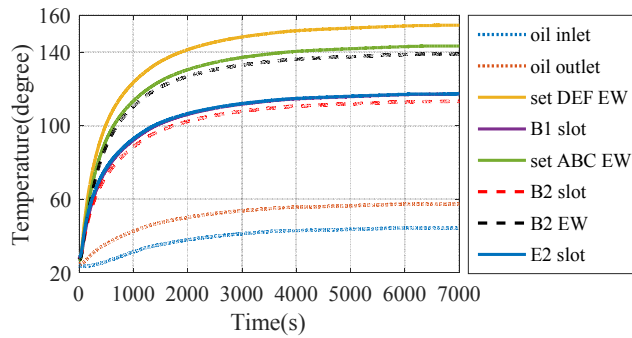
Fig. 6-31 Thermal test results with 120A at 4000rpm in healthy condition

6.5 Load Test under Fault Conditions

In this section, the machine fault behaviour and post fault torque capability are investigated for open circuit, short circuit and inter-turn short circuit fault in a wide operation range.

6.5.1 Load Test under One 3-phase Set in Open Circuit

First, the prototype drive system has been tested under one 3-phase set in open circuit. During the test, set ABC is open-circuited by switching off all the IGBTs of the inverter. Whilst the remaining 3-phase sets, DEF and GHI, are controlled by independent current controller. The reference currents are the same as in healthy condition, 120A in magnitude with 51° gamma angle. The measured currents waveforms at the base speed are shown in Fig. 6-32. As can be seen, the phase currents are no longer well-balanced, and noticeable distortion are present. These are caused by the magnetic coupling between the open-circuited set and the healthy sets, and limited current control bandwidth. The measured torque variation with current magnitude under the open circuit is compared in Fig. 6-33 with that in healthy condition. It can be seen that the machine is capable of providing 58% torque of the healthy condition.
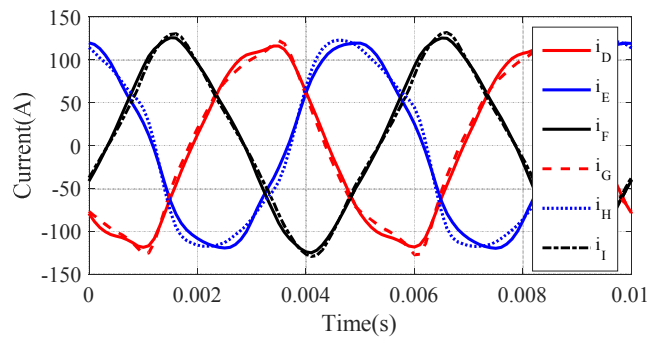
Fig. 6-32 Healthy phase currents at 4000rpm with set ABC open circuited
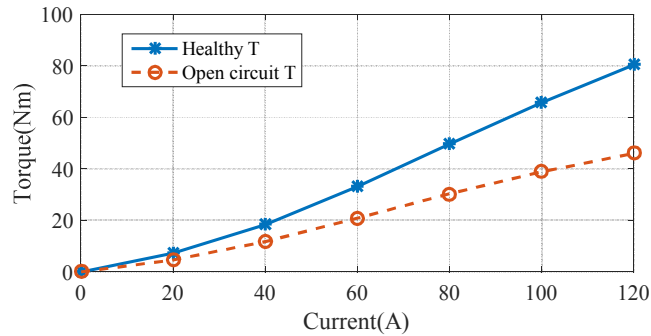
Fig. 6-33 Torque comparison with set ABC open circuited

6.5.2 Load Test under One 3-phase Set in Short Circuit

If a short circuit occurs in the inverter switches or the windings of one 3-phase set, TSC should be applied on the fault set to avoid further damage. The TSC is realized by turning on all three top or bottom switches of the respective inverter or more practically by setting the d- and q-axis voltage commands to zero in the controller. The one set short circuit mode is tested by short circuiting set ABC while the current excitations in the healthy sets DEF and GHI are varied from 20A to 120A at 4000rpm. The resultant torque variation is shown in Fig. 6-34 together with those under healthy conditions. The torque capability is slightly higher than that of the open circuit mode. It is noticed that the machine exhibits a small braking torque with zero current in the two healthy sets.

The induced short circuit currents in set ABC when the two healthy sets are excited with 120A current are shown in Fig. 6-35. It is seen that the phase currents are highly unbalanced due to the mutual magnetic coupling between the three 3-phase sets. The root-mean-square (RMS) current in phase A is much lower than those in phases B and C. Nevertheless, due to the low PM field, the RMS values of the short circuit currents are much lower than the rated. Hence

the machine drive can sustain the short circuit fault without any thermal risk. Fig. 6-36 shows the phase currents in the healthy 3-phase sets where small unbalance and distortion are also observed.
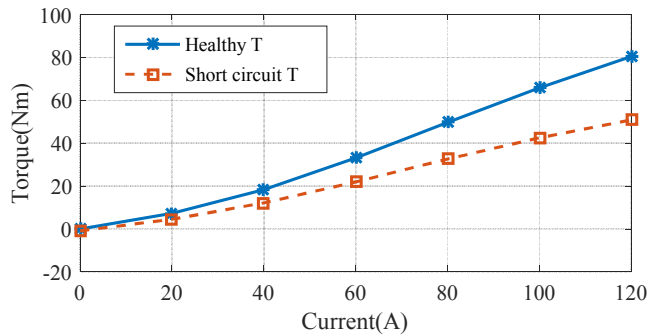
Fig. 6-34 Torque comparison with set ABC short circuited
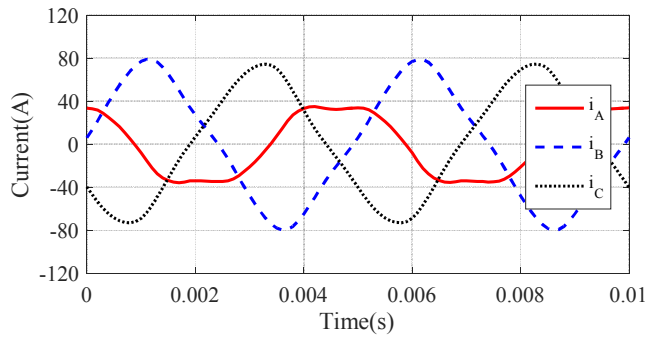
Fig. 6-35 Short circuit phase currents at 4000rpm
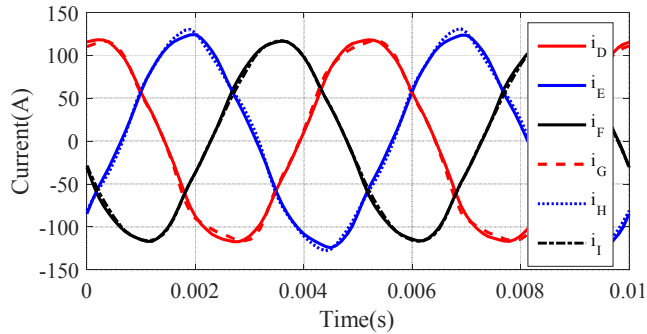
Fig. 6-36 Healthy phase currents at 4000rpm with set ABC short circuited

The torque ripples with the rated current of 120A at 500rpm under healthy, open-circuit and short circuit conditions are measured, and the results are shown in Fig. 6-37. In healthy condition, the torque waveform is quite flat and torque ripple is low due to the stator skew. In open circuit and short circuit conditions noticeable 2nd harmonics appear which can be attributed to their mutual magnetic coupling and imperfect current excitations in the three 3-phase sets. The torque ripple is slight higher in open circuit condition and the peak-to-peak variation is 5Nm, or 6% of the rated.
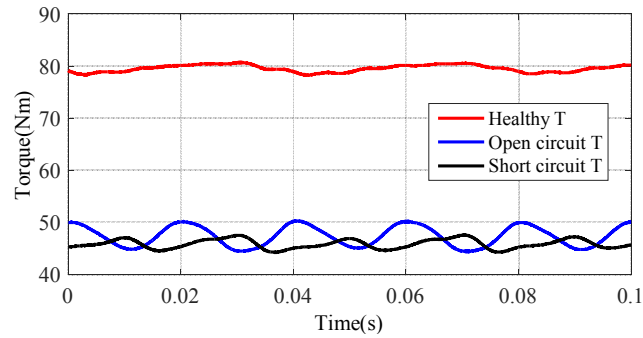
Fig. 6-37 Torque waveform in healthy, set ABC open circuited, set ABC short circuited condition at 500rpm

6.5.3 Inter-turn Short Circuit Test without Terminal Short Circuit

Inter-turn short circuit fault is known as the worst fault scenario since only a few turns are involved in the short circuited path. Significantly large current is induced in the fault turn due to the low impedance. The fault is caused by insulation break down and it accounts for a large percentage of faults in electric machines [62, 100]. Thus, inter-turn short circuit fault should be carefully emulated, detected and mitigated. For the machine under study, the inter-turn fault can be accommodated by application of TSC on the faulty 3-phase set to nullify the flux in the fault turns. Consequently the fault current is reduced to a much lower and sustainable value.

The turn fault may occur in the 6 different coils as shown in Fig. 2-2. According to the investigation in Chapter 2, the fault current after TSC is different if it takes place in different coil locations. After TSC in motoring mode the fault current is the largest if a single turn fault occurs in coil B2 while in generating mode the fault current is the highest if the fault takes place in coil A1.

First, the inter-turn fault is tested in coil B2 without TSC when the machine rotates anti-clockwise. In order to avoid the damage due to excessive fault current, the turn fault is tested at 1000rpm when all 3-phase sets are excited with 80A load current by closing the relay for 0.2s. The induced turn fault current reaches 440A as shown in Fig. 6-38. The turn fault is also tested with variation of load currents from 10A to 80A at 1000rpm in both motoring and generating mode. The measured variation of the RMS fault current with the

load currents are plotted in Fig. 6-39. As can be seen, the RMS fault current under two modes are similar and both increases with load currents.
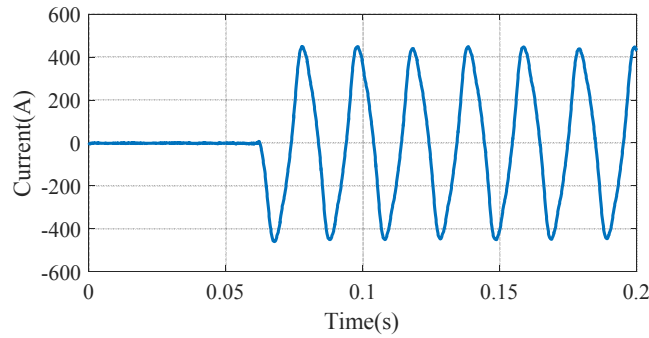
Fig. 6-38 Turn fault current with 80A load current at 1000rpm
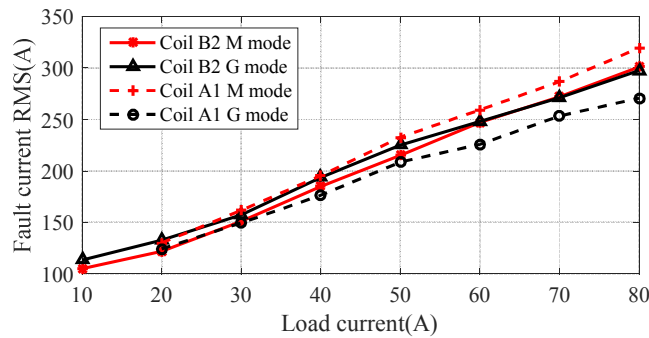
Fig. 6-39 Turn fault current in coil B2 and A1 variations at 1000rpm in motoring and generating mode

Similar turn fault tests are performed in coil A1 by rotating clockwise. The measured variations of the RMS fault current of both operation modes are plotted in Fig. 6-39. They also increase with load current however the difference between the motoring and generating mode is slightly larger. It is worth noting that the fault current will be even higher if the load current or speed increases. Therefore, mitigation action is essential to reduce the large fault current in real operation.

6.5.4 Inter-turn Short Circuit Test with Terminal Short Circuit

The turn fault is also tested with TSC. Application of TSC can reduce the turn fault current effectively. Thus, the fault can be tested at 4000rpm with 120A currents in healthy 3-phase sets. Fig. 6-40 demonstrates that the fault current has been reduced to about 220A. The phase currents in the faulted 3-phase set are similar to that of one set terminal short circuit as shown in Fig.

6-35, whilst the currents in the healthy sets are still well controlled as shown in Fig. 6-41. This allows for continued operation with reduced torque/power.
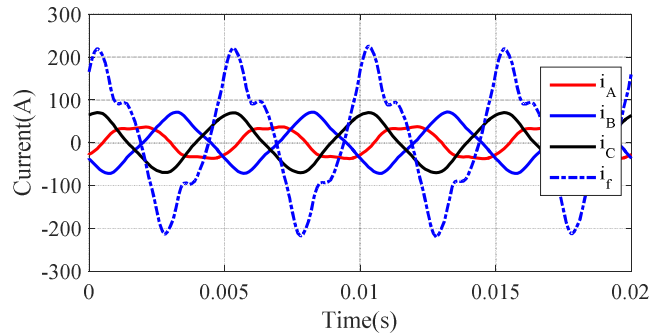
Fig. 6-40 Turn fault current and phase currents with 120A load current at 4000rpm in motoring mode
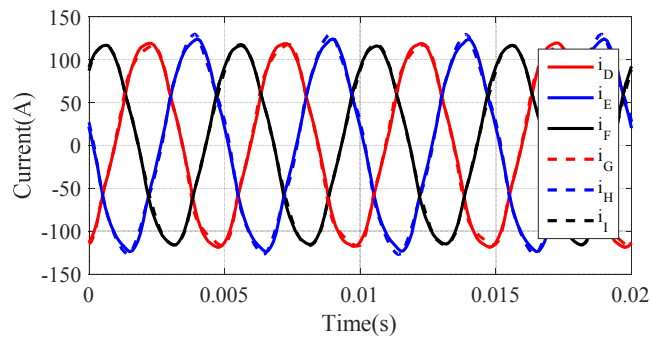
Fig. 6-41 Healthy phase currents with turn fault in coil B2 when load current is set to 120A in motoring mode at 4000rpm after TSC
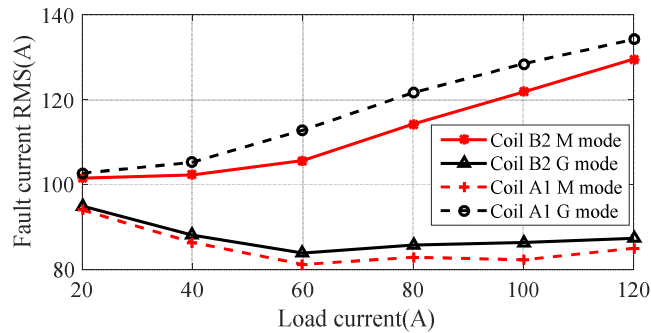
Fig. 6-42 Turn fault current in coil B2 and A1 variation at 4000rpm in motoring and generating mode after TSC

The turn fault with TSC is also tested with variation of currents in the healthy sets from 20A to 120A for emulated turn faults in coil B2 and A1 in both motoring and generating modes, respectively. As will be seen in Fig. 6-42, the fault current in coil B2 is higher than that in coil A1 in motoring mode while the opposite is true in generation mode. These results are consistent with the findings in Chapter 2 [115]. In motoring mode the worst case is determined as a single turn fault in coil B2 when the other healthy 3-phase sets are excited with the rated current. Similar conclusion can be made for

generating mode. It should be noted that after TSC the machine can still output about 2/3 of the torque as that of one set short circuit mode as shown in Fig. 6-34.

6.5.5 Thermal Test under Turn Fault Condition after Terminal Short Circuit

The fault tolerant capability is further examined by measuring the temperature rise under the worst fault scenario in motoring mode. The test is performed by operating the machine for 2 hours with a single turn fault in coil B2 after application of TSC while the remaining two healthy 3-phase sets are loaded with 120A currents. The recorded temperatures in various parts of the machine are shown in Fig. 6-43. As will be seen, the temperatures in the slot and end winding part where the fault turn is located are lower than those in the DEF windings although the fault current is 1.5pu. The temperatures of coil B1 and in the ABC end winding are also lower than those of the DEF windings. Comparing Fig. 6-31 and Fig. 6-43, it is observed that the temperatures of the DEF windings are even lower than that of the healthy condition. This is because the short circuit phase currents in set ABC are much lower than 120A. Thus, the resultant thermal loading and temperature rises are lower than those under the healthy condition. The tests above confirm that the machine drive can sustain the worst turn fault by TSC with about 1/3 torque reduction without any thermal risk.
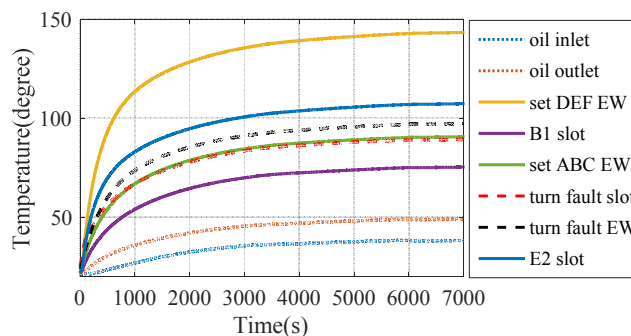
Fig. 6-43 Thermal test results under single turn fault in coil B2 with 120A at 4000rpm in motoring mode after TSC

It should be noted that other faults, like mechanical failure, demagnetization fault, inter-phase turn fault and DC capacitor failure, may also occur in the machine drive which are not tested. Mechanical failure,

including the bearing failure, rotor broken, are usually considered by regular maintenance and replacement. Demagnetization under worst fault conditions has been fully analyzed using the techniques reported in [47, 121]. It has been shown that no demagnetization will take place under any inter-turn short circuit and terminal short circuit conditions. This is because although inter-turn fault current can be many times of the rated, it flows in a few turns, and its overall effect on the magnets which are partly protected by the rotor core is insignificant. As mentioned earlier, the PMA SynRM mainly relies on the reluctance torque. Hence the machine drive can still output considerable torque even if an unlikely demagnetization fault occurs. The inter-phase turn fault is not tested since it is less severe than the single turn intra-phase fault as discussed in Chapter 2. The winding connection has followed those shown in Fig. 2-25 to avoid undesirable inter-phase fault and insulation paper has been inserted between the end windings to enhance the phase insulation. The DC capacitor failure is also not tested. Obviously, it can be sustained by the triple redundant machine drive with appropriate condition monitoring technique in place.

6.6 General Model Validation

In this section, the general model established in Chapter 4 is validated in healthy and various fault conditions, including the open circuit, short circuit, unequal current operation, inter-turn short circuit fault with and without TSC. The accuracy is examined by comparing the measurements with the model predicted values.

6.6.1 Healthy Condition

First the machine is tested in healthy mode with each set fed with 80A currents under the MTPA operating condition. The test results are compared with the model prediction in Fig. 6-44 and Fig. 6-45. The measured currents match well with the predicted results. The predicted voltages are quite close to the test results, though, with small error and less harmonics. It should be noted that the test dq voltages are the control reference voltages in the DSP.

Therefore, they are slightly different from the real voltages applied to the motor.
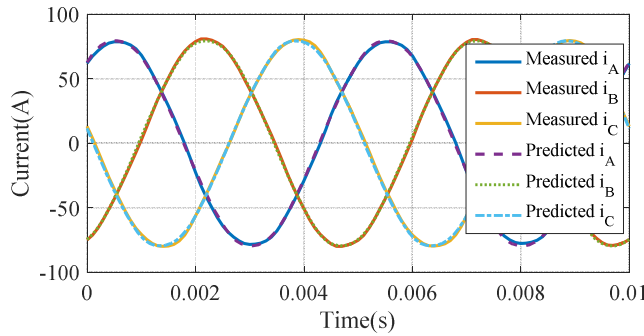
Fig. 6-44 Comparison of measured and predicted currents in in healthy mode
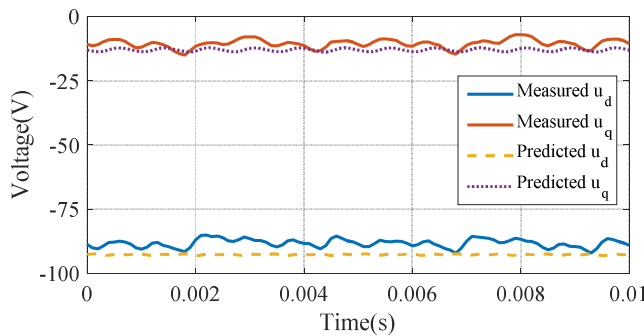
Fig. 6-45 Comparison of measured and predicted voltages in in healthy mode
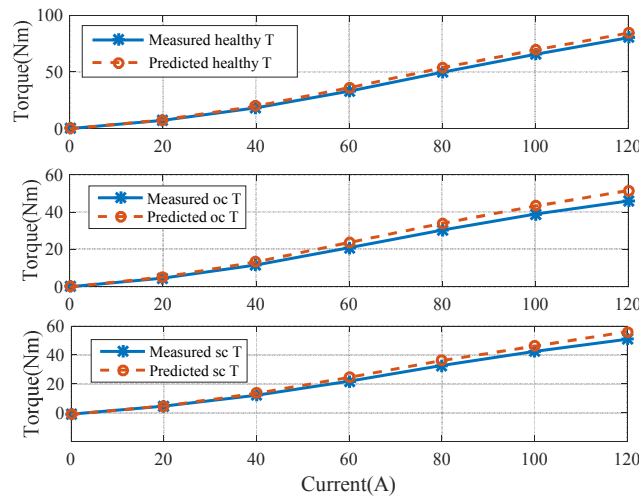
Fig. 6-46 Comparison of measured and predicted torque in in healthy, open circuit, short circuit conditions

As shown in the top graph of Fig. 6-46, the average torque predictions are compared with measurements in healthy condition when the magnitude of phase current is varied from 0 to 120A in MTPA condition. It is shown that the measured torque is a few percent lower than prediction. According to the simulation validation in Chapter 4, the flux linkages and torque predictions match well with FE calculations. Thus the torque error is mainly caused by

the inaccuracy of the 2D FE model as well as neglecting the frictional and windage torque in the model. Since the lookup tables are generated based on the FE model, similar error would be expected in other operation conditions.

6.6.2 One Set Open Circuit

The machine drive is tested when set ABC is open circuited by switching off all the respective IGBTs. Set DEF and GHI are still excited with 80A currents. The measured results for set DEF are compared with the predictions in Fig. 6-47 and Fig. 6-48. Similar behaviours of set GHI are observed but are not shown. In the open circuit mode, the phase currents in DEF set are no longer balanced with noticeable distortion due to insufficient control bandwidth. These unbalance and distortions are well captured by the model with small deviation from the measured current waveforms. The control voltages are also close to the prediction in which the induced 2nd harmonics in the dq voltages are captured.

Though set ABC is open circuited, the currents in other two healthy sets still generates torque for continued operation. The measured torque is compared with the model prediction in the middle graph of Fig. 6-46 and it is a few percent lower than the prediction. The difference may be caused by errors in the FE model and current prediction as well as neglecting friction and windage torque in the prediction.
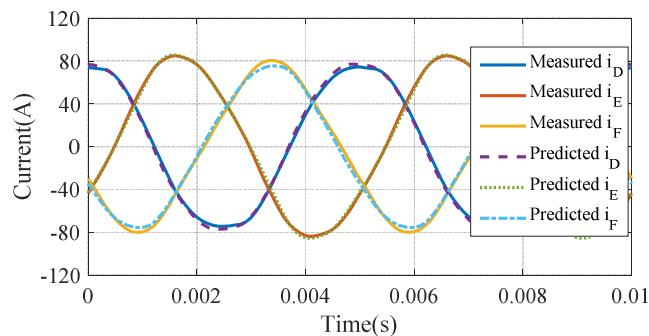
Fig. 6-47 Comparison of measured and predicted currents in open circuit mode
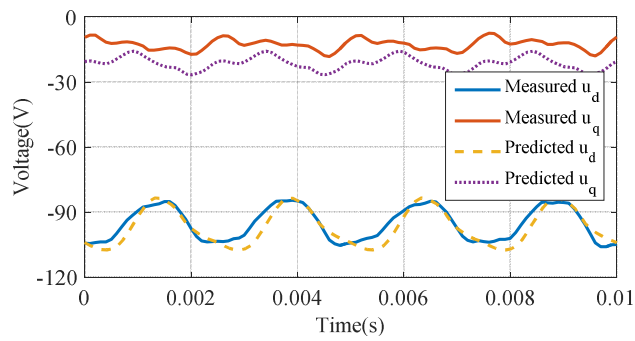
Fig. 6-48 Comparison of measured and predicted voltages in open circuit mode

6.6.3 One Set Short Circuit

The machine is also tested with one set short circuit. Set ABC is short circuited by setting the *d-* and *q*-axis voltage commands to zero in the controller while set DEF and GHI are still excited with healthy currents as previously stated. First, the measured and predicted short circuit currents in set ABC are compared in Fig. 6-49. It is seen that the model has captured the main shapes of the unequal phase currents, being slightly higher than the measurements. The error could be attributed to the additional impedance of the cable leads and the voltage drops on the switches. Again, the measured currents and voltages of the healthy sets are very close to the predictions in Fig. 6-50 and Fig. 6-51.

The short circuit currents in set ABC do not contribute to the torque whilst the currents in other two sets still generates torque. The measured torque is compared with the model prediction in the bottom graph of Fig. 6-46 with different load currents. The difference in a few percent is also attributable to the modelling error and neglect of friction and windage torque in the prediction.
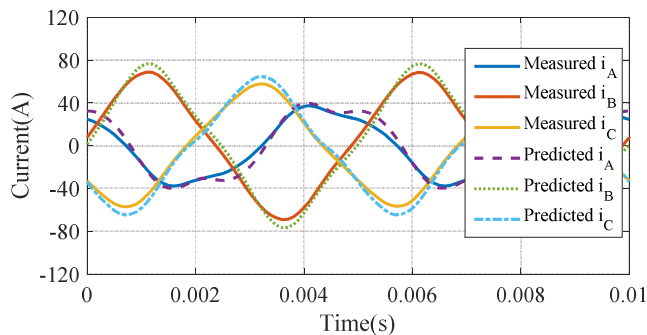
Fig. 6-49 Comparison of measured and predicted short circuit currents
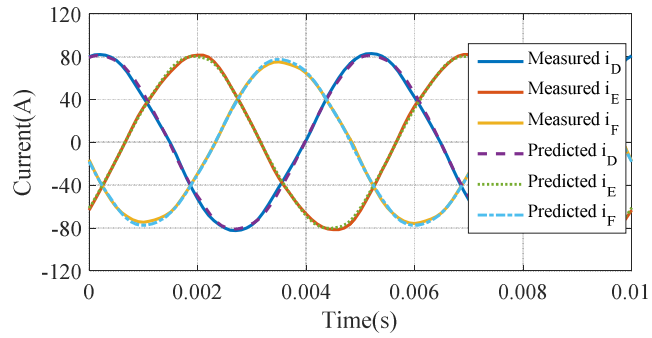
Fig. 6-50 Comparison of measured and predicted currents in healthy DEF set when set ABC in short circuit mode
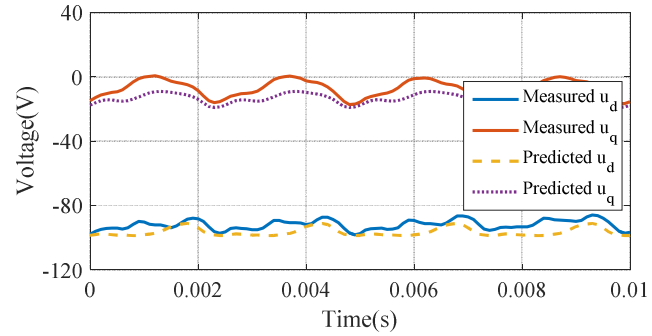
Fig. 6-51 Comparison of measured and predicted voltages in heathy DEF set when set ABC in short circuit mode

6.6.4 Unequal Current Operation

In addition the machine drive is tested under unequal current operation. While this operation is not preferred in healthy conditions, small difference in phase currents may arise due to the disparity in current sensors, inverters and three 3-phase windings. Set ABC is fed with 100A, while set DEF and GHI are fed with 80A and 60A, respectively. The measured and predicted currents and voltages of set ABC are compared in Fig. 6-52 and Fig. 6-53 while the results of other two sets are similar and omitted. The results show that the behaviour under this mode is also well represented by the model albeit mismatches in high order harmonics exist.
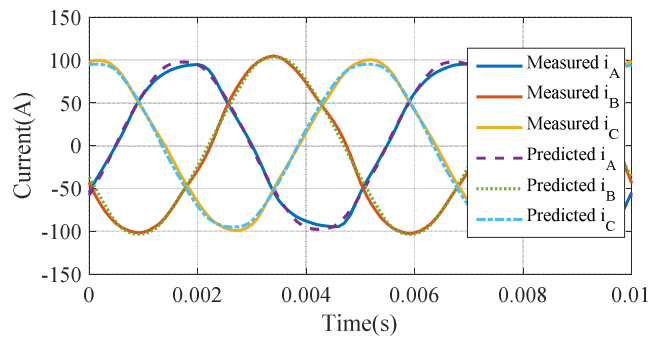
Fig. 6-52 Comparison of measured and predicted phase currents in set ABC under unequal currents operation
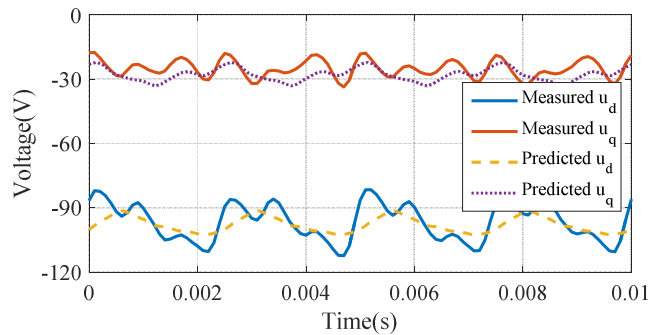
Fig. 6-53 Comparison of measured and predicted voltages under unequal currents operation

6.6.5 Stator Turn Fault without Terminal Short Circuit

According to previous investigation, the turn fault current without TSC is massive at the rated operation point. It is therefore important to investigate experimentally if the developed fault model can predict the fault current with reasonably accuracy. To avoid any potential damage, a single turn short circuit in coil B2 was tested at 2000rpm while all three sets were excited with 50A. The STF was triggered by closing the relay for 0.3s. The measured turn fault current matched well with model prediction as shown in Fig. 6-54. During the test, the fault set was still excited by the 3-phase inverter. The measured phase currents and voltages are compared with the predictions in Fig. 6-55 and Fig. 6-56. Due to the STF, the phase currents are slightly distorted and this distortion is captured by the model prediction. There are small error in the predicted voltages since they are obtained from the DSP reference voltages. Similarly, the currents and voltages of the healthy sets are compared in Fig. 6-57 and Fig. 6-58, which also show high accuracy. The currents and voltages of set DEF and set GHI are similar, thus only the results of set DEF are given.

The STF is also tested with different currents in healthy sets from 10A to 50A at 2000rpm. The RMS value of the fault current is compared with the model prediction in Fig. 6-59. It shows the model is capable of predicting the fault currents under different operation currents with good accuracy.
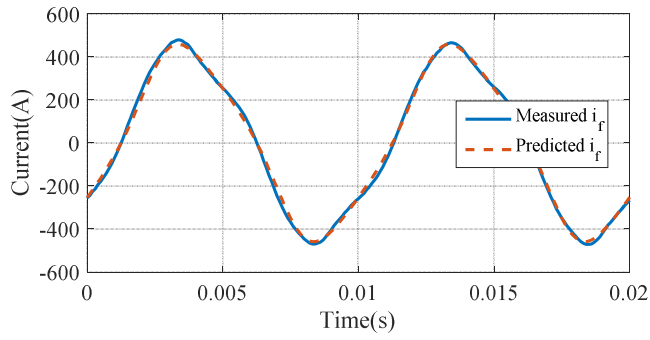
Fig. 6-54 Comparison of measured and predicted turn fault current with STF in B2 coil
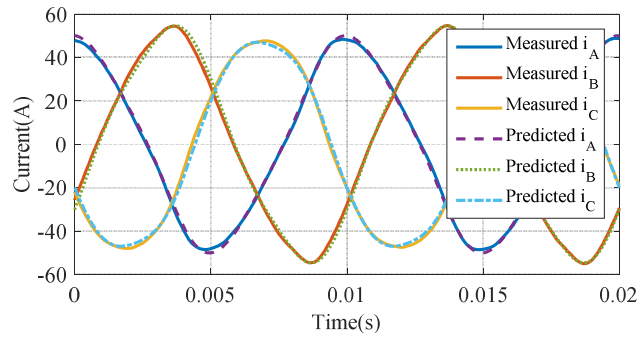
Fig. 6-55 Comparison of measured and predicted phase currents in fault set with STF in B2 coil
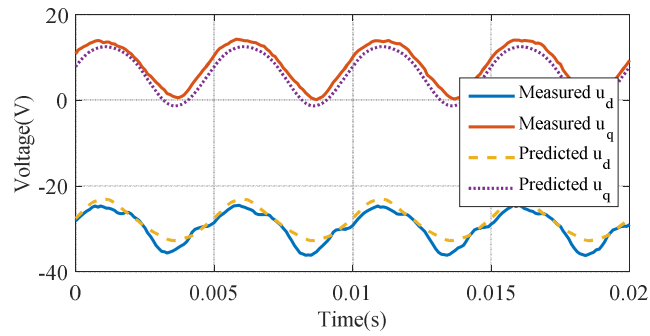
Fig. 6-56 Comparison of command and predicted *dq* axes voltages in fault 3-phase set with STF in B2 coil
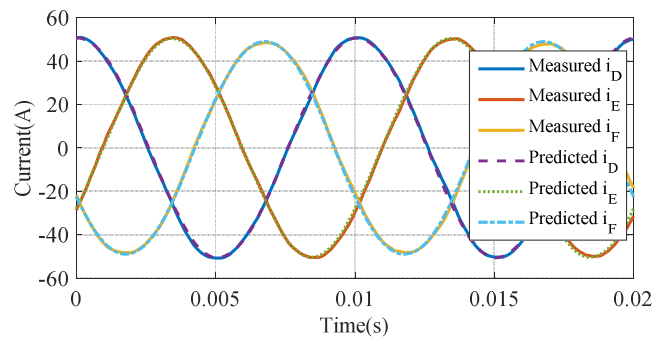
Fig. 6-57 Comparison of measured and predicated phase currents in healthy DEF set currents when a STF occurs in B2 coil
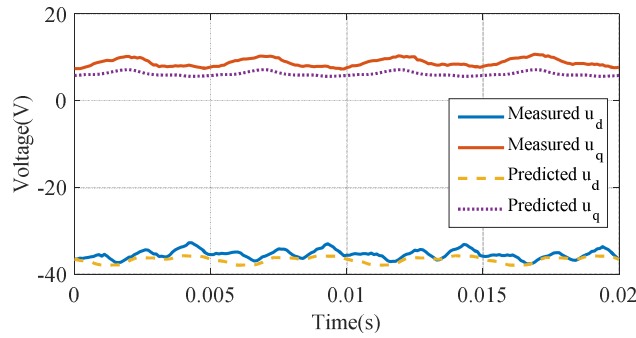
Fig. 6-58 Comparison of command and predicted dq axes voltages in healthy DEF set voltages with STF in B2 coil
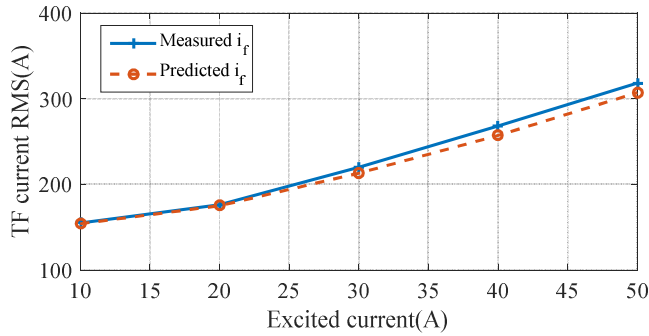
Fig. 6-59 Turn fault current variation with phase currents with STF in B2 coil

The STF behaviour in coil A1 is also tested by rotating the rotor in reversed direction. The measured and predicted fault currents are compared in Fig. 6-60 and Fig. 6-61. The results show the fault currents are also well predicted in different coil locations.
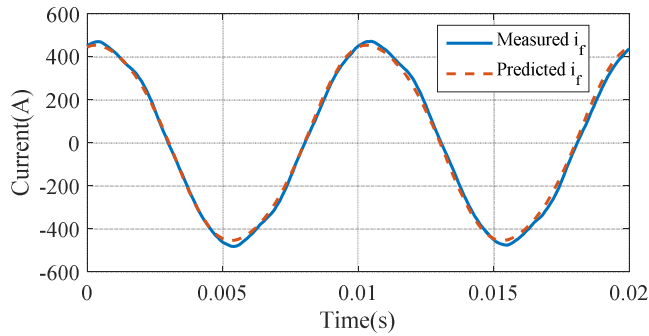
Fig. 6-60 Turn fault current with STF in A1 coil
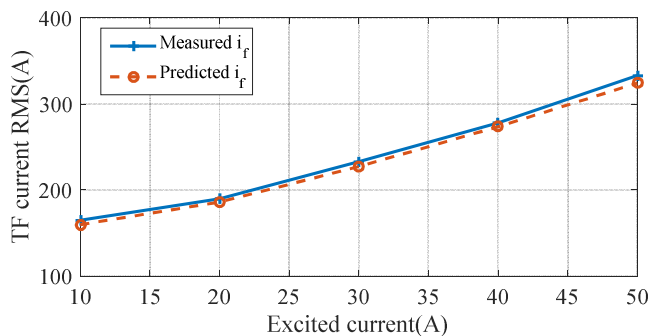
Fig. 6-61 Turn fault current variation with phase currents with STF in A1 coil

6.6.6 Stator Turn Fault with Terminal Short Circuit

The STF will be mitigated by terminal short circuit and the resultant behaviour has also been measured with applying the TSC. After applying TSC to the ABC set, the turn fault current is reduced to a much lower value. Thus, the STF could be tested at 4000rpm with 120A in healthy sets. The measured and predicted fault current is compared in Fig. 6-62. The measured waveform is similar to the FE prediction in Fig. 4-25, however with lower magnitude due to the additional impedance. There is some error of the model prediction near the peak point which may be caused by the inaccurate prediction of phase currents as shown in Fig. 6-63. However, the RMS values of the measure and predicted waveforms are quite close and this is important for thermal analysis. Meanwhile, the currents and voltages of the healthy sets are also well predicted as is evident in Fig. 6-64 and Fig. 6-65. The measured and predicted variations of RMS turn fault current with currents in healthy sets are compared in Fig. 6-66 where it is seen that the maximum error is less than 10%. STF test is also performed in coil A1 with TSC by rotating clockwise in motoring mode. The measured and predicted current behaviours are compared in Fig. 6-67 and Fig. 6-68 which show similar accuracy.
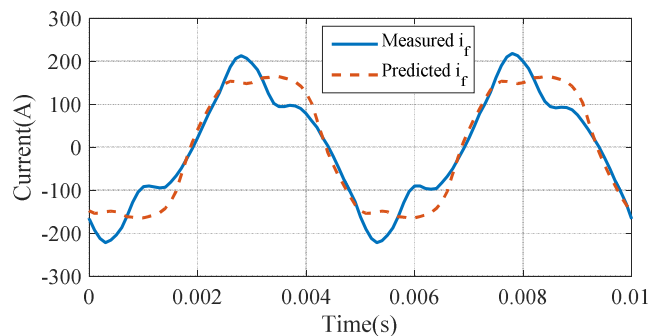
Fig. 6-62 Turn fault current with STF in B2 coil with TSC
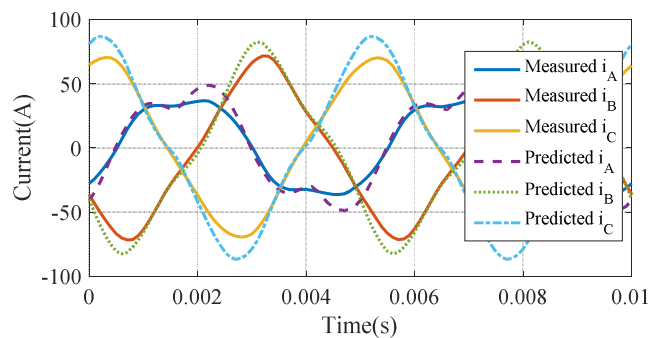
Fig. 6-63 Short circuit phase currents with STF in B2 coil with TSC
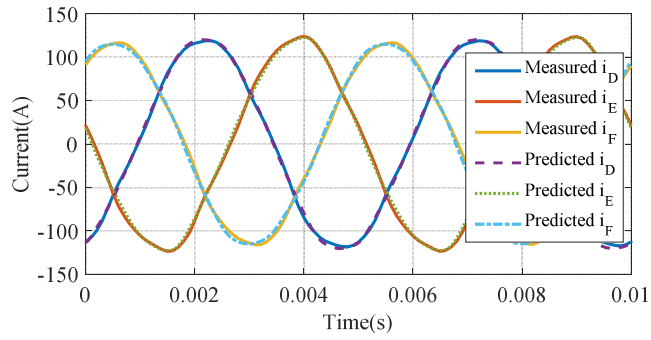
Fig. 6-64 Healthy set currents with STF in B2 coil with TSC
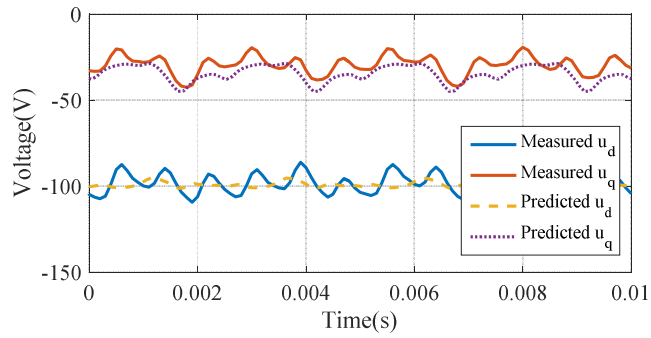
Fig. 6-65 Healthy set voltages with STF in B2 coil with TSC
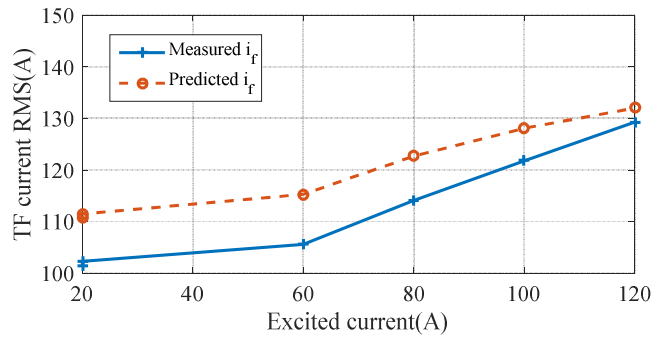
Fig. 6-66 Turn fault current variation with phase currents with STF in B2 coil
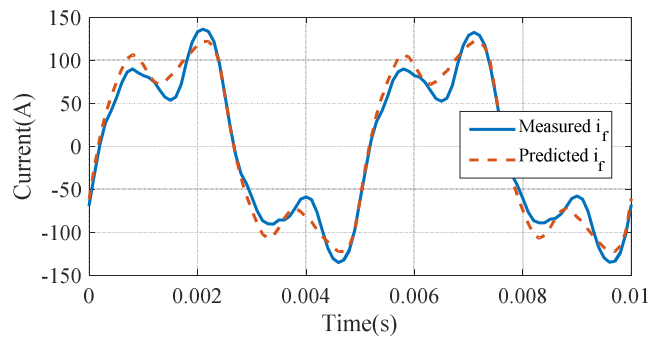
Fig. 6-67 Turn fault current with STF in A1 coil
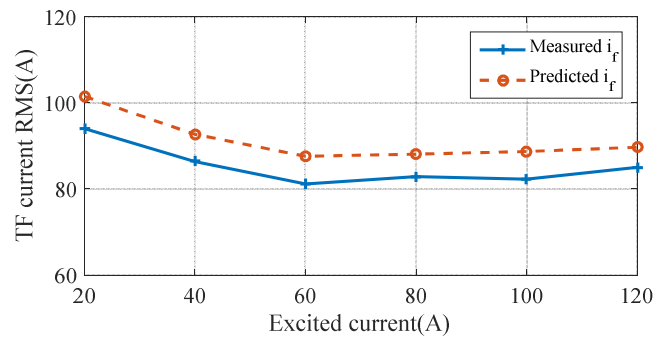
Fig. 6-68 Turn fault current variation with phase currents with STF in A1 coil

6.7 Validation of Fault Detection Algorithm

In this section, the 2nd harmonic based turn fault detection proposed in Chapter 5 is verified in a wide operation range including the transient process. The fault behaviours, including the fault current, dq currents and voltages, and the fault indicators, viz. 2nd harmonics in IAP and IRP, are presented.

To demonstrate the developed fault detection and fault mitigation techniques, an integrated test including the healthy operation, fault injection and fault mitigation is also performed.

6.7.1 Typical Turn Fault Behaviour

Due to the excessive fault current, the turn fault is also tested at low speed to minimize the risk of damage. This does not result in loss of generality as low speed is also the most challenging region for detection. First, the turn fault is injected at 0.06s when the drive operated at 1000rpm with 100A load current and MTPA angle $\gamma = 46°$ in motoring mode. The peak turn fault current shown in Fig. 6-69 reaches 480A or 4pu. The measured dq currents, i_{dq}, and the resultant dq control voltages, u_{dq}, are shown in Fig. 6-70 and Fig. 6-71, where the subscripts 1, 2 and 3 denote the quantities for sets ABC, DEF and GHI, respectively. The IAP and IRP are calculated as shown in Fig. 6-72. In healthy condition when $t < 0.06$s, the currents, voltages, IAP and IRP signals are similar for the three 3-phase sets. After the turn fault, the drive continues to operate by the current feedback control. However, noticeable harmonics appear in all signals, and the dominant is clearly the 2nd harmonic. It can be observed that the amplitudes of 2nd harmonic in voltages and currents are relatively small, only a few volts or amperes. In contrast, the 2nd harmonic in

IAP and IRP are significantly higher resulting in high signal-to-noise ratio. In agreement with the analysis in Chapter 5, the 2nd harmonic in IRP is significantly higher than that of IAP. Therefore, the 2nd harmonic in IRP, q_2, should be chosen as the fault indicator in motoring mode. The extracted 2nd harmonics in IRP for three 3-phase sets are shown in Fig. 6-73. As can be seen, in the healthy condition, q_2^1, q_2^2 and q_2^3 are very small though slightly different due to inherent asymmetries. After the turn fault, q_2^1 increases significantly, whilst q_2^2 and q_2^3 only change slightly in opposite directions. According to the fault judging criteria in (5-12), the fault detection is accurately detected.
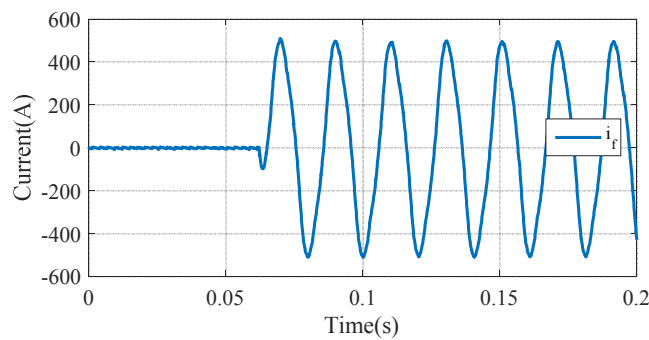
Fig. 6-69 Turn fault current when the drive operates at 1000rpm and 100A
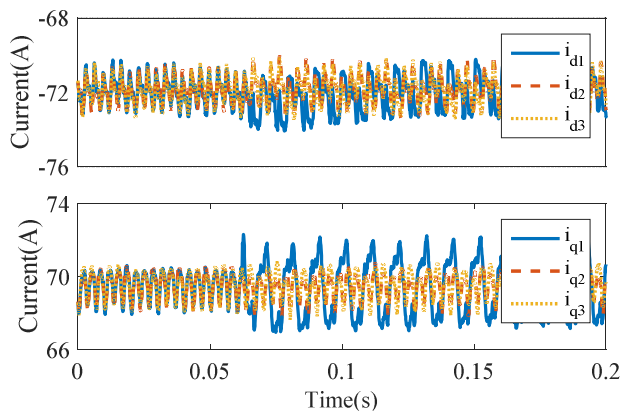
Fig. 6-70 Measured dq currents before and after turn fault
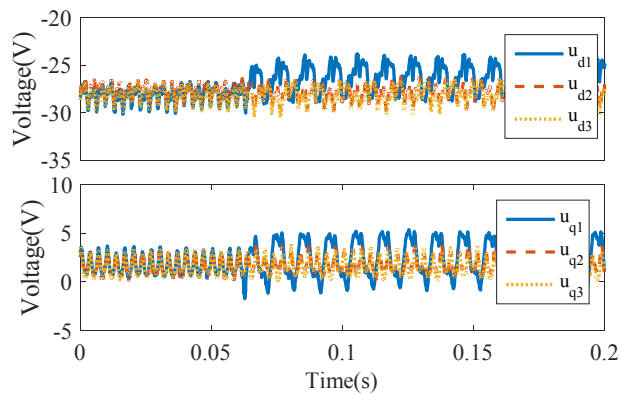
Fig. 6-71 dq control voltages before and after turn fault
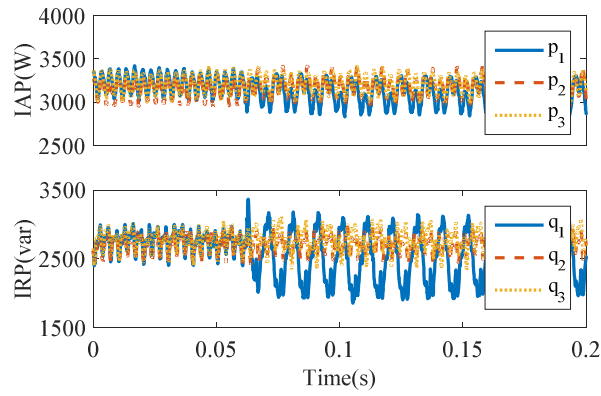
Fig. 6-72 IAP and IRP before and after turn fault
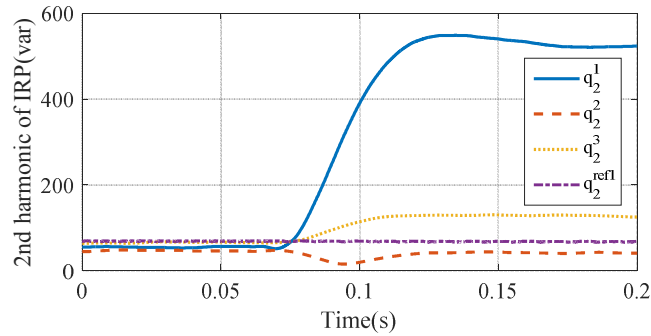
Fig. 6-73 2nd harmonics of IRP before and after turn fault

Further tests are conducted at 1000rpm with 100A in generating mode. The currents and voltages responses are similar, hence only the IAP and IRP are plotted in Fig. 6-74. Different from the motoring mode, now the 2nd harmonic in IAP becomes higher than that of IRP confirming the foregoing analysis. Therefore, in generating mode, the 2nd harmonic of IAP is employed as fault indicator. The processed 2nd harmonics of IAP is shown in Fig. 6-75. The behaviour is similar to that in Fig. 6-73, hence the turn fault can also be detected reliably.
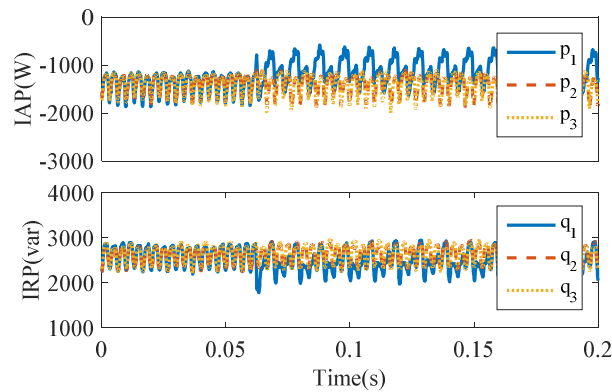
Fig. 6-74 IAP and IRP before and after turn fault in generating mode
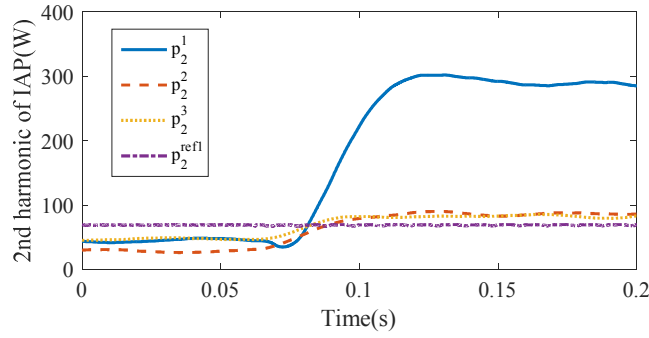
Fig. 6-75 2nd harmonics of IAP before and after turn fault in generating mode

6.7.2 Detectability over the Whole Operating Region

An important criterion for fault detection is its detection zone over the torque-speed operating range of the drive. According to Fig. 5-4, it can be concluded that the most difficult region for the detection is at low speed where the 2nd harmonics in IAP and IRP is quite low. Hence, in addition to the test at 1000 rpm, the proposed detection algorithm is also tested at 500rpm. The ratios of the 2nd harmonic in IRP and IAP, defined as:

$$Ratio = q_2^1/q_2^{ref1} \quad \text{motoring mode}$$

$$Ratio = p_2^1/p_2^{ref1} \quad \text{generating mode}$$

have been measured in a number of operating conditions in order to evaluate the detectability based on the proposed criteria. It should be noted that the reference signals have been captured in a pre-operation up to 4000rpm and stored in the lookup tables. The results, shown in Fig. 6-76, demonstrate that in motoring mode, the ratio is always greater than 2, therefore, the turn fault can be detected in all tested conditions. As expected, the detectability ratio increases with the speed. In generating mode, the ratio under 1000rpm is always higher than 2. However, at 500rpm the ratio drops below 2 when the load current is higher than 90A. This means that turn fault is not detectable in this operating region using a threshold of 2 for the p_2^1/p_2^{ref1} ratio. This effect is caused by a number of reasons. First, at low speed, the turn fault current is intrinsically lower. Furthermore, the resistive drop can no longer be neglected in the fault path and the induced flux linkage in the faulted turn is not exactly opposed to the external flux. The fault influence on i_{dq} and u_{dq} is also limited. The voltage drop due to inverter nonlinearities also affects the voltage applied

to the machine. In motoring mode, the voltage reference signal is higher than the real voltage due to the inverter voltage drop whilst the opposite is true in generating mode. Hence, the amplitudes of u_{dq} in generating mode are reduced compared to the reference values.
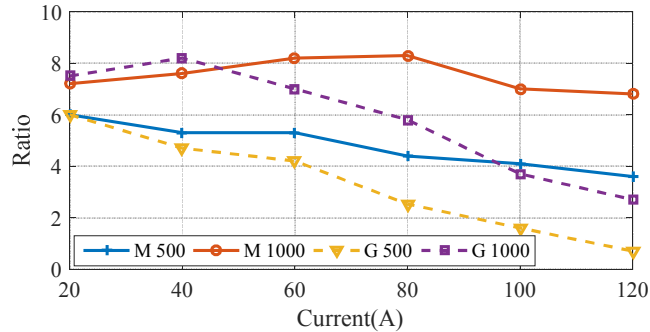
Fig. 6-76 Detection ratio at 500rpm and 1000rpm in motoring (M500, M1000) and generating (G500, G1000) modes
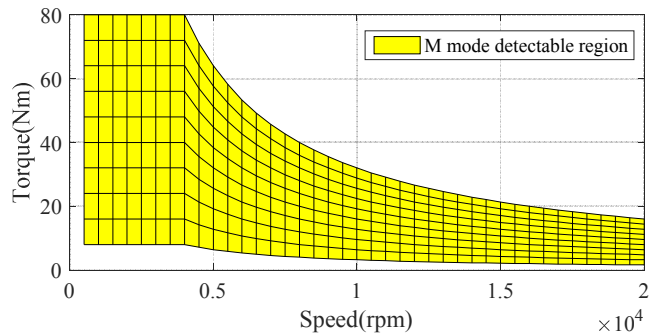
Fig. 6-77 Detection zone under motoring mode
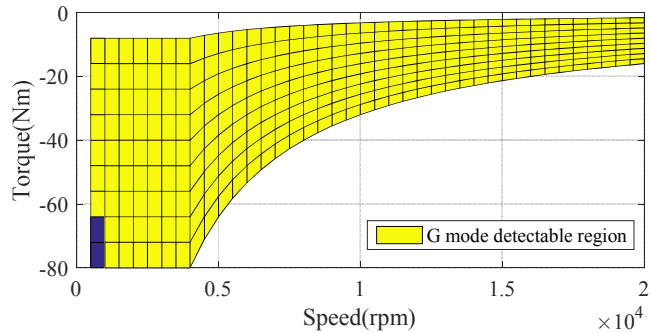
Fig. 6-78 Detection zone under generating mode

Based on the analysis above, the detection zones can be expressed as:

$$abs(T) > 0.1\text{pu}$$

$$speed > 500rpm$$

(6-3)

and they are plotted in Fig. 6-77 and Fig. 6-78. In motoring mode, all the operating region is detectable whereas in generating mode, only a small region when speed is below 1000rpm and torque is less than -60Nm is not detectable.

6.7.3 Detection under Transient Conditions

Fault detection based on harmonics can trigger false alarms during load and speed transients. Robustness of the proposed fault detection is examined for a transient process as shown in Fig. 6-79. Initially, the machine is loaded with 40A current and MTPA angle $\gamma = 33°$ at 1000rpm, and at t = 0.13s a step change in the current reference from 40A to 60A ($\gamma = 33°$) is applied for all three sets. The filtered responses of the 2nd harmonics are shown in Fig. 6-80 and they all undergo a transient process during which their magnitudes increase significantly. As can be seen, although the 2nd harmonic amplitude of any 3-phase set is two times higher than the reference value, no false alarm is triggered because the differences in the 2nd harmonics are less than 1.5 times or the second inequality in (5-12) is not true. A test is also performed when the current step change takes place at 1000 rpm and a single turn fault is injected simultaneously. The 2nd harmonic responses are shown in Fig. 6-81. In this case, although the 2nd harmonics of all three sets increase during the transient, the 2nd harmonic in the fault set is particularly higher. Thus, the fault can be detected during the transient.
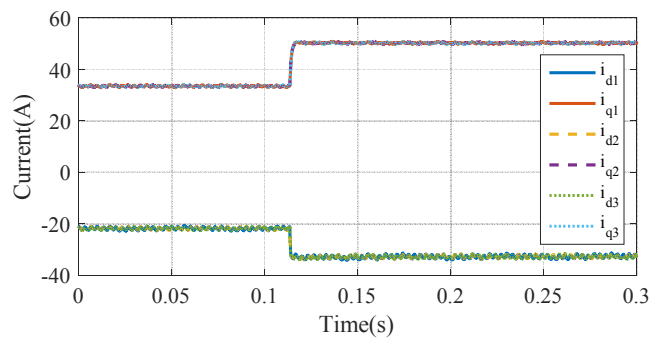
Fig. 6-79 i_{dq} response in transient
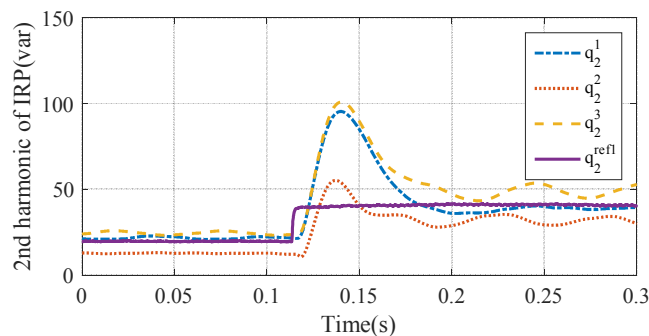
Fig. 6-80 2nd harmonic of IRP in transient
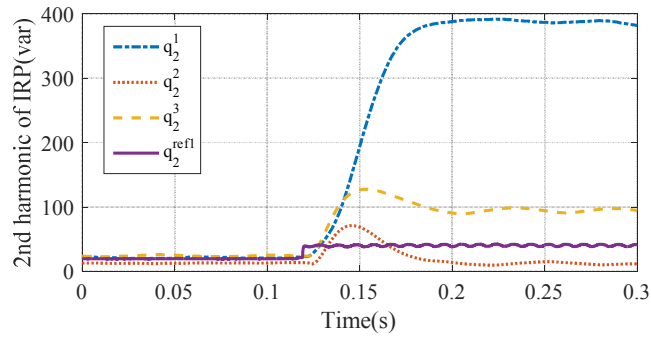
Fig. 6-81 2nd harmonic of IRP in transient with turn fault

To avoid risk of damage in repeated tests with turn fault, simulations have been performed in various operating conditions with speed and torque changes as in Chapter 5. The results show that the fault criterion in (5-12) yields correct detection in all cases. It follows that by cross-referencing the 2nd harmonics of the three 3-phase sets the proposed fault detection is also effective during transient while false alarm can be avoided.

6.7.4 Fault Mitigation Test

As previously discussed, the turn fault can be effectively mitigated by applying a terminal short circuit to the faulty set. Experimental validation of the integrated fault tolerant mechanism including the fault detection and mitigation strategy is demonstrated. One turn fault scenario with mitigation is tested at 1000rpm with 60A current under MTPA operation in motoring mode as shown in Fig. 6-82. Initially, the machine is operating in healthy condition when a single turn fault is triggered by the relay. The fault current increases to 340A which could cause further damage to the machine if no remedial action is applied immediately. This turn fault is detected within one fundamental cycle (less than 15ms) and the mitigation is applied. After the terminal short circuit, the fault current is reduced to 135A which can be thermally sustained indefinitely by the machine. In addition, operation of the other two 3-phase sets are almost not affected, as evident in measured current waveforms of other two sets in Fig. 6-83, continuing to generate torque.
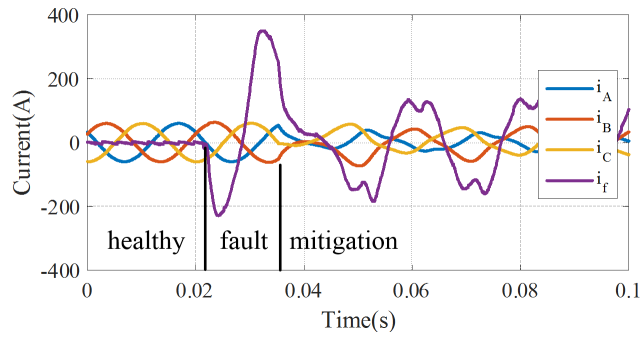
Fig. 6-82 Integrated fault detection and mitigation behaviour of fault set
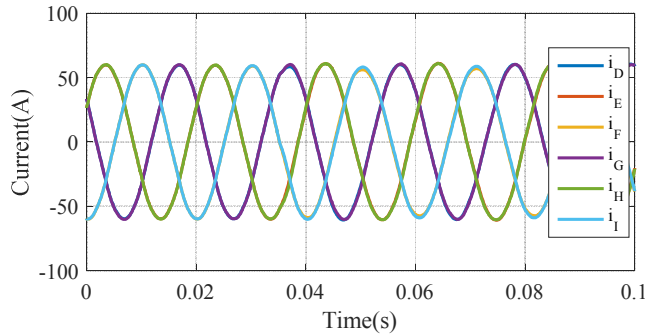
Fig. 6-83 Healthy sets currents in transient process

6.8 Summary

In this chapter, a fault tolerant triple redundant 3x3-phase PMA SynRM drive has been built according to the design optimization. The manufacturing tolerances are analyzed and considered in the machine model. Comprehensive experimental tests have been performed on the machine drive to assess its performance in healthy conditions and compared with prediction results. Its ability to tolerate various faults, including open circuit, short circuit and turn fault is also investigated.

The test results demonstrate that the machine drive exhibits high efficiency, high torque capability and wide field weakening operation. And they are in good agreement with the predictions. It has been shown that the machine drive is capable of one set open circuit/short circuit operation with about 2/3 of the output torque. The inter-turn fault can be accommodated by application of TSC without any thermal risk. The test shows that under turn fault condition, the machine drive still provide about 2/3 of the torque with appropriate mitigation actions. Thus, the test results validate the machine design optimisation and the machine drive exhibits high performance and excellent fault tolerance.

The accuracy of the general model is assessed by extensive tests under healthy and various fault conditions. The model can be used to predict the machine behaviour under healthy operations, open circuit, short circuit, inter-turn faults with and without TSC. And the effect of coil location of the fault turn also can be accounted in case of a turn fault. Thus, it provides as an effective tool for assessing fault level/severity, post fault control and fault detection development.

The turn fault detection technique based on 2nd harmonic in IAP and IRP has been implemented on the machine drive. It has been confirmed that the 2nd harmonic in IRP is higher than that of IAP in motoring mode, whilst the opposite is true in generating mode. The effectiveness of the detection technique has been examined over the whole operation region. It is shown that, with the exception of a small low speed region, the proposed technique can detect the turn fault reliably and facilitate the mitigation action to minimize the turn fault current without affecting the healthy sets operation.

Therefore, the proposed machine drive has proven to be a practical candidate for safety critical applications. And it can be implemented in a simple and cost-effective manner.

CHAPTER 7

A Fault Tolerant PMA SynRM Drive with Hybrid Pitched Segregated Windings

7.1 Introduction

A triple redundant PMA SynRM drive with segregated windings has been proposed, designed and analysed in previous Chapters. According to the fault analysis and modelling in Chapter 2 and Chapter 4, it has been shown that different 3-phase winding sets are not magnetically decoupled though they are physically and electrically isolated. They affect each other via the pulsating MMF offset components. In healthy condition, the MMF offset components are cancelled by each other due to the same current excitation. However, in fault conditions, the MMF distribution becomes asymmetric and MMF offset components are present in all three sets. It has been demonstrated that the asymmetric MMF causes uneven flux distribution and leads to current distortion and increased torque ripple. The MMF offset component also contributes to higher turn fault current through magnetic coupling with the currents in other healthy sets. Thus, it would be desirable if the pulsating MMF offset components can be reduced.

7.2 A PMA SynRM with Hybrid Pitched Segregated Windings

In order to obtain a segregated winding configuration with reduced mutual coupling, a novel PMA SynRM with hybrid pitched segregated windings is proposed as shown in Fig. 7-1. The windings have also been separated to three non-overlapped windings. Each module forms a balanced 3-phase winding set which can be driven by a standard 3-phase inverter. Compared with the previous winding configuration in Chapter 2, only the coil layout of phases B, E, H is changed while the coils of phases A and C, phases D and F, and phases G and I remain the same. For the previous winding configuration, all the winding coils are full pitched with winding span of 6 slots over one pole region.

However, for the proposed winding configuration, the coils for phases B, E, H are short-pitched with a span of 5 slots, which are short pitched. And the coils of phases A and C, D and F, G and I remain full pitched. Therefore, this novel winding configuration is named as hybrid pitched segregated windings. For simplicity, the original full pitched winding configuration is denoted as winding 1# while the hybrid pitched winding configuration is denoted as winding 2#.

As can be seen, if winding 2# is excited with the same currents as that of winding 1# in healthy conditions, the current distribution in the slots are exactly the same since the currents in phases B, E and H are identical. The resultant MMF of winding 2# has no difference from that of winding 1#. Hence, the two winding configurations have the same performance in healthy conditions. Thus, all the merits of the PMA SynRM, such as reduced magnet usage, low back emf, inherent large reluctance torque, high efficiency and high torque density are also maintained for winding 2#. Meanwhile, the segregated windings and independent inverters also lead to excellent fault tolerance against various faults. The open circuit, short circuit, intra-phase and inter-phase turn fault can be sustained similarly as winding 1# with appropriate mitigation actions as will be investigated.

It will be shown that the winding 2# has less mutual coupling effect between the different 3-phase sets than that of winding 1#.

(a)

(b)
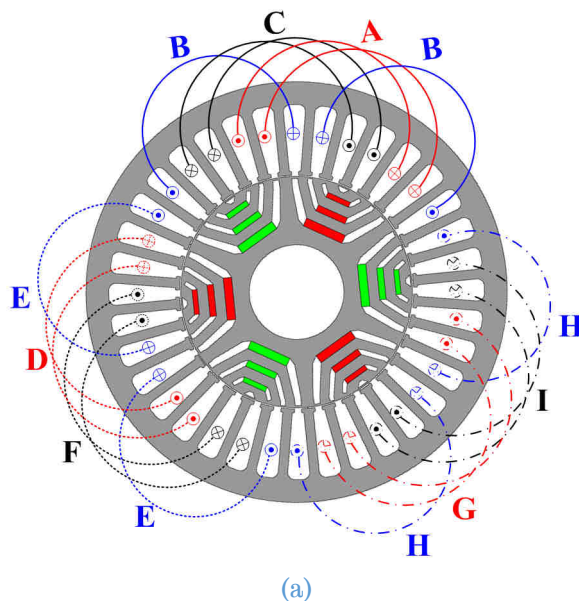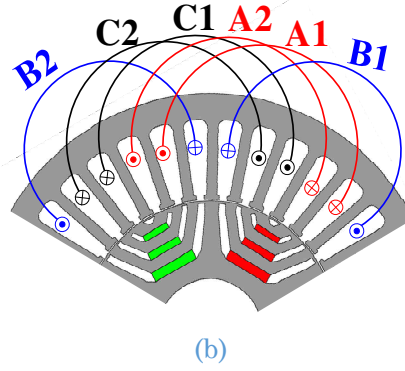
Fig. 7-1 Novel PMA SynRM with hybrid pitched segregated windings (a) Full machine view (b) Illustration of one 3-phase module

7.3 MMF Analysis of Two Winding Configurations

In order to demonstrate that the winding 2# has less mutual coupling effect than winding 1#, the MMF produced by one 3-phase set is analysed. The MMF of winding 1# has been analysed in Chapter 4. It is concluded that the currents in set ABC produce MMF not only over the set itself, but also over the other two sets. The MMF over set ABC region consists of an AC component F_{ac}^1 and an offset component F_{os}^{11} while only an offset component $(F_{os}^{21}, F_{os}^{31})$ exists over sets DEF and GHI.

Since the mutual coupling is only related to the MMF offset components, only the values of the MMF offset components are analysed which are re-written in (7-1). It is seen that the magnitude of F_{os}^{11} are two times of $(F_{os}^{21}, F_{os}^{31})$ but they have opposite signs. Hence, the following analysis will focus on F_{os}^{11} only.

$$F_{os}^{11} = \frac{2}{3}(i_A + i_B - i_C)$$

$$F_{os}^{21} = -\frac{1}{3}(i_A + i_B - i_C)$$

$$F_{os}^{31} = -\frac{1}{3}(i_A + i_B - i_C)$$

(7-1)

i_A, i_B, i_C can be expressed by the dq axes currents (i_d, i_q) in (7-2) where θ is the electrical rotor angle.

$$i_A = i_d \cos\theta - i_q \sin\theta$$

$$i_B = i_d \cos(\theta - 120) - i_q \sin(\theta - 120)$$

$$i_C = i_d \cos(\theta + 120) - i_q \sin(\theta + 120)$$

(7-2)

Substituting equation (7-2) into (7-1), F_{os}^{11} can be expressed as in (7-3). The MMF offset component F_{os}^{11} changes with rotor angle and it is dependent on (i_d, i_q). This value indicates the level of mutual coupling between the three 3-phase sets for winding 1#.

$$F_{os}^{11} = \frac{4}{3}\left(i_d \cos(\theta - 60) - i_q \sin(\theta - 60)\right)$$

$$= \frac{4}{3}\sqrt{i_d^2 + i_q^2}\cos(\theta - 60 + \delta_1), \; \delta_1 = \tan^{-1}\frac{i_q}{i_d}$$

(7-3)

The MMF distribution of the proposed winding 2# can be derived in the same way. The turn functions of 6 coils in set ABC are plotted in Fig. 7-2. It is seen that the turn function of coil B1 is negative while it is positive for coil B2 as a result of the modified coil layout of phase B.
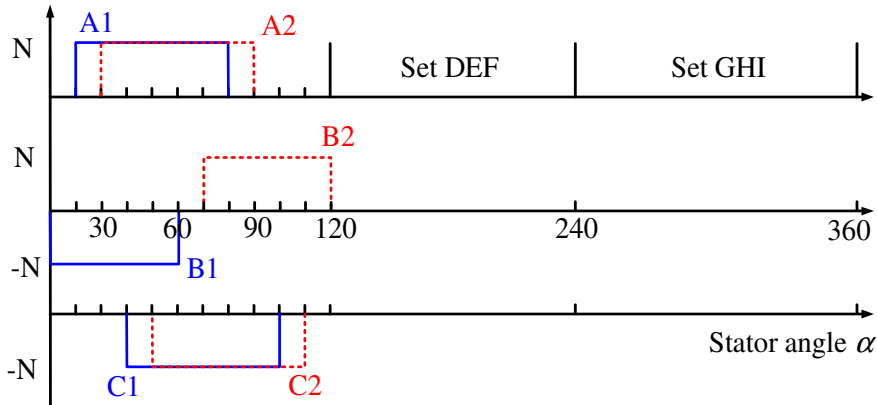
Fig. 7-2 Turn functions of 6 coils in set ABC of winding 2#

Similarly, the ampere-turns of each coil with the rated current are denoted as 1 pu. Assuming at time instant $t = 0$, the phase currents are $i_A = 1pu$, $i_B = i_C = -0.5pu$, according to the turn functions and equation in (4-2), the MMF produced by set ABC of winding 2# can be derived and is plotted in Fig. 7-3.
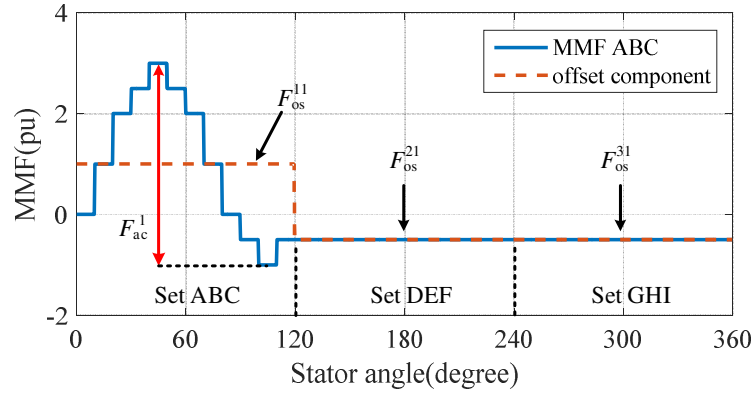
Fig. 7-3 MMF produced by set ABC of winding 2#

As can be seen, the MMF produced by set ABC of winding 2# has similar distribution with that of winding 1# in Fig. 4-3. The MMF over the ABC winding region consists of an AC component and an offset component while only an offset component exists over other regions. They can be expressed as:

$$MMF_{ABC} = \begin{cases} F_{ac}^1 + F_{os}^{11} & 0° \leq \alpha < 120° \\ F_{os}^{21} & 120° \leq \alpha < 240° \\ F_{os}^{31} & 240° \leq \alpha < 360° \end{cases}$$

$$F_{ac}^1 = \sum_{n=1,3,5\ldots} A_n \cos(3n\alpha + \delta_n)$$

$$F_{os}^{11} = \frac{2}{3}(i_A - i_C)$$

(7-4)

$$F_{os}^{21} = -\frac{1}{3}(i_A - i_C)$$

$$F_{os}^{31} = -\frac{1}{3}(i_A - i_C)$$

The variables are defined similarly as in Chapter 4. The AC component is the same as that in (4-3), however the offset component is different. The phase B current i_B does not contribute to the offset component. This is attributed to the fact that the MMF of coils B1 and B2 cancel each other due to the reversed coil polarity. Substituting equation (7-2) into (7-4), F_{os}^{11} can be expressed in (7-5).

$$F_{os}^{11} = \frac{2\sqrt{3}}{3}(i_d \cos(\theta - 30) - i_q \sin(\theta - 30))$$

(7-5)

$$= \frac{2\sqrt{3}}{3} \sqrt{i_d^2 + i_q^2} \cos(\theta - 30 + \delta_2), \ \delta_2 = \tan^{-1} \frac{i_q}{i_d}$$

Comparing equation (7-5) with (7-3), it can be found that the maximum offset component value of winding 2# is 14% lower than that of winding 1#. It indicates that one 3-phase set has less influence on the other 3-phase sets. Thus, the mutual coupling between the different sets is reduced. The resultant negative effects of the coupling, like current distortion, torque ripple and excessive turn fault current, will be alleviated. The performance of the two winding configurations in both healthy and fault conditions will be compared in the following section.

It should be noticed that the hybrid pitched winding configuration is also achieved with no additional cost. Only the winding layout is reconfigured, so it can be implemented on the same machine as winding 1#. The three 3-phase drives are the same as the full pitched windings and can be cost-effectively implemented. The configuration of winding 2# is also applicable to other 3x3-phase, 6-pole machines with distributed windings to obtain fault tolerance with reduced mutual coupling such as synchronous reluctance machines, surface mounted PM machines, synchronous wound field machines and induction machines.

7.4 Performance Comparison for the Two Winding Configurations

In this section, the machine behaviours for winding 2# are evaluated and compared with winding 1# for both healthy and fault conditions. Without loss of generality, the two machines will be based on the same machine dimensions of the optimised machine in Chapter 3. The various faults as listed in Table 1-1 are investigated and the corresponding fault tolerance is assessed using FE analysis. All simulations are performed at the base speed 4000rpm with the rated current excitation unless otherwise stated.

7.4.1 Healthy condition

First, the back emfs of the two machines with different winding configurations are calculated under healthy condition. Due to the periodicity, only the back emfs of set ABC are shown in Fig. 7-4. It is seen that the back emfs of winding 2# are symmetrical, and the back emfs of the two machines are exactly the same. In addition, the line back emfs are also the same. So the machine with winding 2# is also free from the uncontrolled generation fault at high speed.
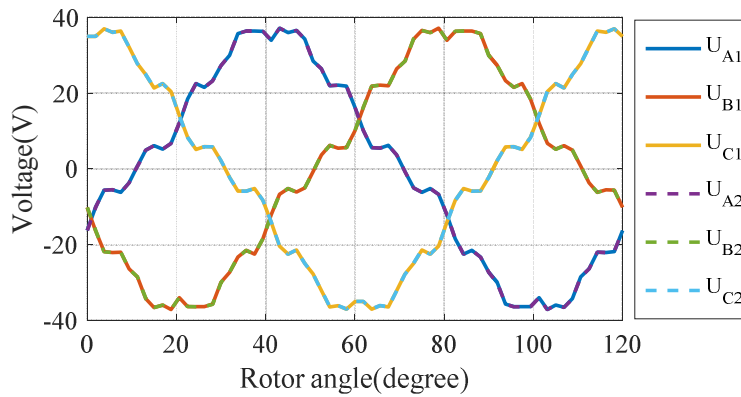
Fig. 7-4 Back emf comparison of the two winding configurations

As a result, the same current excitation can be applied to the two machines. The rated currents have been loaded to the two machines and the output torque waveforms are compared in Fig. 7-5. Again, the two waveforms overlap, confirming the same torque performance. In addition, the flux linkages of set ABC of the two machines are compared in Fig. 7-6 and no difference is seen. Thus, the two machines could employ the same drive configuration and control scheme, and they exhibit the same behaviours in healthy conditions.
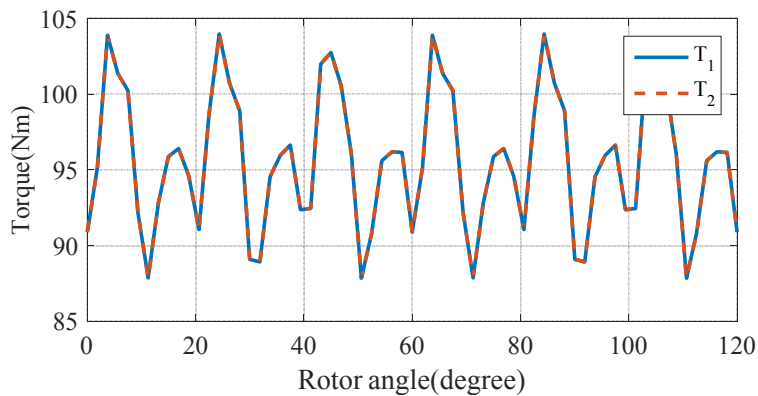
Fig. 7-5 Output torque comparison of the two winding configurations
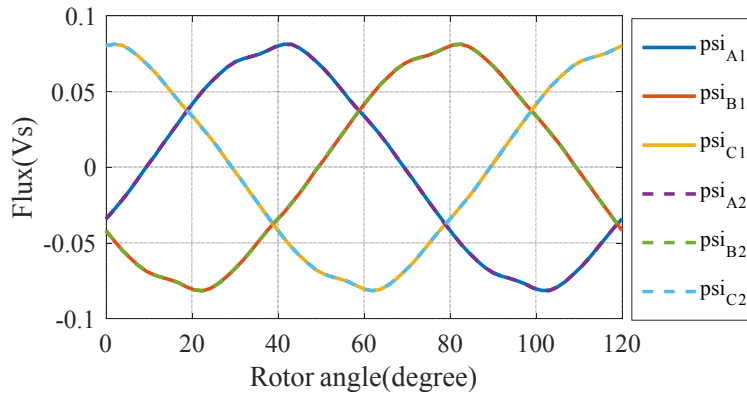
Fig. 7-6 Flux comparison of the two winding configurations

7.4.2 Open Circuit Fault

In case of an open circuit failure in the windings or switches, the faulty 3-phase set could be deactivated by turning off the gate drive signals of that set. The currents in the faulty set become zero, leading to one set open-circuit failure mode. The remaining two 3-phase sets are still excited by the same currents. The resulting torque waveform is compared with that of winding 1# in Fig. 7-7. The average torque of the machine in this condition is 55.8Nm which is slightly higher than that of winding 1#. Its open circuit torque capability ρ_{oc} can be calculated as:

$$\rho_{oc} = T_{oc}/T_r \times 100\% = 58.4\% \tag{7-6}$$
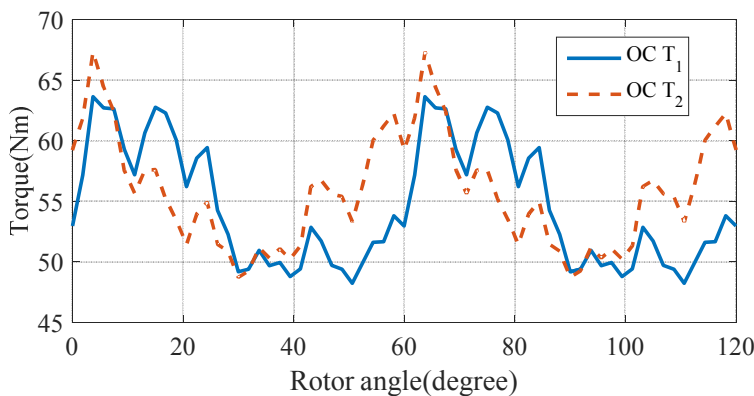
Fig. 7-7 Open circuit torque comparison of the two winding configurations

Similar to the machine with winding 1#, the torque ripple of the machine with winding 2# under the open circuit fault is also dominated by the 2nd harmonic. However, it is seen that the 2nd harmonic has a different phase shift from that of winding 1#. This can be explained by comparing equations (7-3) and (7-5). With the same current excitation, the resultant MMF offset

component has 30 degree phase shift. Thus, the 2nd torque ripple harmonic is also shifted.

7.4.3 Short Circuit Fault

If a switch in the inverter or the phase winding is short-circuited, that particular inverter should turn-on all its top or bottom switches to create a TSC for the faulty 3-phase set. The healthy sets are excited by the inverter for continuous operation.

For the machine with winding 2#, its back emf is also quite low as shown in Fig. 7-4, thus the induced short circuit currents are also much lower than the rated value as shown in Fig. 7-8. Hence, no excessive heat will be produced in the faulty set and the machine will be safe to continue its operation. It is observed that the short circuit phase currents are asymmetrical. Again, this is attributed to the mutual coupling between the healthy sets and the faulty set though this coupling is reduced in the machine with winding 2#. The resultant torques of the two machines are compared in Fig. 7-9. The mean torque and torque ripple of the new winding configuration are almost the same as the original one. Its short circuit torque capability ρ_{sc} can be calculated as:

$$\rho_{sc} = T_{sc}/T_r \times 100\% = 65.9\%$$ (7-7)
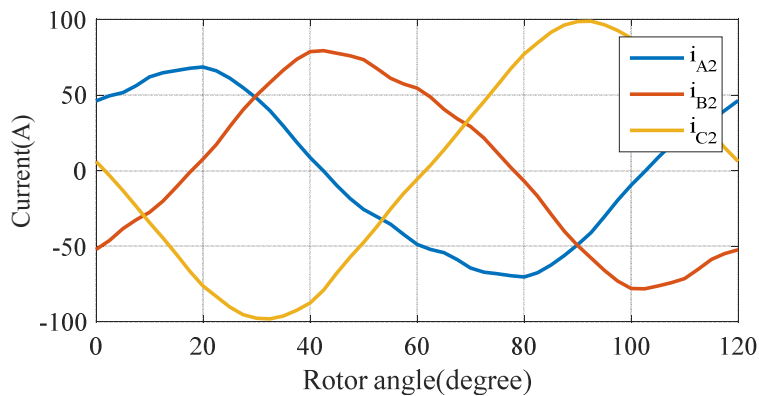
Fig. 7-8 Short circuit currents in set ABC of winding 2#
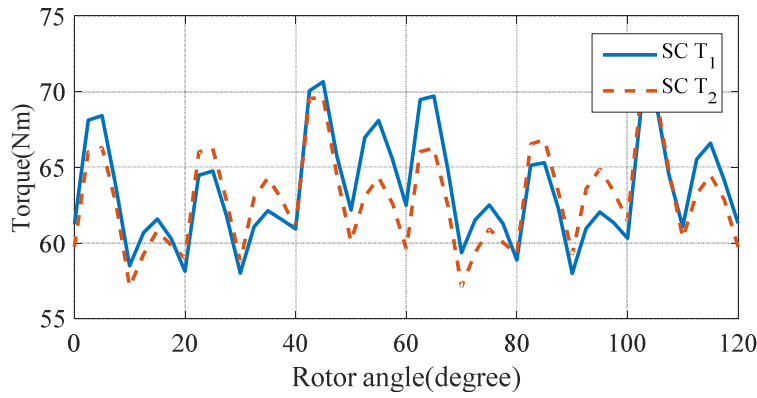
Fig. 7-9 Short circuit torque comparison of the two winding configurations

As discussed in section 7.3, the machine with winding 2# has less mutual coupling effect than that of winding 1#. Asymmetric short circuit currents in the fault set is due to the mutual coupling effect. Thus, the short circuit currents in the machine with winding 2# should be more balanced than that of winding 1#. For comparison purpose, the short circuit currents in the machine with winding 1# are plotted in Fig. 7-10.
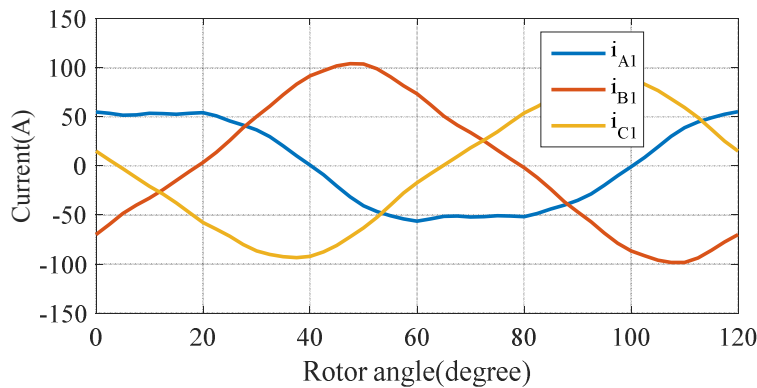
Fig. 7-10 Short circuit currents in set ABC of winding 1#

It has been shown that the mutual coupling is caused by the pulsating MMF offset component in the form of a standing wave. It will induce both positive and negative sequence field for the 3-phase windings. Consequently, both the positive and negative sequence currents will be induced in the short circuit set. The positive and negative sequence components in the short circuit currents of the two windings [1, 2] are compared in Table 7-1.

It is seen that the short circuit currents consist of mainly positive sequence components which are induced by the positive sequence PM field. The negative sequence components in winding 1# is 30% higher than those of

winding 2#. Thus, the short circuit currents in winding 2# are more balanced and less affected by the mutual coupling which confirms the conclusion above.

Table 7-1 Positive and negative sequence components comparison of short circuit currents

		Winding 1#	Winding 2#
Positive sequence components	i_{d+}/A	-78.2	-77
	i_{q+}/A	4.7	2.37
Negative sequence components	i_{d-}/A	2.35	14.2
	i_{q-}/A	19	3.5

7.4.4 Intra-phase Turn Fault

In the worst case for the machine with winding 2# when one turn intra-phase short-circuit occurs, TSC can be applied on the fault 3-phase set to reduce the fault current. After the application of TSC, the flux linkage of short-circuited turn will be significantly reduced by the currents in the healthy turns, leading to lower turn fault current.

Similarly, the phenomenon of unequal turn fault current in different coil locations also exists. The trends of the fault current variations with the load currents in the healthy sets are analysed as shown in Fig. 7-11. Again, in motoring mode, the turn fault current will be the highest if the fault occurs in coil B2 which is the same as winding 1#. Thus, the worst case with 120A load currents is simulated and compared with that of winding 1#. As shown in Fig. 7-12, the turn fault current of winding 2# has a phase shift with respect to that of winding 1# due to the coil layout. And its RMS value is 240A which is about 10% lower than that of the winding 1#. The short circuit phase currents and the post fault torque is quite close to that of one set short circuit mode, and therefore, they are not provided here.

The reduced turn fault current in the machine winding 2# is due to the reduced mutual coupling between the healthy sets and the fault set. As discussed previously, the turn fault current is mainly determined by the PM flux and the currents in the healthy sets while the currents in the healthy part

of the fault set help reduce the flux linkage of the faulted turn, and hence the fault current. Owing to the reduced mutual coupling for winding 2#, the fault turn is less affected by the currents in the other two healthy 3-phase sets and hence the fault current is lower.
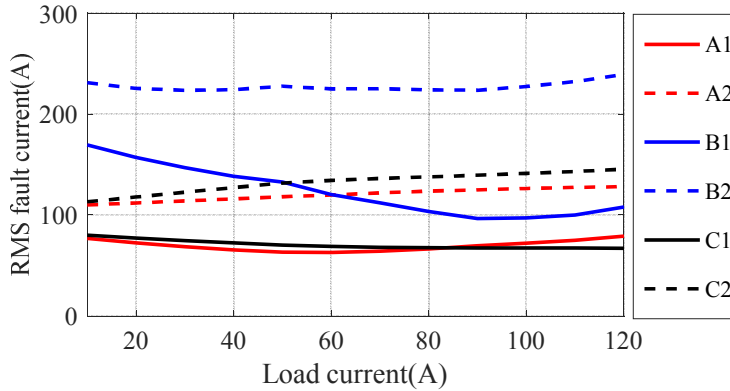
Fig. 7-11 Variations of RMS turn fault currents in 6 coils with load current in healthy 3-phase sets in motoring mode
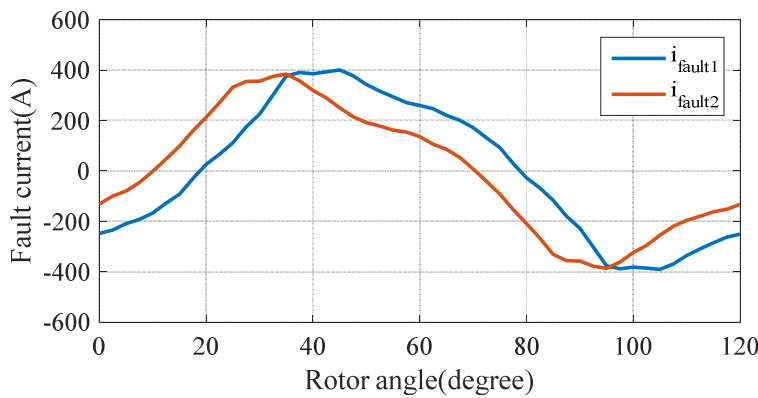
Fig. 7-12 Turn fault current comparison of the two winding configurations with turn fault in coil B2 set after TSC

If the machine with winding 2# operates in generating mode, the turn fault current variation with fault position in 6 coils may change similarly to that seen in the machine with winding 1#. The trends are also investigated as shown in Fig. 7-13. Now the highest fault current is located in coil B1 in most operation ranges. The maximum magnitude of the fault current is close to that of motoring mode.

It is interesting to note that for winding 1#, the largest turn fault current in coils B2 and A1 for motoring and generating mode, respectively. They are placed in the leading slot (the first slot in the direction of rotation) and the trailing slot (the last slot in the direction of rotation) of a 3-phase set. Similarly, for winding 2#, the highest turn fault current in coil B2 and B1 for motoring

and generating mode, respectively. In fact, they are also placed in the leading slot (the first slot in the direction of rotation) of a 3-phase set and the trailing slot (the last slot in the direction of rotation).
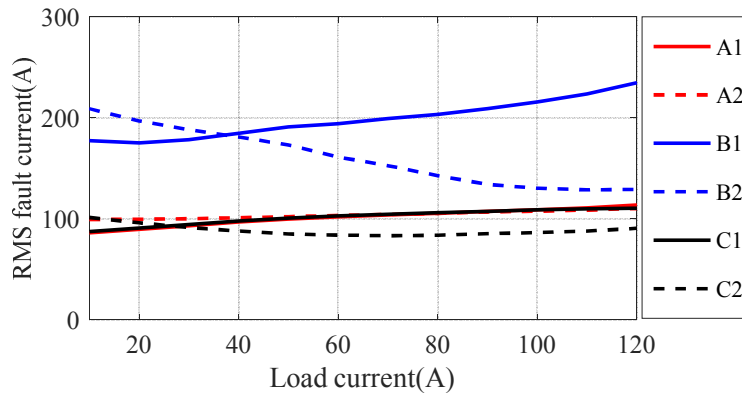
Fig. 7-13 Variations of RMS turn fault currents in 6 coils with load current in healthy 3-phase sets in generating mode

7.4.5 Inter-phase Turn Fault

For the proposed winding 2#, the end windings of one 3-phase set are still bundled together. So the possibility of inter-phase short circuit failure still exists. Thus, the inter-phase short circuit fault is analysed.
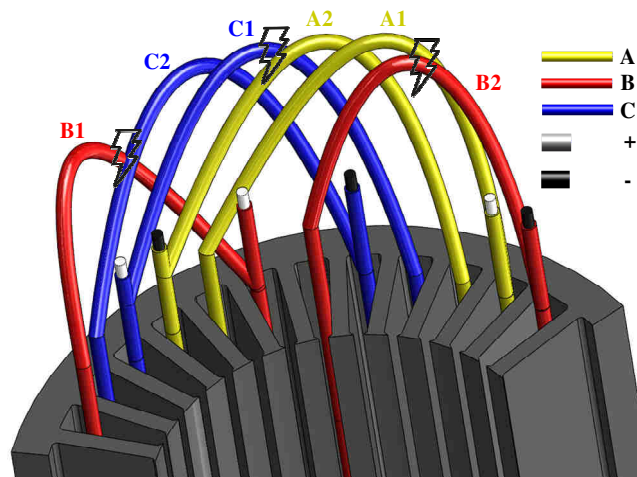
Fig. 7-14 3D winding configuration of set ABC of winding 2#

For more clear illustration, the 3D winding configuration is shown in Fig. 7-14. The inter-phase turn fault is most likely to occur in the end winding part as well. Considering the winding layout, the inter-phase turn fault most probably occurs where two phase windings contact with each other. Due to the new winding configuration, the inter-phase faults between phases AB, BC and CA are all possible. Take phases AB fault as an example, it would most

probably occur between the last few turns of phase B and the first few turns of phase A due to the winding terminal connections as shown in Fig. 7-15. For the other fault cases, it can be analysed similarly. The phases BC fault is most likely to happen between the first coil of phase B and the last coil of phase C whilst the phases AC fault may take place between the last coil of phase A and the first coil of phase C. It is worth noting that in all cases, at least one coil of 8 turns is in the short circuited loop according to Fig. 7-15. Thus, the resultant fault current is also much lower than the intra-phase fault.
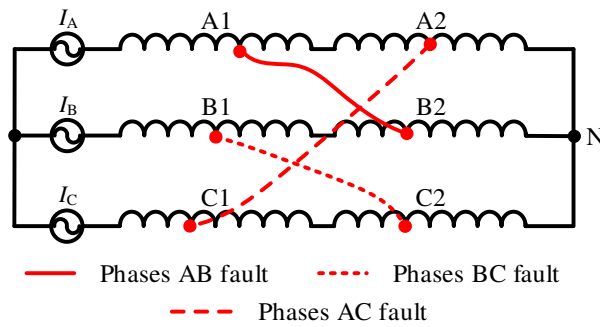
Fig. 7-15 Inter-phase fault illustration

In case of an inter-phase turn fault for the machine with winding 2#, TSC also should be applied on the faulty set to reduce the fault current. It is known that the short circuit current increases with the decrease of the number of the short circuited turns. Thus, the least number of the short circuited turns after TSC is determined by varying the position of the fault point in Fig. 7-15. The blue coils represent where the inter-phase fault may take place. The worst 6 scenarios for the inter-phase faults are illustrated in Fig. 7-16.

(a)

(b)
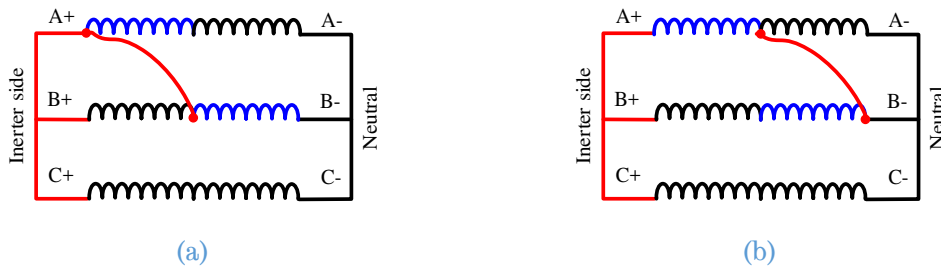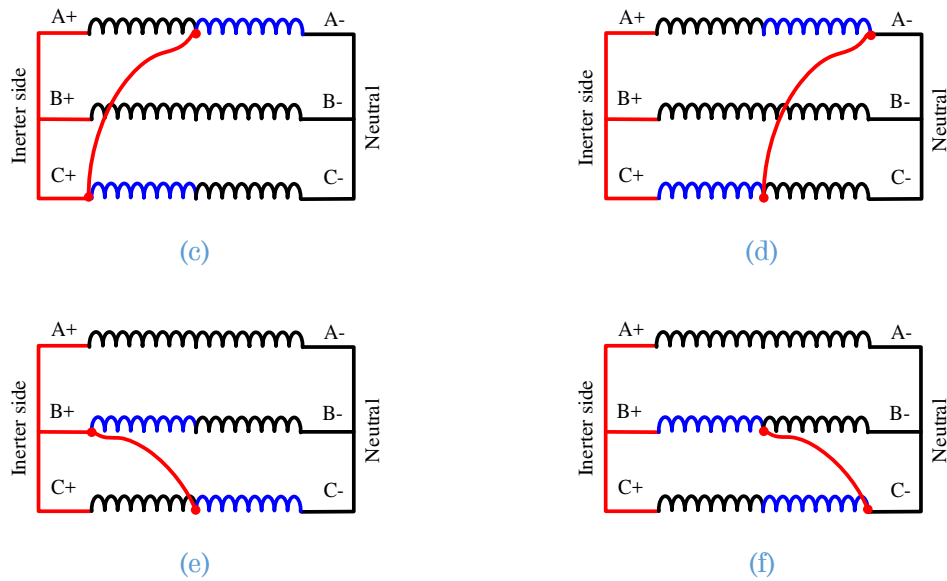
Fig. 7-16 Extreme inter-phase short circuit faults (a) Case 1 for phases AB fault (b) Case 2 for phases AB (c) Case 3 for fault phases AC fault (d) Case 4 for fault phases AC fault (e) Case 5 for phases BC fault (f) Case 6 for phases BC fault

These 6 extreme inter-phase faults have been simulated in FE analysis. Again, the results show that the fault current is highest in fault case 6 as shown in Fig. 7-16 (f) where B2 coil is short circuited. The fault currents and output torque is shown in Fig. 7-17 and Fig. 7-18. The fault current in B2 coil is only 0.92pu. It is lower than that of winding 1# (1.1pu) which is also attributed to the reduced mutual coupling effect. It does not cause any thermal risk for the machine. The output torque is also around 2/3pu with dominant 2nd and 12th torque ripple. Therefore, the inter-phase turn fault can be accommodated for the machine with winding 2#.
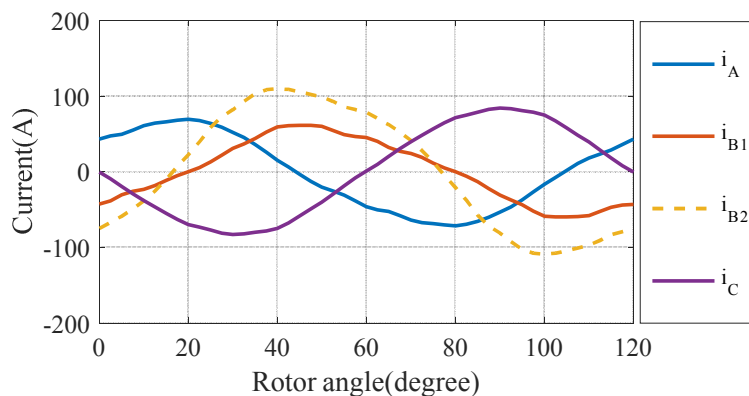
Fig. 7-17 Currents for case 6 of phases BC fault
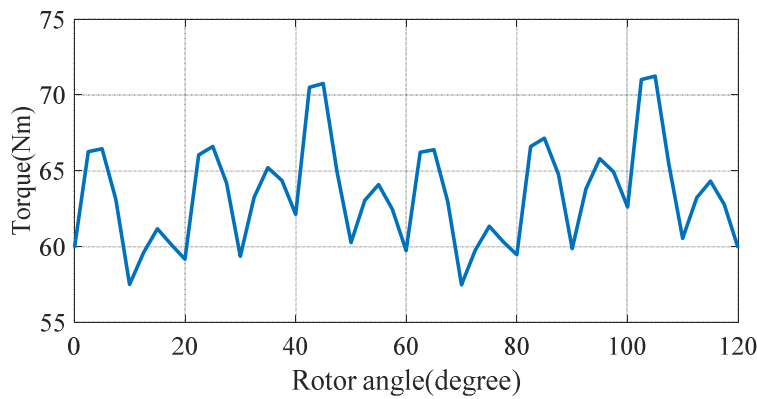
Fig. 7-18 Torque for case 6 of phases BC fault

It should be noted that the winding layout and coil connection should follow Fig. 7-14 and Fig. 7-15. The reason is the same as explained in section 2.3.5 for winding 1#. Similarly, insulation paper should be inserted between the phases to enhance the phase-to-phase insulation and reduce the risk of insulation failure.

7.4.6 Other faults

Other faults, like the demagnetization fault and DC link capacitor fault, can also be accommodated by the machine with winding 2#. They have no significant differences from those of winding 1#. These faults can be analysed similarly as in Chapter 2, therefore they are not repeated here.

7.5 Summary

In this chapter, a novel hybrid pitched segregated winding configuration is proposed for the same PMA SynRM. It also achieves physical, thermal and electrical isolation between different 3-phase sets, and can be realised without additional cost. Owing to the proposed winding configuration, the mutual coupling effect between different 3-phase sets is reduced and the fundamental reason is explained using the concept of MMF distribution. The machine performance in healthy conditions and its fault tolerance against various electric faults are investigated and compared with the machine with winding 1#. It shows that the machine has the same performance as winding 1# in healthy conditions. And it has improved fault tolerance due to the reduced mutual coupling. In particular, this winding configuration shows 10% lower fault current than winding 1# in the worst intra-phase turn fault case.

CHAPTER 8
Conclusion and Future Work

In this Chapter, the research work and the main findings of the PhD studies are summarised and possible future work based on the PhD research is outlined.

8.1 Work Summary

Although the electrical drives outperform the mechanical, hydraulic or pneumatic systems in terms of high efficiency, low emission, and flexible regulation etc., high reliability is an essential requirement to employ them for the safety critical applications. They should be capable to continue operation if a fault occurs, or at least fail safely without catastrophic damage. Thus, fault tolerance should be addressed in the electrical drives development to attain the reliability requirement for the targeted applications.

An integrated fault tolerant electrical drive necessitates the techniques of advanced machine and inverter topology, fault tolerant machine design, fault modelling, fault detection and fault mitigation strategy. All these aspects should be considered during the machine drive development. Thus, a fault tolerant machine drive has been developed and demonstrated to exhibit high performance in healthy operation as well as excellent fault tolerance against various faults with simple and cost-effective implementation.

After reviewing the current state-of-art fault tolerant machine drive topologies, a triple redundant 3x3-phase PMA SynRM drive with segregated windings is proposed in **Chapter 2** for the safety critical applications. Owing to the segregated windings and independent drives, the three 3-phase sets have good physical, electrical and thermal isolation between each other. Hence, a fault in one 3-phase set does not affect the operation of the other two sets significantly. The machine drive can continue to provide about 2/3 of the torque/power. The machine has comparable performance with conventional

PM machines by employing both PM torque and reluctance torque. The reluctance torque enables use of less magnet material and results in improved fault tolerance. The machine drive's fault behaviour has been investigated against various fault scenarios. It is shown that the machine can cope with the winding/switch open circuit, short circuit, intra-phase and inter-phase turn fault, uncontrolled rectification, demagnetization and DC link capacitor fault. The influence of the turn fault location has also been investigated and it is shown that the fault current will be the highest if the turn fault occurs in the trailing slot (coil) B2 in motoring mode and the leading slot (coil A1) in generating mode. These understandings are employed in the machine design stage.

In order to obtain a fault tolerant machine drive, an integrated design procedure is developed in **Chapter 3** for the fault tolerant PMA SynRM to maximize the efficiency while satisfying all the electrical, thermal and mechanical constraints. The machine's electromagnetic, thermal and mechanical behaviours are computational efficiently assessed by various developed design tools for healthy and the worst case, viz. turn fault in coil B2 in motoring mode. The evaluated results are sent to the optimisation tool GOT-It in which the machine parameters are optimised to achieve the optimum efficiency subject to those constraints. The optimised machine has been examined in various operation modes. The results confirm that these faults can be tolerated by the optimised machine which exhibits high efficiency in healthy operation.

The optimally designed machine has been prototyped and a systematic test rig is established to operate the machine in healthy condition and to emulate various fault scenarios in a controlled manner. Comprehensive experimental tests have been performed on the machine drive to validate the machine design. It is shown that the machine drive exhibits high efficiency and the test results are close to the predictions. It is also demonstrated that the machine drive is capable of one set open circuit/short circuit operation with about 2/3 of the output torque. The inter-turn fault can be accommodated by application

of TSC without any thermal risk. The machine drive is also fail-safe to the uncontrolled generation fault since the line back emf at the maximum speed is lower than the DC link voltage. It is worth noting that the implementation of the machine drive is simple and cost-effective.

Accurate and computationally efficient fault modelling is essential for the fault tolerant machine drive. It serves as an efficient tool for the fault behaviour assessment, development of post fault control, fault detection and mitigation strategy. Thus, a general modelling technique has been proposed for the triple redundant PMA SynRM in **Chapter 4**. The MMF of the machine is divided into three parts with each associated with one 3-phase set. The MMF of each 3-phase set can be described by four variables $(\theta, i_d, i_q, F_{os})$. The influence of other two sets currents is represented by the MMF offset component F_{os} which indicates the mutual coupling between each other. It is capable of accurately predicting the behaviour by the established 4D tables in all operating modes, including the healthy operation, open circuit, short circuit and unequal current operation. The general model has also been adapted to incorporate the prediction of machine behaviour under STF. The coil location, slot position, number of fault turns all can be considered. The model is also capable of analysing STF behaviour with and without TSC. The accuracy of the model has been examined on the prototyped machine drive. Good agreements are observed in both the healthy and various fault conditions. The influence of the coil location of the turn fault is well represented by the model. Thus, the fault behaviour is accurately captured by the proposed model which can aid the fault detection development in **Chapter 5**.

Fast and reliable detection of stator turn faults is of key importance for fail-safe and fault tolerant machine drives in order to immediately trigger appropriate fault mitigation actions. A turn fault detection technique has been developed in **Chapter 5** based on the 2nd harmonic in IAP and IRP for the triple redundant PMA SynRM drive under closed loop control. It is shown that the 2nd harmonic in IAP and IRP during turn fault conditions is

comparatively higher than that of voltage and current, making them ideal candidates as turn fault indicators. Particularly, the 2nd harmonic in IRP is higher than that of IAP in motoring mode, whilst the opposite is true in generating mode. Thus, the 2nd harmonics in IRP and IAP are employed as indicators for turn fault detection in motoring mode and generating mode, respectively. And for the machine drive under study, the fault indicator of each 3-phase set could serve as a cross reference to avoid the false alarm during transients. The effectiveness of the detection technique over the whole operation region has been examined by extensive simulation and experimental tests. It is shown that, with the exception of a small low speed region, the proposed technique can detect the turn fault reliably and facilitate the mitigation action to minimize the turn fault current without affecting the healthy sets operation.

According to the previous analysis, it has been shown that different 3-phase winding sets are not magnetically isolated. They affect each other via the pulsating MMF offset components. The MMF offset components lead to current distortion, increased torque ripple and turn fault current. In order to reduce the adverse effects of the MMF offset components, a novel PMA SynRM with hybrid pitched segregated windings is proposed in **Chapter 7**. It inherits all the merits of the original full pitched winding machine while its MMF offset component is reduced by 14% compared with the full pitched windings. Hence the mutual coupling effect between different 3-phase sets is reduced and the resultant negative impacts are alleviated. The proposed winding machine has the same performance in healthy condition as the original one and it is also fault tolerant to the various faults discussed above. In particular, it exhibits 10% lower fault current in the worst intra-phase turn fault case which further improves the fault tolerance.

8.2 Future Work

Based on the PhD research work, some possible future work is indicated as follows.

1. Novel fault tolerant machine drive topology. According to the previous investigation, different 3-phase winding sets affect each other via the MMF offset component. Though it is partially reduced by the hybrid pitched segregated windings, considerable MMF offset component still exists which causes those negative effects. Thus, it would be desirable that the MMF offset components could be further reduced or even eliminated. The noticeable unbalanced magnetic pull force and the resultant vibration and noise should be restrained in fault conditions.

2. Analysis of the machine operation under fault operation. As discussed, the machine drive operates in asymmetrical condition under failure modes, the behaviour of the machine and how the MMF offset component affects the machine operation is worth in-depth investigation.

3. Advanced post fault control technique. Increased current distortion, torque ripple are noticed in fault conditions. Advanced fault management and control strategy could be in place to reduce the negative effects of a fault. For example, under one phase open circuit fault, instead of disabling one 3-phase set, the two remaining healthy phases and inverter legs may be utilized to enhance the torque output and reduce torque ripple. In addition, the influence of the 2nd harmonics in the voltages and currents due to a fault on the drive control should be further investigated. And the MTPA operation and field weakening in post fault operation are worth to be analysed.

4. Fault detection and classification techniques. The proposed 2nd harmonic based detection still requires a pre-operation to obtain the lookup tables in healthy conditions. This process is undesirable for large-scale industrial applications. Instead, an automatic process should be employed to establish the table during healthy operations. In addition, various faults may occur in the fault tolerant machine drive, fault classification technique is required to distinguish the different faults for appropriate remedy action.

5. Analysis of unequal turn fault current in different coil locations. It is shown that the turn fault current is unequal if it occurs in different coil locations. The underlining cause of the difference should be analyzed and it may stimulate novel fault tolerant machine drive topology and fault mitigation strategy.

8.3 List of Publications

The publications as a result of PhD studies include:

Journal papers:

[J1]   **Bo Wang**, Jiabin Wang, A. Griffo, and B. Sen, "A Fault Tolerant Machine Drive Based on Permanent Magnet Assisted Synchronous Reluctance Machine," *Industry Applications, IEEE Transactions on*, Accepted, Early Access.

[J2]   **Bo Wang**, Jiabin Wang, A. Griffo, and B. Sen, "Experimental Assessments of a Triple Redundant 9-Phase Fault Tolerant PMA SynRM Drive," *Industrial Electronics, IEEE Transactions on*, Accepted, Early Access.

[J3]   **Bo Wang**, Jiabin Wang, A. Griffo, and B. Sen, "Stator Turn Fault Detection by 2nd Harmonic Power for a Closed Loop Controlled Triple 3-phase PMA SynRM Machine," *Industrial Electronics, IEEE Transactions on*, Accepted, Early Access.

[J4]   **Bo Wang**, Jiabin Wang, A. Griffo, and B. Sen, "A General Modelling Technique for a Triple Redundant 3x3-phase PMA SynRM," *Industrial Electronics, IEEE Transactions on*, Accepted, Early Access.

[J5]   **Bo Wang,** Jiabin Wang, A. Griffo, and Y. Shi, "Investigation into Fault Tolerant Capability of a Triple Redundant PMA SynRM Drive", *Power Electronics, IEEE Transactions on*, Under Review.

[J6]   **Bo Wang**, Jiabin Wang, A. Griffo, " Stator Turn Fault Modelling for a Triple Redundant 3x3-phasePMA SynRM," *Industrial Electronics, IEEE Transactions on*, In preparation.

Conference papers:

[C1]   **Bo Wang**, Jiabin Wang, A. Griffo, and V. I. Patel, "Permanent Magnet Generator Turn Fault Detection Using Kalman Filter Technique," *in Energy Conversion Congress and Exposition (ECCE)*, 2016 IEEE, 2016.

[C2]   **Bo Wang**, Jiabin Wang, and A. Griffo, "A Fault Tolerant Machine Drive Based on Permanent Magnet Assisted Synchronous Reluctance Machine " *in Energy Conversion Congress and Exposition (ECCE)*, 2016 IEEE, 2016.

[C3]   **Bo Wang**, Jiabin Wang and A. Griffo, "Overall assessments of dual inverter open winding drives," *2015 IEEE International Electric Machines & Drives Conference (IEMDC)*.

[C4]   **Bo Wang**, Jiabin Wang, and A. Griffo, "A Fault Tolerant PMA SynRM Drive with Mixed Pitch Segregated Windings," *2018 Energy Conversion Congress and Exposition (ECCE)*, Under Review.

[C5]   Yanwen Shi, Jiabin Wang, and **Bo Wang**, "Performance assessment of triple redundant 9-phase delta- and wye-connected Permanent Magnet-assisted Synchronous Reluctance Motor under healthy and fault conditions," *The 9th IET International Conference on Power Electronics, Machines and Drives (PEMD 2018)*, Accepted.

[C6]   Fernando Alvarez-Gonzalez, Antonio Griffo, and **Bo Wang**, "Permanent Magnet Synchronous Motor Stator Winding Fault Detection by Means of Hilbert-Huang Transform," *The 9th IET International Conference on Power Electronics, Machines and Drives (PEMD 2018)*, Accepted.

[C7]   Yanwen Shi, Jiabin Wang, and **Bo Wang**, "Lumped-parameter and 3D thermal model of a PMA SynRM under fault conditions with asymmetric temperature distribution," *2018 Energy Conversion Congress and Exposition (ECCE)*, Under Review.

[C8]   Yanwen Shi, Jiabin Wang, and **Bo Wang**, "EM-thermal coupled simulation under various fault conditions of a triple redundant 9-phase PMA SynRM," *2018 Energy Conversion Congress and Exposition (ECCE)*, Under Review.

References

[1]   Y. Song and B. Wang, "Survey on Reliability of Power Electronic Systems," *Power Electronics, IEEE Transactions on,* vol. 28, pp. 591-604, 2013.

[2]   J. A. Tegopoulos, "Electrical machines for electromotion and their design," in *Electrical and electronic engineers in israel, 2000. the 21st ieee convention of the*, 2000, pp. 209-212.

[3]   W. Cao, B. C. Mecrow, G. J. Atkinson, J. W. Bennett, and D. J. Atkinson, "Overview of Electric Motor Technologies Used for More Electric Aircraft (MEA)," *Industrial Electronics, IEEE Transactions on,* vol. 59, pp. 3523-3531, 2012.

[4]   K. T. Chau, C. C. Chan, and C. Liu, "Overview of Permanent-Magnet Brushless Drives for Electric and Hybrid Electric Vehicles," *Industrial Electronics, IEEE Transactions on,* vol. 55, pp. 2246-2257, 2008.

[5]   J. Wang, Z. P. Xia, and D. Howe, "Three-phase modular permanent magnet brushless Machine for torque boosting on a downsized ICE vehicle," *Vehicular Technology, IEEE Transactions on,* vol. 54, pp. 809-816, 2005.

[6]   A. Mohammadpour, S. Mishra, and L. Parsa, "Fault-Tolerant Operation of Multiphase Permanent-Magnet Machines Using Iterative Learning Control," *IEEE Journal of Emerging and Selected Topics in Power Electronics,* vol. 2, pp. 201-211, 2014.

[7]   N. Bianchi and S. Bolognani, "Design of a Fault-tolerant IPM Motor for Electric Power Steering," in *Power Electronics Specialists Conference, 2005. PESC '05. IEEE 36th*, 2005, p. 2873.

[8]   A. Boglietti, A. Cavagnino, A. Tenconi, and S. Vaschetto, "The safety critical electric machines and drives in the more electric aircraft: A survey," in *Industrial Electronics, 2009. IECON '09. 35th Annual Conference of IEEE*, 2009, pp. 2587-2594.

[9]   D. A. Rennels, "Fault Tolerant Computing Concepts and Examples," *Computers, IEEE Transactions on,* vol. C-33, pp. 1116-1129, 1984.

[10]   R. V. White, "Fault tolerance in distributed power systems," in *Power Electronics Congress, 1995. Technical Proceedings. CIEP 95., IV IEEE International*, 1995, pp. 121-128.

[11]   A. G. Jack, B. C. Mecrow, and J. A. Haylock, *A comparative study of permanent magnet and switched reluctance motors for high-performance fault-tolerant applications*.

[12]   B. C. Mecrow, D. J. Atkinson, A. G. Jack, S. Green, J. A. Haylock, and J. Coles, "The need for fault tolerance in an aeroengine electric fuel control system," in *Electrical Machines and Systems for the More Electric Aircraft (Ref. No. 1999/180), IEE Colloquium on*, 1999, pp. 9/1-9/5.

[13] "Report of Large Motor Reliability Survey of Industrial and Commercial Installations, Part I," *Industry Applications, IEEE Transactions on,* vol. IA-21, pp. 853-864, 1985.

[14] O. V. Thorsen and M. Dalva, "A survey of faults on induction motors in offshore oil industry, petrochemical industry, gas terminals and oil refineries," in *Petroleum and Chemical Industry Conference, 1994. Record of Conference Papers., Institute of Electrical and Electronics Engineers Incorporated Industry Applications Society 41st Annual*, 1994, pp. 1-9.

[15] A. Sarikhani and O. A. Mohammed, "Demagnetization Control for Reliable Flux Weakening Control in PM Synchronous Machine," *Energy Conversion, IEEE Transactions on,* vol. 27, pp. 1046-1055, 2012.

[16] S. Yang, A. Bryant, P. Mawby, D. Xiang, L. Ran, and P. Tavner, "An Industry-Based Survey of Reliability in Power Electronic Converters," *Industry Applications, IEEE Transactions on,* vol. 47, pp. 1441-1451, 2011.

[17] J. Yu-Seok, S. Seung-Ki, S. E. Schulz, and N. R. Patel, "Fault detection and fault-tolerant control of interior permanent-magnet motor drive system for electric vehicle," *Industry Applications, IEEE Transactions on,* vol. 41, pp. 46-51, 2005.

[18] J. W. Bennett, B. C. Mecrow, A. G. Jack, D. J. Atkinson, S. Sheldon, B. Cooper*, et al.*, "A prototype electrical actuator for aircraft flaps and slats," in *Electric Machines and Drives, 2005 IEEE International Conference on*, 2005, pp. 41-47.

[19] P. Sun, C. Gong, X. Du, Q. Luo, H. Wang, and L. Zhou, "Online Condition Monitoring for Both IGBT Module and DC-Link Capacitor of Power Converter Based on Short-Circuit Current Simultaneously," *IEEE Transactions on Industrial Electronics,* vol. 64, pp. 3662-3671, 2017.

[20] N. Bianchi, S. Bolognani, and M. Zigliotto, "Analysis of PM synchronous motor drive failures during flux weakening operation," in *Power Electronics Specialists Conference, 1996. PESC '96 Record., 27th Annual IEEE*, 1996, pp. 1542-1548 vol.2.

[21] A. M. E.-. Refaie, M. R. Shah, and K. K. Huh, "High-Power-Density Fault-Tolerant PM Generator for Safety-Critical Applications," *IEEE Transactions on Industry Applications,* vol. 50, pp. 1717-1728, 2014.

[22] B. Vaseghi, N. Takorabet, J. P. Caron, B. Nahid-Mobarakeh, F. Meibody-Tabar, and G. Humbert, "Study of Different Architectures of Fault-Tolerant Actuator Using a Two-Channel PM Motor," *Industry Applications, IEEE Transactions on,* vol. 47, pp. 47-54, 2011.

[23] M. Beltrao de Rossiter Correa, C. B. Jacobina, E. R. Cabral da Silva, and A. M. N. Lima, "An induction motor drive system with improved fault tolerance," *Industry Applications, IEEE Transactions on,* vol. 37, pp. 873-879, 2001.

[24] B. Wang, G. Localzo, G. E. Murr, J. Wang, A. Griffo, C. Gerada*, et al.*, "Overall assessments of dual inverter open winding drives," in *2015*

IEEE International Electric Machines & Drives Conference (IEMDC), 2015, pp. 1029-1035.

[25] N. Bianchi, S. Bolognani, Pre, x, M. D., and E. Fornasiero, "Post-fault operations of five-phase motor using a full-bridge inverter," in *Power Electronics Specialists Conference, 2008. PESC 2008. IEEE*, 2008, pp. 2528-2534.

[26] M. Bermudez, I. Gonzalez-Prieto, F. Barrero, H. Guzman, M. J. Duran, and X. Kestelyn, "Open-Phase Fault-Tolerant Direct Torque Control Technique for Five-Phase Induction Motor Drives," *IEEE Transactions on Industrial Electronics,* vol. 64, pp. 902-911, 2017.

[27] E. Levi, R. Bojoi, F. Profumo, H. A. Toliyat, and S. Williamson, "Multiphase induction motor drives - a technology status review," *Electric Power Applications, IET,* vol. 1, pp. 489-516, 2007.

[28] J.-R. Fu and T. A. Lipo, "Disturbance-free operation of a multiphase current-regulated motor drive with an opened phase," *Industry Applications, IEEE Transactions on,* vol. 30, pp. 1267-1274, 1994.

[29] A. Tani, M. Mengoni, L. Zarri, G. Serra, and D. Casadei, "Control of Multiphase Induction Motors With an Odd Number of Phases Under Open-Circuit Phase Faults," *Power Electronics, IEEE Transactions on,* vol. 27, pp. 565-577, 2012.

[30] J. Wang, K. Atallah, and D. Howe, "Optimal torque control of fault-tolerant permanent magnet brushless machines," *Magnetics, IEEE Transactions on,* vol. 39, pp. 2962-2964, 2003.

[31] S. Dwari, L. Parsa, and T. A. Lipo, "Optimum Control of a Five-phase Integrated Modular Permanent Magnet Motor Under Normal and Open-Circuit Fault Conditions," in *Power Electronics Specialists Conference, 2007. PESC 2007. IEEE*, 2007, pp. 1639-1644.

[32] N. Bianchi, S. Bolognani, Pre, x, and M. D., "Strategies for the Fault-Tolerant Current Control of a Five-Phase Permanent-Magnet Motor," *Industry Applications, IEEE Transactions on,* vol. 43, pp. 960-970, 2007.

[33] H. Zhou, W. Zhao, G. Liu, R. Cheng, and Y. Xie, "Remedial Field-Oriented Control of Five-Phase Fault-Tolerant Permanent-Magnet Motor by Using Reduced-Order Transformation Matrices," *IEEE Transactions on Industrial Electronics,* vol. 64, pp. 169-178, 2017.

[34] L. Alberti and N. Bianchi, "Experimental Tests of Dual Three-Phase Induction Motor Under Faulty Operating Condition," *Industrial Electronics, IEEE Transactions on,* vol. 59, pp. 2041-2048, 2012.

[35] L. Parsa and H. A. Toliyat, "Fault-Tolerant Interior-Permanent-Magnet Machines for Hybrid Electric Vehicle Applications," *Vehicular Technology, IEEE Transactions on,* vol. 56, pp. 1546-1552, 2007.

[36] Y. Fan, W. Zhu, X. Zhang, M. Cheng, and K. T. Chau, "Research on a Single Phase-Loss Fault-Tolerant Control Strategy for a New Flux-Modulated Permanent-Magnet Compact In-Wheel Motor," *IEEE Transactions on Energy Conversion,* vol. PP, pp. 1-9, 2016.

[37]   M. J. Duran, I. G. Prieto, M. Bermudez, F. Barrero, H. Guzman, and M. R. Arahal, "Optimal Fault-Tolerant Control of Six-Phase Induction Motor Drives With Parallel Converters," *IEEE Transactions on Industrial Electronics,* vol. 63, pp. 629-640, 2016.

[38]   S. Gopalakrishnan, A. M. Omekanda, and B. Lequesne, "Classification and remediation of electrical faults in the switched reluctance drive," *Industry Applications, IEEE Transactions on,* vol. 42, pp. 479-486, 2006.

[39]   Y. Hu, C. Gan, W. Cao, W. Li, and S. J. Finney, "Central-Tapped Node Linked Modular Fault-Tolerance Topology for SRM Applications," *IEEE Transactions on Power Electronics,* vol. 31, pp. 1541-1554, 2016.

[40]   B. Lequesne, S. Gopalakrishnan, and A. M. Omekanda, "Winding short circuits in the switched reluctance drive," *Industry Applications, IEEE Transactions on,* vol. 41, pp. 1178-1184, 2005.

[41]   B. C. Mecrow, A. G. Jack, J. A. Haylock, and J. Coles, "Fault-tolerant permanent magnet machine drives," *Electric Power Applications, IEE Proceedings -,* vol. 143, pp. 437-442, 1996.

[42]   J. T. Chen and Z. Q. Zhu, "Comparison of All- and Alternate-Poles-Wound Flux-Switching PM Machines Having Different Stator and Rotor Pole Numbers," *Industry Applications, IEEE Transactions on,* vol. 46, pp. 1406-1415, 2010.

[43]   J. Chai, J. Wang, K. Atallah, and D. Howe, "Performance Comparison and Winding Fault Detection of Duplex 2-Phase and 3-Phase Fault-Tolerant Permanent Magnet Brushless Machines," in *Industry Applications Conference, 2007. 42nd IAS Annual Meeting. Conference Record of the 2007 IEEE*, 2007, pp. 566-572.

[44]   J. Dusek, P. Arumugam, C. Brunson, E. K. Amankwah, T. Hamiti, and C. Gerada, "Impact of Slot/Pole Combination on Inter-Turn Short-Circuit Current in Fault-Tolerant Permanent Magnet Machines," *IEEE Transactions on Magnetics,* vol. 52, pp. 1-9, 2016.

[45]   S. H. Han, T. M. Jahns, M. Aydin, M. K. Guven, and W. L. Soong, "Impact of Maximum Back-EMF Limits on the Performance Characteristics of Interior Permanent Magnet Synchronous Machines," in *Conference Record of the 2006 IEEE Industry Applications Conference Forty-First IAS Annual Meeting*, 2006, pp. 1962-1969.

[46]   J. Wang, K. Atallah, R. Chin, W. M. Arshad, and H. Lendenmann, "Rotor Eddy-Current Loss in Permanent-Magnet Brushless AC Machines," *Magnetics, IEEE Transactions on,* vol. 46, pp. 2701-2707, 2010.

[47]   V. I. Patel, J. Wang, and S. S. Nair, "Demagnetization Assessment of Fractional-Slot and Distributed Wound 6-Phase Permanent Magnet Machines," *Magnetics, IEEE Transactions on,* vol. 51, pp. 1-11, 2015.

[48]   W. Wang, M. Cheng, B. Zhang, Y. Zhu, and S. Ding, "A Fault-Tolerant Permanent-Magnet Traction Module for Subway Applications," *IEEE Transactions on Power Electronics,* vol. 29, pp. 1646-1658, 2014.

[49]   D. C. Patel and M. C. Chandorkar, "Modeling and Analysis of Stator Interturn Fault Location Effects on Induction Machines," *IEEE Transactions on Industrial Electronics,* vol. 61, pp. 4552-4564, 2014.

[50]   B. Sen and J. Wang, "Analytical modelling of stator turn fault in surface mounted permanent magnet machines," in *Energy Conversion Congress and Exposition (ECCE), 2013 IEEE*, 2013, pp. 4445-4452.

[51]   O. A. Mohammed, Z. Liu, S. Liu, and N. Y. Abed, "Internal Short Circuit Fault Diagnosis for PM Machines Using FE-Based Phase Variable Model and Wavelets Analysis," *Magnetics, IEEE Transactions on,* vol. 43, pp. 1729-1732, 2007.

[52]   L. Romeral, J. C. Urresty, J. R. Riba Ruiz, and A. Garcia Espinosa, "Modeling of Surface-Mounted Permanent Magnet Synchronous Motors With Stator Winding Interturn Faults," *Industrial Electronics, IEEE Transactions on,* vol. 58, pp. 1576-1585, 2011.

[53]   B. A. Welchko, T. M. Jahns, and S. Hiti, "IPM synchronous machine drive response to a single-phase open circuit fault," *Power Electronics, IEEE Transactions on,* vol. 17, pp. 764-771, 2002.

[54]   B. A. Welchko, T. M. Jahns, W. L. Soong, and J. M. Nagashima, "IPM synchronous machine drive response to symmetrical and asymmetrical short circuit faults," *Energy Conversion, IEEE Transactions on,* vol. 18, pp. 291-298, 2003.

[55]   A. M. S. Mendes and A. J. M. Cardoso, "Fault-Tolerant Operating Strategies Applied to Three-Phase Induction-Motor Drives," *Industrial Electronics, IEEE Transactions on,* vol. 53, pp. 1807-1817, 2006.

[56]   R. Kianinezhad, B. Nahid-Mobarakeh, L. Baghli, F. Betin, and G. A. Capolino, "Modeling and Control of Six-Phase Symmetrical Induction Machine Under Fault Condition Due to Open Phases," *IEEE Transactions on Industrial Electronics,* vol. 55, pp. 1966-1977, 2008.

[57]   A. Pantea, A. Yazidi, F. Betin, M. Taherzadeh, S. Carriere, H. Henao*, et al.*, "Six-Phase Induction Machine Model for Electrical Fault Simulation Using the Circuit-Oriented Method," *IEEE Transactions on Industrial Electronics,* vol. 63, pp. 494-503, 2016.

[58]   R. Hyung-Min, K. Ji-Woong, and S. Seung-Ki, "Synchronous-frame current control of multiphase synchronous motor under asymmetric fault condition due to open phases," *IEEE Transactions on Industry Applications,* vol. 42, pp. 1062-1070, 2006.

[59]   Z. Weidong, B. Fahimi, and S. Pekarek, "A field reconstruction method for optimal excitation of permanent magnet synchronous machines," *IEEE Transactions on Energy Conversion,* vol. 21, pp. 305-313, 2006.

[60]   M. Dai, A. Keyhani, and T. Sebastian, "Fault analysis of a PM brushless DC Motor using finite element method," *Energy Conversion, IEEE Transactions on,* vol. 20, pp. 1-6, 2005.

[61]   B. Sen, J. Wang, and P. Lazari, "A detailed transient model of Interior Permanent Magnet motor accounting for saturation under stator turn

fault," in *Energy Conversion Congress and Exposition (ECCE), 2013 IEEE*, 2013, pp. 3548-3555.

[62]   A. Gandhi, T. Corrigan, and L. Parsa, "Recent Advances in Modeling and Online Detection of Stator Interturn Faults in Electrical Motors," *Industrial Electronics, IEEE Transactions on,* vol. 58, pp. 1564-1575, 2011.

[63]   R. M. Tallam, T. G. Habetler, and R. G. Harley, "Transient model for induction machines with stator winding turn faults," *Industry Applications, IEEE Transactions on,* vol. 38, pp. 632-637, 2002.

[64]   S. Nandi, "A detailed model of induction machines with saturation extendable for fault analysis," *IEEE Transactions on Industry Applications,* vol. 40, pp. 1302-1309, 2004.

[65]   I. Jeong, B. J. Hyon, and K. Nam, "Dynamic Modeling and Control for SPMSMs With Internal Turn Short Fault," *IEEE Transactions on Power Electronics,* vol. 28, pp. 3495-3508, 2013.

[66]   B. Vaseghi, B. Nahid-mobarakh, N. Takorabet, and F. Meibody-Tabar, "Inductance Identification and Study of PM Motor With Winding Turn Short Circuit Fault," *Magnetics, IEEE Transactions on,* vol. 47, pp. 978-981, 2011.

[67]   N. Leboeuf, T. Boileau, B. Nahid-Mobarakeh, N. Takorabet, F. Meibody-Tabar, and G. Clerc, "Inductance Calculations in Permanent-Magnet Motors Under Fault Conditions," *IEEE Transactions on Magnetics,* vol. 48, pp. 2605-2616, 2012.

[68]   F. Wu, P. Zheng, and T. M. Jahns, "Analytical modeling of inter-turn short circuit for multiphase fault-tolerant PM machines with fractional-slot concentrated windings," in *Energy Conversion Congress and Exposition (ECCE), 2015 IEEE*, 2015, pp. 6970-6977.

[69]   K. Kyung-Tae, P. Jun-Kyu, H. Jin, and K. Byeong-Woo, "Comparison of the Fault Characteristics of IPM-Type and SPM-Type BLDC Motors Under Inter-Turn Fault Conditions Using Winding Function Theory," *Industry Applications, IEEE Transactions on,* vol. 50, pp. 986-994, 2014.

[70]   T. Kim, H. W. Lee, and S. Kwak, "The Internal Fault Analysis of Brushless DC Motors Based on the Winding Function Theory," *IEEE Transactions on Magnetics,* vol. 45, pp. 2090-2096, 2009.

[71]   X. Tu, L. A. Dessaint, M. E. Kahel, and A. O. Barry, "A New Model of Synchronous Machine Internal Faults Based on Winding Distribution," *IEEE Transactions on Industrial Electronics,* vol. 53, pp. 1818-1828, 2006.

[72]   X. Tu, L. A. Dessaint, N. Fallati, and B. D. Kelper, "Modeling and Real-Time Simulation of Internal Faults in Synchronous Generators With Parallel-Connected Windings," *IEEE Transactions on Industrial Electronics,* vol. 54, pp. 1400-1409, 2007.

[73]   B. Sen, J. Wang, and P. Lazari, "A High-Fidelity Computationally Efficient Transient Model of Interior Permanent-Magnet Machine With Stator Turn Fault," *IEEE Transactions on Industrial Electronics,* vol. 63, pp. 773-783, 2016.

[74]   Z. Sun, J. Wang, D. Howe, and G. Jewell, "Analytical Prediction of the Short-Circuit Current in Fault-Tolerant Permanent-Magnet Machines," *Industrial Electronics, IEEE Transactions on,* vol. 55, pp. 4210-4217, 2008.

[75]   P. Arumugam, "Design Optimization on Conductor Placement in the Slot of Permanent Magnet Machines to Restrict Turn-turn Short-Circuit Fault Current," *IEEE Transactions on Magnetics,* vol. 52, pp. 1-8, 2016.

[76]   M. Trabelsi, N. Nguyen, and E. Semail, "Real-Time Switches Fault Diagnosis Based on Typical Operating Characteristics of Five-Phase Permanent Magnetic Synchronous Machines," *IEEE Transactions on Industrial Electronics,* vol. PP, pp. 1-1, 2016.

[77]   Q. T. An, L. Z. Sun, K. Zhao, and L. Sun, "Switching Function Model-Based Fast-Diagnostic Method of Open-Switch Faults in Inverters Without Sensors," *IEEE Transactions on Power Electronics,* vol. 26, pp. 119-126, 2011.

[78]   J. Zhu, N. Ertugrul, and W. L. Soong, "Detection and Remediation of Switch Faults on a Fault Tolerant Permanent Magnet Motor Drive with Redundancy," in *2007 2nd IEEE Conference on Industrial Electronics and Applications*, 2007, pp. 96-101.

[79]   J. Sottile and J. L. Kohler, "An on-line method to detect incipient failure of turn insulation in random-wound motors," *IEEE Transactions on Energy Conversion,* vol. 8, pp. 762-768, 1993.

[80]   R. M. Tallam, L. Sang Bin, G. C. Stone, G. B. Kliman, Y. Ji-Yoon, T. G. Habetler*, et al.*, "A Survey of Methods for Detection of Stator-Related Faults in Induction Machines," *Industry Applications, IEEE Transactions on,* vol. 43, pp. 920-933, 2007.

[81]   S. Nandi, H. A. Toliyat, and X. Li, "Condition monitoring and fault diagnosis of electrical motors-a review," *IEEE Transactions on Energy Conversion,* vol. 20, pp. 719-729, 2005.

[82]   J. Sottile, F. C. Trutt, and J. L. Kohler, "Experimental investigation of on-line methods for incipient fault detection " in *Industry Applications Conference, 2000. Conference Record of the 2000 IEEE*, 2000, pp. 2682-2687 vol.4.

[83]   S. M. A. Cruz and A. J. M. Cardoso, "Stator winding fault diagnosis in three-phase synchronous and asynchronous motors, by the extended Park's vector approach," *IEEE Transactions on Industry Applications,* vol. 37, pp. 1227-1233, 2001.

[84]   A. J. M. Cardoso, S. M. A. Cruz, and D. S. B. Fonseca, "Inter-turn stator winding fault diagnosis in three-phase induction motors, by Park's vector approach," *IEEE Transactions on Energy Conversion,* vol. 14, pp. 595-598, 1999.

[85]   L. Sang Bin, R. M. Tallam, and T. G. Habetler, "A robust, on-line turn-fault detection technique for induction machines based on monitoring the sequence component impedance matrix," *IEEE Transactions on Power Electronics,* vol. 18, pp. 865-872, 2003.

[86] S. Cheng, P. Zhang, and T. G. Habetler, "An Impedance Identification Approach to Sensitive Detection and Location of Stator Turn-to-Turn Faults in a Closed-Loop Multiple-Motor Drive," *IEEE Transactions on Industrial Electronics,* vol. 58, pp. 1545-1554, 2011.

[87] R. M. Tallam, T. G. Habetler, and R. G. Harley, "Stator winding turn-fault detection for closed-loop induction motor drives," *IEEE Transactions on Industry Applications,* vol. 39, pp. 720-724, 2003.

[88] S. T. Lee and J. Hur, "Detection technique for stator inter-turn faults in BLDC motors based on third harmonic components of line currents," in *2015 IEEE Energy Conversion Congress and Exposition (ECCE)*, 2015, pp. 1899-1904.

[89] G. M. Joksimovic and J. Penman, "The detection of inter-turn short circuits in the stator windings of operating motors," *IEEE Transactions on Industrial Electronics,* vol. 47, pp. 1078-1084, 2000.

[90] S. M. A. Cruz and A. J. M. Cardoso, "Diagnosis of stator inter-turn short circuits in DTC induction motor drives," *IEEE Transactions on Industry Applications,* vol. 40, pp. 1349-1360, 2004.

[91] S. Nandi, "Detection of Stator Faults in Induction Machines Using Residual Saturation Harmonics," *IEEE Transactions on Industry Applications,* vol. 42, pp. 1201-1208, 2006.

[92] C. H. D. Angelo, G. R. Bossio, S. J. Giaccone, M. I. Valla, J. A. Solsona, and G. O. Garcia, "Online Model-Based Stator-Fault Detection and Identification in Induction Motors," *IEEE Transactions on Industrial Electronics,* vol. 56, pp. 4671-4680, 2009.

[93] M. Yi Lu, M. A. Masrur, C. ZhiHang, and Z. Baifang, "Model-based fault diagnosis in electric drives using machine learning," *IEEE/ASME Transactions on Mechatronics,* vol. 11, pp. 290-303, 2006.

[94] B. Sen and J. Wang, "A fast detection technique for stator inter-turn fault in multi-phase permanent magnet machines using model based approach," in *Power Electronics, Machines and Drives (PEMD 2014), 7th IET International Conference on*, 2014, pp. 1-6.

[95] S. Nadarajan, S. K. Panda, B. Bhangu, and A. K. Gupta, "Online Model-Based Condition Monitoring for Brushless Wound-Field Synchronous Generator to Detect and Diagnose Stator Windings Turn-to-Turn Shorts Using Extended Kalman Filter," *IEEE Transactions on Industrial Electronics,* vol. 63, pp. 3228-3241, 2016.

[96] A. Sarikhani and O. A. Mohammed, "Inter-Turn Fault Detection in PM Synchronous Machines by Physics-Based Back Electromotive Force Estimation," *IEEE Transactions on Industrial Electronics,* vol. 60, pp. 3472-3484, 2013.

[97] F. Briz, M. W. Degner, A. Zamarron, and J. M. Guerrero, "Online stator winding fault diagnosis in inverter-fed AC machines using high-frequency signal injection," *Industry Applications, IEEE Transactions on,* vol. 39, pp. 1109-1117, 2003.

[98]   F. Briz, M. W. Degner, P. Garcia, and A. B. Diez, "High-Frequency Carrier-Signal Voltage Selection for Stator Winding Fault Diagnosis in Inverter-Fed AC Machines," *IEEE Transactions on Industrial Electronics,* vol. 55, pp. 4181-4190, 2008.

[99]   J. Arellano-Padilla, M. Sumner, and C. Gerada, "Winding condition monitoring schemefor a permanent magnet machine using high-frequency injection," *Electric Power Applications, IET,* vol. 5, pp. 89-99, 2011.

[100]   B. Sen and J. Wang, "Stator Interturn Fault Detection in Permanent-Magnet Machines Using PWM Ripple Current Measurement," *IEEE Transactions on Industrial Electronics,* vol. 63, pp. 3148-3157, 2016.

[101]   K. H. Kim, "Simple Online Fault Detecting Scheme for Short-Circuited Turn in a PMSM Through Current Harmonic Monitoring," *IEEE Transactions on Industrial Electronics,* vol. 58, pp. 2565-2568, 2011.

[102]   T. Boileau, N. Leboeuf, B. Nahid-Mobarakeh, and F. Meibody-Tabar, "Synchronous Demodulation of Control Voltages for Stator Interturn Fault Detection in PMSM," *IEEE Transactions on Power Electronics,* vol. 28, pp. 5647-5654, 2013.

[103]   B. Du, S. Wu, S. Han, and S. Cui, "Interturn Fault Diagnosis Strategy for Interior Permanent-Magnet Synchronous Motor of Electric Vehicles Based on Digital Signal Processor," *IEEE Transactions on Industrial Electronics,* vol. 63, pp. 1694-1706, 2016.

[104]   M. Wolkiewicz, G. Tarcha, x, T. Or, x, K. owska*, et al.*, "Online Stator Interturn Short Circuits Monitoring in the DFOC Induction-Motor Drive," *IEEE Transactions on Industrial Electronics,* vol. 63, pp. 2517-2528, 2016.

[105]   S. F. Legowski, A. H. M. S. Ula, and A. M. Trzynadlowski, "Instantaneous power as a medium for the signature analysis of induction motors," *IEEE Transactions on Industry Applications,* vol. 32, pp. 904-909, 1996.

[106]   M. Drif and A. J. M. Cardoso, "Airgap Eccentricity Fault Diagnosis, in Three-Phase Induction Motors, by the Instantaneous Power Signature Analysis," in *Power Electronics, Machines and Drives, 2006. The 3rd IET International Conference on*, 2006, pp. 349-353.

[107]   M. B. Abadi, S. M. A. Cruz, and A. P. Gon, "Detection of stator and rotor faults in a DFIG based on the stator reactive power analysis," in *IECON 2014 - 40th Annual Conference of the IEEE Industrial Electronics Society*, 2014, pp. 2037-2043.

[108]   M. Drif and A. J. M. Cardoso, "On-line fault diagnostics in operating three-phase induction motors by the active and reactive power media," in *Electrical Machines, 2008. ICEM 2008. 18th International Conference on*, 2008, pp. 1-6.

[109]   M. Drif and A. J. M. Cardoso, "Stator Fault Diagnostics in Squirrel Cage Three-Phase Induction Motor Drives Using the Instantaneous Active

and Reactive Power Signature Analyses," *IEEE Transactions on Industrial Informatics,* vol. 10, pp. 1348-1360, 2014.

[110] M. Drif and A. J. M. Cardoso, "The Use of the Instantaneous-Reactive-Power Signature Analysis for Rotor-Cage-Fault Diagnostics in Three-Phase Induction Motors," *IEEE Transactions on Industrial Electronics,* vol. 56, pp. 4606-4614, 2009.

[111] M. Drif and A. J. M. Cardoso, "Discriminating the Simultaneous Occurrence of Three-Phase Induction Motor Rotor Faults and Mechanical Load Oscillations by the Instantaneous Active and Reactive Power Media Signature Analyses," *IEEE Transactions on Industrial Electronics,* vol. 59, pp. 1630-1639, 2012.

[112] M. Ferrari, N. Bianchi, A. Doria, and E. Fornasiero, "Design of Synchronous Reluctance Motor for Hybrid Electric Vehicles," *Industry Applications, IEEE Transactions on,* vol. 51, pp. 3030-3040, 2015.

[113] P. Guglielmi, N. G. Giraudo, G. M. Pellegrino, and A. Vagati, "P.M. assisted synchronous reluctance drive for minimal hybrid application," in *Industry Applications Conference, 2004. 39th IAS Annual Meeting. Conference Record of the 2004 IEEE*, 2004, pp. 1-306.

[114] Q. Dinyu, L. Xiaogang, and T. A. Lipo, "Reluctance motor control for fault-tolerant capability," in *Electric Machines and Drives Conference Record, 1997. IEEE International*, 1997, pp. WA1/1.1-WA1/1.6.

[115] B. Wang, J. Wang, and A. Griffo, "A Fault Tolerant Machine Drive Based on Permanent Magnet Assisted Synchronous Reluctance Machine " in *Energy Conversion Congress and Exposition (ECCE), 2016 IEEE*, Milwaukee, WI, 2016, pp. 1-8.

[116] J. Wang, V. I. Patel, and W. Wang, "Fractional-Slot Permanent Magnet Brushless Machines with Low Space Harmonic Contents," *Magnetics, IEEE Transactions on,* vol. 50, pp. 1-9, 2014.

[117] Q. Chen, G. Liu, W. Zhao, L. Sun, M. Shao, and Z. Liu, "Design and Comparison of Two Fault-Tolerant Interior-Permanent-Magnet Motors," *IEEE Transactions on Industrial Electronics,* vol. 61, pp. 6615-6623, 2014.

[118] T. M. Jahns and V. Caliskan, "Uncontrolled generator operation of interior PM synchronous machines following high-speed inverter shutdown," *IEEE Transactions on Industry Applications,* vol. 35, pp. 1347-1357, 1999.

[119] L. Chong-Zhi, W. L. Soong, B. A. Welchko, and N. Ertugrul, "Uncontrolled generation in interior permanent-magnet Machines," *IEEE Transactions on Industry Applications,* vol. 41, pp. 945-954, 2005.

[120] G. Pellegrino, A. Vagati, and P. Guglielmi, "Design Tradeoffs Between Constant Power Speed Range, Uncontrolled Generator Operation, and Rated Current of IPM Motor Drives," *IEEE Transactions on Industry Applications,* vol. 47, pp. 1995-2003, 2011.

[121]   S. S. Nair, V. I. Patel, and J. Wang, "Post-Demagnetization Performance Assessment for Interior Permanent Magnet AC Machines," *IEEE Transactions on Magnetics,* vol. 52, pp. 1-10, 2016.

[122]   A. Fasolo, L. Alberti, and N. Bianchi, "Performance Comparison Between Switching-Flux and IPM Machines With Rare-Earth and Ferrite PMs," *IEEE Transactions on Industry Applications,* vol. 50, pp. 3708-3716, 2014.

[123]   T. Kamel, C. Diduch, Y. Bilestkiy, and L. Chang, "Fault diagnoses for the Dc filters of power electronic converters," in *2012 IEEE Energy Conversion Congress and Exposition (ECCE)*, 2012, pp. 2135-2141.

[124]   J. Wang and D. Howe, "A Power Shaping Stabilizing Control Strategy for DC Power Systems With Constant Power Loads," *IEEE Transactions on Power Electronics,* vol. 23, pp. 2982-2989, 2008.

[125]   J. W. Bennett, G. J. Atkinson, B. C. Mecrow, and D. J. Atkinson, "Fault-Tolerant Design Considerations and Control Strategies for Aerospace Drives," *Industrial Electronics, IEEE Transactions on,* vol. 59, pp. 2049-2058, 2012.

[126]   B. C. Mecrow, A. G. Jack, D. J. Atkinson, S. R. Green, G. J. Atkinson, A. King*, et al.*, "Design and testing of a four-phase fault-tolerant permanent-magnet machine for an engine fuel pump," *Energy Conversion, IEEE Transactions on,* vol. 19, pp. 671-678, 2004.

[127]   T. Raminosoa, C. Gerada, and M. Galea, "Design Considerations for a Fault-Tolerant Flux-Switching Permanent-Magnet Machine," *Industrial Electronics, IEEE Transactions on,* vol. 58, pp. 2818-2825, 2011.

[128]   P. Arumugam, T. Hamiti, C. Brunson, and C. Gerada, "Analysis of Vertical Strip Wound Fault-Tolerant Permanent Magnet Synchronous Machines," *Industrial Electronics, IEEE Transactions on,* vol. 61, pp. 1158-1168, 2014.

[129]   L. Chen, J. Wang, P. Lazari, and X. Chen, "Optimizations of a permanent magnet machine targeting different driving cycles for electric vehicles," in *Electric Machines & Drives Conference (IEMDC), 2013 IEEE International*, 2013, pp. 855-862.

[130]   L. Chen, J. Wang, P. Lombard, P. Lazari, and V. Leconte, "Design optimisation of permanent magnet assisted synchronous reluctance machines for electric vehicle applications," in *Electrical Machines (ICEM), 2012 XXth International Conference on*, 2012, pp. 2647-2653.

[131]   F. Fiorillo and A. Novikov, "An improved approach to power losses in magnetic laminations under nonsinusoidal induction waveform," *Magnetics, IEEE Transactions on,* vol. 26, pp. 2904-2910, 1990.

[132]   P. H. Mellor, R. Wrobel, and D. Holliday, "A computationally efficient iron loss model for brushless AC machines that caters for rated flux and field weakened operation," in *Electric Machines and Drives Conference, 2009. IEMDC '09. IEEE International*, 2009, pp. 490-494.

[133] V. I. Patel, J. Wang, W. Wang, and X. Chen, "Analysis and design of 6-phase fractional slot per pole per phase permanent magnet machines with low space harmonics," in *Electric Machines & Drives Conference (IEMDC), 2013 IEEE International*, 2013, pp. 386-393.

[134] P. H. Mellor, D. Roberts, and D. R. Turner, "Lumped parameter thermal model for electrical machines of TEFC design," *Electric Power Applications, IEE Proceedings B,* vol. 138, pp. 205-218, 1991.

[135] J. Wang, W. Wang, K. Atallah, and D. Howe, "Design of a linear permanent magnet motor for active vehicle suspension," in *2009 IEEE International Electric Machines and Drives Conference*, 2009, pp. 585-591.

[136] P. Lazari, J. Wang, and L. Chen, "A Computationally Efficient Design Technique for Electric-Vehicle Traction Machines," *Industry Applications, IEEE Transactions on,* vol. 50, pp. 3203-3213, 2014.

[137] M. Palmieri, M. Perta, F. Cupertino, and G. Pellegrino, "High-speed scalability of synchronous reluctance machines considering different lamination materials," in *IECON 2014 - 40th Annual Conference of the IEEE Industrial Electronics Society*, 2014, pp. 614-620.

[138] L. Chen, X. Chen, B. Wang, and P. Lazari, "A computationally efficient multi-physics optimization technique for permanent magnet machines in electric vehicle traction applications," in *2015 IEEE International Electric Machines & Drives Conference (IEMDC),*, 2015, pp. 1644-1650.

[139] T. M. Jahns and W. L. Soong, "Pulsating torque minimization techniques for permanent magnet AC motor drives-a review," *IEEE Transactions on Industrial Electronics,* vol. 43, pp. 321-330, 1996.

[140] C. M. Spargo, B. C. Mecrow, and J. D. Widmer, "A Seminumerical Finite-Element Postprocessing Torque Ripple Analysis Technique for Synchronous Electric Machines Utilizing the Air-Gap Maxwell Stress Tensor," *IEEE Transactions on Magnetics,* vol. 50, pp. 1-9, 2014.

[141] J. A. Haylock, B. C. Mecrow, A. G. Jack, and D. J. Atkinson, "Operation of fault tolerant machines with winding failures," *Energy Conversion, IEEE Transactions on,* vol. 14, pp. 1490-1495, 1999.

[142] N. A. Al-Nuaim and H. Toliyat, "A novel method for modeling dynamic air-gap eccentricity in synchronous machines based on modified winding function theory," *IEEE Transactions on Energy Conversion,* vol. 13, pp. 156-162, 1998.

[143] J. Faiz, I. T. Ardekanei, and H. A. Toliyat, "An evaluation of inductances of a squirrel-cage induction motor under mixed eccentric conditions," *IEEE Transactions on Energy Conversion,* vol. 18, pp. 252-258, 2003.

[144] X. Chen, J. Wang, V. I. Patel, and P. Lazari, "A Nine-Phase 18-Slot 14-Pole Interior Permanent Magnet Machine With Low Space Harmonics for Electric Vehicle Applications," *IEEE Transactions on Energy Conversion,* vol. 31, pp. 860-871, 2016.

[145] X. Chen, J. Wang, B. Sen, P. Lazari, and T. Sun, "A High-Fidelity and Computationally Efficient Model for Interior Permanent-Magnet Machines Considering the Magnetic Saturation, Spatial Harmonics, and Iron Loss Effect," *IEEE Transactions on Industrial Electronics,* vol. 62, pp. 4044-4055, 2015.

[146] J. Faiz and I. Tabatabaei, "Extension of winding function theory for nonuniform air gap in electric machinery," *Magnetics, IEEE Transactions on,* vol. 38, pp. 3654-3657, 2002.

[147] A. H. Bonnett and G. C. Soukup, "Cause and analysis of stator and rotor failures in three-phase squirrel-cage induction motors," *Industry Applications, IEEE Transactions on,* vol. 28, pp. 921-937, 1992.

[148] H. Akagi, Y. Kanazawa, and A. Nabae, "Instantaneous Reactive Power Compensators Comprising Switching Devices without Energy Storage Components," *IEEE Transactions on Industry Applications,* vol. IA-20, pp. 625-630, 1984.

[149] C. Dae-Woong and S. Seung-Ki, "Analysis and compensation of current measurement error in vector-controlled AC motor drives," *IEEE Transactions on Industry Applications,* vol. 34, pp. 340-345, 1998.

[150] P. Lazari, B. Sen, J. Wang, and X. Chen, "Accurate d and q Axis Modeling of Synchronous Machines With Skew Accounting for Saturation," *IEEE Transactions on Magnetics,* vol. 50, pp. 1-4, 2014.

[151] V. I. Patel, "Novel 6-phase fractional slot PM machine for electric vehicle applications," in *the University of Sheffield*, PhD thesis, 2014.

[152] B. Bossmanns and J. F. Tu, "A Power Flow Model for High Speed Motorized Spindles—Heat Generation Characterization," *Journal of Manufacturing Science and Engineering,* vol. 123, pp. 494-505, 2000.

List of Figures

List of Tables

APPENDIX A
Machine Prototype Solidworks Drawings

The Solidworks drawings of the machine prototype drawings are shown as follows. They are manufactured in the University mechanical workshop.
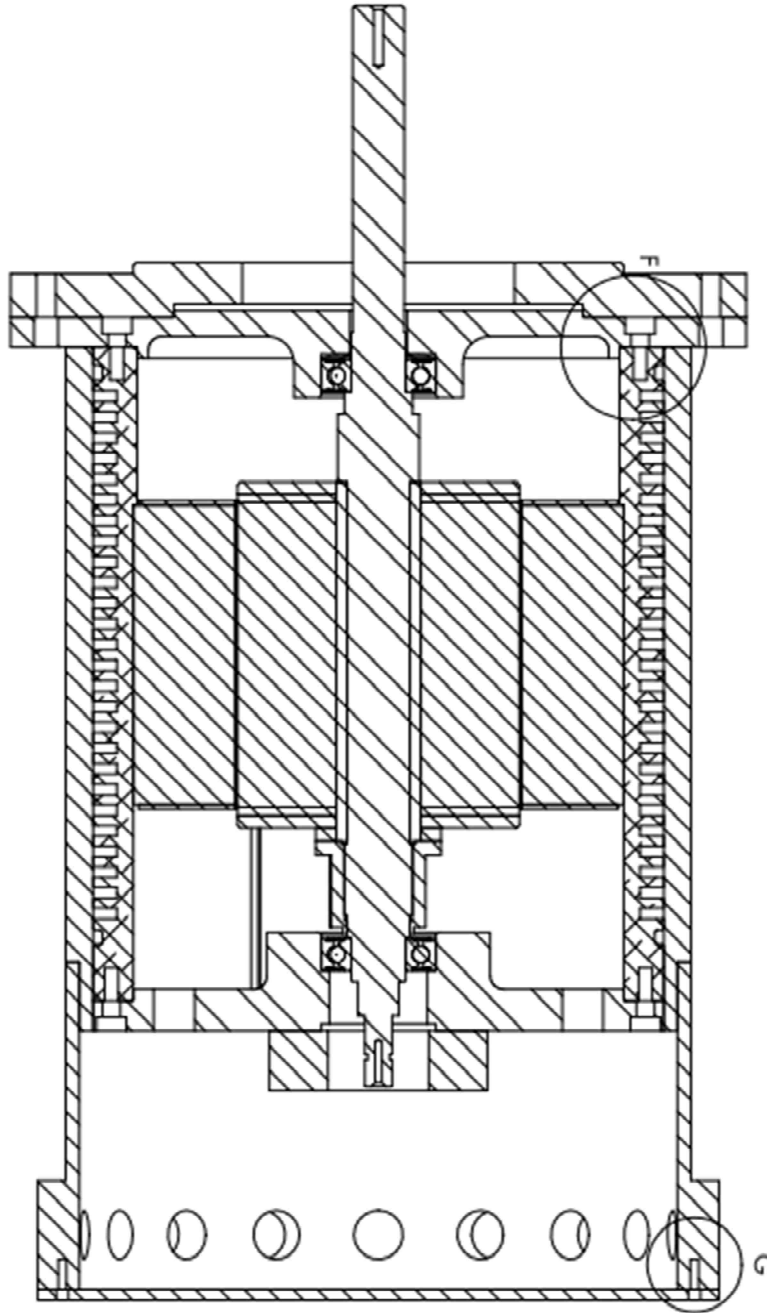

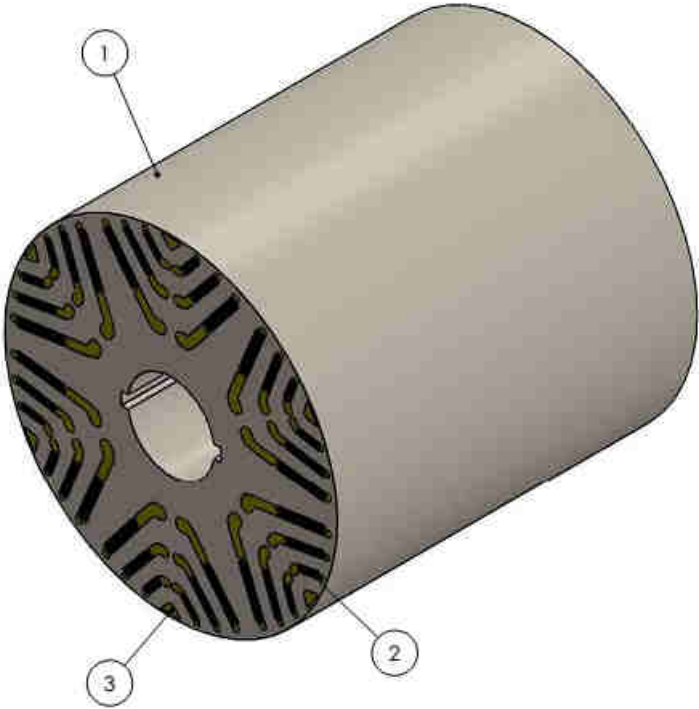Fig. A-1. Cross section of machine assembly

Fig. A-2. Skewed stator stack

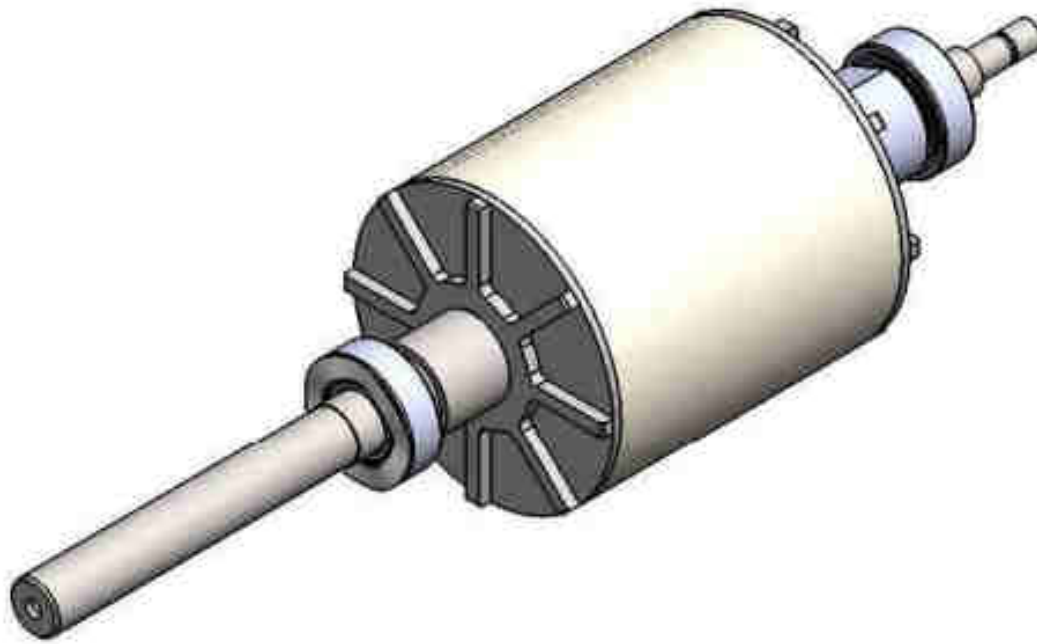

Fig. A-3. Rotor stack with magnets and epoxy

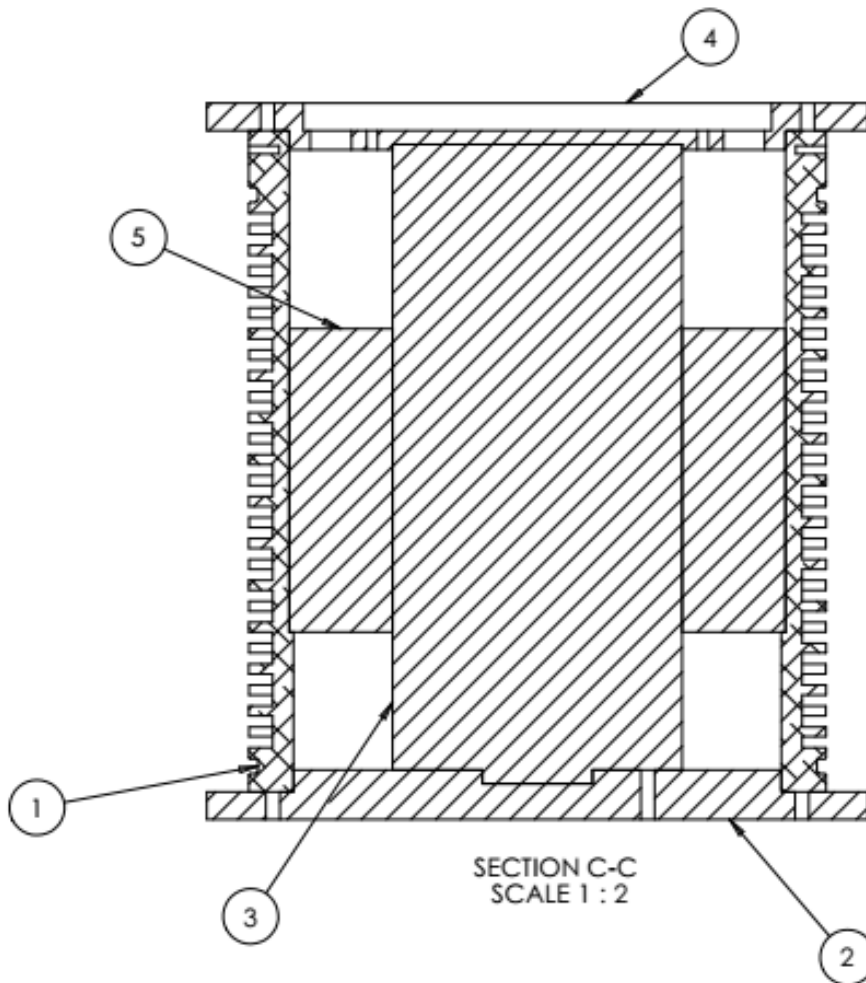Fig. A-4. Solidworks drawing of rotor assembly

Fig. A-5. Cross section of stator potting too assembly

APPENDIX B Winding Layout for Manufacturing

The winding layout illustration for manufacturing is described as follows. The turn fault is emulated in set ABC by bringing one turn tap out in coil B2 as shown in Fig. B-1. The winding layout of the healthy sets DEF and GHI are shown in Fig. B-2 and Fig. B-3.
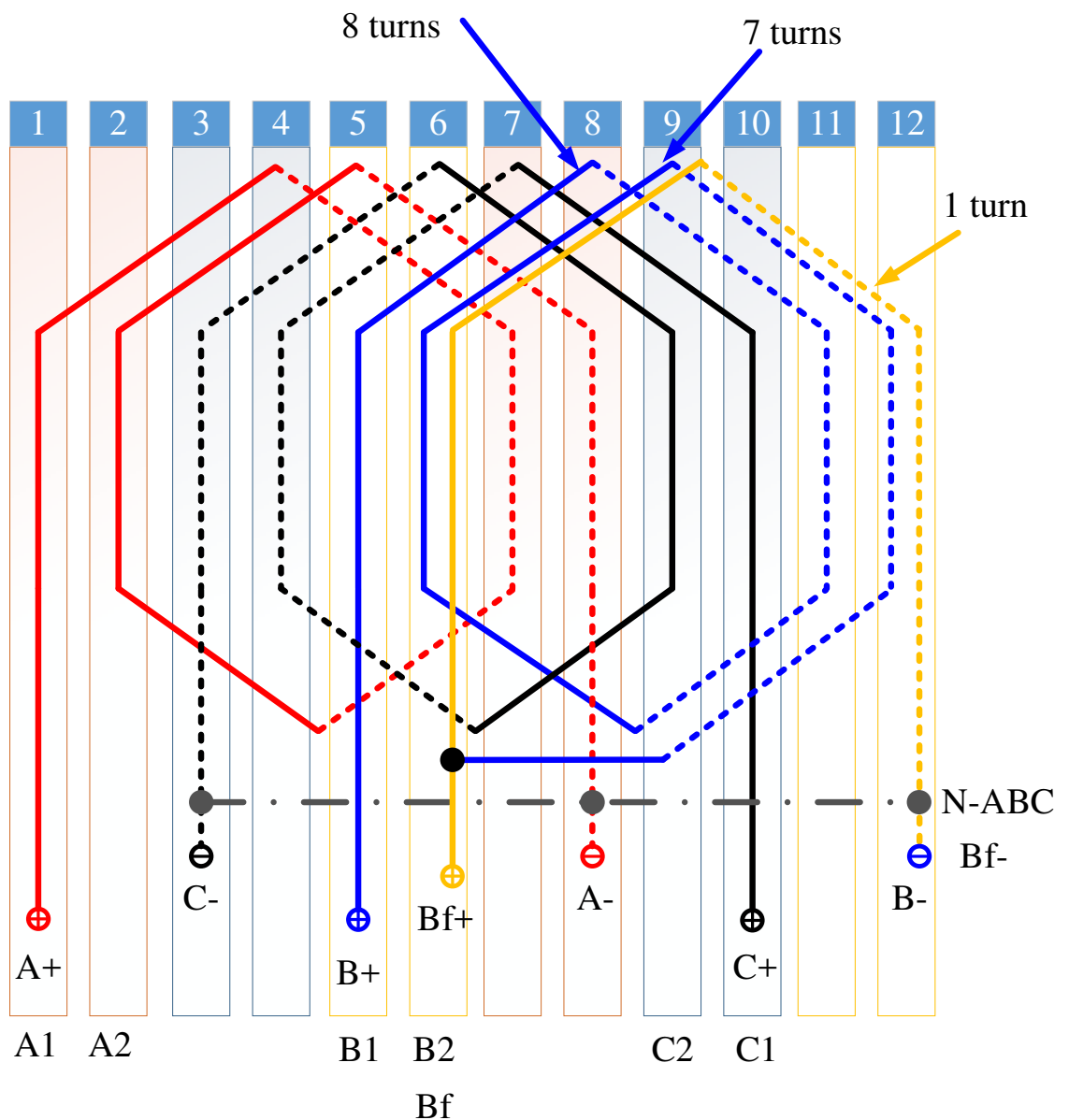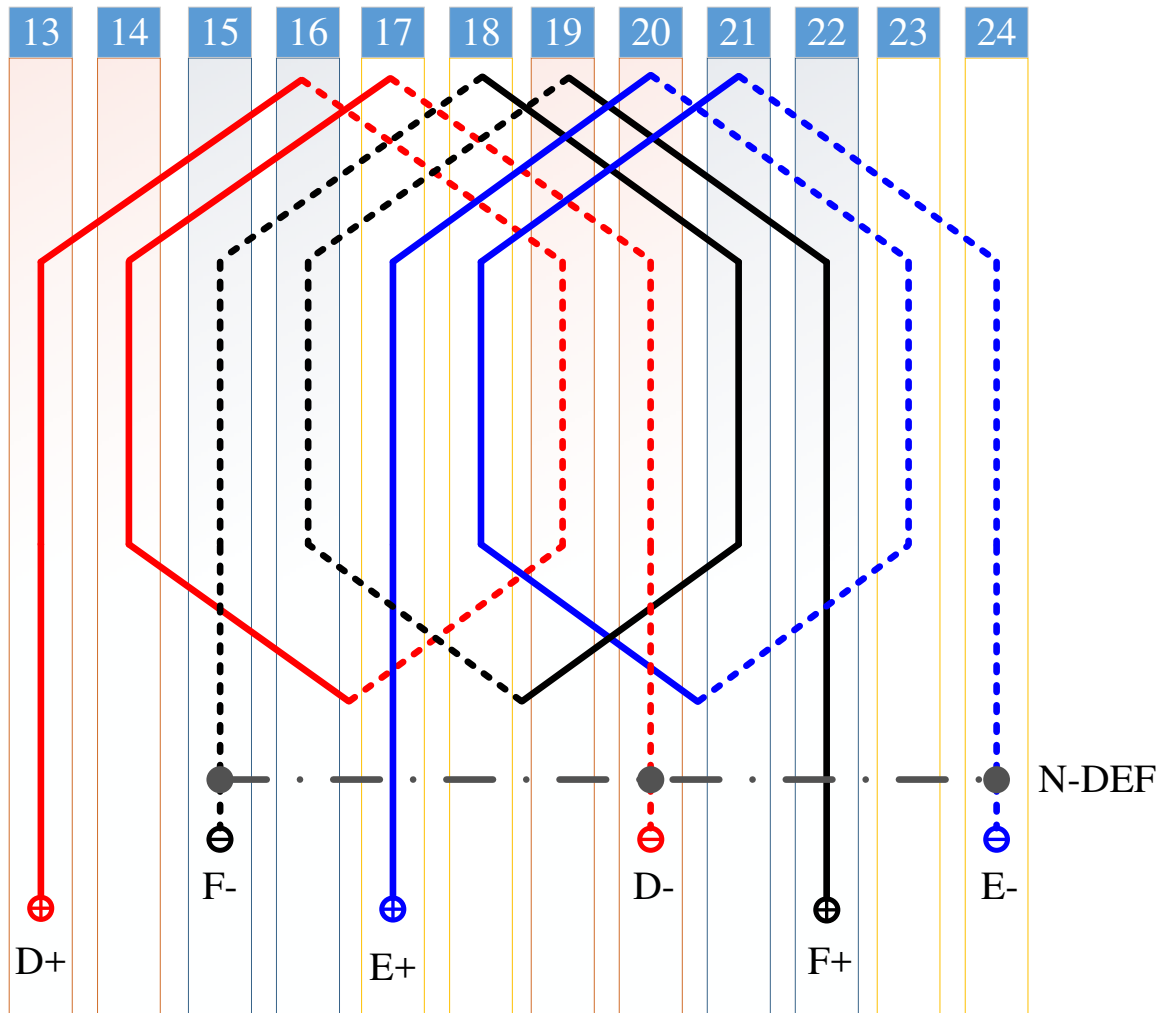

Fig. B-1. Winding diagram in set ABC

Fig. B-2. Winding diagram in set DEF

Fig. B-3. Winding diagram in set GHI

APPENDIX C   General Model in Matlab

The general model proposed in Chapter 4 is implemented in Matlab. For simple illustration, the model has been decomposed into several function blocks as below.
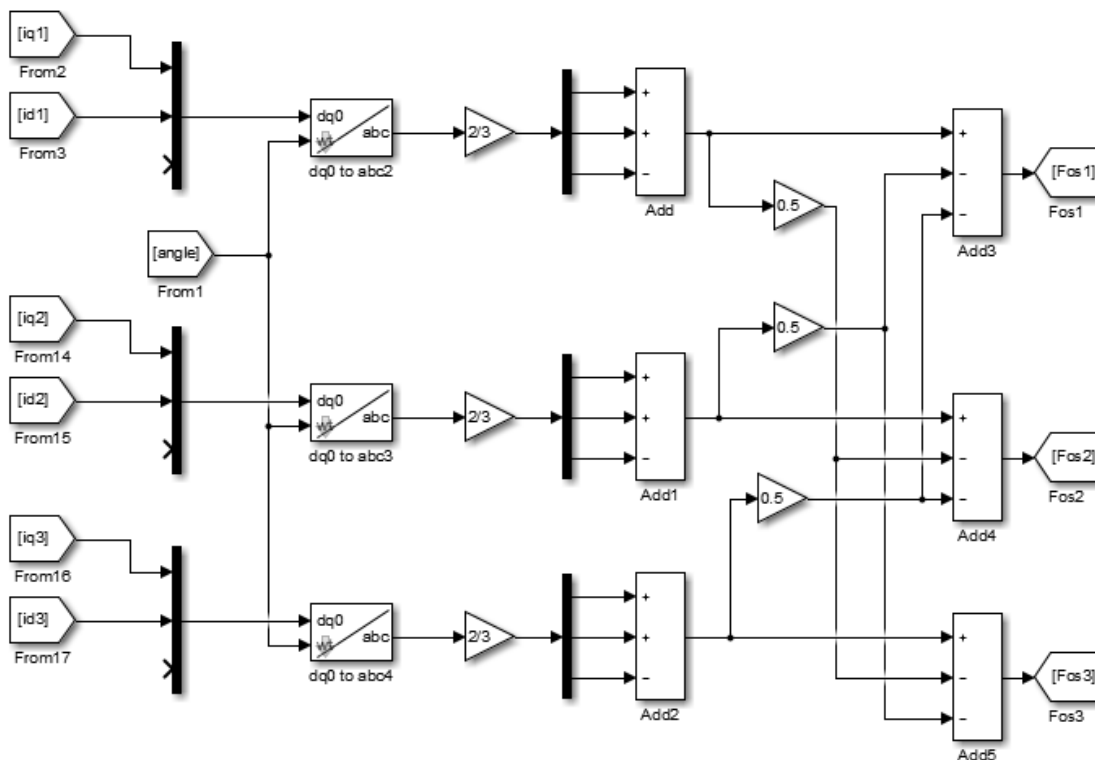

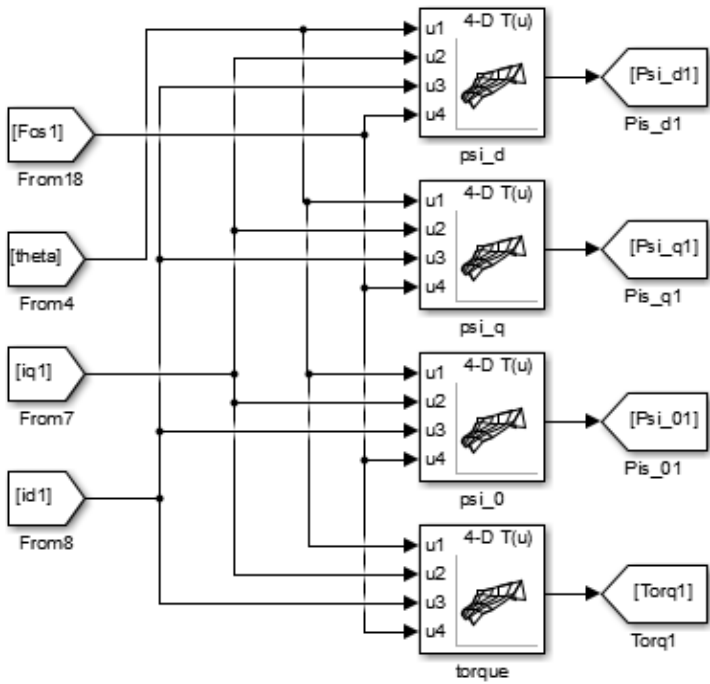
Fig. C-1. F_{os} calculation block

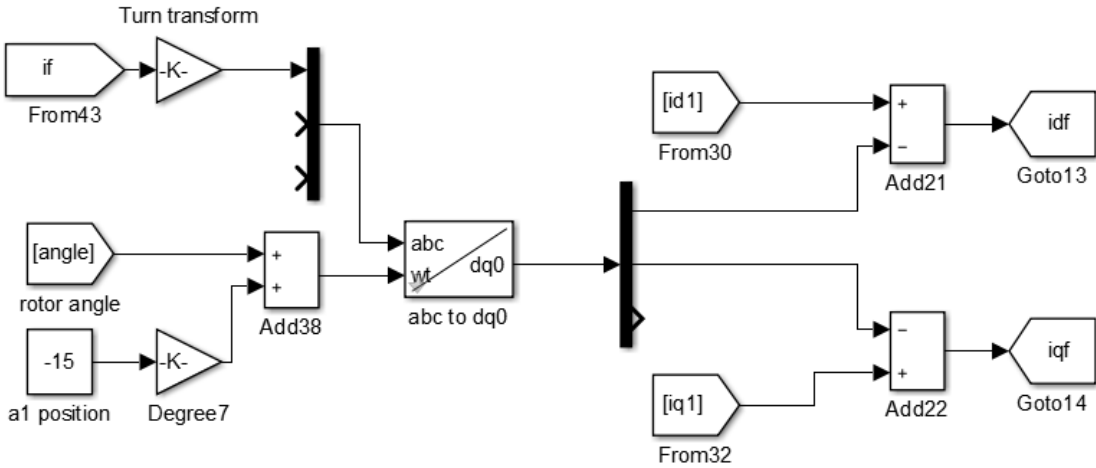Fig. C-2. Lookup table interpolation for set ABC

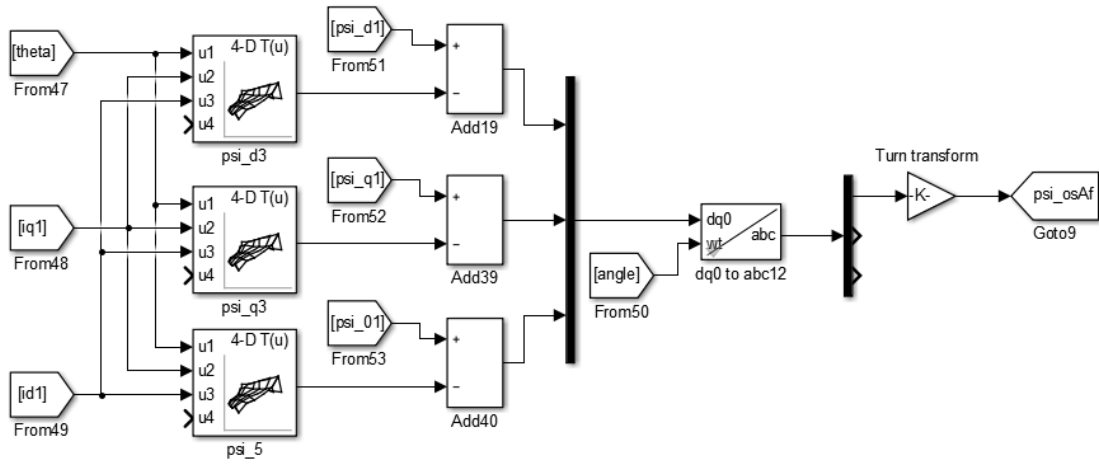Fig. C-3. Equivalent inputs for fault set ABC

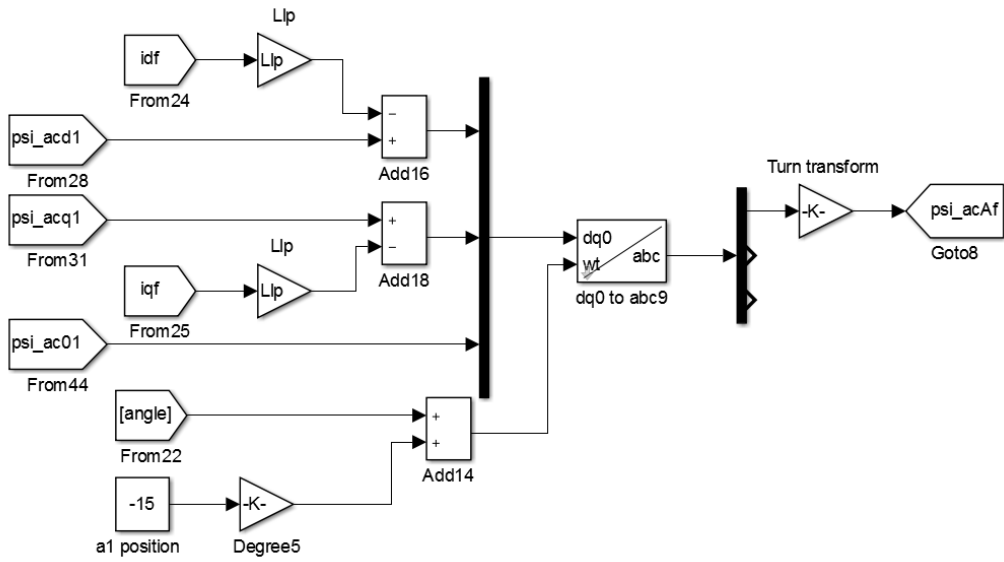Fig. C-4. Flux linkage of the fault turn induced by MMF offset component

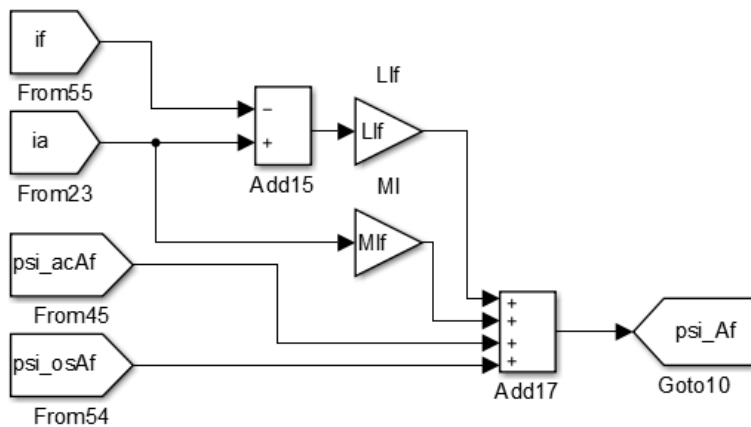Fig. C-5. Flux linkage of the fault turn induced by MMF AC component and PM

Fig. C-6. Total flux linkage of the fault turn

APPENDIX D   Turn Fault Detection Code

The 2nd harmonic in IAP and IRP based turn fault detection code is attached as below. It is mainly based on the flowchart in Fig. 5-5 and fault judging criteria in equation (5-12).

```
#include "UsrHeader.h"

#define ENABLE              1

#define DISABLE        0

#define WETEST        2*3.1415926*400.0

#define  Ts           100e-6

#define PWMANGCONST 0.00015

#define PSIM 0.0247

#define Ls        1.3e-3

#define Ld 0.4e-3

#define Lq 1.3e-3

//Core to Core Communications

#pragma DATA_SECTION(Cpu1toCpu2,"Cpu1toCpu2MsgsFile");

volatile CPU1TOCPU2 Cpu1toCpu2;

#pragma DATA_SECTION(Cpu2toCpu1,"Cpu2toCpu1MsgsFile");

volatile CPU2TOCPU1 Cpu2toCpu1;

struct CPU1TOCPU2CTRL_REGS Cpu1toCpu2Signal;

struct CPU2TOCPU1CTRL_REGS Cpu2toCpu1Signal;

Uint16 IPC1CPU2Counter =0, IPC1CPU1Counter=0;

Uint16 Cpu1CtrlFlag=0,Cpu2CtrlFlag=0;

Uint32 FaultCounter = 0;
```

```
//PLL

// Alpha = 5;

#define PLL_I_gain   195312.5 //800000.0 //alpha =5

#define PLL_K  1250.0 //2000.0 //alpha=5

#define WE2RPM 3.183098861837907 //

#define COEFF_PLLRPMFLT_U 0.00624599554512887 // we = 2*pi*20

#define COEFF_PLLRPMFLT_Y 0.987508008909742

float PLL_t=0.0, PLL_t_prev =0.0, PLL_cos_t=0.0, PLL_sin_t=0.0;

float       PLL_error=0.0,PLL_error_prev=0.0,       PLL_WeInt       =0.0,
PLL_WeInt_prev =0.0, PLL_We=0.0;

float    PLL_RPM    =0.0,    PLL_RPM_flt    =0.0,    PLL_RPM_k_1    =0.0,
PLL_RPM_flt_prev=0.0;

float sign = -1, time = 0, tcmd = -1 , cycle_count = 0;//for relay control

float pqsh = 0, pqshtemp = 0, pqshtemp1 = 0, pqshtemp0 = 0, pqsh_cpu2 = 0,
harmonic_reference = 100000;//for fault detection.

float rotor_freq = 0,    wf = 0, damp = 0.71, omega = 0, sin_value = 0,
cos_value = 0, Tflpf=1/(2*PI*20);

float pq = 0, pq_1 = 0, pqtemp = 0, y1 = 0, y1_2 = 0, y1_1 = 0, y1H = 0;

float y1_s = 0, y1_s_L = 0, y1_s_L_2 = 0, y1_s_L_1 = 0;

float y1_c = 0, y1_c_L = 0, y1_c_L_2 = 0, y1_c_L_1 = 0;//for fault detection.

Uint16 Fault_alarm = 0, Fault_count = 0, Fault_tsc = 0, transientstart = 0;


float pqsh_filter(float pq)

{    //please relate this function to the bottom graph of Fig. 5-5.

    //filter the instantaneous active power and reactive power to get the
magnitude of the 2nd hamronics

    rotor_freq=abs(rotor.RPM)/20;//calculate the electrical frequency
```

```
damp=0.71;//damping ratio

omega=omega+2*PI*(rotor_freq*2)*Ts;

if (omega>2*PI)

        {omega=omega-2*PI;}

sin_value=sin(omega);

cos_value=cos(omega);

//set1 pq as input active power or reactive power;

//y1_1=y1(n-1);y1_2=y1(n-2);// initialized as zero;

//second order low pass filter

wf=4*PI*rotor_freq;//filter frequency

y1          =          (2*damp*(pq-pq_1)*wf*Ts+(2+2*damp*wf*Ts)*y1_1-
y1_2)/(1+2*damp*wf*Ts+wf*wf*Ts*Ts);

pq_1=pq;

y1_2=y1_1;

y1_1=y1;

y1H=y1;//make it as bandpass pass filter

wf=0.5*PI*rotor_freq;

//sin multiplication;

y1_s=y1H*sin_value;

//low pass filter for y1_s

y1_s_L          =          ((y1_s)*wf*wf*Ts*Ts+(2+2*damp*wf*Ts)*y1_s_L_1-
y1_s_L_2)/(1+2*damp*wf*Ts+wf*wf*Ts*Ts);

y1_s_L_2=y1_s_L_1;

y1_s_L_1=y1_s_L;

//cos multiplication;

y1_c=y1H*cos_value;

//low pass filter for y1_c
```

yl_c_L = ((yl_c)*wf*wf*Ts*Ts+(2+2*damp*wf*Ts)*yl_c_L_1-yl_c_L_2)/(1+2*damp*wf*Ts+wf*wf*Ts*Ts);

yl_c_L_2=yl_c_L_1;

yl_c_L_1=yl_c_L;

pqshtempl=__sqrt(yl_c_L*yl_c_L+yl_s_L*yl_s_L)*2;

pqshtemp=(pqshtempl*Ts+Tflpf*pqshtemp0)/(Tflpf+Ts);

pqshtemp0=pqshtemp;

return pqshtemp;

}

//fault detection part: Bo Wang 20170424

//**

//the active and reactive power is calculated. The detection is also realized in this section.

harmonic_reference=extrap2(current_fd,spd_fd,harmonic_lkp,6,4,__sqrt(current.d*current.d+current.q*current.q),abs(rotor.RPM));

//determine the reference signal from the lookup table.

if (rotor.we > 0)

{   if (current.q > 0)

                pqtemp=1.5*(current.d*vcmd.q-current.q*vcmd.d);

        else

                {pqtemp=1.5*(current.d*vcmd.d+current.q*vcmd.q);}

}

else

        {if (current.q > 0)

                pqtemp=1.5*(current.d*vcmd.d+current.q*vcmd.q);

        else

                {pqtemp=1.5*(current.d*vcmd.q-current.q*vcmd.d);}

}

pqsh=pqsh_filter(pqtemp);//using the 2nd harmonic extraction function

```
#if defined(CPU2USR)

    Cpu2toCpu1.fault_harmonic = pqsh; // send fault signal to cpu1

#endif

#if defined(CPU1USR)

    pqsh_cpu2 = Cpu2toCpu1.fault_harmonic; // send fault signal to cpu1

    if (pqsh > 1.5*pqsh_cpu2 && pqsh > 2*harmonic_reference )//two inequations for fault judgement.

//fault judging criterion

        Fault_alarm = 1;

    else

        {Fault_alarm = 0;// clear all the bits

        Fault_count = 0;     }

    if (Fault_alarm == 1 )

        {

        Fault_count = Fault_count + 1;// record for 10 samples to trigger the fault_tsc

        if (Fault_count > 10)

            Fault_count = 11;

        }


    if (Fault_count > 10 )

    {Fault_tsc = 10000;}
```

```
if (Fault_tsc > 0 )//&& GpioDataRegs.GPCDAT.bit.GPIO94 == 1

{       //vcmd.d = 0; vcmd.q = 0;//applying terminal short circuit;

        //Fault_tsc = Fault_tsc - 1;

}

else

        Fault_tsc=0;

if (cmd.ctrlbit.bit.CTRL_EN == 0 )

{

        Fault_tsc = 0;

        Fault_count=0;

        Fault_alarm=0;

}

#endif
```